Multi-Band Dual-Polarized Shared Aperture Microstrip Phased Array

by

Zhu Sun

Dissertation submitted in fulfillment of the requirements

for the degree of

DOCTOR OF PHILOSOPHY

Department of Engineering

Faculty of Science Macquarie University

Sydney, Australia

August - 2014

ABSTRACT

Multi-band systems are becoming increasingly popular in both military and civil applications such as tactical radar systems and synthetic aperture radar (SAR) systems because their information capacity is significantly higher than single-band counterparts. As the interface between free space and an internal waveguide, a multi-band antenna plays an important role in such systems.

A multi-band dual-polarized (MBDP) antenna array can be realized by simply positioning several single-band antenna arrays side-by-side. However, this approach is not desirable because it significantly increases the aperture size and antenna weight. The MBDP shared aperture antenna arrays studied in this thesis can minimize the array size and weight by sharing the aperture of each band. Therefore, it is attractive for some compact systems like space-borne SAR antennas and vehicle based tactical radars.

In this thesis, several contributions are made to the knowledge in MBDP shared aperture arrays. They are listed below.

1) Performance improving methods are presented for dual-band dual-polarized shared aperture (DBDP-SA) array. The inter-polarization isolation of the array was improved and the lower-band bandwidth was enhanced for a given antenna thickness. A prototype S/X DBDP-SA microstrip array has been designed and fabricated to verify these methods. Fractional frequency ratio is also achieved in a prototype array by adopting an interleaved dual band embedding structure.
2) A multi-band dual-polarized shared aperture (MBDP-SA) array design method is

proposed for SAR applications. To verify the feasibility of this method, an L/S/X tri-band dual-polarized shared aperture (TBDP-SA) array has been designed and fabricated. Good performance has been achieved in all three bands.

3) A novel sandwiched stacked-patch DBDP array is presented, with an aim to enhance the bandwidth in the lower band. Dual band embedding methods are also studied and compared in terms of their bandwidth performance. An L/C DBDP-SA sandwiched stacked patch array has been designed and fabricated to validate this new concept.

STATEMENT OF CANDIDATE

I certify that the work in this thesis has not previously been submitted for a degree nor has been submitted as part of the requirements for a degree to any other university or institute other than Macquarie University.

I also certify that the thesis is an original piece of research and has been written by me.

In addition, I certify that all information source and literature used are indicated in the thesis.

Zhu Sun, 17-Aug, 2014.

……..

Zhu Sun

ACKNOWLEDGEMENT

First of all, I want to give my deepest gratitude to my principal supervisor, Professor Karu P. Esselle, for his tutorial and help during the research work and my Ph.D. study. Without his consistent support, suggestions and encouragement, this work is less likely to be completed.

I am also grateful to my Chinese supervisor, Professor Shun-Shi Zhong (Shanghai University, China), for leading me to the antenna research field. His instruction gives me a clear perspective of the modern antenna. I deeply appreciate his support and dedication to me during these years.

I would express my profound thanks to my adjunct supervisor, Dr. Y. Jay Guo (CSIRO ICT center, Australia), for his guidance, inspiring ideas and supports throughout this research work. Besides, he broadens my horizons and enlightens me the way of thinking and analyzing.

Many thank to my sincerely friends and associated supervisor, Dr. Basit Zeb, for his contributions in thesis preparation and helps in paper writing.

I acknowledge the financial support from the International Macquarie University Research Scholarship (iMQRES) and Chinese Scholarship Council (CSC) that made this study possible.

I also acknowledge the support of my friends and fellows of the research group (CELANE) who spend their times and energies discussing, inspiring and brainstorming new

ideas in this research work.

Last but not least, many thanks to my parents, who paid all what they have to support me throughout my studies and my life. I also appreciate my wife for her understanding to support my studies.

To my Parents and Wife

List of Figures

List of Tables

Contents

Chapter 1
Introduction

Multi-band dual-polarized shared-aperture (MBDP-SA) arrays are antenna arrays that operate in two (or more) frequency bands with dual-polarization in each band, and whose elements are integrated together into a common physical space by sharing the single aperture. They are also known as multi-band co-aperture dual-polarized arrays in the literature.

1.1 Motivation

The space-/air-borne synthetic aperture radar (SAR) is the main motivation and perhaps the most important application for MBDP-SA antenna arrays.

Because the back scattering matrix of a ground target depends on frequency, polarization and incidence angle of the incident wave, as shown in the Fig.1-1. The higher-band wave reflects primarily at the crown of the tree, while lower-band wave can penetrate the leaves and reflect at the root of the forest. Hence, a MBDP SAR system can obtain more information to better distinguish and retrieve ground targets [1-6], as presented in Fig.1-2 [1], SAR images

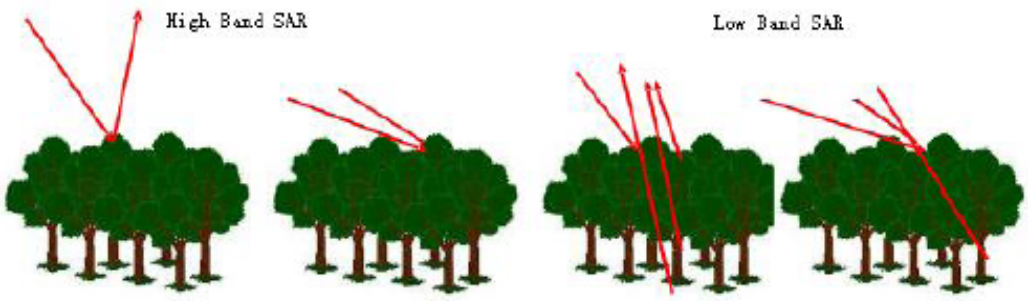

Fig.1 - 1 Scattering model of high- or low-band SAR [1]

(b) X-band SAR image

(c) L-band SAR image

(d) C-band HV polar SAR image

(e) C-band HH polar SAR image

(c) C-band VV polar SAR image

Fig.1 - 2 SAR images of different bands and polarizations [1]

(a) Photo of antenna

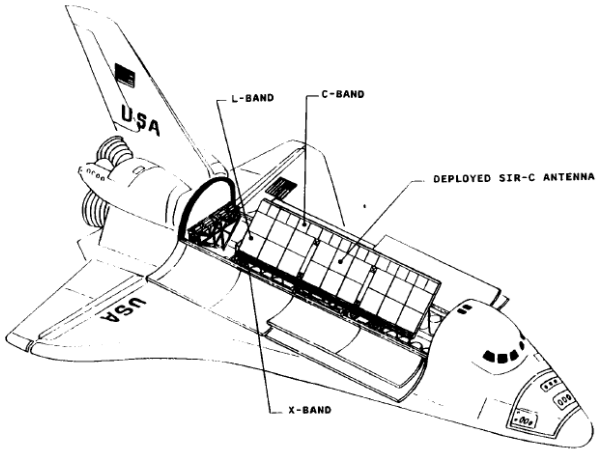

(b) Deployed antenna in the Shuttle Payload Bay

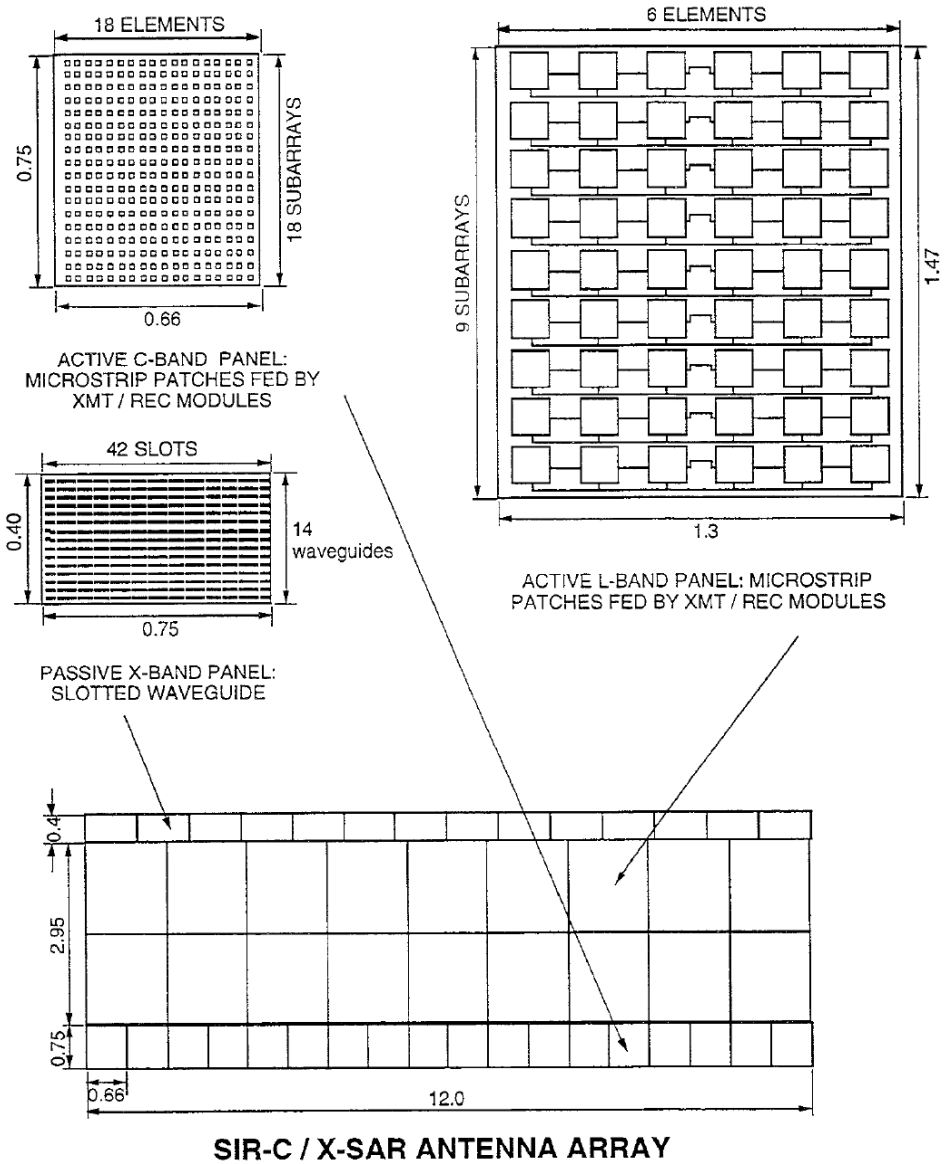

(c) Antenna Aperture Configuration

Fig.1 - 3 SIR-C/X-SAR antenna [7-10]

with different resolution and textures can be obtained through utilizing different bands and polarizations. This merit makes MBDP SAR systems more advantageous than their single-band peers. In general, the relationship between MBDP- and single-band SAR systems is analogous to that between color and black-white cameras, respectively.

Side-by-side configured independent single-band arrays, such as the SIR-C/X-SAR antenna [7-10] shown in Fig.1-3, can fulfill the multi-band operating requirements. However, a minimum aperture area in each band is required to avoid image ambiguity [11], which results in a bulky antenna for independent sub-array designs, such as the SIR-C/X-SAR antenna in Fig.1-3, whose L/C/X tri-band independent antennas occupies 44% of the overall system (3.3 tons of 7.5 tons) weight and has a width of more than 4m [12]. The MBDP-SA array technique can reduce the antenna weight and size by sharing the aperture in each band, increasing the payload efficiency, and hence is perhaps the most promising antenna techniques for such applications at present.

1.2 Thesis Organization

The thesis is organized in six chapters including this introductory chapter, which introduces the MBDP-SA array and provides an overview of the thesis. The main contents of the thesis are briefly discussed below.

Chapter 2 presents some general principles of DBDP-SA array design, followed by a literature review and the current state of the art on MBDP aperture integration. Some specific techniques, such as isolation improving method, are further reviewed in Chapters 3, where they are employed.

Chapter 3 presents an S/X DBDP-SA microstrip antenna with fractional frequency ratio of 3.5:1. The polarization ports of both bands are highly decoupled by implementing a hybrid feeding method and an H-shaped configuration in higher- and lower-bands, respectively. The inter-band coupling is discussed and a solution is presented.

Chapter 4 presents an L/S/X tri-band dual-polarized shared-aperture (TBDP-SA) array. The array consists of L/S and L/X DBDP-SA arrays and an L single-band dual-polarized (SBDP) array. Good bandwidth and radiation patterns are confirmed in all three bands, and especially for the L band, whose aperture consists of L/S, L/X and L array.

In Chapter 5, a sandwiched perforated DBDP-SA array is proposed based on the studies of overlapped DBDP structure and perforated patch structure with the aim of improving the lower-band bandwidth for the given overall antenna profile. The measured results show that the proposed structure has a better bandwidth-to-profile ratio. The advantages and disadvantages are also discussed.

The thesis is concluded in the Chapter 6 where some suggestions for future work are also provided.

1.3 Thesis Contributions

In the thesis, three different MBDP-SA antenna arrays are designed, analyzed and compared. Based on the MBDP design experience, the contributions of this thesis are listed below:

Major Achievements:

1. An S/X interleaved DBDP-SA microstrip array with highly decoupled polarization ports

in both bands is designed and tested in Chapter 3. The array isolation of better than 35dB and 45dB is achieved in S and X band, respectively, which is about 5dB better than the best results [119] the author ever known.

2. A novel MBDP-SA SAR array design method, called 'assembling' method, is proposed for SAR applications in Chapter 4. This method take the different DBDP-SA sub-arrays as basic modules, and construct MBDP-SA full array by joining the different modules together. The feasibility of the proposed method is validated by the L/S/X TBDP-SA prototype array, which is realized by joining two well designed DBDP-SA and a SBDP sub-arrays together. This method can be further extended to a quad-band dual-polarized shared-aperture array by adopting more DBDP-SA sub-arrays. For the best of author's knowledge, the L/S/X TBDP prototype array is the first tri-band microstrip planar array reported.
3. A modified perforated patch structure, called the sandwiched perforated DBDP array is proposed in Chapter 5, aiming to improve the lower-band bandwidth for the given overall antenna profile. The perforation number in the proposed structure is reduced as compared to perforated patch structure, to avoid the bandwidth reduction in lower-band patch. The bandwidth improvement of this structure is estimated to be about 2.5 percentages. The feasibility of this structure is validated by the prototype array, and its better lower-band bandwidth-to-profile ratio is also observed.

Other Achievements:

1. The fractional frequency ratio of 1:3.5 in interleaved DBDP-SA array design has been validated in Chapter 3.

2. Tri-resonate design is achieved to improve the lower-band bandwidth in S/X DBDP-SA array in Chapter 3. A $|S_{11}| \leq$ -15 dB bandwidth of 10% is achieved in the lower band, which is the best bandwidth ever realized for the similar antenna profile in interleaved DBDP structure.
3. The higher-band elements' polarization isolation in DBDP-SA array is studied in Chapter 3. The relationship between the elements' polarization isolation and inter-band coupling is disclosed using an experimental method. The possible methods of improving element polarization isolation are analyzed and recommended.
4. The overlapped DBDP structure is preliminarily studied in Chapter 5. A unit cell composes 1 x 1 L-band element and 2 x 2 C-band elements is designed and tested, where the merits (mainly refer to lower-band bandwidth) and limitations (frequency ratio choice and feeding restriction) are concluded.

1.4 List of Publications

Some published research outputs during my PhD study are listed as below:

Refereed Journal papers

1. Zhu Sun, Shunshi Zhong, Lingbing Kong, Chu Gao, Wei Wang and Mouping Jin, "Dual-Band Dual-Polarised Microstrip Array with Fractional Frequency Ratio", Electronics Letters, vol. 48, no. 12, pp. 674-676, Jun. 2012.

2. Zhu Sun, Karu P. Esselle, Shunshi Zhong and Y. Jay Guo, "Shared-Aperture Dual-Band Dual-Polarization Array Using Sandwiched Stacked Patch", Progress In Electro-magnetics Research C, (Accepted), 2014.

3. Shunshi Zhong, Zhu Sun, Lingbing Kong, Chu Gao, Wei Wang and Mouping Jin, "Tri-Band Dual-Polarization Shared-Aperture Microstrip Array for SAR Applicat-

ions", IEEE Transactions on Antennas and Propagation, vol.60, no.9, pp. 4157-4165, Sept. 2012.

4. Lingbing Kong, Shunshi Zhong and Zhu Sun, "Broadband Microstrip Element Design of a DBDP Shared-Aperture SAR Array", Microwave and Optical Technology Letters, vol.54, no.1, pp. 133-136. Jan. 2012.

5. Basit Ali Zeb, Yuehe Ge, Karu P. Esselle, Zhu Sun and Michael E. Tobar, "A Simple Dual- Band Electromagnetic Band Gap Resonator Antenna Based on Inverted Reflection Phase Gradient", IEEE Transactions on Antennas and Propagation, vol. 60, no. 10, pp. 4522-4529, Oct. 2012.

6. Min Guo, J. J. Yan, Shunshi Zhong and Zhu Sun, "Wideband Circularly Polarized Dielectric Rod Antenna", International Journal Antennas Propagation, vol. 2012, ID: 324197.

7. Jianjun Liu, Karu P. Esselle, Stuart Hay, Zhu Sun and Shunshi Zhong, "A Compact Super-Wideband Antenna Pair With Polarization Diversity", IEEE Antennas and Wireless Propagation Letters, vol. 12, Issue. 1, pp. 1472-1475, 2013.

Refereed Conference papers

1. Zhu Sun and Shunshi Zhong, "High-Gain Thinned Array with limited scan capability", 2011 China-Japan Joint Microwave Conference Proceedings (CJMW 2011), Hangzhou, China, pp. 1-4, Apr. 2011.

2. Zhu Sun, Shunshi Zhong, Xiaorong Tang and Jianjun Liu, "C-Band Dual-Polarized Stacked-Patch Antenna with Low Cross-Polarization and High Isolation", 2009 European Conference on Antennas and Propagation (EuCAP 2009), Berlin, Germany, pp. 2994-2997, Mar. 2009.

3. Shunshi Zhong, Zhu Sun, Lingbing Kong, Chu Gao, Wei Wang and Mouping Jin, "Design of TBDP Shared-Aperture SAR Array", 2011 Asia-Pasific Microwave Conference (APMC 2011) Proceedings, Melbourne, Australia, pp. 159-162, Dec.

2011.

4. Chunxiang Meng, Wenhui Shen, Zhu Sun, Shunshi Zhong and Karu P. Esselle, “A Novel L/C- Band Dual-Polarized Half-Perforated Antenna Element for SAR Arrays”, 2011 Asia-Pasific Microwave Conference (APMC 2011) Proceedings, Melbourne, Australia, pp. 701-704, Dec. 2011.

5. Yuehe. Ge, Zhu Sun and Karu P. Esselle, “Simple Thin Partial Reflective Surface for Dual-band Fabry-Parot Resonator Antennas”, Proceedings of the 2011 International Symposium on Antennas and Propagation (ISAP2011), Jeju, South Korea, Oct. 2011.

Patents

1. Shunshi Zhong and Zhu Sun, "S/X Dual-Band Dual-Polarized Microstrip Dipole/ Microstrip Stacked Patch for Phased Array", Chinese Patent, accepted by China Patent Bureau (CPB), Publish Number: CN101982899B.

2. Shunshi Zhong, Zhu Sun and Lingbing Kong, "L/S/X Tri-Band Dual-Polarized Planar antenna array", Chinese Patent, accepted by China Patent Bureau (CPB), Publish Number: CN101982900B.

Chapter 2
Literature Review

2.1 Introduction

The multi-band dual-polarized shared-aperture (MBDP-SA) arrays introduced in the thesis refer to the array that have several bands embedded in the same array aperture. By sharing part- or full-aperture, the array can reduce the size and weight of overall antenna (compare to independent MBDP array). The origins of MBDP-SA array can be traced back to 1990s as potential antennas for multi-band space-borne SAR systems.

Ideally speaking, an UWB or SWB array such as a Vivaldi antenna [15-21] or a connected dipole array [22-28] can also be employed to minimize the aperture size, because it can cover multi-bands with only a single aperture. However, from engineering point of view, the UWB and SWB arrays are less suitable for the space-borne SAR applications, because:

1) The element spacing is based on the smallest wavelength in the operating bandwidth to avoid the grating lobes at higher frequency. Thus, at lower frequency, the elements are too densely distributed. For example, an UWB array covering four octaves will have a lower frequency element spacing of 1/8 wavelength, assuming it is half-wavelength spaced at the higher frequency. More elements and corresponding T/R modules are thus required than the MBDP-SA antenna actually needs. Hence, UWB and SWB arrays are less feasible due to the high cost, large weight and difficulties in heat control of large amount of T/R module.
2) They need higher antenna profile to operate on wide frequency range (e.g., Vivaldi

antenna [15-21] and slab-covered connect dipoles [26, 27]), which make them difficult to fold and fit inside the rocket launching stage.

3) A long multi-section impedance transition line is needed in the feed network for wide band matching, which results in higher insertion loss as compared to the well designed narrow band feed network in MBDP-SA array. Linear array in azimuth direction is a general requirement for SAR antenna full array [21, 28].

4) As the UWB and SWB array provide wider bandwidth than that of signal, they need filters in receive channel (in T/R module) to remove the noise out of the narrower signal bandwidth so as to increase signal to noise ratio (SNR). This means that the wideband merits of the UWB and SWB array does not make them suitable for SAR applications.

For the aforementioned reasons, MBDP-SA array is the most promising solution for multi-band space- or air-borne SAR antenna applications at present stage.

2.2 Specifications of MBDP-SA Array

To understand the MBDP-SA array designs, some related specifications are briefly introduced in this section first.

2.2.1 Operating Band

Due to the reasons such as overall system requirements, microwave component level and affordable antenna size, etc, SAR systems generally operate from L band to Ku band [7-10, 29-43]. Specifically, most of the current space-borne SAR systems operate from L to X band [7-10, 32-43] due to the atmosphere attenuation, as shown in Fig.2 - 1 [44]. The operating frequency below L band will suffer reflections from the ionosphere, while radiated energy

higher than the X band radiation is increasingly absorbed by water and oxygen molecules in the atmosphere, and thus become sensitive to weather condition. Ka band is also frequently used for SAR applications (climate surveillance or fine imaging), as it offers less attenuation to signal due to its location between the water and oxygen absorption peak at 23GHz and 63GHz, respectively. The general spectrum allocation for different radar applications is shown in Table 2-1 [45].

For MBDP-SA antenna array, most of the designs employ frequencies from L band to X

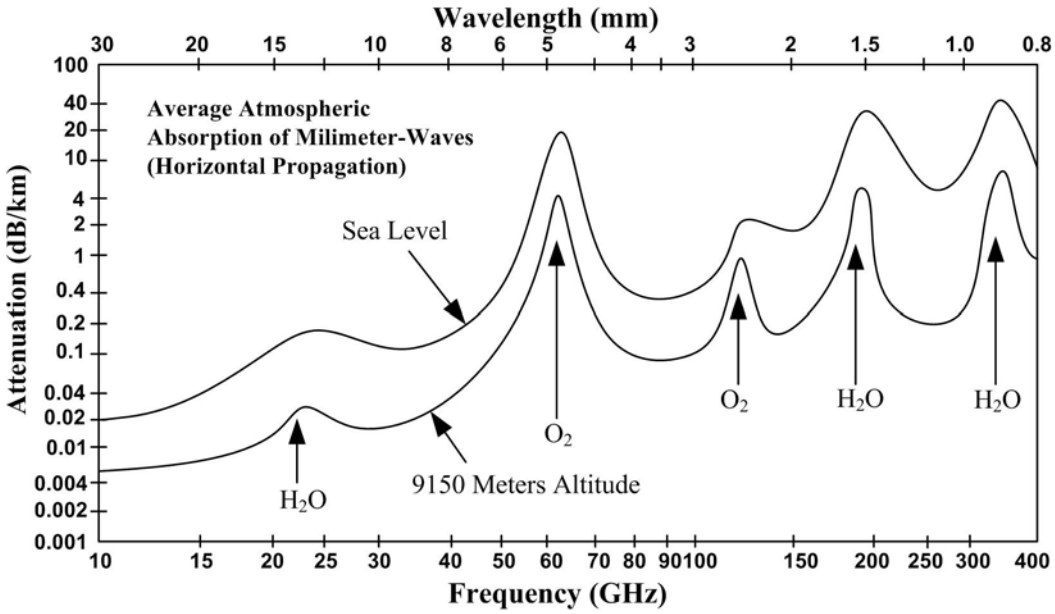

Fig.2 - 1 Atmosphere absorption [44]

Table 2 - 1 Commonly applied bands for radar applications [45]

Band	Frequency Range	Radar Frequency
UHF	300-1000MHz	420-450MHz,890-940MHz
L	1000-2000MHz	1215-1400MHz
S	2000-4000MHz	2300-2500MHz,2700-3700MHz
C	4000-8000MHz	5250-5925MHz
X	8000-12000MHz	8500-10680MHz
Ku	12-18G	13.4-14GHz,15.7-17.7GHz
K	18-26G	24.05-24.25GHz
Ka	26-40G	33.4-36GHz

size is required. The aperture sharing technique, in this case, brings limited aperture and weight reduction. Furthermore, the array aperture-sharing in operating bands higher than the X band adds design complexity and leads to higher system cost. Certainly, the choice of operating frequency band and polarization in a SAR system is dictated by its mission requirement, as recommended in Table 2-2.

Table 2 - 2 Recommended band and polarizations for different SAR missions [46, 47]

Mission	Band	Polarization	Incident angle(°)	Resolution(m)
Geology	L / C	HH / HV	30-60	20
Agriculture	C / X	--	40-60	10
Forest	L / C / X	HH / HV	30-40	10
Soil	C	HH	10-20	15
Water	L / C	HH / VV	10-20、60	<5
Ocean	C / X	HH / HV	40-50	25

2.2.2 Bandwidth

A SAR system's elevation resolution is limited by the signal bandwidth, as shown in eq.1-1 [47]:

$$\rho_{elevation} = \frac{c}{2 \cdot B \cdot \sin\theta} \tag{1-1}$$

where c, B and θ refers to the velocity of light, signal bandwidth and the angle of incidence, respectively. Clearly, better resolution can be obtained by employing larger signal bandwidth (after pulse compression). As the interface between the air and the system, a SAR antenna should have a broad band performance in order to support the signal bandwidth. Currently, a common bandwidth requirement for SAR antenna is 3~8% [49].

To meet the demands of higher resolution, the future SAR systems need larger bandwidth. So, to design a MBDP-SA SAR array becomes quite challenging, particularly for the lower frequency band due to its wider percentage bandwidth requirement.

The antenna bandwidth cannot be defined uniquely. For the resonant antenna, the bandwidth is commonly the narrowest of all the bandwidths (including impedance bandwidth, radiation pattern bandwidth and polarization bandwidth, etc). The antenna bandwidth in this thesis refers to the impedance bandwidth (i.e. $|S_{11}| \leq -10$ dB or VSWR ≤ 2).

2.2.3 Polarization Isolation

Polarization isolation is a key specification for any dual-polarized antenna. It refers to how small is the coupling of field components from the orthogonally polarized ports. For antenna with poor isolation, energy which is coupled from the other polarization will reduce the signal-to-interference ratio, and even damage the receiver channel (in case of the strong transmit energy couples to the receive channel). This coupled energy cannot be removed from frequency domain because the cross-talk occupies the same spectrum with the echo signal. However, the problem is not so serious from system's point of view, as transmit and receive time circles are separated in time, thus the energy coupled from orthogonal polarization transmit port can be shielded by switching off the receive channel in the time window. The polarization isolation specification is thus not very tough. A common polarization isolation requirement for a SAR antenna is 30dB or better [50].

2.2.4 Inter-Band Isolation

Inter-band isolation, which only exists in multi-band shared aperture arrays, is the quality of coupling between the co-polarized ports from the elements operating in different frequency bands. Because elements in each band operate at a different frequency, inter-band coupling can be further eliminated by using a filter or by implementing coherent demodulation in

receiver. Generally, SAR antenna inter-band isolation should at least be better than 25dB.

2.2.5 Cross-Polarization

The cross-polarization level is defined as the ratio of the orthogonal-polarized field component to the dominant-polarized field component in the main lobe direction. The asymmetry in the radiator shape generally leads to undesired orthogonal-polarized components being radiated. Specifically, cross-polarization can be illustrated in several forms in different coordinate systems [51], including 1) Cartesian coordinate, 2) spherical polar coordinate, and 3) arbitrary direction in spherical polar coordinate, as shown in Fig.2-2.

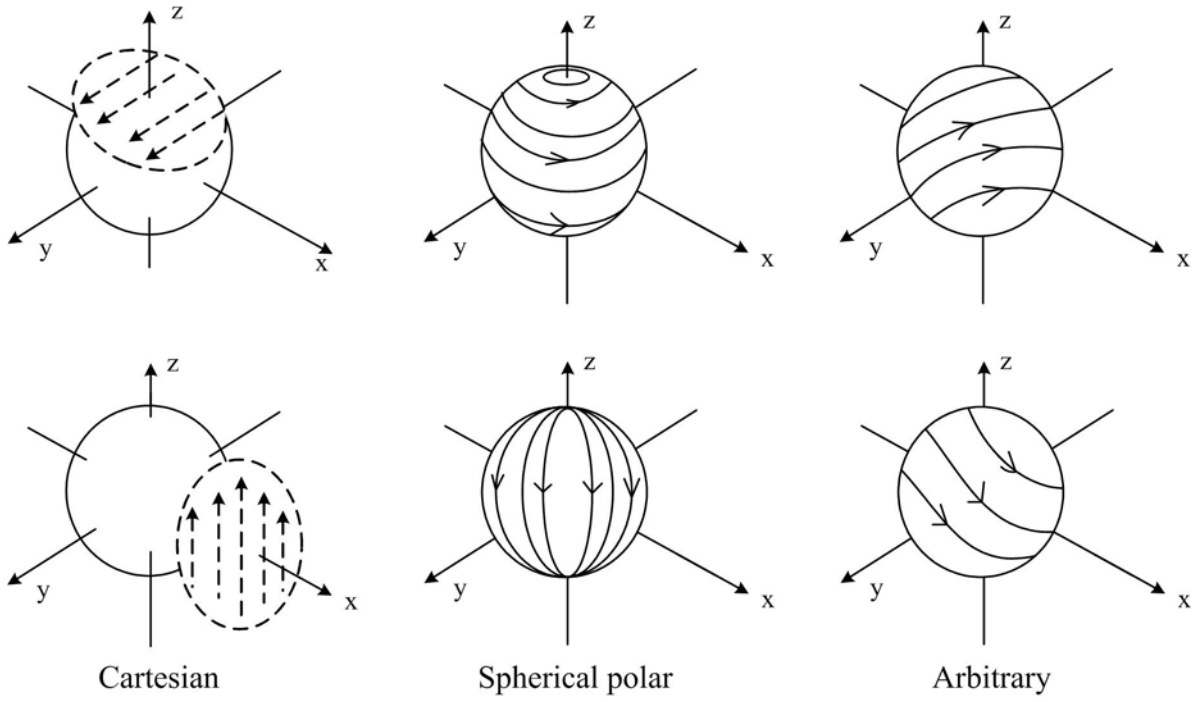

Fig.2 - 2 Illustration of cross-polarization [51]

The cross-polarization will degrade the performance of a polarimetric radar because the cross-polarized component can corrupt the polarized scattering matrix of the ground target. Besides, the cross-polarized energy cannot be suppressed by the other methods except for improving antenna polarization purity. A common cross-polarization requirement for SAR

antenna is -30dB [47].

2.2.6 Scan Ability

As compared to the mechanical scanning, electronic phase scanning has many advantages for space-borne system, such as flexibility, non-inertial and non satellite perturbance motion. Two commonly applied array scan range definitions are: 1) side lobes (grating lobe) remain 10 dB lower than the main lobe scan range; 2) main lobe gain drops by 3dB scan range. These two definitions respectively focus on the SIR and radiation power. In the thesis, the former definition is used.

For a space-borne SAR array, a ±20° scan range is commonly required in the elevation direction for scan mode to cover a wide swath (Scan SAR mode); while in the azimuth direction, ±1° ~ ±12° scan range is sometimes needed to achieving staring mode (spot SAR mode) for higher resolution [52].

2.3 Multi-Band Aperture Sharing Methods – State of the Art

From the review of open literatures, studies of MBDP-SA array mainly describe dual-band dual-polarized shared-aperture (DBDP-SA) arrays. In the following part, DBDP-SA microstrip array techniques are thus reviewed.

It should be noted that other types of antenna (excluding the microstrip array) can also be used to make DBDP-SA array. They are shown in Fig.2-3 and include:

1) Interleaved slotted-waveguide antenna [53-57] (Fig.2-3(a)).
2) Interleaved slotted-waveguide antenna with dipole (slot) array [58, 59].

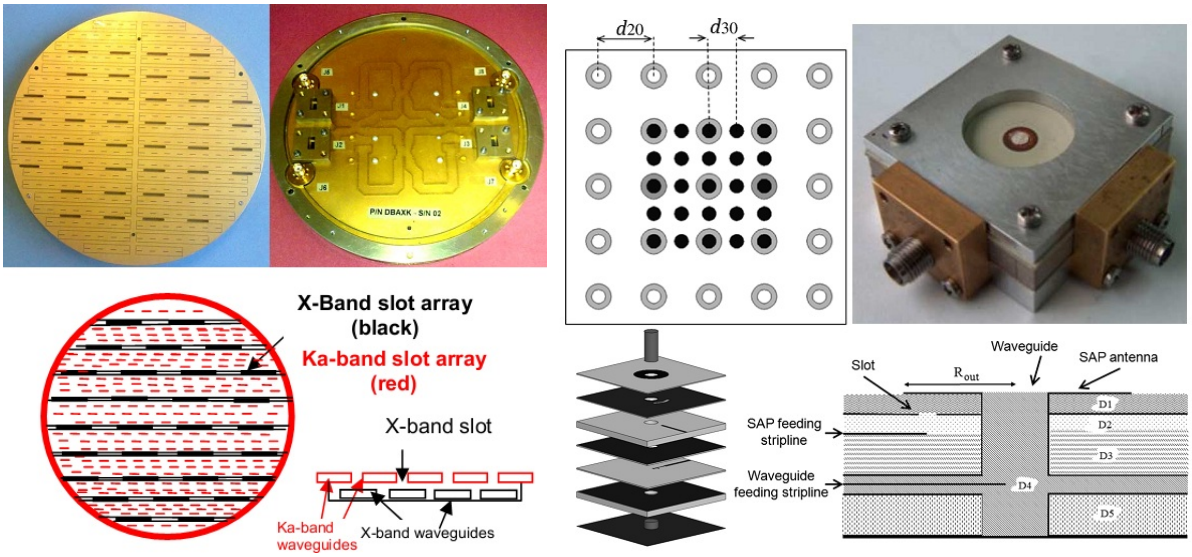

(a) X/Ka slotted waveguide [57] (b) Open-ended waveguide/shorted annular patch [60]

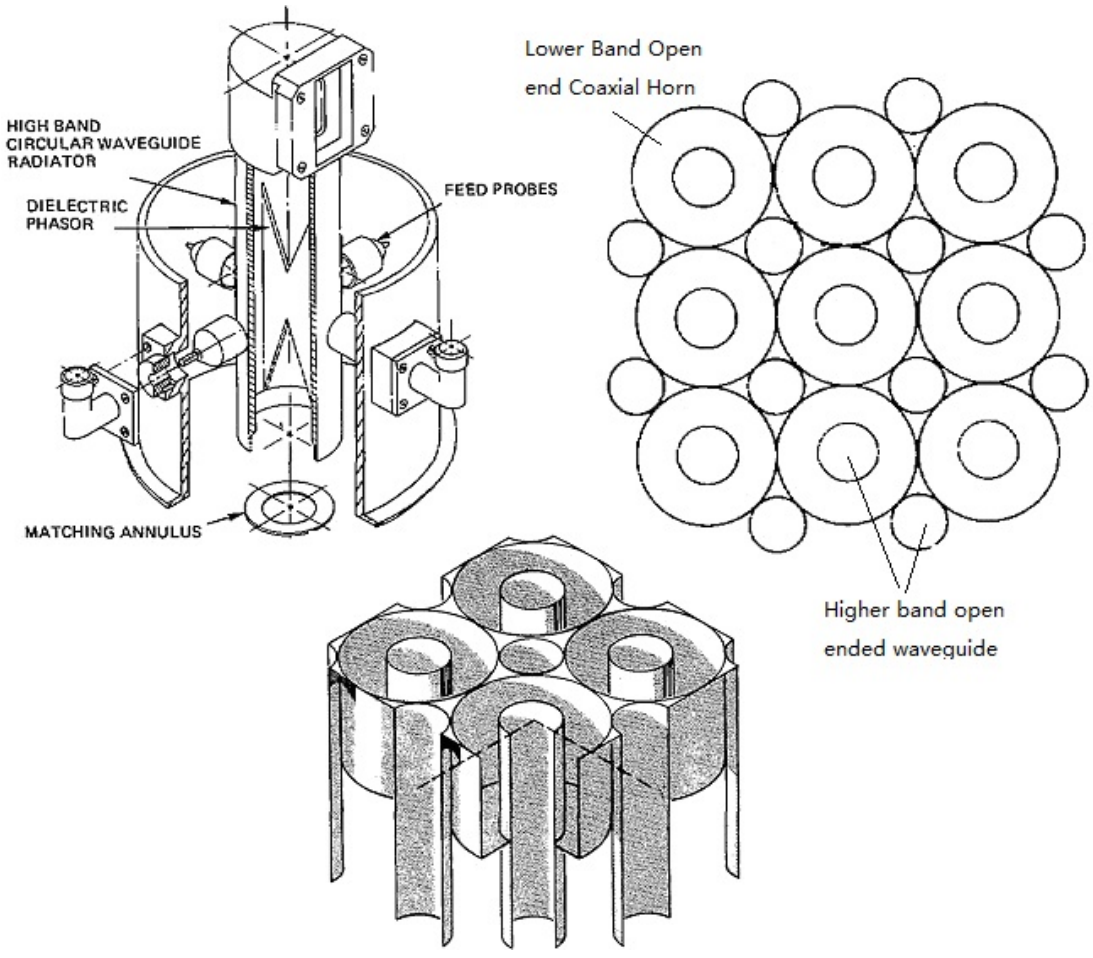

(c) Horn / open-ended coaxial array [64]

Fig.2 - 3 Different types (except for microstrip array) of multi-band shared aperture arrays

3) Interleaved open-ended waveguide array with shorted-annular ring patch array [60-63]

(Fig.2-3(b)).

4) Horn and open-ended coaxial horn embedding array [64-66] (Fig.2-3(c)).

5) Parabolic and microstrip compound array [67, 68].

Due to the scope of this thesis, these dual-band antennas are not discussed. Moreover, multi-band planar reflector array [69-73] (shown in Fig.2-4) is also not considered in this thesis, despite it is made using microstrip fabrication technology, because it is more similar to the reflector antenna rather than the dual-band shared aperture array.

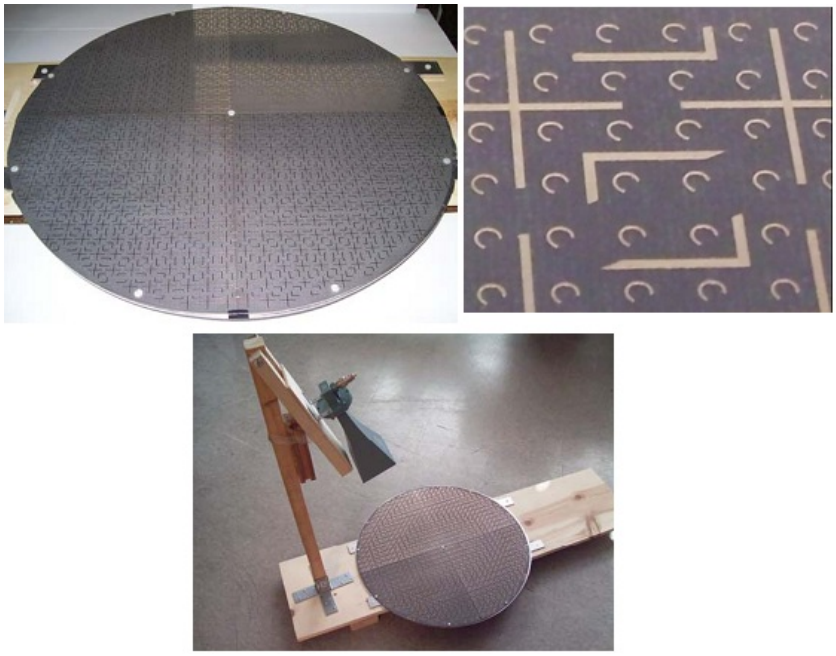

Fig.2 - 4 Multi-band planar reflector array [69]

2.3.1 Dual-Band Element Arraying

A natural consideration for DBDP-SA array is arraying the elements that can operate in dual band (called dual-band element below). However, this idea is less likely to be adopted in DBDP-SA array for the following reasons [a3]:

1) From the designs reported in the literature [74-81], dual-band elements can hardly support large frequency ratio (generally smaller than 2:1) if all other specifications are

met. However, SAR antenna frequency bands are widely separated, requiring a frequency ratio of greater than 2:1.

2) Some common dual-band elements, such as slotted-patch [78, 80] and PIFA [81], can hardly achieve dual-polarized operation. Orthogonally set dual-band operation elements can solve this problem, however, it will make the aperture more congested.

3) Even if dual-band element with large frequency ratio can be designed, the element distance should be at least smaller than one wavelength in higher band to suppress grating lobes in both operating bands. This element distance will be electrically small in the lower band, which is likely to deteriorate the lower-band inter-element isolation. Moreover, as the dimension of dual-band element usually scales according to its lower frequency wavelength, a small element distance will bring difficulties for element arraying, and sometimes even impossible to array.

Hence, the arraying of dual-band element can only be employed in DBDP-SA arrays with smaller frequency ratios (generally smaller than 2:1). Therefore, the higher- and the lower-band element embedding is currently the most appropriate solution for large frequency ratio DBDP-SA arrays. Based on different elements embedding methods, the DBDP-SA array solutions can be classified into the following types.

2.3.2 Lower-Band Array with Higher Band Aperture-Fitted

An X/Ka dual-band single-polarized shared-aperture (DBSP-SA) microstrip array, shown in Fig.2-5, is considered in [82]. As can be seen, four X band elements from the array center are removed (center truncation) to fit the Ka band array. The structure is actually a quasi-aperture sharing solution, where X and Ka band occupy independent apertures. The

design limitations of this array are discussed as follows:

1) Since the X band array is center truncated, side lobe level (SLL) will rise when compared to the uniformly distributed array. Although the amplitude weighting employed in [82] can suppress the SLLs to some extent, it will reduce aperture efficiency and increase the complexity in the feed network.

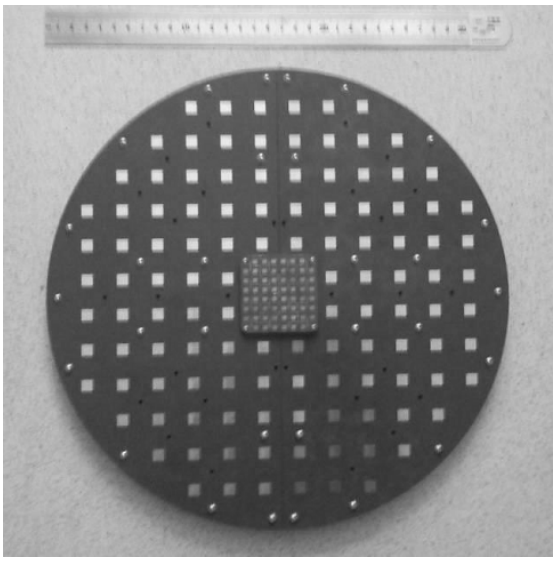

Fig.2 - 5 X/Ka DBSP-SA microstrip array with X band center truncation [82]

2) This structure can only produce moderate gain levels in the higher band. The higher band aperture size need to be increased to achieve higher gain, however more lower-band elements from the array center need to be removed rather than the limited X band elements (2 × 2) in the sample. This will deteriorate the radiation patterns significantly, which perhaps cannot be simply compensated by amplitude weighting.

3) The structure can hardly be extended to the large array by making periodical arrangement. Because when the sample is treated as a sub-array for aperture extension, higher band apertures will located quite far, which will result in grating lobes in higher band.

In conclusion, this structure is a cost effective solution to realize a DBDP-SA array with

moderate gain in the higher band.

2.3.3 Interleaved Structure

An interleaved structure is a commonly used method in DBDP-SA array. In this structure, the higher-band elements are generally periodically distributed with thin lower-band radiators interleaved in the gaps of the higher-band elements. Due to the regular distribution, higher-band elements have fewer design limitations, and almost any element type can be employed. On the contrary, the lower-band element design has stricter requirements in terms of broader percentage bandwidth and lower antenna profile within a limited available space. Thus, the lower-band element design is quite crucial for the efficient operation of DBDP-SA array. An interleaved structure can be classified into several types according to its lower-band element type.

The commonly employed lower-band elements types are patch- and slot-type while in terms of the elements' shape, strip-, cross- and annular-shapes are most widely used. Most of the interleaved structures reported in the literature can be classified into the combination of element types and shapes, as briefly listed below:

1) Strip-like patch for lower-band element including the interleaved printed dipole with patch [83-85] (Fig.2-6 and Fig.2-7), and the interleaved dipole with dipole (slot) [86-92], *etc*.

2) Strip-like slots for lower band such as the interleaved slot with patch [93] (Fig.2-8) and the interleaved slot with slot [94].

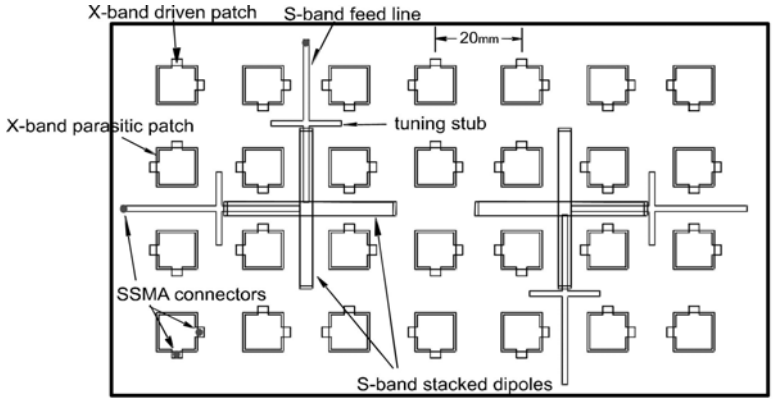

Fig.2 - 6 Interleaved print dipole with patch [83, 84]

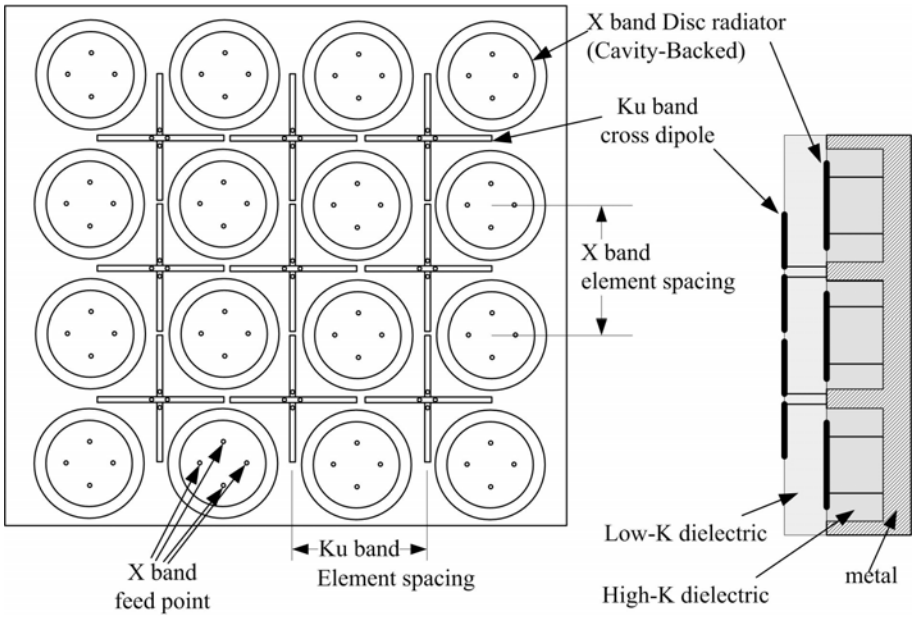

Fig.2 - 7 Interleaved print dipole with patch [85]

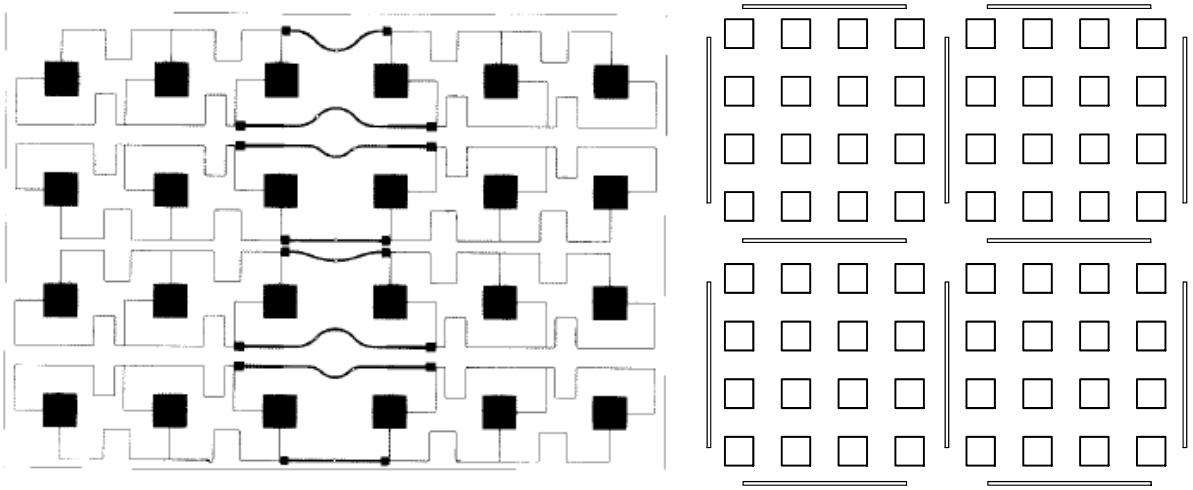

(a) C/X interleaved array [94] (b) L/C interleaved array [93]

Fig.2 - 8 Slot/patch interleaved array

3) Annular patch (ring) for lower band such as the interleaved annular patch with patch [95-97] (Fig.2-9) and the interleaved annular patch with printed dipole [98].

4) Annular slot for lower band [99, 100] as shown in Fig.2-10.

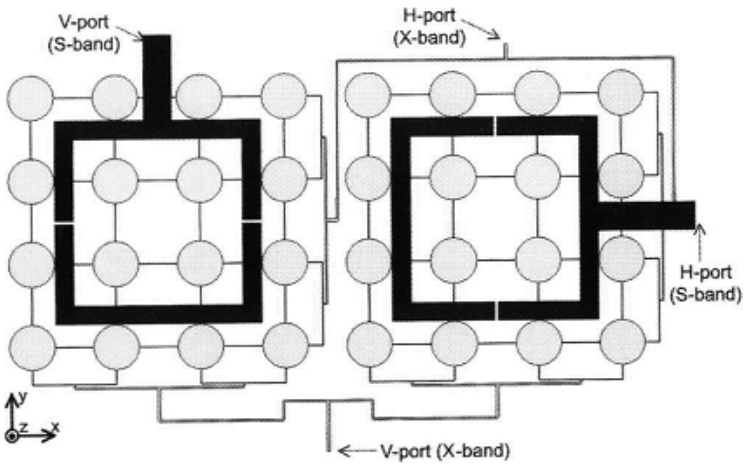

Fig.2 - 9 Annular patch / patch interleaved array [96].

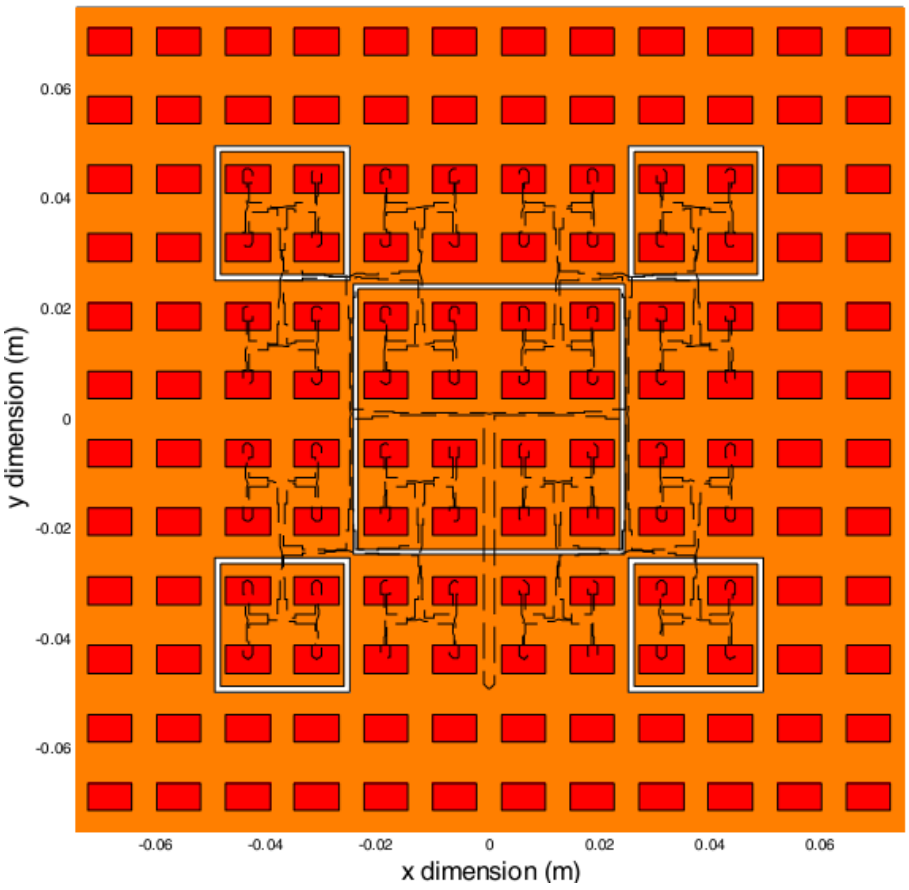

Fig.2 - 10 Annular slot / patch interleaved array [99].

(a) P/L dual band interleaved array [101]

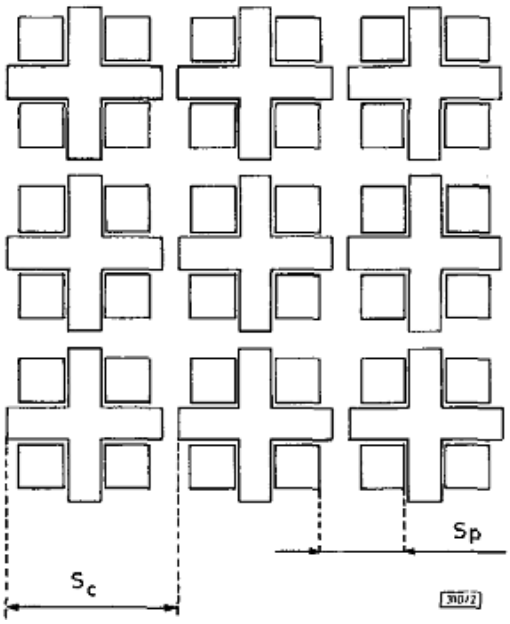

(b) S/X dual band interleaved array [102]

Fig.2 - 11 Cross patch / patch interleaved array

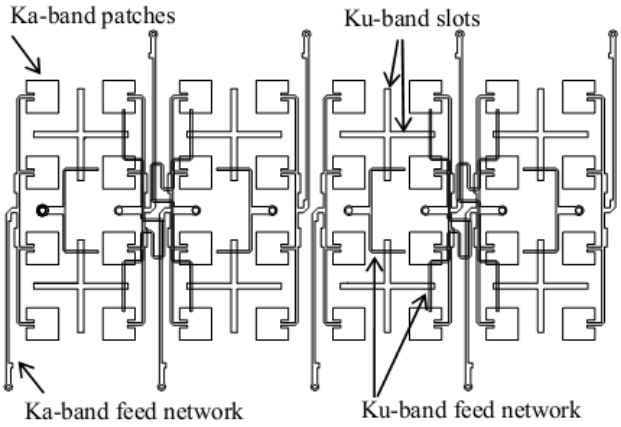

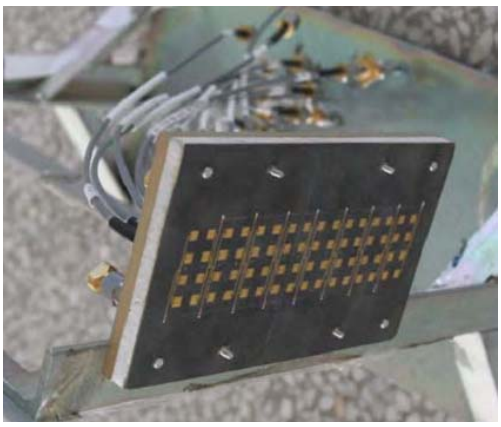

Fig.2 - 12 Cross slot / patch interleaved array [103]

5) Cross patch for lower band including the interleaved cross patch with patch [101, 102] as shown in Fig.2-11.

6) Cross slot for lower band such as the interleaved cross slot with patch [103-105] as shown in Fig.2-12.

Moreover, for some DBDP-SA array with small frequency ratio (with $f_h : f_l \leq 2 : 1$) and limited scan requirements, the gaps of the higher-band patches are wide enough to fit the

lower-band patch. Patch and patch interleaving structure can also be implemented [106], as shown in Fig.2-13.

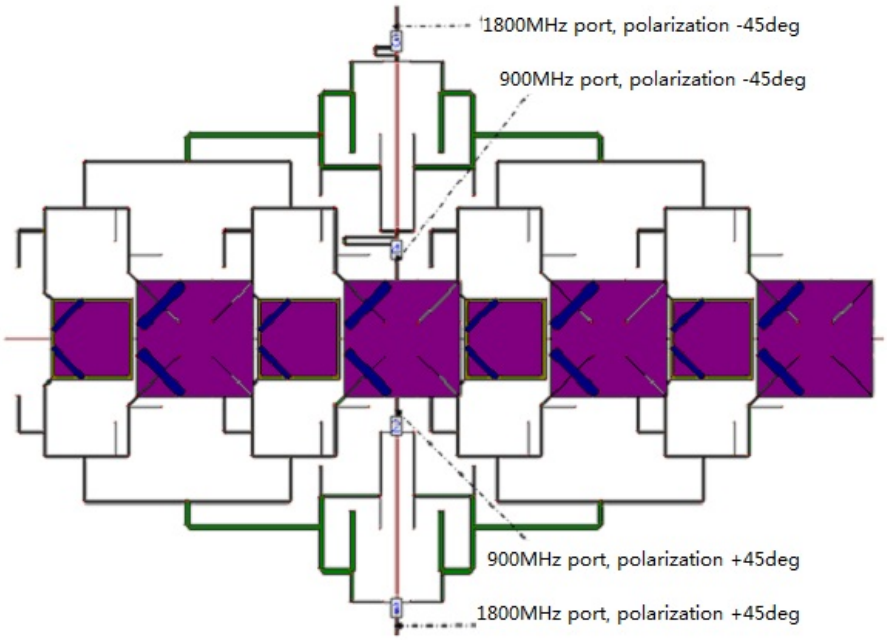

(a) 900/1800MHz interleaved array [107]

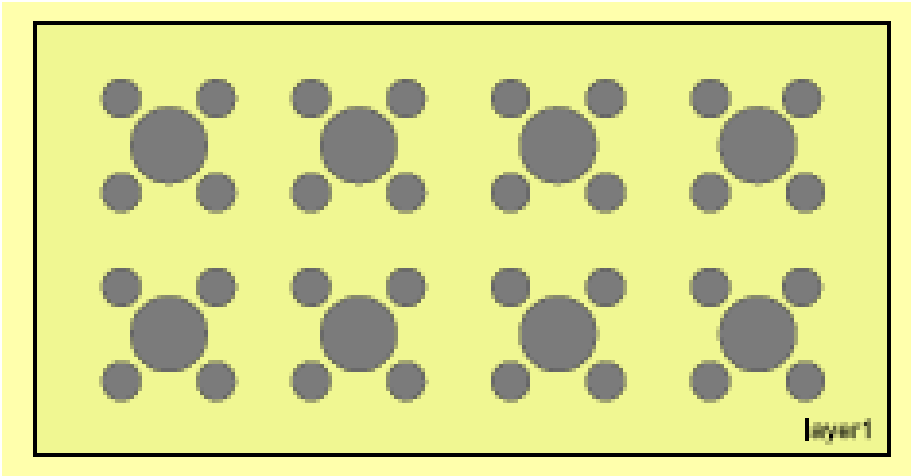

(b) S/C band interleaved array [108]

Fig.2 - 13 Patch / patch interleaved array

In general, the flexibility of array configuration and the capacity to operate with any frequency ratio are the two main merits of the interleaved structure. A drawback is its narrow bandwidth in the lower band, which is narrower than the bandwidths of perforated patch and overlapped structure dual-band embedding method.

In terms of the lower-band element type, slot element has advantages due to its simplicity and broadband nature, however, bidirectional radiation does not make it suitable for array applications. A reflector or back cavity is needed behind the slots to improve the front-to-back ratio at the expense of higher profile. Patch element's feature is just the opposite of the slot.

2.3.4 Perforated Patch

To the best of author's knowledge, perforated patch was first considered in 1990s when Shafai and Pozar proposed the design principals of perforated-patch DBDP-SA array and fabricated them for verification. These prototypes are shown in Fig.2-14 [109, 110]. As of today, the literature survey [111-122] shows that the perforated patch is the most classical method for DBDP-SA array.

To achieve the element spacing requirements in the higher-band, lower-band patches are perforated to fit the higher-band elements within 'perforations'. Regular periodical arraying is thus possible for higher bands, which eliminates the grating lobes. In [109], $\text{cosec}^2\theta$ pattern synthesis is presented in higher band of a DBDP-SA array, which verifies good radiation performance of the perforated-patch structure.

A variety of perforated patch DBDP-SA array have been investigated for wide frequency ratios ($f_H : f_l$) from 3:1 to 8:1 [109-124]. In the recent years, other shapes of perforated patches are also reported [123, 124], such as circular perforated patch DBDP-SA array (Fig.2-15(b)), and corner-truncated perforated patch (or can be seen as a perforated cross patch) as illustrated in Fig.2-15(a). Furthermore, the interleaved ring patch with patch structure [95-98] can also be classified as the heavily perforated patch structure.

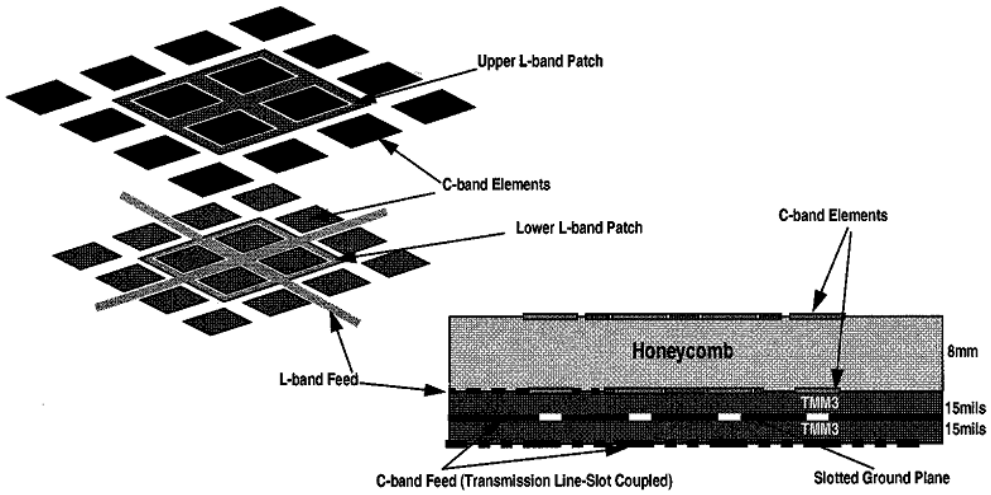

(a) L/C band perforated patch [109]

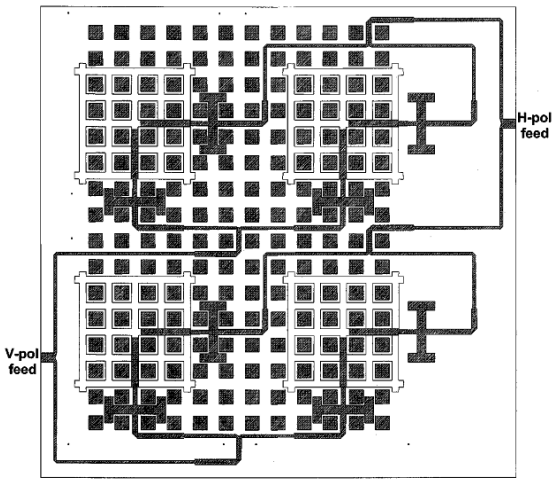

(b) L/X band perforated patch [110]

Fig.2 - 14 The classical perforated patch arrays.

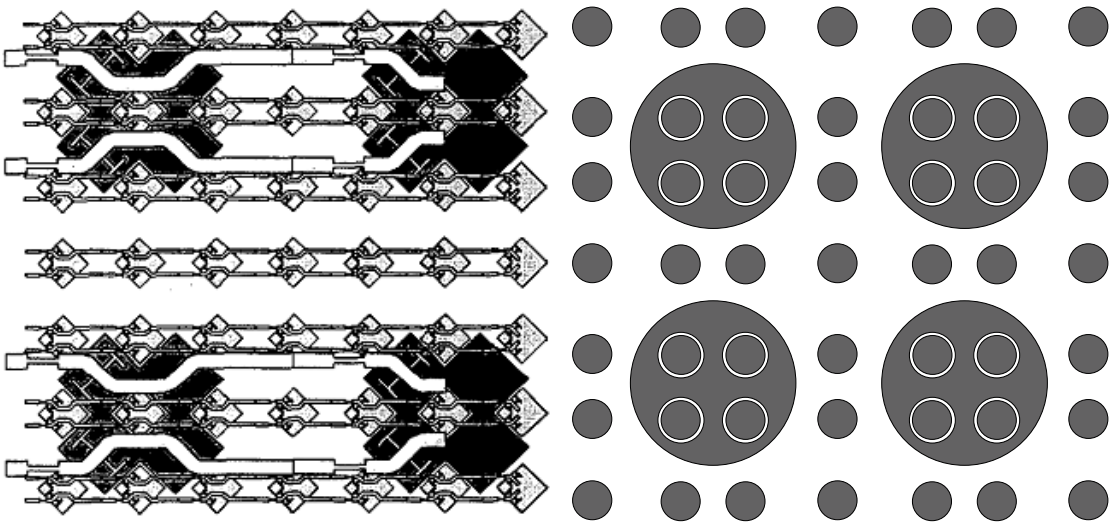

(a) Perforated cross patch [123] (b) Perforated circular patch [124]

Fig.2 - 15 Published samples of different perforated patches

The perforated patch is actually a special type of interleaved structure, in which the grid-meshed lower band patch is interleaved in the gap of the higher-band elements (see Fig.2-14 (b)). However, the perforated-patch structure is separately discussed in this section due to its unique merits, including:

1) For the same bandwidth requirement, the perforated-patch has lower profile than that of the other interleaved structures [97], which offers great advantage in conformal array or folded array design and makes it suitable for space- or air-borne applications.
2) The design technique is quite mature and well-studied, and hence is more reliable. Indeed, perforated patch design is less flexible than the interleaved structure, because its lower-band operating frequency depends on the perforation position, perforation size and the higher-band spacing. A detailed comparison between the perforated patch and the interleaved structure is given in [104, 105], where their advantageous and disadvantageous are discussed.

2.3.5 Overlapped Structure

In the overlapped structure, lower-band patches are located in the bottom layers, with higher-band patches overlapped from topside. The lower-band patch also serves as the ground of the higher-band patch. Hence, compared to the interleaved structure (including perforated patch), the overlapped structure has the following advantages:

1) Lower-band cavities are not restricted or perforated and a lower Q factor and corresponding larger bandwidth is achieved in the lower band.
2) The elements from both bands are separated by lower-band parasitic patch in height, thus ensuring good inter-band isolation.

However, the overlapped structure has overall higher profile, due to the sum of element thicknesses in both bands.

A. Array Example

Two similar overlapped patch arrays [125, 126], which operate respectively at UHF/VHF and L/S band, are presented as shown in Fig.2-16. The square patch element is employed in both bands of each array. The array size is same in each array, and includes 3 × 1 lower-band elements (VHF and L-band) and 6 × 1 higher-band elements (UHF and S-band). According to the published results, both antennas serve very well as DBDP source for reflectors.

(a) UHF/VHF band overlapped array [124]

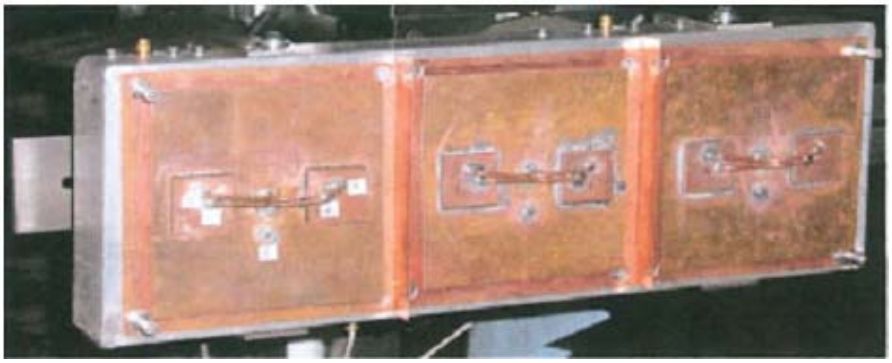

(b) L/S band overlapped array [125]

Fig.2 - 16 Published overlapped array

However, these designs are not suitable for DBDP-SA SAR application due to the following reasons:

1) A single-layer patch element with thin substrate is used which has narrow bandwidth, thus resulting in poor range resolution in SAR system.
2) Lower-band patches are tightly configured in two arrays, (perhaps due to the limited size) and even through it may not be a serious problem for narrow bandwidth designs such as [125, 126], where high Q-factor patch is probably less sensitive to the cross-talk between the lower-band elements, it will deteriorate the lower band inter-element isolation for large bandwidth elements such as stacked patch or thick patch.

B. Feed Mechanism

Various patch shapes such as square [125, 126, 129-132], round [128], triangle [127] or fractal patch [127], and different feeding methods, such as probe [126, 127], coplanar [125, 132], aperture coupling [129, 130] or L probe feed [128, 131], can be employed in both bands, as shown in Fig.2-17.

Broadly speaking, a feed mechanism has a minor effect on the microstrip bandwidth, but has considerable influence on isolation and cross-polarization performance. On the contrary to the simple probe-feed and co-planar feed, aperture-coupled feeds generally provide better cross-polarization level and isolation performances, at the expense of a complex feed structure, particularly for the higher-band element in overlapped DBDP structure.

A 900M/2.5GHz overlapped unit-cell is presented in [129], which consists of 2 × 2 higher-band square patches located on the lower band square patch, as shown in Fig.2-18. An obvious contribution of this unit cell is to use an aperture-coupled feed in both bands. The

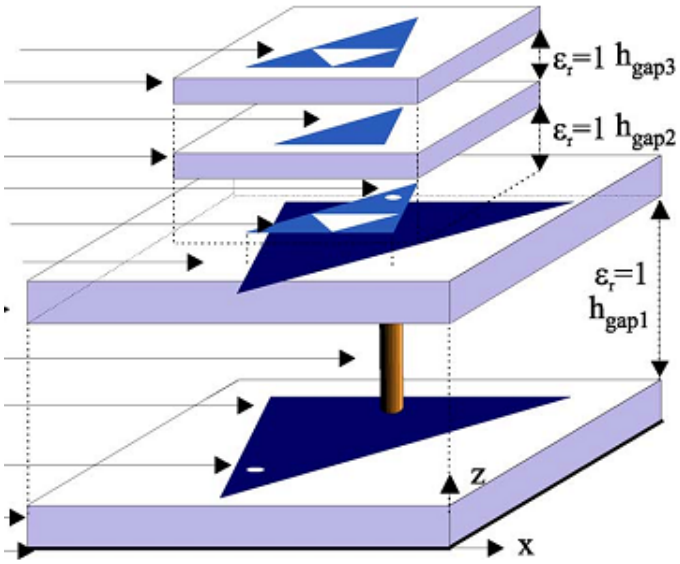

(a) Triangle patch (fractal structure with probe feed) [127]

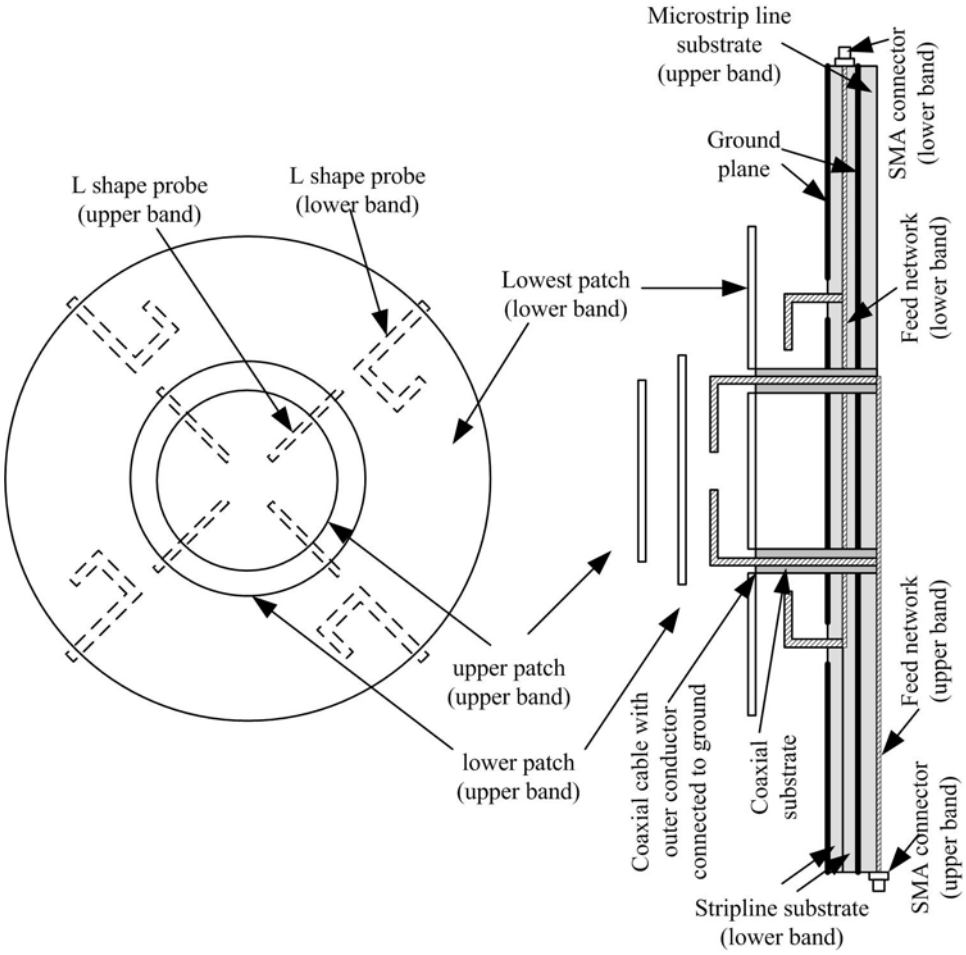

(b) Round patch (L probe feed) [128]

Fig.2 - 17 Overlapped dual-band array (unit cell) with different shapes and feed methods

higher-band strip feed line layer, which consists of two substrates, is inserted between the lower-band upper patch and the higher-band patch ground. It is vertically excited at one edge of the lower patch, and coupled to the higher-band through the coupling slots made on higher-band patch ground. As shown in Fig.2-18, three holes can be seen at the vertical feeding point, where the center one is the RF connector feeding hole while the other two are metalized holes to connect the upper and the lower grounds.

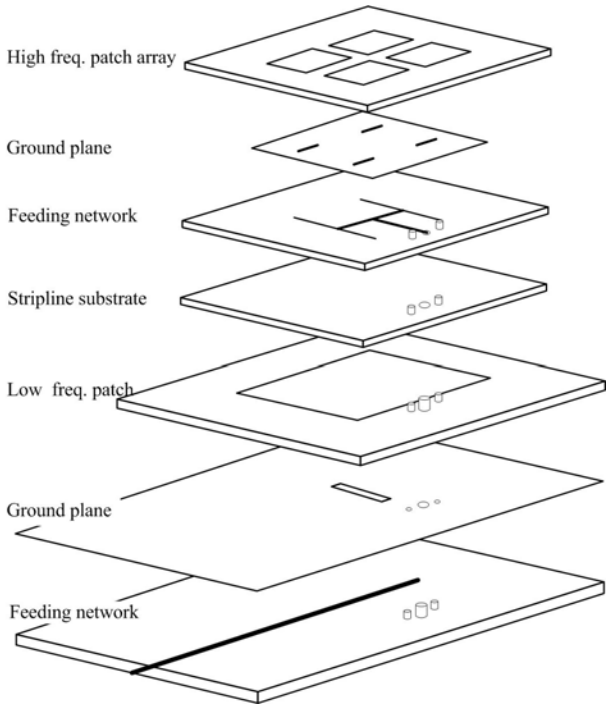

Fig.2 - 18 Overlapped patch unit [129]

This example verifies the feasibility of aperture coupling in overlapped structure configuration. A small drawback of this design is the vertical feedings of higher-band elements which passes through the lower-band patch at the center of one edge. This method can only be applied for single-polarized lower-band patches. Because the vertical transition structure is treated as a shortening pin in the lower-patch cavity, it will suppress orthogonally polarized mode in dual-polarized patch configuration.

A GSM / DCS dual-band overlapped patch is presented in [130] and shown in Fig.2-19. The design employs a smart feeding structure: for lower frequency, the lower-band patch is excited through a cross coupling slot on the ground, the director patch (in lower-band cavity) is not resonating due to the small dimension. As for higher-band, the director patch 'bridge' the energy from the cross slot on ground to the higher-band patch, through the cross slot on the lower-band patch (it also serves as higher-band ground). Only one port is required to excite elements of both bands.

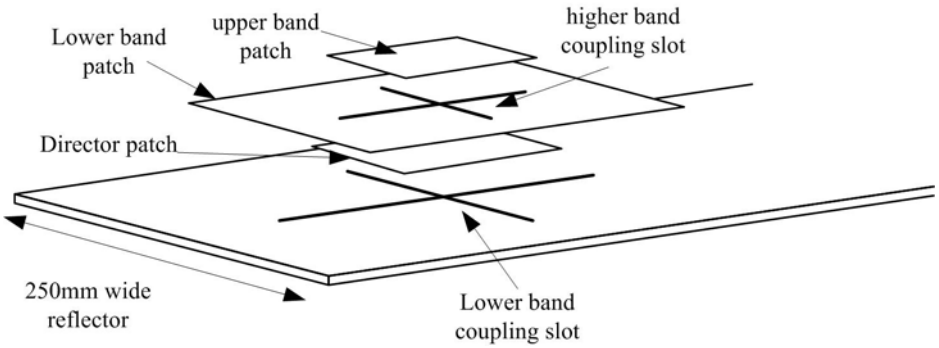

Fig.2 - 19 GSM/DCS overlapped patch [130]

This design is quite attractive and simple but is not suitable for DBDP-SA SAR array due to the following reasons:

1) Only one feed point is employed to achieve dual-band operation which implies that the two bands cannot be controlled separately. Although using duplexer can divide the higher- and lower-band, but it adds complexity in design.
2) The higher-band element is excited due to the coupling from the lower-band cavity, hence, the inter-band isolation needs to be further investigated.
3) The design employs only one higher-band element, making it difficult to extend as a full array.

C. Broadband Element

Two similar overlapped patch unit cells operating respectively, at L/S and P/S band are reported in [128, 131]. They are shown in Fig.2-17(b) and Fig.2-20. In these designs, one higher and one lower thick air-filled patches are employed to form the unit cell, with L-probe feed excitation to ensure good bandwidth. Two sets of independent feeding structure are employed for higher- and lower-band elements, so that two bands can be controlled independently.

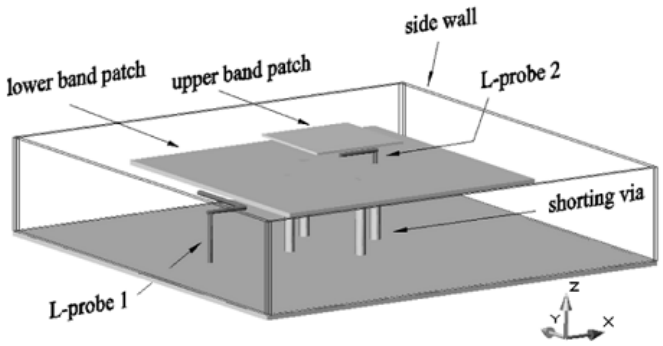

Fig.2 - 20 P/S broadband overlapped patch [131]

The vertical transition structures (for higher-band L-probe) in the lower cavity are not configured at the center of the lower-patch in order to fit the higher-band L-probe position. However, additional reactance will be introduced for lower-band element, which will increase the size of the lower patch.

D. Derived Overlapped Structure

Some other structures can be derived from the overlapped structure, such as dual-band short annual patch (SAP) [61-65], as shown in Fig.2-21. The open-ended waveguide passes through the lower-band patch cavity to serve as the higher-band radiator. Because SAP antenna has just one higher-band element, it is only suitable for some DBDP-SA arrays that

operate with small frequency ratio.

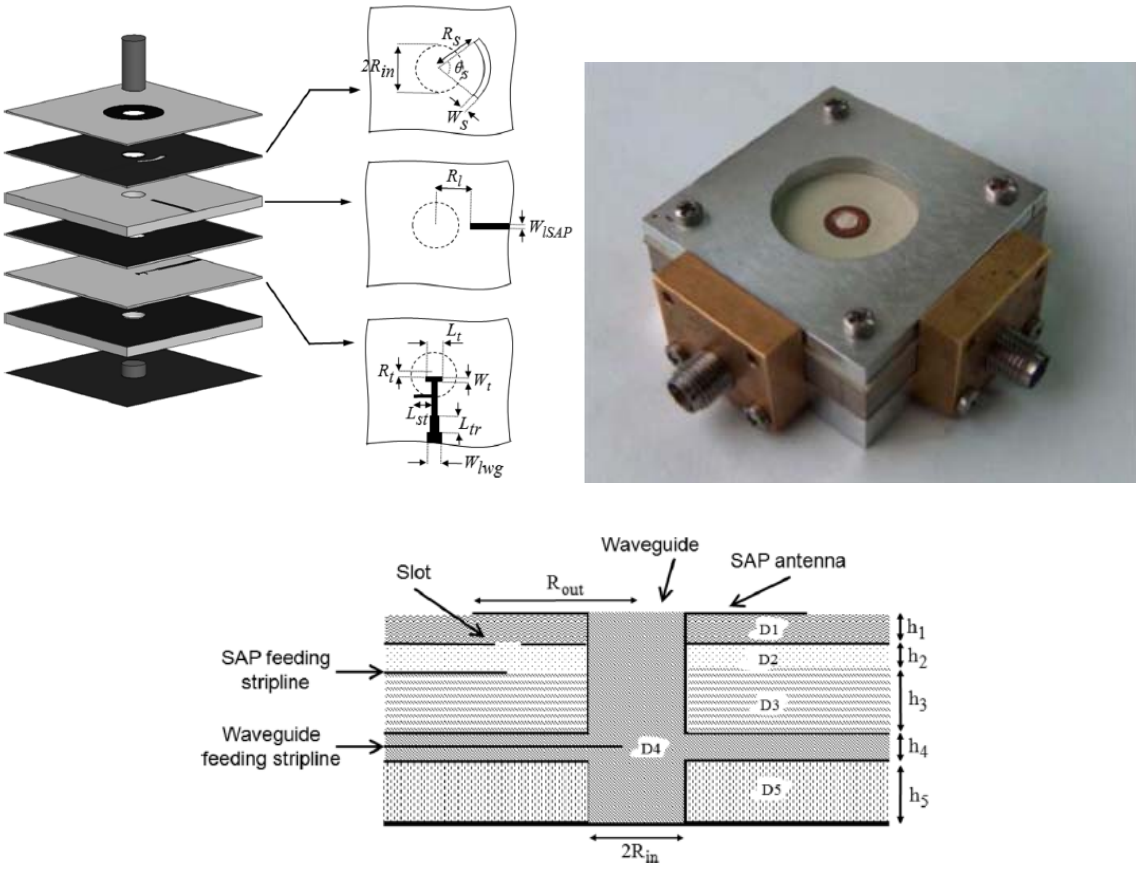

Fig.2 - 21 Short annual patch [61]

2.4 Dual-Band Embedding Method – Comparison

Three different multi-band aperture sharing methods have been reviewed and discussed in this chapter. More specified techniques and detailed analysis of MBDP-SA arrays will be introduced in Chapter 3 where they are employed.

In general, the DBDP-SA array, including perforated-patch, interleaved-structure or overlapped structure, essentially uses boundary condition to restrict field energy of two bands into different space of the same aperture to realize aperture sharing.

From this perspective, the perforated-patch and the interleaved-structure DBDP-SA array

are of the same type. They restrict the lower-band field energy into higher-band elements gaps, as shown in Fig.2-22. Hence, a small cavity area is formed, which leads to narrower bandwidth.

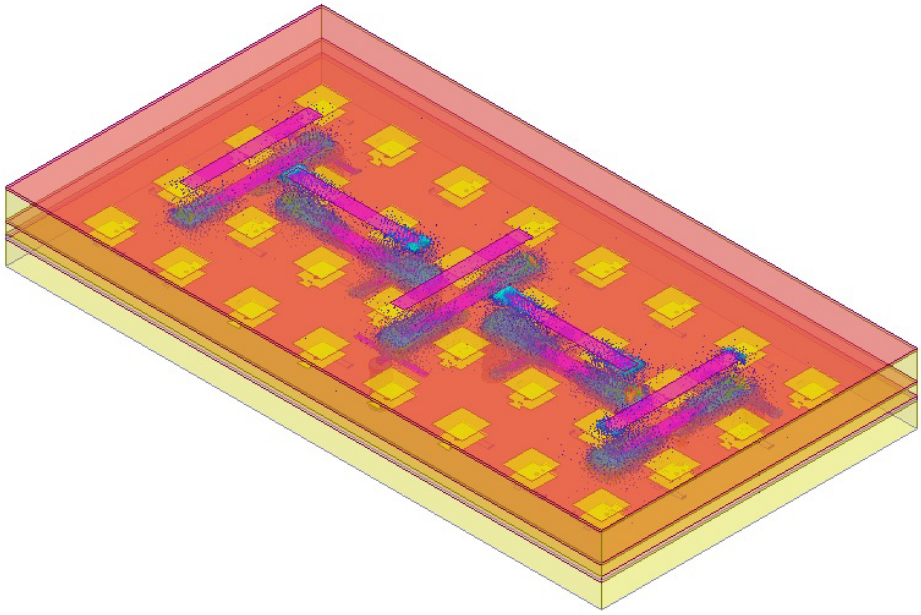

Fig.2 - 22 Energy distribution in the lower-band element of the interleaved structure

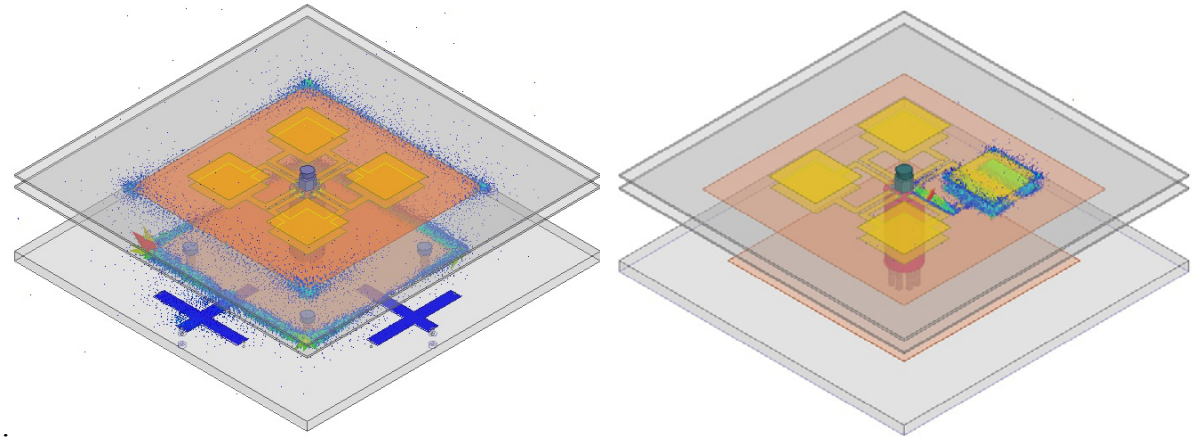

(a) Lower-band (b) Higher-band

Fig.2 - 23 Energy distribution in the overlapped structure

On the other hand, the overlapped DBDP-SA array places lower- and higher-band elements on the different heights to obtain sufficient cavity volumes for both bands elements (shown in Fig.2-23), thus resulting in large bandwidth.

A few features of the overlapped-structure DBDP antenna, as analyzed from the published papers, are briefly described below:

Although the non-perforated stacked patch has larger bandwidth (see Section5.2), the advantage of overlapped DBDP structure (based on the non-perforated stacked patch) is not very obvious. The overall profile of the overlapped DBDP array is determined by the thickness of lower-band and higher-band element whereas the profile of the perforated patch and the interleaved structure is the same as the lower band element thickness.

This implies that for the given antenna profile specification, the lower-band elements in overlapped structure should be thinner than that in perforated patch or the interleaved structure as an additional thickness should be reserved for the higher-band element. The broadband feature of non-perforated stacked patch in lower band is weakened for the given overall antenna thickness.

In DBDP array with large frequency ratio, the overlapped structure is potentially more suitable theoretically, because a very thin space is enough for the higher-band element. However, the feed structure will become more complicated in this case. Because more higher-band elements should be placed on the lower patch, the higher-band feeding network adds more design complexity.

In overlapped DBDP structure, vertical feeding structure of the higher-band element passes through the lower element's cavity, which requires a complicated feeding structure.

2.5 Summary

The MBDP-SA array is more suitable for the multi-band SAR antenna than the UWB and

SWB array due to its lower cost, weight and better efficiency. Hence, it is the most promising antenna solution in these areas at present. Besides, it perhaps has potential applications in future tactical radar [13] and base station [15] application.

For dual-band embedding method, the dual-band element arraying is only suitable for DBDP-SA array with frequency ratio of no more than 2:1. Hence, it cannot be employed in SAR antenna or radar applications that cover a frequency band from L to X band with frequency ratio of 2:1 to 8:1.

The interleaved structure, perforated patch and overlapped structure are three possible design methods of DBDP-SA array with large frequency ratio ($\geq 2:1$). The former two methods are well studied, and have advantages for easier structure and flexible designs. The overlapped structure, on the contrary, has better bandwidth nature but with complex antenna structure. The study of overlapped structure DBDP array is still in progress.

Chapter 3
Improved S/X DBDP-SA Microstrip Array

This chapter addresses two key issues in the design of dual-band dual-polarized shared-aperture (DBDP-SA) array antennas. They are: 1) how to embed two antenna arrays with far-separated operation frequencies into the same aperture; and 2) how to improve performance of a DBDP-SA array, especially for unique specifications of the DBDP-SA array. Because the research in this chapter are the subsequent works of the preliminary S/X DBDP-SA array study conducted in 2007 [83, 84], we aim mainly at isolation performance improvement of a prototype array. A sample design is given in this chapter to validate the proposed methods.

3.1 Introduction

Compared with traditional single-band single-polarized (SBSP) array antennas, DBDP-SA array antennas have two additional key specifications, they are: 1) isolation between orthogonally polarized ports on the element; and 2) isolation between co-polarized ports from different bands. For brevity, they are called inter-polarization isolation and inter-band isolation in the rest of this thesis. Apparently, the inter-polarization isolation level is closely related to the independence of each channels (HH/ HV/ VH/ VV), which is an important specification for polarimetric radar. On the other hand, the inter-band isolation describes whether the co-aperture configured two arrays can work without interfering each other.

Main focus of this chapter is on the improvement of inter-polarization isolation and inter-band isolation. Some other performance improving or related aspects in DBDP-SA

arrays are also addressed and validated, including:

1) Employing fractional frequency ratio ($f_l : f_h = 1 : 3.5$) in an interleave configured DBDP-SA array design;
2) How to reach the potential bandwidth of the lower-band element, and the in-band ripple response improvement;
3) Inter-polarization isolation and inter-band isolation exacerbation factors in an interleaved structure DBDP-SA array. Corresponding isolation improvement methods are proposed.

As a technique exploration project, only prototype sub-arrays were required to validate the effects of these solutions. These sub-arrays are extendable. The electrical specifications for the project are summarized in Table 3-1.

Table 3 - 1 Specifications for improved S/X DBDP-SA microstrip array

Specifications	S-band	X-band
Center frequency (GHz)	2.85	10
Bandwidth (MHz)	200	600
Polarization	dual-linear	dual-linear
Cross-polarization (dB)	-30	-30
Polarization isolation (dB)	30	30
Scan range	±25° in two dimension	±25° in two dimension

3.2 Array Configuration

3.2.1 Aperture Sharing Consideration

Interleaved structure and perforated patch structure are two verified dual-band aperture sharing techniques, which are suitable for two bands with far separated operation frequencies like S- and X-band. Specifically, the perforated patch structure has a lower antenna profile for a given bandwidth [97], while the interleaved structure is more flexible for dual band configureation [83, 84], as explained in Section 2.3.

Considering the fractional frequency ratio requirement ($f_l : f_h = 1 : 3.5$) in this project, the interleaved structure is more suitable to meet the improved S/X DBDP-SA requirements specified in Table 3-1. This is because in an interleaved structure, the higher- and lower-band elements are relatively more independent of each other, and thus, frequency ratio can be tuned by simply changing lower-band resonant frequency [83, 84]. Although the interleaved structure has a slightly higher antenna profile than the perforated patch, it is not a serious problem for this project.

The schematic diagram of an improved DBDP-SA microstrip sub-array is depicted in Fig.3-1(a).

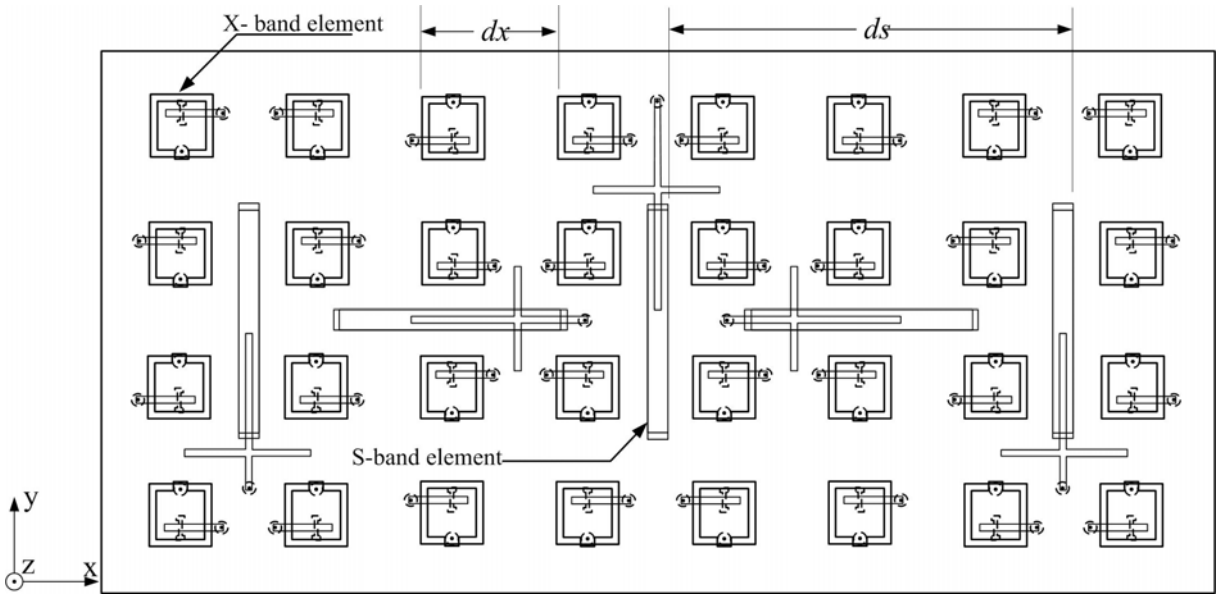

(a) Over view

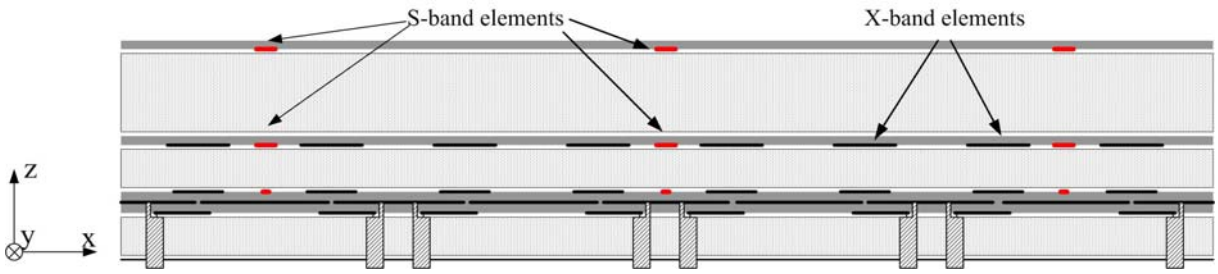

(b) Cross section

Fig.3 - 1 Schematic diagram of an improved S/X DBDP-SA microstrip sub-array

3.2.2 Full-Array Configuration

Although only a prototype sub-array is required for S/X DBDP-SA antenna technique verification, the sub-array should be extendable to a large array. This is due to the fact that potential DBDP-SA array applications, both in SARs and radars, need a large aperture to avoid imaging ambiguity [11] or to increase operation range.

A slim radiator is employed as the S-band element, because it can interleave with the X-band elements easily. The S-band elements are orthogonally configured for dual polarization. To achieve the inter-polarization isolation requirement, the dual-polarized elements are laid out in a T-shape, as further explained in Section 3.3. This configuration, however, raises two problems:

1) In T-shaped configuration, the phase centers of horizontally (H) polarized elements and vertically (V) polarized elements do not overlap automatically. An extra S-band vertically polarized element should be added to make the array geometrically symmetrical, as shown in Fig.3-2, and hence, make the phase centers of H- and V-polarization to re-overlap. The different H- and V-polarized element numbers will result in different beamwidths for H- and V-polarized radiation patterns. However, this beamwidth difference is negligible when the aperture is large. This is indeed the case in true space-borne SAR antennas or tactical

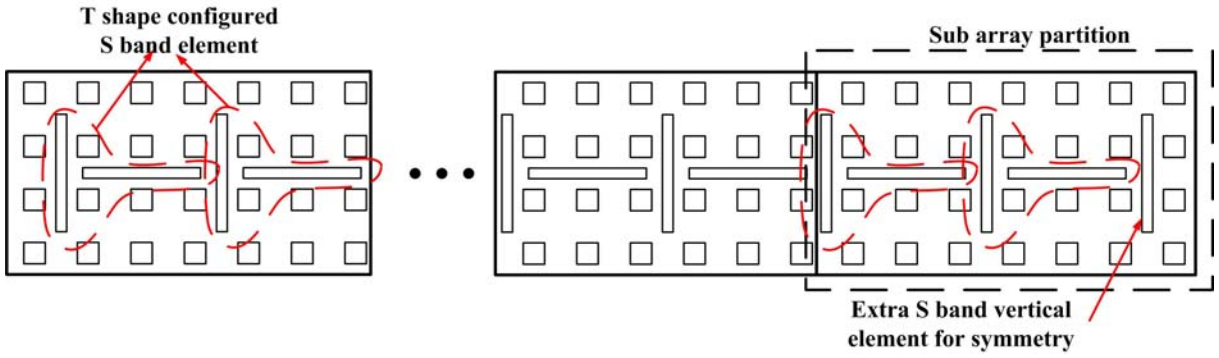

Fig.3 - 2 Full array configuration of the improved S/X DBDP-SA microstrip array

radar arrays, which generally have aperture sizes larger than 10m and 4 m, respectively.

2) The T-shaped configuration requires uniformly distributed S- and X-band elements, which leaves narrower gap for sub-array partition, as shown in Fig.3-2. Although radiators with some other shapes, like cross-shaped dipoles [83, 84], can make sub-array partition easier, the T-shaped configuration is still employed due to its good inter-polarization isolation, even though it brings some difficulties in fabrication and array assembly.

For demonstration, a fully symmetric structure in Fig.3-1, rather than the area surrounded by the dotted line in Fig.3-2, is chosen as sub-array. This sub-array includes 4 × 8 X-band dual-polarized elements, 2 H-polarized S-band element and 3 V-polarized S-band elements.

3.2.3 Sub-Array Configuration

A. X-band Sub-Array

Rectangular and triangular element distributions are two commonly adopted array configurations for large arrays. The triangular distributed elements can cover 13% more area than a square distributed array for the given scan range. This is helpful for dual-band interleaving because of its wider element distance. However, due to the T-shape configured S-band elements, square distribution of X-band elements is more compatible to this improved S/X DBDP-SA microstrip array, and hence it is employed.

The X-band element spacing is expected to be as wide as possible, to facilitate S-band element interleaving and sub-array partition. For the purpose of maximizing the element distance in a two-dimensional scan array, the scan range is generally projected into Sinc space, which can provide an intuitive view of relationship between grating lobe position and the required scan coverage [133].

Fig.3-3 illustrates the scan range area (blue line, 25° × 25°), grating lobe coverage (red lines) and visible area (gray dotted line) at 10.5GHz, when X-band element distance is $d_x = d_y = 20mm$. It shows that the main beam scan range is just touching the grating lobe coverage without overlapping. This infers that the X-band element distance has been maximized for the specified scan range.

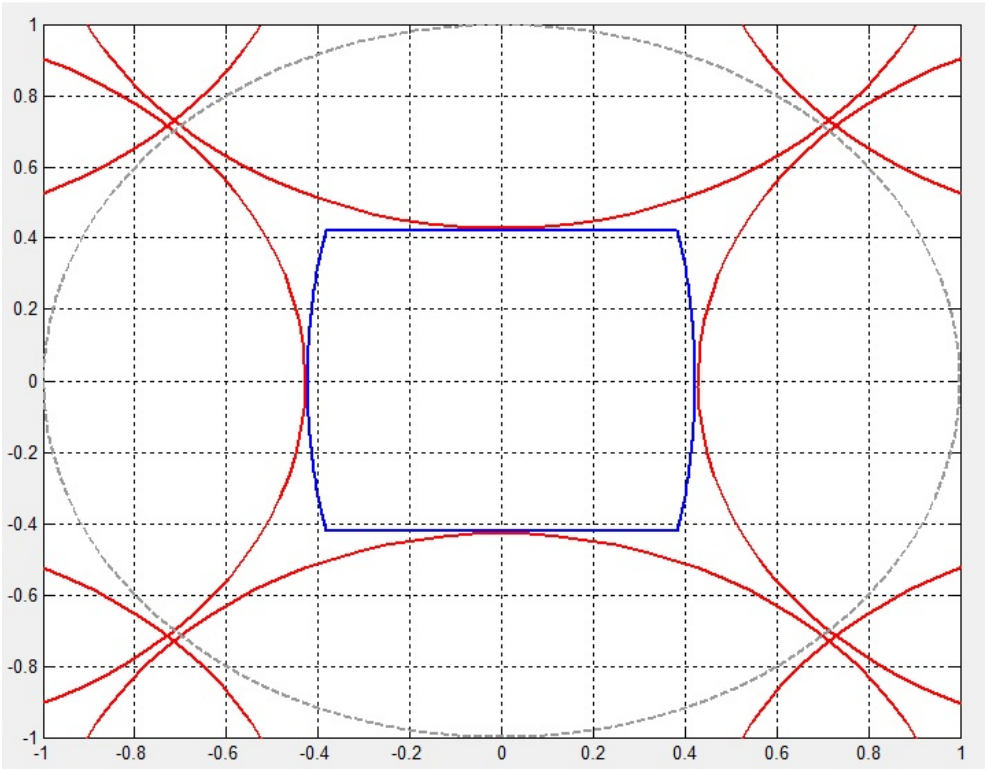

Fig.3 - 3 Scan range and grating lobe coverage in Sinc space

The selected X-band element distance of $d_x = d_y = 20mm$ was further checked using a Matlab program which is based on array theory. The element pattern (obtained by HFSS) was also taken into account. As shown in Fig.3-4, no grating lobes were found in the scan range. This further verifies the choice of X-band elements spacing.

In addition, a pair-wise anti-feed technique [134-136] is employed in the X-bands array, *i.e.*, the adjacent elements are mirror configured and out-of-phase excited to make the cross-

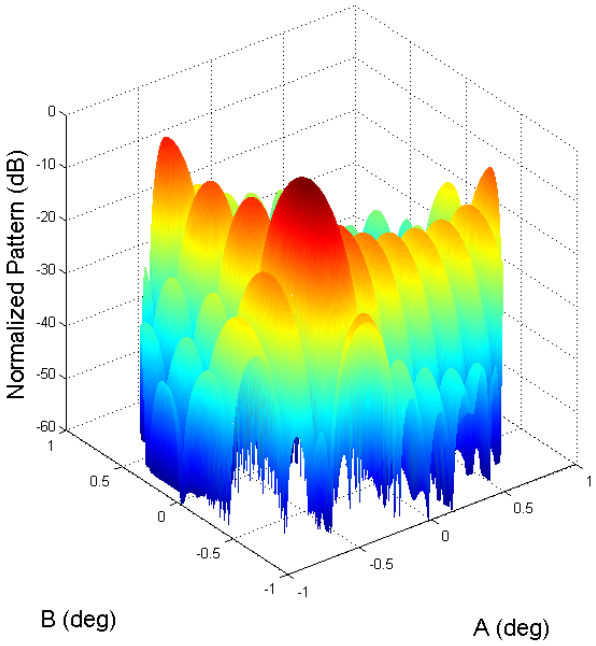

(a) A=25° / B=25°

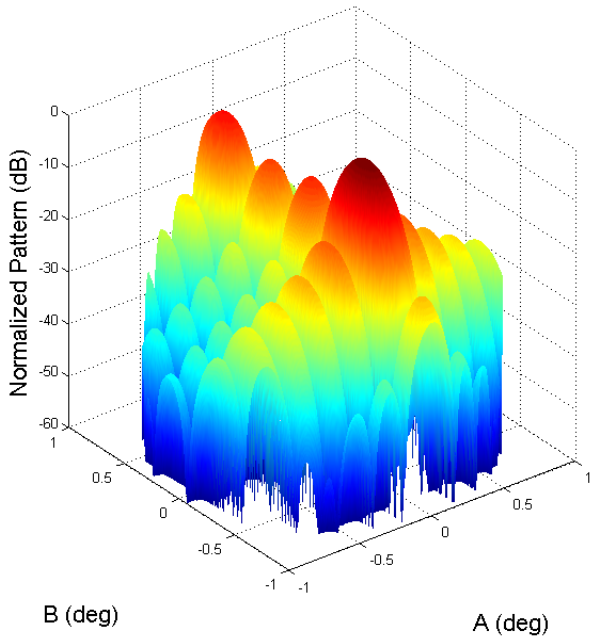

(b) A=0° / B=25°

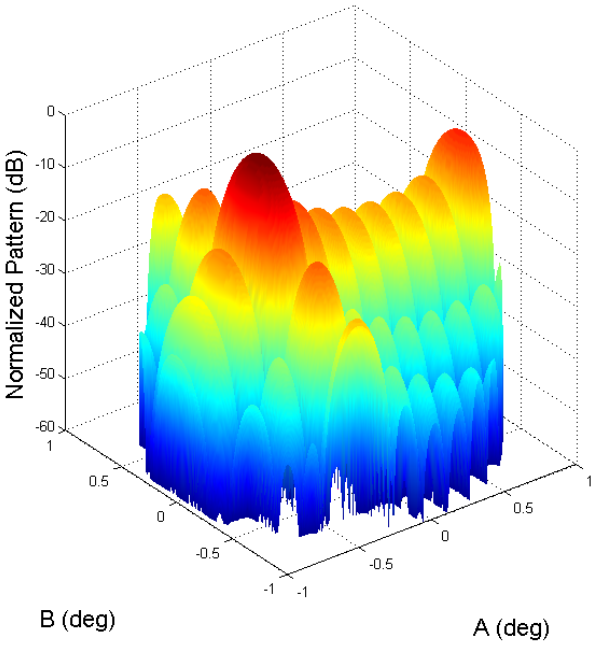

(c) A=25° / B=0°

Fig.3 - 4 Radiation patterns of extreme scan situation

polarized wave from adjacent elements cancel each other. The cross-polarization level as well as the symmetry of pattern is thus improved.

B. S-Band Sub-Array

In an interleaved structure, S-band elements must stay in the gaps of X-band elements.

This restricts S-band configuration than that of the X-band. Considering that S-band has the same scan range requirement (±25° in two dimensions) as X-band, it should have the same or shorter electric length than X-band, *i.e.*, the interleave ratio should be smaller or at least equal to the frequency ratio. Because the frequency ratio from X-band to S-band is 3.5:1, the S-band elements are interleaved in every three X-band elements, *i.e.*, S-band element spacing is $d_x=3 \times 20mm = 60mm$, as shown in Fig.3-1.

It should be noted that, the sub-array introduced in Fig.3-1 has only one S-band element in y-direction. That means if we construct a large aperture based on this sub array, the S-band element space in y-direction would be $d_y= 4 \times 20mm = 80mm$. This element space cannot support a scan range of ±25° in y-direction. This problem (refer to the consistency of dual band scan capacity) actually comes from the sub-array partition. The rational sub-array partition method in multi-band dual-polarized shared-aperture (MBDP-SA) array will be presented to address this problem later in Chapter 4. In this chapter, an improved S/X DBDP-SA sub-array is presented only to demonstrate some performance improvement methods and this problem is thus temporarily neglected.

3.3 X-Band Element

Element design is an important stage of the array, because some array specifications are determined by element performance, such as bandwidth and inter-polarization isolation. For higher-band elements in an interleaved DBDP-SA array, a broad bandwidth with a compact structure is preferred, to allow more room for lower-band elements. The higher-band element height is not such important, because the DBDP-SA sub-array's profile is entirely determined by the lower band element thickness. The microstrip stacked patch fits well to these require-

ments, and is employed for the X-band element.

In the next section, some performance enhancement techniques of microstrip stacked patch elements are reviewed first. It is followed by a description of the X-band element design.

3.3.1 Stacked Patch Review

A. Impedance Matching

The element impedance matching is closely related to the bandwidth, and is a key specification for the antenna. For some applications, minimum return loss of 10dB or even 6dB is sufficient, but for SAR application considered here, 15dB return loss is required. Hence, the bandwidth quoted in this chapter is the 15dB return loss bandwidth.

The potential bandwidth of stacked patch is determined by its Q factor, which is related to laminate material and resonant cavity thickness. Whether the potential bandwidth can be realized or not depends on impedance matching, in which feeding methods play a key role. Probe feed and aperture coupling are two commonly adopted feeding methods for stacked patches. They are briefly discussed below.

A.1. Probe Feed

A design method for the probe-feed stacked patch is introduced in [106], and some suggestions for stacked patch matching are also given. A main principal is that an over-coupled driven patch with less coupled parasitic patch will be easier to match. In [137], a more detailed analysis is presented. An equivalent circuit model for the probe-fed stacked patch (shown in Fig.3-5) is introduced in [138]. Using this model, the input impedance of a

probe feed stacked patch antenna (Z_{in}) can be derived as [138]:

$$Z_{in} = \frac{Y_{12}^{p} + N^2 Y_{in2}}{Y_{in1}(Y_{12}^{p} + N^2 Y_{in2}) + N^2 Y_{in2} Y_{12}^{p}} + jX_p \tag{3-1}$$

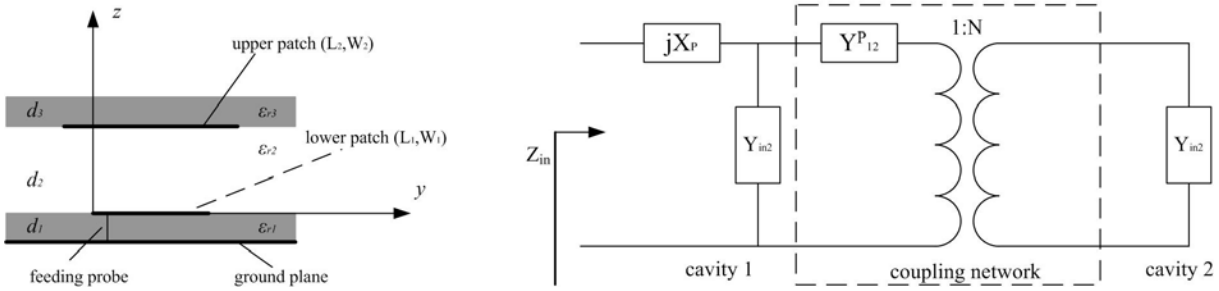

(a) Probe feed stacked patch antenna (b) Equivalent circuit model

Fig.3 - 5 Probe-fed stacked patch antenna and its equivalent circuit model [138]

where Y_{in1}, Y_{in2} and Y^{p}_{12} represent admittance of lower patch cavity, upper patch cavity and admittance from coupling of two cavities. The jX_p is the reactance from the probe and value N is the coupling factor of the two cavities. The cavity admittances, Y_{in1} and Y_{in2} are not further cited; they can be treated as a parallel resonant circuit in a transmission line model.

A.2. Aperture Coupling

Aperture-coupled stacked patch antennas have excellent cross-polarization levels and inter-polarization isolation. Besides, the aperture-coupled stacked patch has more parameters for tuning, which makes impedance matching easier. Complicated configuration is an apparent deficiency which limits its application. A detailed introduction on impedance matching of aperture-coupled stacked patch is given in [139]. Besides, according to [140], tri-resonance can be introduced by resonating the coupling slot, and hence, the 10dB return loss bandwidth can be extended to more than 69%. However, this impressive bandwidth is achieved at the expense of stronger backside radiation from the resonant coupling slot. The authors of [141] propose the equivalent circuit model for a single-layer aperture-coupled patch antenna, shown in Fig.3-6.

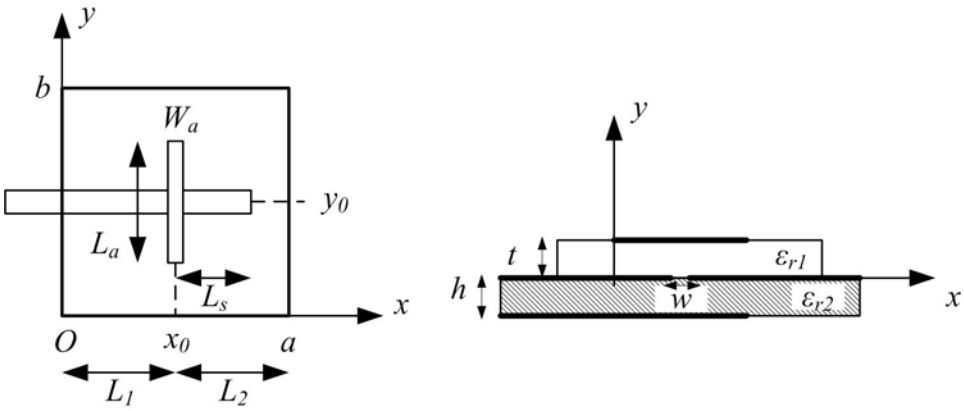

(a) Aperture-coupled patch antenna

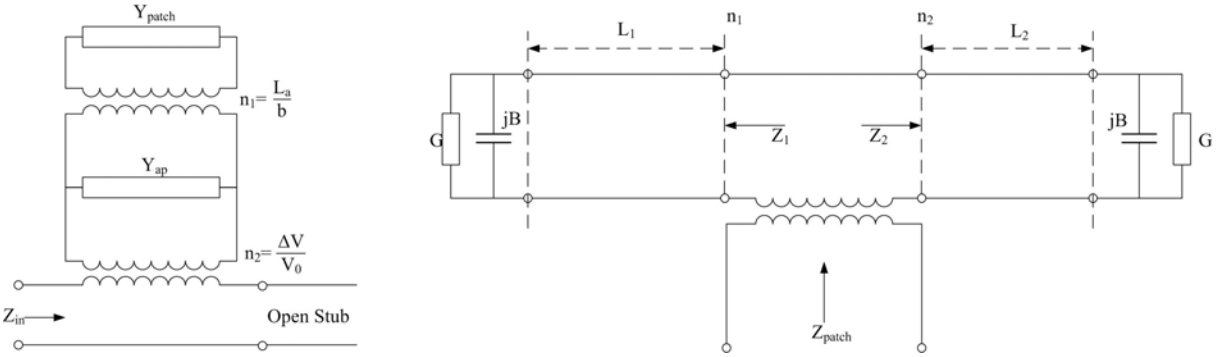

(b) Feeding model (c) Patch cavity model

Fig.3 - 6 A single layer aperture-coupled patch antenna and its equivalent circuit [141]

In Fig.3-6(b), Y_{patch} and Y_{ap} represent the admittance of patch cavity and coupling aperture, respectively, where the detailed equivalent circuit of Y_{patch} is shown in Fig.3-6(c). The *n1* and *n2* in Fig.3-4(b) are the coupling factors between feed line to aperture and aperture to patch, respectively.

Compared with the equivalent circuit model of the probe-feed patch in Fig.3-5, the aperture coupled patch introduces admittance from the coupling slot, which has some impact on the element bandwidth. A resonant aperture will lead to a Y_{ap} with a large real part, and thus improve element bandwidth (this is the case of [140]). Even the coupling slot is not resonant, the existence of Y_{ap} can slightly vary element bandwidth. Some other parameters, such as coupling factor between feed line and patch and the open-ended stub length, can also

be tuned for impedance matching, but they contribute little to the bandwidth.

B. Inter-Polarization Isolation

The inter-polarization isolation is a main concern in this project. Higher order modes [142] and asymmetric shapes of radiators are two factors degrading isolation. Hence, higher order mode suppression and element symmetry improvement are two ways for polarization isolation enhancement, and they can be realized by employing well designed feeding methods and symmetric element shapes, as introduced below:

B.1. Element shape

A symmetric element shape, or in another word, a symmetric boundary condition will excite a regular field distribution, resulting in good inter-polarization isolation [143]. Some commonly used two-dimensional symmetric patch shapes include rectangular patch [144], round patch [145] and annular patch [146], are shown in Fig.3-7. Among these, the annular

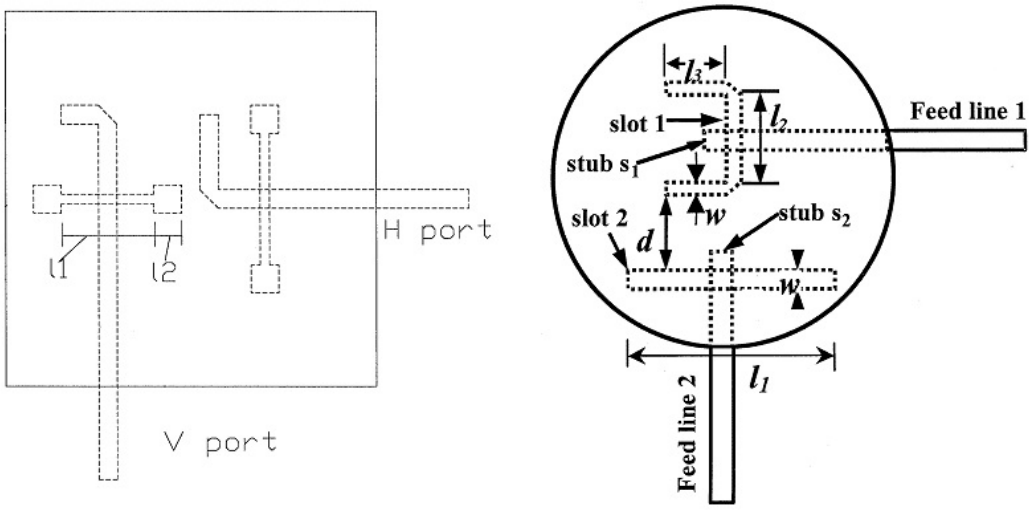

(a) Square patch [144] (b) Round patch [145]

Fig.3 - 7 Two commonly adopted 2-D symmetric patch shapes

shape can be seen as a patch with a large perforation in the center. This perforation decreases

element bandwidth, and hence makes annular patch less effective for this application. Hence, annular shape is excluded in this design, and is not considered here.

In general, rectangular patch and round patch have similar polarization isolation performance. The inter-polarization isolation and cross-polarization of round patch are slightly worse than the rectangular patch, because round patch has more cross current components [143]. This is evidenced in [144] and [145], where similar T-shaped aperture coupling feeding method are applied to rectangular and round patches, as shown in Fig.3-7. The results confirm that polarization isolation of rectangular patch is about 8dB better than that of the round one.

B.2. Feeding method

In a microstrip stacked patch, feeding method has a close relation to the higher order mode suppression, and will also inevitably introduce asymmetry. For example, a classical inter-polarization isolation level of a dual probe-feed microstrip patch is around 20dB [137], while the aperture coupling can inherently achieve inter-polarization isolation of better than 30dB.

Adopting symmetric feeding structure and avoiding higher-order mode excitation can further improve the inter-polarization isolation of microstrip stacked patch. The reported inter-polarization isolation improving solutions can be classified into the following types:

- Symmetric single point feed method can provide better inter-polarization isolation by moving feed point towards patch center, and thus, make feeding structure symmetric. In most cases, this method employs aperture coupling, because a probe feed cannot excite the patch at the center position. The classical examples are T-shaped (Fig.3-7) aperture coupling, whose coupling slot is located at the center of one dimension of the patch. The

cross slots (Fig.3-8) are more symmetric than T-shaped aperture coupling, and will provide better inter-polarization isolation. However, one more layer is required than T-shaped aperture coupling, to keep feeding structure completely symmetric, as shown in Fig.3-8(b).

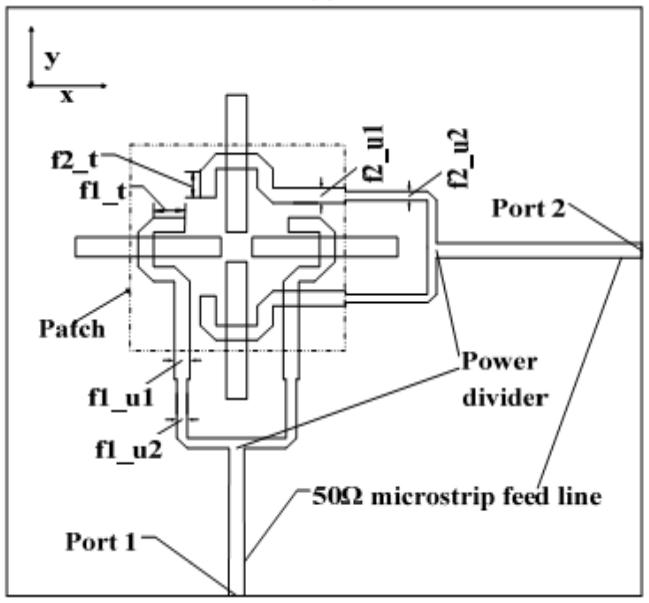

(a) Isolation ≥ 50dB [147]

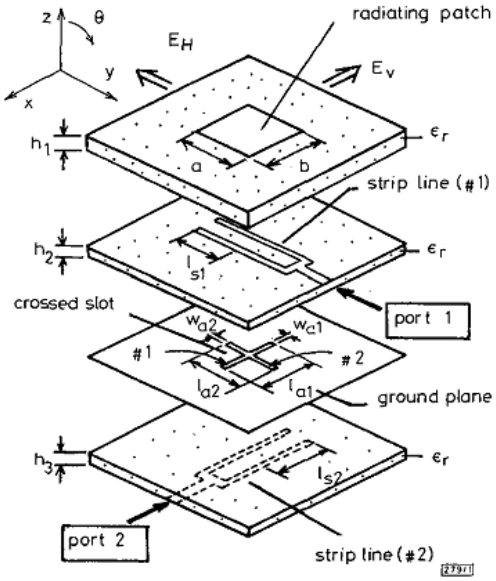

(b) Isolation ≥ 30dB [148]

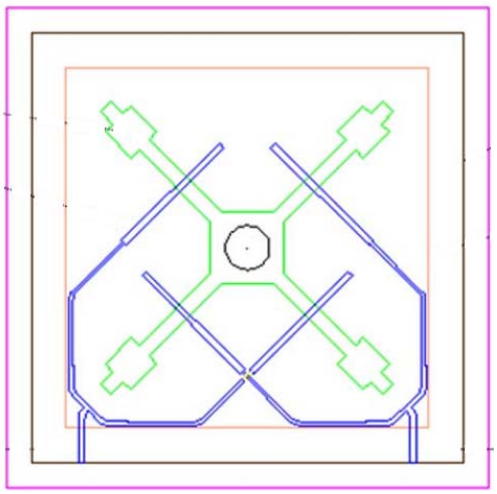

(c) Isolation ≥ 30dB [149]

Fig.3 - 8 Aperture coupling feed with cross coupling slots

- Balanced feed (multi-feed) is usually employed in the offset feed cases, like probe feed or L-shaped probe. Pairwise of feed points are mirror configured and excited out-of-phase,

as shown in Fig.3-9. Due to the out-of-phase excitation, some higher order modes from the mirrored excitation points cancel each other. Besides, the symmetry of feeding structure is also improved. Thus, better cross-polarization level and inter-polarization isolation are achieved. A disadvantage is that an external out-of-phase feed network is required, which has a complicated structure and needs extra space.

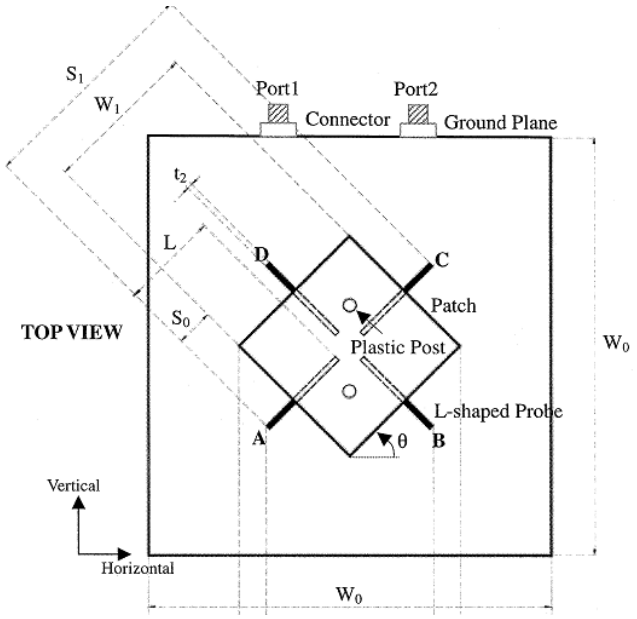

(a) L probe/balanced feed [150]

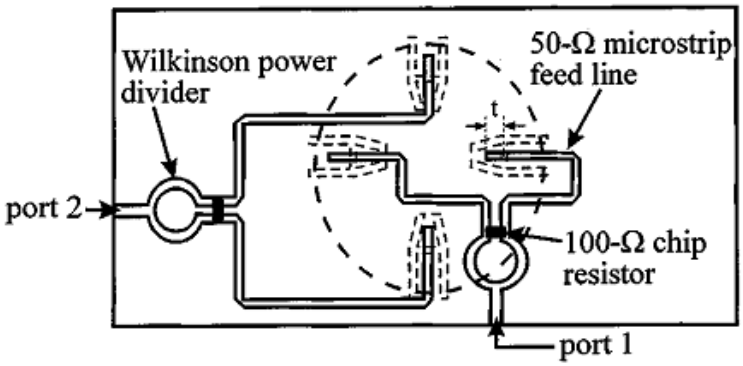

(b) Aperture-coupled/balanced feed [151]

Fig.3 - 9 Two balanced feed arrangements

- Hybrid feed employs different feeding methods for each polarization. A common adopted hybrid feed combination is aperture coupling and probe feed (or proximity coupling) [152,

153]. In this configuration, the feed line of two polarization ports are physically shielded from each other by the ground, and thus provide good isolation [154], as shown in Fig.3-10.

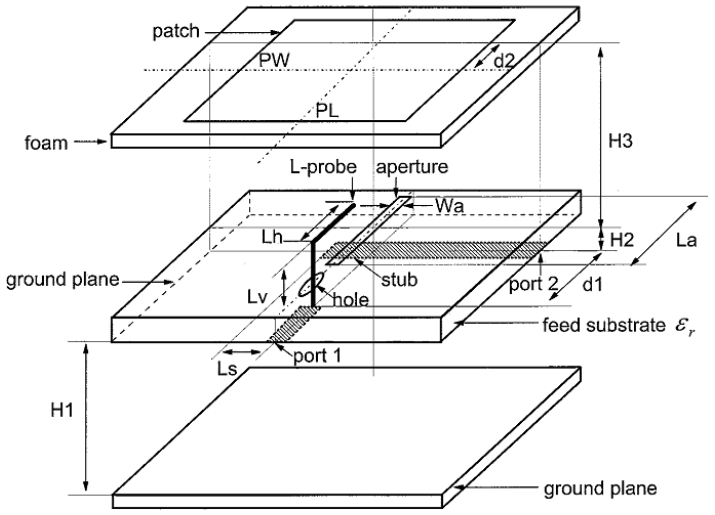

(a) L probe/aperture-coupled (isolation ≥ 25dB) [152]

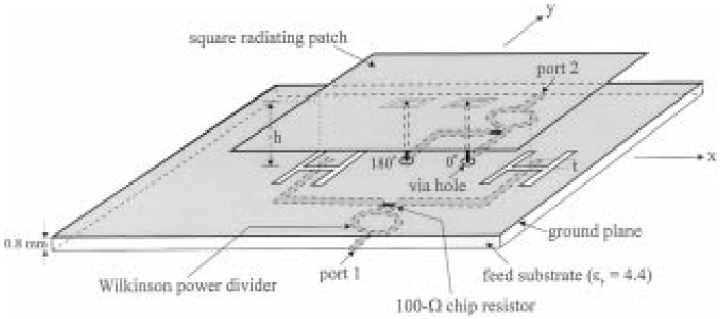

(b) Capacitive probe/aperture-coupled (isolation ≥ 40dB) [153]

Fig.3 - 10 Two hybrid feed arrangements

Comprehensive use of three solutions will perhaps provide better isolation performance. The element in Fig.3-10(b) uses both a hybrid feed and a balanced feed to achieve element polarization isolation of higher than 40dB.

3.3.2 X-Band Element Design

A. Feed Selection

The rectangular shape microstrip stacked patch is employed for the X-band element of the improved S/X DBDP-SA array, due to the reason that a rectangular stacked patch requires less space than a round one. This advantage makes it more suitable as more room will be available to interleave the lower-band elements. Besides, rectangular patch also provides

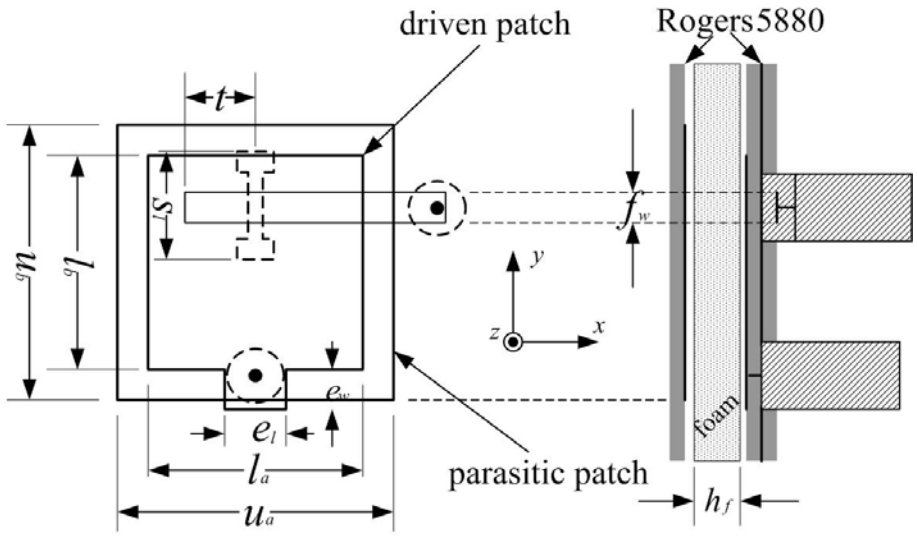

(a) Hybrid feed (Solution A)

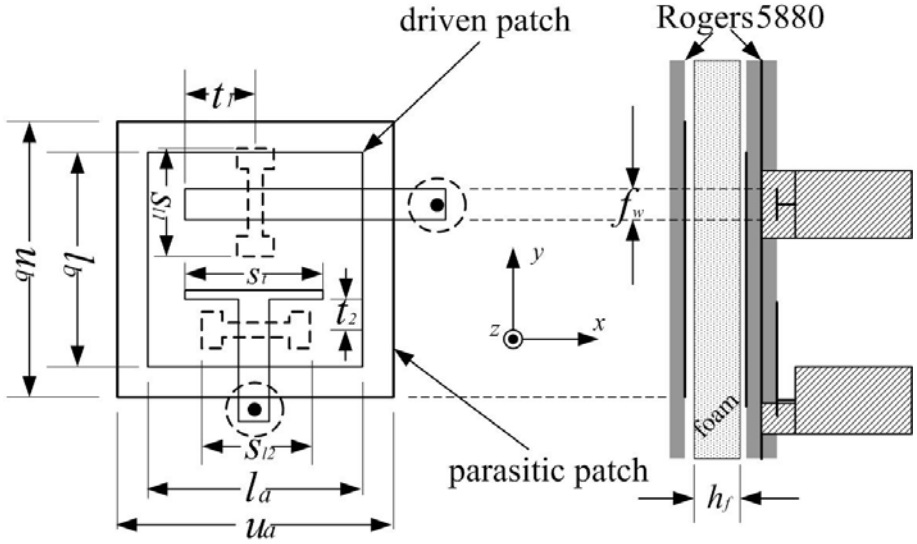

(b) Aperture coupling (Solution B)

Fig.3 - 11 X-band element configurations designed in this chapter

better inter-polarization isolation and fabrication robustness.

As for excitation, dual probe feed is excluded at first due to its poor inter-polarization isolation level. The cross slot and balanced feeding methods are also abandoned, because they need more layers or more space to fit feed network, making them less compatible for a compact DBDP-SA array. Hybrid feeding and T-shaped aperture coupling are the two most promising candidates for the current design, because they can achieve good inter-polarization isolation with an easier element configuration. In this chapter, the hybrid feed (aperture coupling / probe-feed) patch shown in Fig.3-11(a) is called Solution A and the T-shape aperture-coupled patch shown in Fig.3-11(b) is called Solution B. Both solutions were designed to compare their advantages and disadvantages.

B. Feed Design

In Solution A, the aperture coupling slot is located at the center of the l_a edge for symmetry in x-direction, and is offset to a side in *y*-direction to leave enough space for probe feed. Because aperture coupling slot introduces extra admittance than probe-feed port (refer to the explanation in Section 3.3.1), the aperture coupling edge length (l_a and u_a) is slightly shorter than that of the probe-feed edge length (l_b and u_b), to ensure that the two polarized ports operate in the same frequency range. In other words, the patch is rectangular rather than square.

Solution B adopts T-shape configured aperture coupling slots, as shown in Fig.3-11(b). The horizontally polarized feeding port has same structure as that in Solution A. The vertically aperture coupling slot is set aside in the *y*-direction and remains symmetrical in *x*-direction for inter-polarization isolation improvement. Bone-shape coupling slots are em-

ployed in both polarized ports to increase the coupling between the patch and feed line, as well as to suppress backward radiation [155, 156].

Both solutions were simulated using Ansoft HFSS 10.0. The parameters are optimized and the values of the fined designs are listed in Table 3-2. The predicted S parameters are

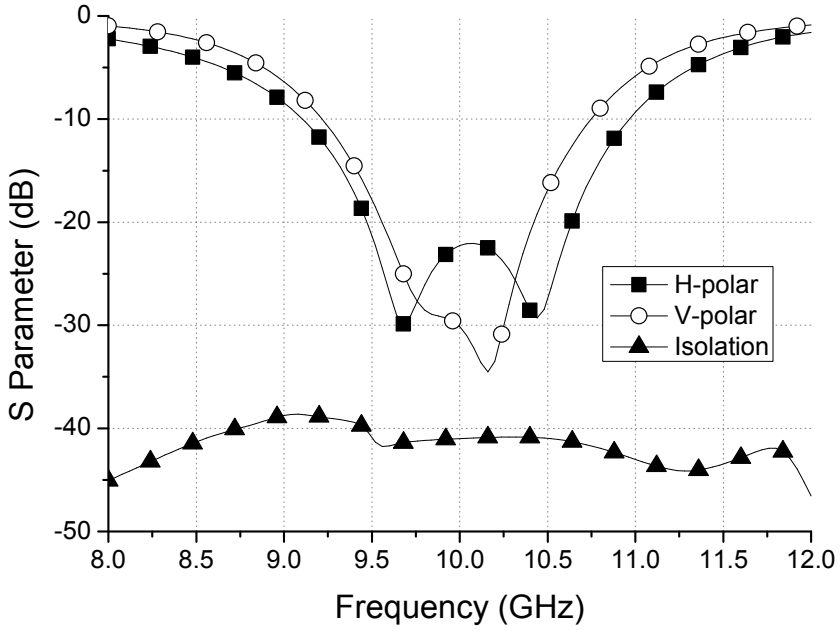

(a) With Hybrid feed (Solution A)

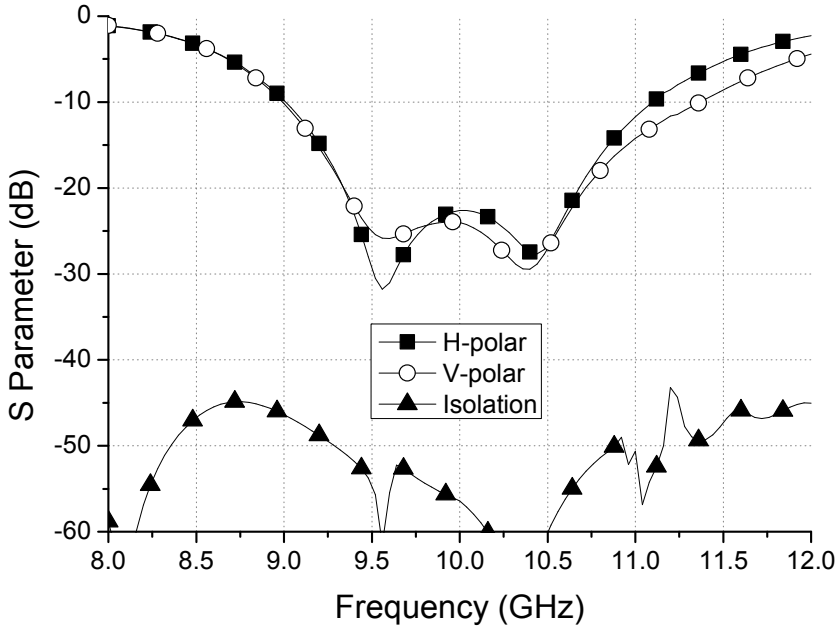

(b) With T-shaped aperture coupling (Solution B)

Fig.3 - 12 Predicted S parameters of two X-band element designs

Table 3 - 2 The optimized parameters for X-band elements

Solution A (Unit: mm)					
l_a	7	u_a	8.4	e_l	3.2
l_b	7.6	u_b	8.4	e_w	1.5
s_l	4.1	t	2.7	h_f	2.8
Solution B (Unit: mm)					
l_a	7	u_a	8.4	s_{l1}	3.9
l_b	7	u_b	8.2	s_{l2}	5
t_1	2.8	t_2	0.75	s_t	4.6
f_w	1.3	h_f	2.6		

shown in Fig.3-12. From the computed results, the following pros and cons of two solutions are found:

- Both methods provide isolations of better than 40dB, where Solution B has a 7dB advantage over Solution A;
- In Solution A, different port impedances (or $|S_{11}|$) are observed at the two ports. Apparently, this is caused by the different feeding methods employed for the ports. Solution B, adopting aperture coupling in both ports, is free from this problem.
- Some efforts were made when tuning Solution A, to make the port bandwidth uniform. It was found that because of the reactance introduced by the probe and coupling slot, both ports can hardly realize their best bandwidth simultaneously. In Fig.3-12(a), the bandwidth of the probe-fed port is slightly narrower than the aperture-coupled port.

In general, both methods reach the requirements of the design. Solution A is finally employed for the following reasons:

1) Solution A is more compact than solution B because the probe (connector) is right below the patch, while in solution B, the vertical aperture-coupled port needs a short feed line, which occupies extra space, as shown in Fig.3-13. It is extremely advantageous in an

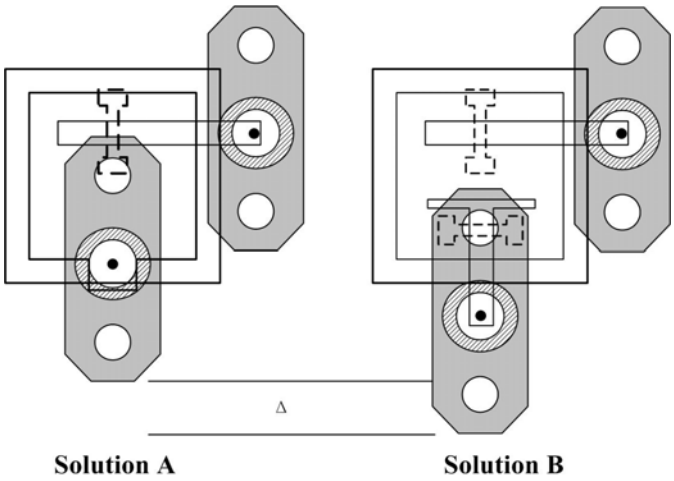

Fig.3 - 13 Connector space for the two solutions

X-band two-dimensional scan array, because X-band elements require a considerable amount of connectors. Pair-wise anti-feed array configuration makes aperture further congested. Thus, Solution B is hardly achieved because its SMP connectors will conflict with each other in the connector mapping stage (please refer to Section 3.4). P.S. The SMP connector is the smallest reliable connector which is commercially available in the market.

2) The multi-layer hybrid feed technique adopted in Solution A is more challenging, and its fabrication method also makes sense for some complicated feeding methods that have two sets of feed network above and below ground plane.

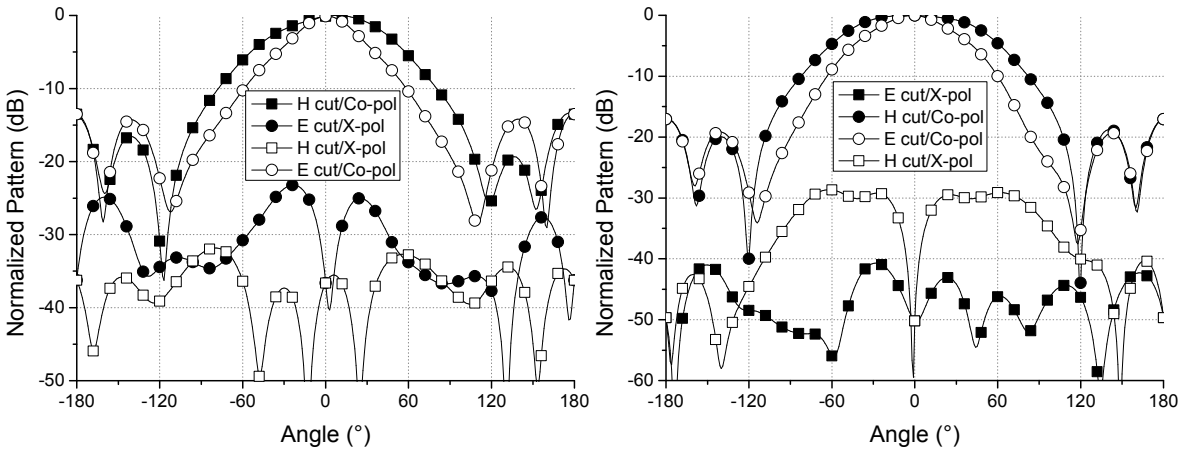

(a) Horizontal port (b) Vertical port

Fig.3 - 14 Predicted radiation patterns of Solution A

The predicted radiation patterns of employed X band element (Solution A) are shown in Fig.3-14. The predicted bandwidth and inter-polarization isolation can trace back to Fig.3-12.

3.4 S-Band Element

3.4.1 Element Consideration

Microstrip dipole (also called narrow edge patch) is adopted as the S-band element due to its slim structure, shown in Fig.3-15. Similar to the X-band element, a stacked structure is employed for bandwidth improvement. Proximity coupled feeding method is applied in the S-band microstrip dipole, where a vertical feeding structure to the driven dipole and the associated insertion loss are avoided. The non-vertical feed structure also ease the fabrication. For economic reasons, the proximity coupled feed line and driven dipoles are co-planar etched in the gap of X-band driven patches and parasitic patches. The parasitic dipole is printed on the lower surface of the top superstrate, as shown in Fig.3-1. The symmetric stubs,

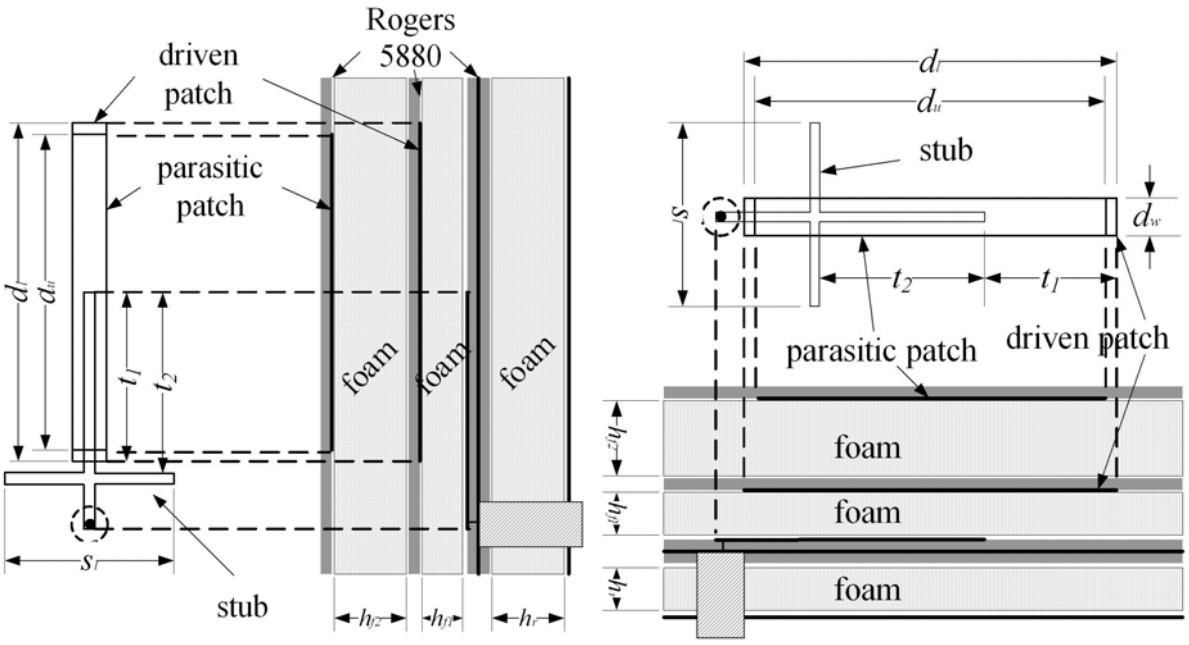

(a) Vertically polarized element (b) Horizontally polarized element

Fig.3 - 15 S-band element configurations

which are expected to reduce spurious stub radiation [109], are employed on the feed line for impedance matching. The horizontally and vertically polarized microstrip dipoles have a similar structure, with only difference being their stubs positions, which are decided by the X-band element gap position, as shown in Fig.3-1.

3.4.2 Bandwidth Enhancement

Unlike in the case of the X-band stacked patch, the bandwidth of the S-band microstrip dipole can not improved by simply increasing element thickness, because that will increase the overall profile of the improved S/X DBDP-SA sub-array. The worse is, this microstrip dipole has a narrower radiation edge than the square stacked patch, which results in a higher Q factor and a narrower bandwidth. A main effort of the S-band element design is how to reach the microstrip dipole's potential bandwidth within the given element thickness.

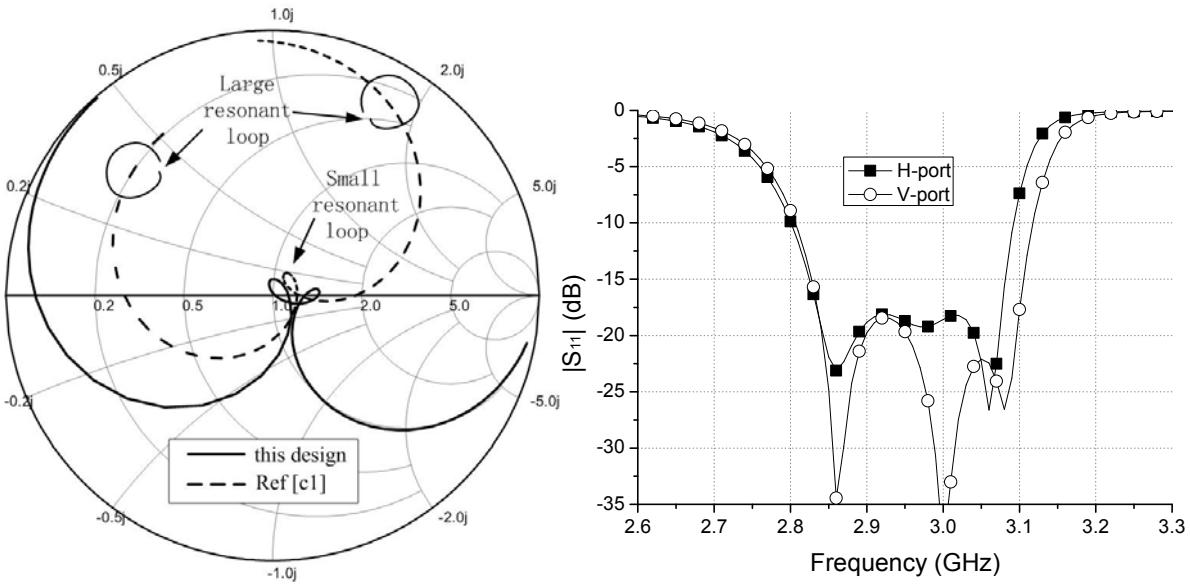

(a) Smith Chart (b) $|S_{11}|$ with tri-resonance

Fig.3 - 16 Predicted S-band element performance

A. Tri-Resonance

The S-band microstrip dipole was improved with the help of Ansoft HFSS 10.0. The predicted return loss curves are plotted in Fig.3-16 with that of a previous S-band element in the preliminary work [83, 84] for comparison. Two resonant loops can be observed in the previous study (marked as the dotted line). The smaller resonant loop, which is generated by the coupling between stacked dipoles, is located at the center of the Smith chart. The result is a dual-resonance return loss pattern. However, the potential bandwidth of the stacked dipole is not fully exploited. By adjusting the stub length and position, the large resonant loop size can also be reduced and matched to form tri-resonance, as shown in Fig.3-16(a). The potential bandwidth (refer to the frequency range in which the input impedance varies slowly) is reached according to the port response on Smith Chart. One more advantage is that the port impedance changes rapidly at the edges of the bandwidth, giving good cut-off performance.

Table 3 - 3 Optimized parameters of S-band elements

Vertical polarized microstrip dipole (Unit: mm)					
d_l	39.2	d_u	36.6	d_w	4
t_1	18.8	t_2	18.55	s_l	20
h_{fr}	6.8	h_{f1}	2.8	h_{f2}	7.5
Horizontal polarized microstrip dipole (Unit: mm)					
d_l	39.6	d_u	36.9	d_w	4
t_1	10.6	t_2	18.55	s_l	19.8
h_{fr}	6.8	h_{f1}	2.8	h_{f2}	7.5

All the parameters of S-band stacked microstrip dipoles (both horizontally and vertically polarized ones) are optimized using Ansoft HFSS 10.0. They are listed in Table 3-3 for reference.

B. Principle of Tri-Resonance

The microstrip dipole tri-resonance principle can be explained in both transmission line

model (TLM) and cavity mode theory:

1) TLM: the feed line and stubs of proximity coupling have a fixed length, and they can only accurately match at one frequency point. At other frequencies, they will inevitably introduce reactance. In the design, the feed line and the stub are matched accurately at the lower edge of bandwidth. At the higher end of bandwidth, the reactance from feed line and stub are conjugated with that from the microstrip dipole. The imaginary part of port impedance is cancelled, the port is thus re-matched, and tri-resonance is formed. A detailed theoretical analysis of how to introduce an extra resonance by stub line can be found in [157].

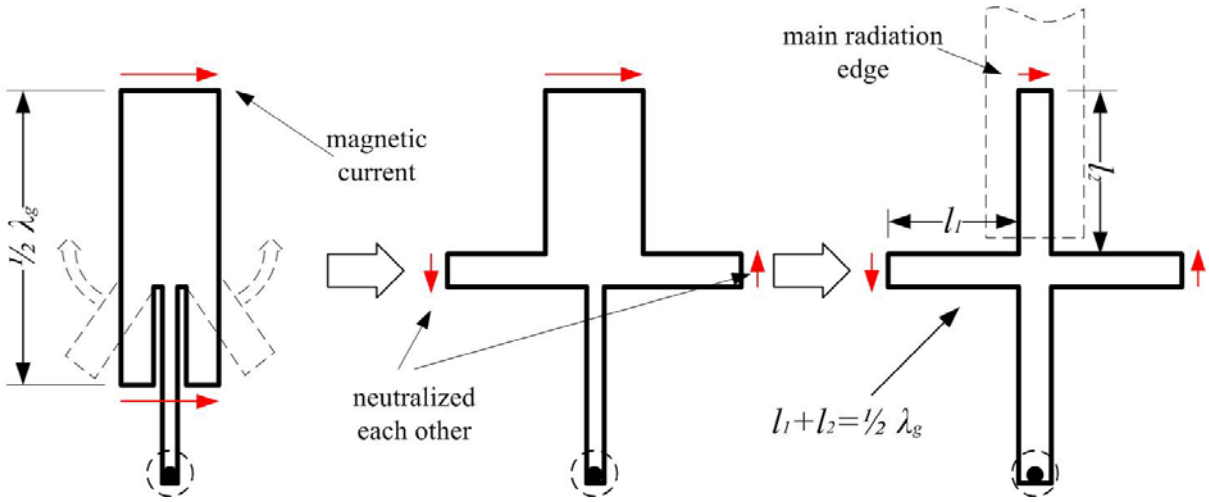

Fig.3 - 17 Deformation from half-wave narrow patch to feed line & stub cavity

2) Cavity mode theory: from the radiation theory, the tri-resonance implies that the structure has the appropriate radiation part. In this design, the feed line together with the stub line forms a half-wavelength radiator. They can be seen as a deformed patch, as illustrated in Fig.3-17.

The feed line and stub will contribute to the radiation when feed line and stub's total length ($l_1 + l_2$ in Fig.3-17) approaches the half-wavelength. It should be noted that the $l_1 + l_2$ is

slightly shorter than the exact half effective wavelength due to the reactance from the microstrip dipole.

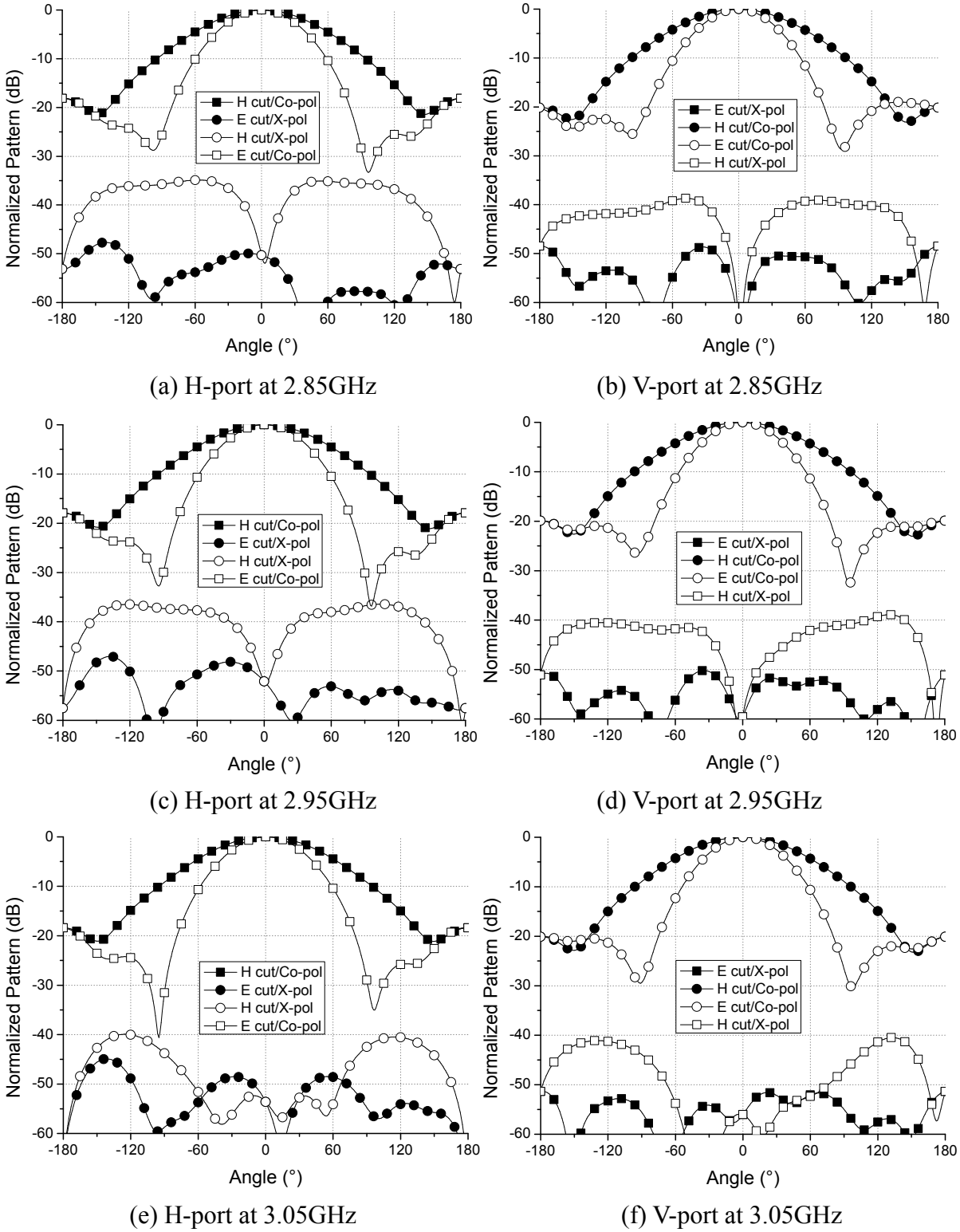

(a) H-port at 2.85GHz (b) V-port at 2.85GHz

(c) H-port at 2.95GHz (d) V-port at 2.95GHz

(e) H-port at 3.05GHz (f) V-port at 3.05GHz

Fig.3 - 18 Predicted S-band radiation patterns

Since the feed line layer is quite thin (0.508mm) in this design, the Q factor of feed line and stub resonance cavity is quite high. Hence, the bandwidth improvement is not so much significant after introducing tri-resonance. The 15dB return loss bandwidth increases from 6.6% to 10% due to tri-resonance.

An aperture coupled tri-resonant stacked patch is also reported in [140], which is realized by resonating the coupling slot. Because aperture coupling slot has a very low Q factor, an impressive bandwidth of 69% is achieved. The resonant coupling slot cannot be employed in S-band element considered in this chapter for three reasons: 1) resonant aperture will also produce backward radiation, which deteriorates front-to-back ratio. 2) Using reflector, backward radiation can be overcome at the expense of thickness (1/4 wavelength of S-band); however, the bandwidth will also decrease with the increasing of Q factor. 3) Because the microstrip dipole has a slim structure, it cannot cover a long resonant coupling slot, and this coupling slot will conflict with other elements.

The magnetic currents (M-currents) at the end of the symmetric stubs are in opposite directions, and hence they cancel each other at the broadside. They contribute little to the cross-polarization level inside the mainlobe area. The M-current in the front of feed line is the main radiation source of the feed line and stub resonance cavity. To show the radiation performance of tri-resonant S-band element, the predicted radiation patterns and cross-polarization at 2.85 GHz, 2.95 GHz and 3.05 GHz are shown in Fig.3-18. The parameter definitions can be found in Fig.3-15. A symmetric radiation pattern and cross-polarization levels of less than -35dB are noted over the bandwidth.

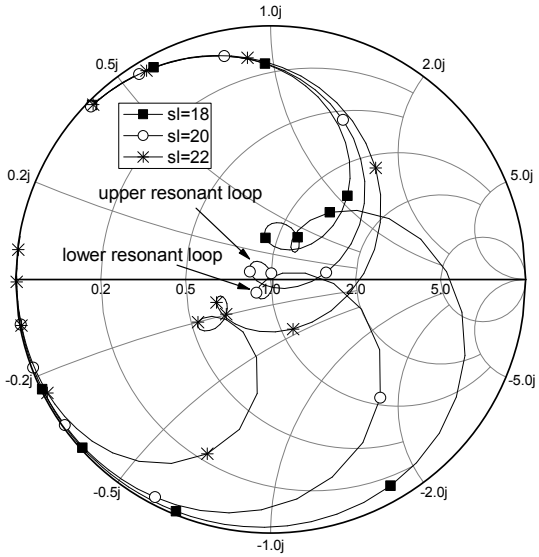

(a) S_l

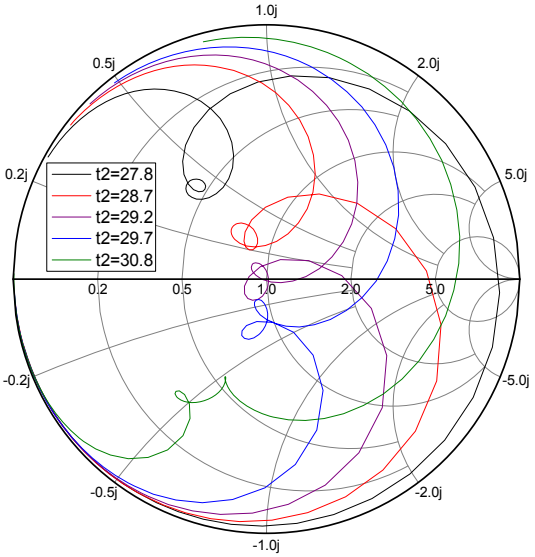

(b) t_2

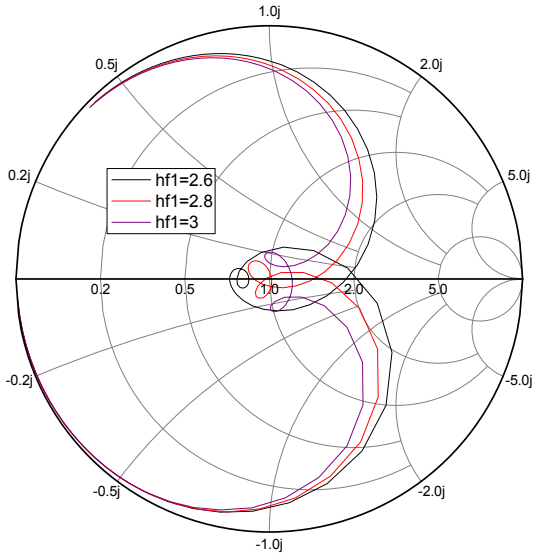

(c) h_{f1}

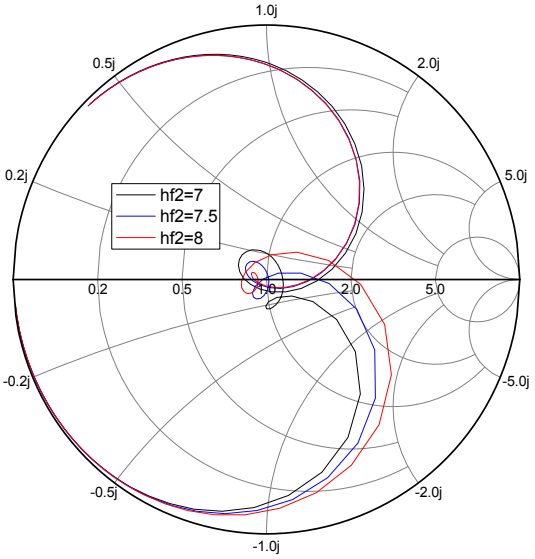

(d) h_{f2}

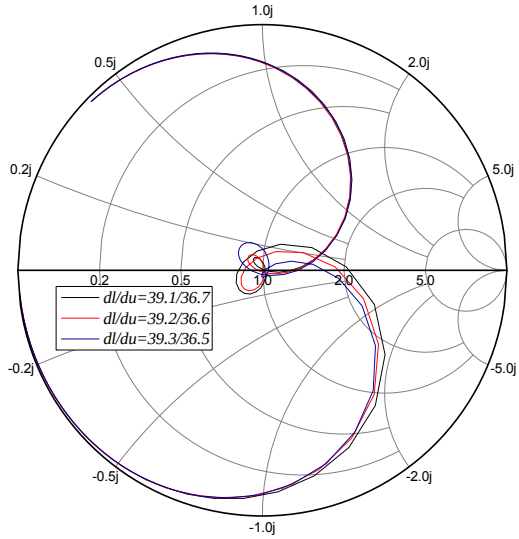

(e) d_l / d_u

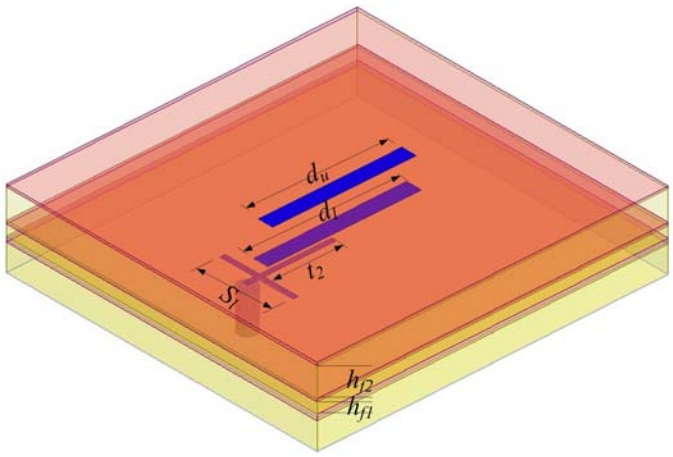

(f) Definitions in parameter study

Fig.3 - 19 Parameters study

C. Parameter Study

The vertical microstrip dipole is taken as an example, to briefly analyze some sensitive parameters relating to tri-resonance and their contributions to the bandwidth.

As the stubs must be located in the gap of X-band elements (as shown in Fig.3-1), the tunable parameters (as defined in Fig.3-19(f)) are: 1) stub length S_l, 2) feed line length t_2, 3) upper-lower patch edge length ratio d_l/d_u, 4) foam height h_1 and h_2. As tri-resonance has two resonant loops in the Smith Chart, to avoid confusion, they are called the upper loop and the lower loop as defined in Fig.3-19(a). They are formed by coupling among feed line cavity, lower cavity and higher cavity. The results of the parametric studies are summarized below:

- Fig.3-19(a) shows the variation of impedance with stub length. Two trends can be observed: 1) stub length variations modify the reactance. The impedance curve moves toward capacitive area with the increasing of stub length; 2) The resonant frequency, as well as coupling, will be affected. That is, the upper loop will be enlarged with decreasing stub length while the lower loop remains almost unchanged.
- The higher-cavity and lower-cavity heights, h_{f1} and h_{f2}, have similar influence on the

impedance curve, as shown in Figs.3-19(c) & (d). By decreasing h_{f1} or h_{f2}, the upper loop positions move towards lower and higher impedance, respectively, with loop size enlarged. The lower loop moves towards higher impedance region with the loop size unchanged.

- The upper-to-lower patch edge ratio mainly affects resonant loops size, as shown in Fig.3-19(e): with the increasing patch edge ratio, the upper loop enlarges gradually, while the lower loop gets smaller. The loop position roughly remains unchanged.
- Feed line length t_2 has an impact on coupling between all three cavities, and therefore, affects both sizes and positions of the upper and the lower loops. The resonant loop shape variation and moving track is shown in Fig.3-19(b).

Summary: By tuning these five parameters, the resistance, reactance and resonant loop size of the element can be controlled individually for matching. Besides, from the parametric study, it was found that:

1) Tri-resonance is insensitive to the foam height. The resonant loops can still roughly stay at the center of Smith Chart even when the foam heights have 5-10% fabrication error. This is extremely advantageous from engineering point of view, because the foam is relatively soft. Its deformation and thermal expansion cannot be completely avoided in the fabrication.
2) The impedance is quite sensitive to the upper-to-lower edge ratio and feed line length. Hence, the vertical positioning accuracy of each layer is crucial during fabrication.
3) Although the impedance is sensitive to stub length, its fabrication tolerance can be neglected, as the photonic etching fabrication method we employed is accurate enough at

present.

3.4.3 Inter-Polarization Isolation

Inter-polarization isolation is an important specification for SAR array. For the dual-polarized element, the inter-polarization isolation depends only on the element field distribution. Symmetric boundary condition will be helpful to obtain good isolation. For dual-polarization designs that use two orthogonally placed elements with single polarization, the good inter-polarization isolation can be achieved more easily, because dual-polarized elements are separated in space.

In the preliminary study [83, 84], the similar microstrip dipole is employed for S band, however, they are cross-shape configured to achieve dual-polarization, as shown in Fig.3-20 (a). This structure can be treated as a dual-polarized element entity with an isolation level of about 25dB. This value is not sufficient for the specifications given in Table 3-1.

Thus, the S band elements are T-shape configured to improve the inter-polarization isolation (See Fig.3-20(b)), as mentioned in Section 3.2.1. Compared with the cross-shape in [83, 84], the T-shape configuration actually moves H-polarized dipole outside, and thus obtains extra isolation from this space separation. The inter-polarization isolation of T-shape configured S-band elements are analyzed by parametric study, and the computed results are shown in Fig.3-21.

It is observed that the symmetric configuration in vertical direction (*i.e. dy = 0*, defined in Fig.3-20(b)) can provide the best inter-polarization isolation. Besides, in this structure, the

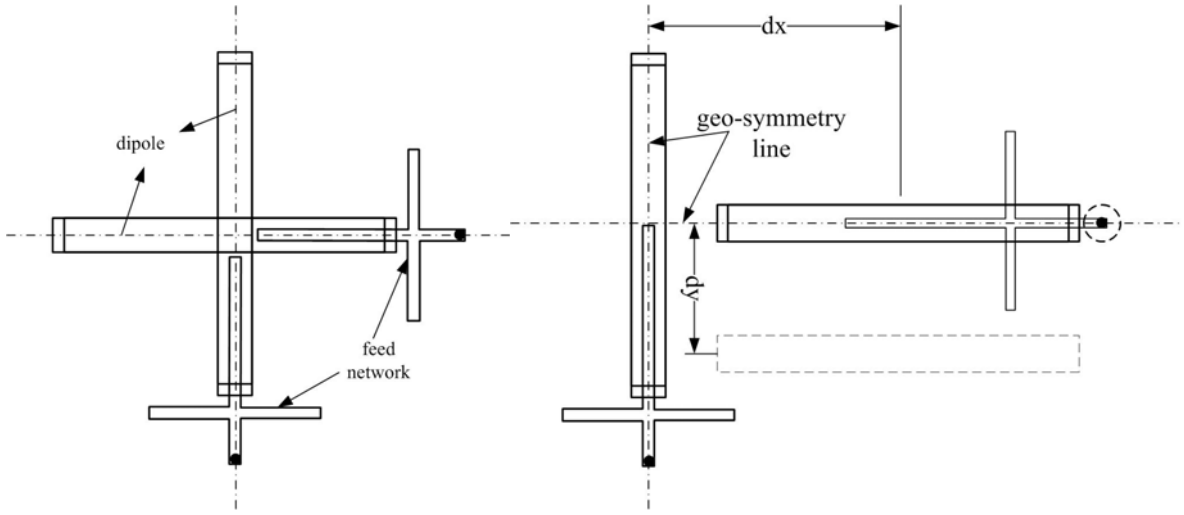

(a) Cross-shape configured in [83, 84] (b) T-shape configured in the thesis

Fig.3 - 20 S band element configurations

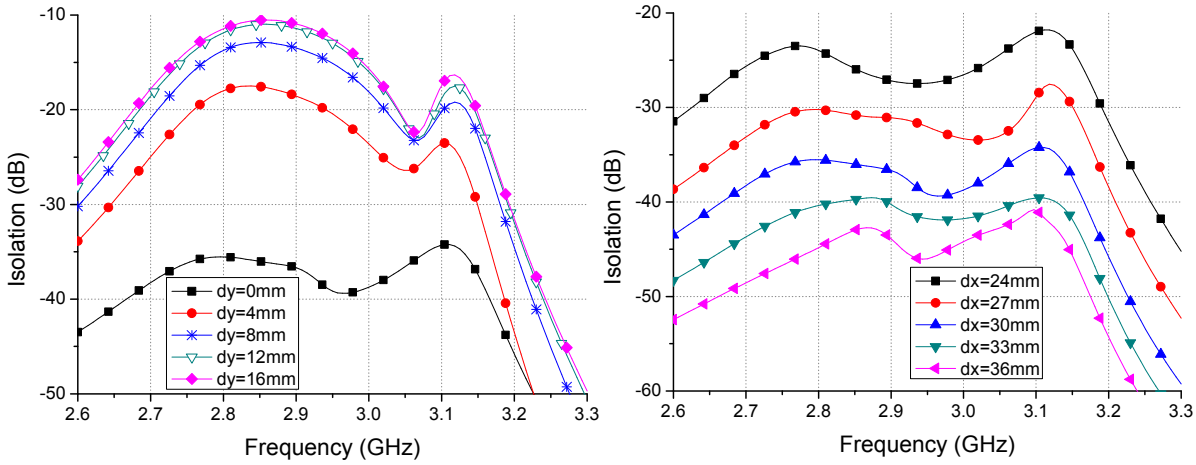

(a) Vertical bias (b) Horizontal bias

Fig.3 - 21 The effects of microstrip dipoles' relative position on isolation

isolation is very sensitive to the vertical deviation, it deteriorates rapidly with the increasing value of '*dy*'. For horizontal deviation (value '*dx*', defined in Fig.3-20(b)), the inter-polarization isolation improves linearly with the increasing of element spacing. Although in the design, the element distance between horizontal and vertical microstrip dipoles cannot be tuned freely (it is decided by the scan requirement), the parameter study of '*dx*' reveals the essence why T-shape configuration has a better isolation performance than that of the cross-shape config-

uration.

3.5 Prototype Array Fabrication

To validate the design, four sub-arrays were fabricated. Each sub-array contains 8 × 4 X-band dual-polarized stacked patches, 2 × 1 S-band horizontally polarized elements and 3 × 1 vertically polarized elements, as shown in Fig.3-22.

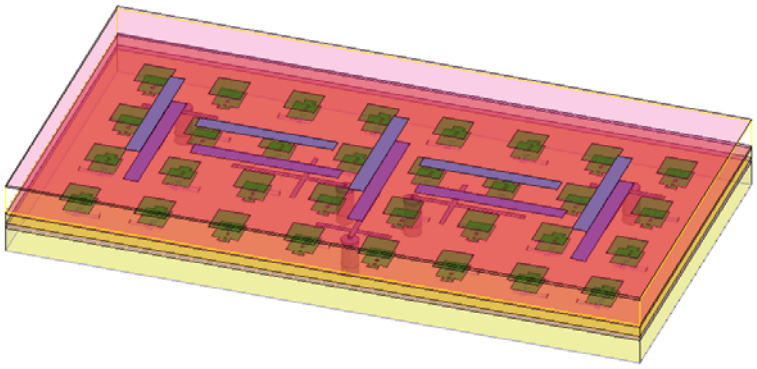

(a) Perspective view

(b) Front

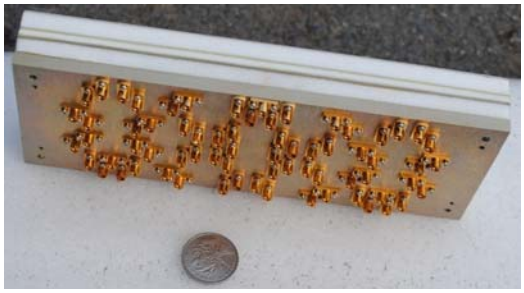

(c) Rear

Fig.3 - 22 S/X DBDP-SA prototype sub-array

3.5.1 Vertical Feeding Connector

Because the feed line of aperture coupling port is located in the lower side of the ground, effective vertical feeding is quite difficult in fabrication. For some approaches, side-feed connectors are usually enough. However, vertical connector mounting methods are necessary for aperture-coupled elements in this array, *e.g.*, as reported in [83, 84] and shown in Fig.3-23. However, it still has two deficiencies:

1) Half annular shaped connector should pass through the feed line layer to touch the ground (See Fig.3-23(b)). It is inconvenient for fabrication. Besides, the half annular-shape slot will obviously reduce the mechanical strength of substrates, especially for the thin laminate of this X-band feed line. Actually, the half round projection substrate was broken several times in the preliminary study.

2) The outer conductor grounding is not very reliable. As grounding is realized by surface touching between the ground and outer conductor, some factors like prepreg thickness, the substrate deformation and thermal expansion can make the outer conductor grounding ineffectively.

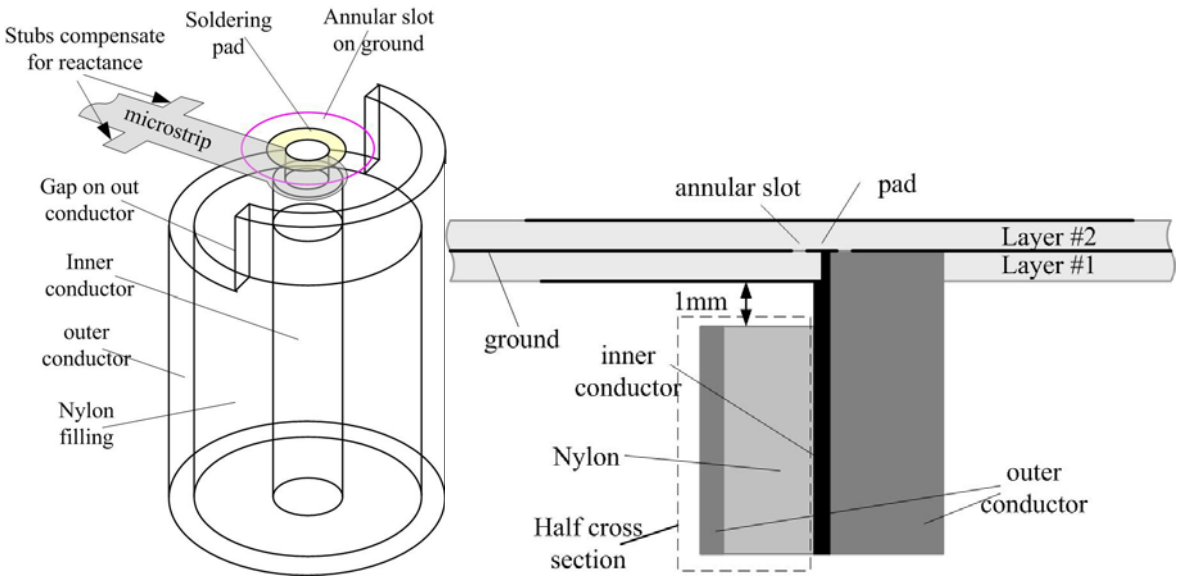

(a) Perspective view (b) Side view

Fig.3 - 23 Vertical transfer of aperture coupling to coaxial line [83, 84]

This vertical feeding solution can hardly be applied in a two dimensional scan array, because each element has a vertical connector. That is, it is quite difficult to ensure all elements are grounded well. Hence, a custom made SMP connector was adopted in the fabrication, as shown in Fig.3-24.

- **Aperture coupling port:** Layer #1 is a double sided substrate, where the ground and the feed lines are located on the upper and lower surfaces, respectively. A thin annular slot is etched around the feed point to make an isolated 'island' on ground, and it is connected to the lower feed line using a metalized hole. The SMP connectors with several custom-made contacts at the top of outer conductor are applied to connect the feed line. The inner and outer conductors get through the layer #1 via metalized hole, and they are soldered

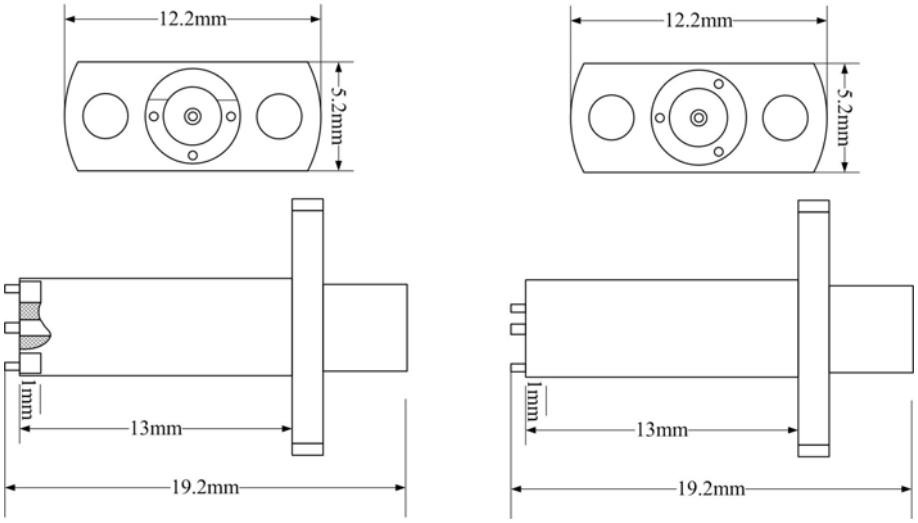

(a) Aperture coupling port (b) Probe-fed port

(c) Photo of the custom-made probe port connector

Fig.3 - 24 Custom-made SMP connector

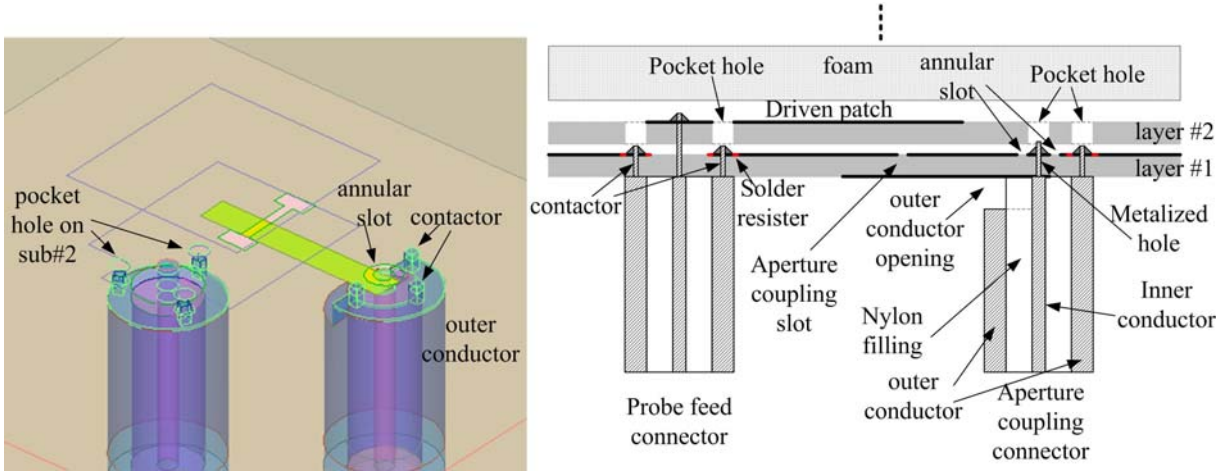

(a) Perspective view (b) Cross-section view (layer #1 & #2)

Fig.3 - 25 Custom-made connector and its fitting method

with the ground or pad on the upper surface of the layer #1. Considering that the welding spot has some height, to avoid conflict with the layer #2, some pocket holes are pre-drilled in layer #2 to contain these welding spots, as shown in Fig.3-25(b). To avoid the feed line short-circuited by the SMP outer connector, a part of outer connector at the upper end of SMP is removed, as shown in Fig.3-25(b).

- **Aperture coupling connector:** The removed part at the end of outer conductor should have a suitable height and get thinner if possible. The coaxial line characteristic impedance is no longer 50Ω with a part of the outer conductor removed, and a large gap will also introduce reactance. On other side, the removed part at SMP upper end cannot be too small, because in that case, the edge of the removal part will have a considerable effect on microstrip feed line. Besides, the annular slot on the ground will also introduce inductance to the port impedance. The stubs can be employed on the feed line to compensate for the reactance, as shown in Fig.3-25(a).
- **Probe-fed connector:** Similar to the aperture coupling connector, the contactors on the top surface of the outer conductor should get through the layer #1, and weld with the

ground. The inner conductor should further get through the layer #2 to weld with the driven patch. Because the inner conductor gets through two layers, more risk is introduced due to the gap between the two layers (prepreg thickness).

- **Welding:** For aperture-coupled port, the annular slot on ground forms an isolated soldering pad for inner conductor, while for the contactors on outer conductor, ring-shaped solder resistor is painted on the ground to restrict the welding spot size.

Compared with the vertical feeding method in [83, 84], the custom made SMP connector actually uses several contactors instead of a half annular outer conductor. As welding is adopted rather than surface touch, the new connector is more reliable. However, a large amount of inner conductors and contactors need to get through the layers #1 and #2, which requires accurate positioning when drilling holes through the substrates.

3.5.2 Auxiliary Hole on Patch

As shown in Fig.3-25(a), the probe-fed connector is right under the patch. The pocket hole of contactors on the outer conductor is thus drilled on the patch, as shown in Fig.3-26(b). To reduce the influence on the patch, the pocket holes are symmetrically configured. The effects of contactors and their positioning holes on S parameter were simulated and the results are shown in Fig.3-27.

The aperture-coupled port is seldom affected except for the slight rise of in-band ripple factor. With the contactors, the operation band of the probe-fed port moves slightly towards higher frequencies, and the in-band isolation remains better than 40dB. In brief, the symmetric contactors have a very limited impact on both ports.

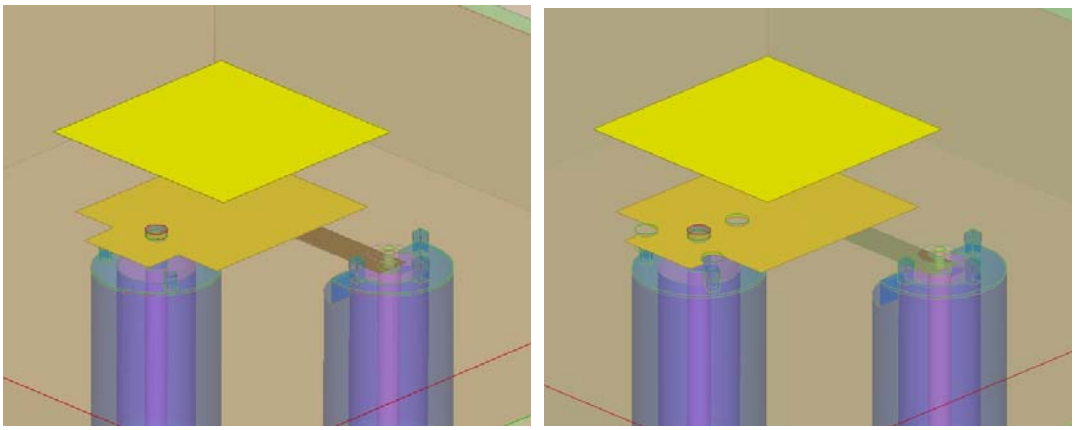

(a) Ideal patch (b) Patch with pocket holes

Fig.3 - 26 Pocket holes on patch

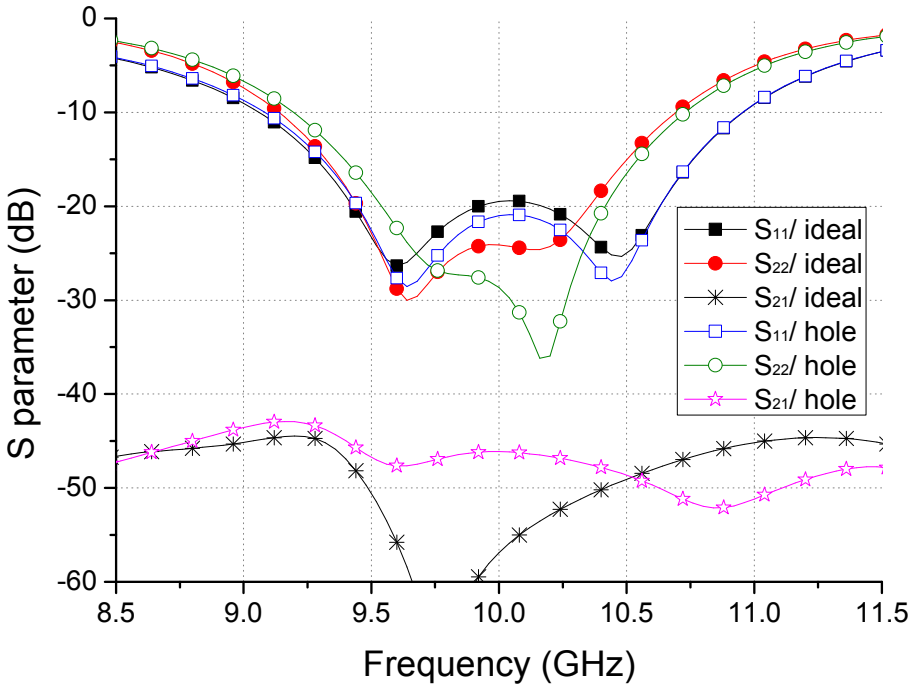

Fig.3 - 27 Effects of auxiliary holes on driven patch S parameter

3.5.3 Connector Configuration

The X-band element spacing is only 20mm, which is quite close to the connector flange size (12mm) we adopted. The pair-wise anti-feed technique [134-136] further increases the difficulties with the connectors' configuration, especially for vertically polarized port. Although some self-fixed connectors are more compact because of their flange free geometry,

shown in Fig.3-28, an ordinary SMP connector with two-hole flange is adopted due to the reliability. The connector configuration is shown in Fig.3-29. Four types of SMP connectors, marked in different colors in Fig.3-29, are employed to fit the hybrid feed and to avoid conflict with each other.

Fig.3 - 28 Flange free connectors

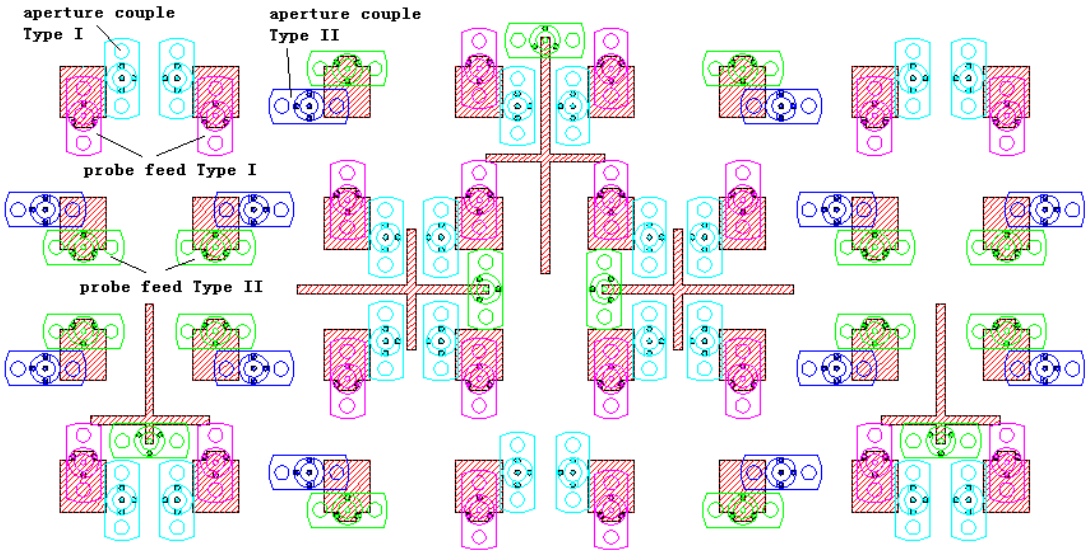

Fig.3 - 29 Connector configuration of the improved S/X DBDP-SA sub-array

3.6 Measurements

The port parameters of the improved S/X DBDP-SA prototype array were measured using Agilent 8722ES vector network analyzer (VNA), as shown in Fig.3-30, while the radiation patterns are obtained in the anechoic chamber of the China Electronic Technology Corporation (CETC) 38th research institute. Insertion loss of coaxial lines and power dividers were measured and compensated at the data post-processing stage. To avoid repetition, only #3 sub array's measured results are given in the following sections.

(a) Rear (b) Front

Fig.3 - 30 Prototype array under test

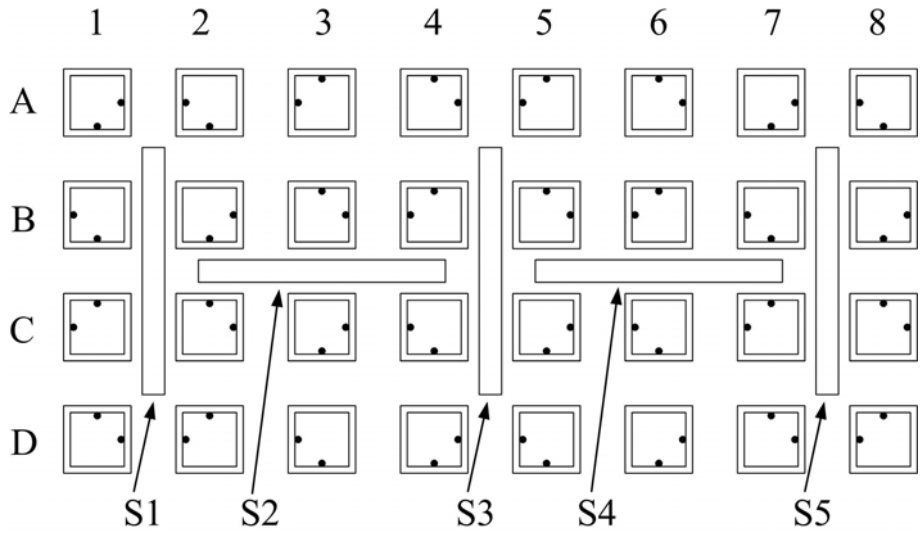

Fig.3 - 31 Element mark definition

For clarity, the elements in the sub-array are identified by row and column indices as defined in Fig.3-31. The X-band elements, from top to bottom, are marked in rows from A to D, and marked in columns from 1 to 8 from left to right. For example, the left bottom element is called D1. S-band elements are simply marked as S1 to S5 from left to right.

3.6.1 X-Band Port Parameters

In general, the measured X-band VSWR curves agree well with predicted results, as shown in Fig.3-32. Specifically, the measured VSWR curves of aperture-coupled ports have

good agreement with the prediction except for one fault element, which implies that the vertical feeding method of aperture coupling ports and the custom-made SMP connectors are reliable. The measured probe-fed port results, however, shift slightly towards higher frequencies, at the expense of raising in-band ripples. Fabrication tolerance is believed to be a main contribution to this deviation, including inaccuracy in inter-layer vertical positioning and inter-layer gap (prepreg) thickness.

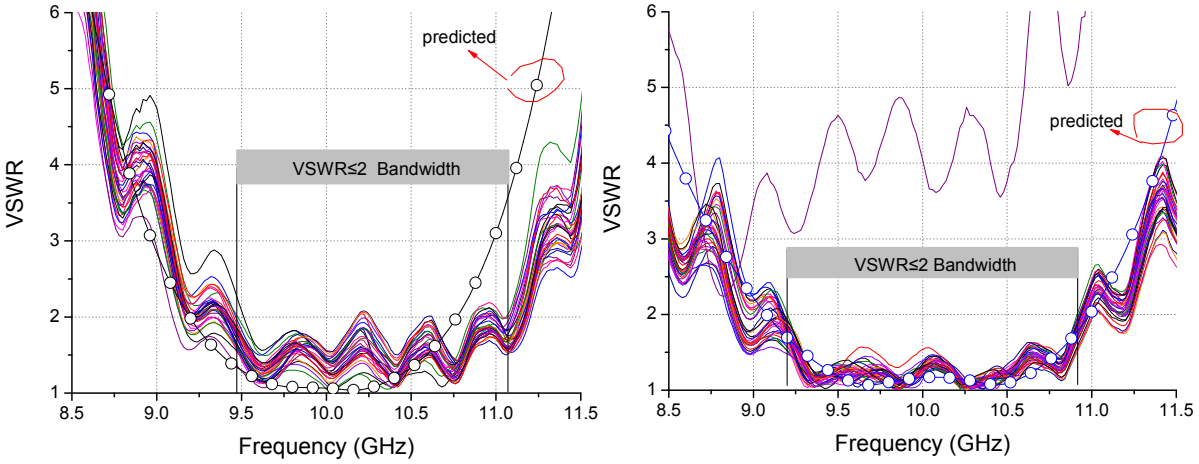

(a) Probe-fed ports (b) Aperture-coupled ports

Fig.3 - 32 Measured and predicted X-band element VSWR

The measured VSWR ≤ 2 bandwidth, defined as the overlapped VSWR ≤ 2 frequency range of both polarization ports, is 13.1% (9.52 GHz to 10.83 GHz); while the VSWR ≤ 1.5 ($|S_{11}| \leq$ -15 dB) bandwidth is 10% (9.52 GHz to 10.51 GHz).

The array isolation refers to the insertion loss between overall horizontal (H) and overall vertical (V) polarized ports, whom are formed respectively by connecting all the H- and V-polarized ports using coaxial lines and power dividers. The coaxial lines and power dividers insertion losses are measured and compensated in the post-processing stage. Because of the use of pair-wise anti-feed technique, the polarization cross talks of adjacent elements are out

of phase and they cancel each other in the feed network. The array isolation is therefore improved. The array isolation of better than 40dB is confirmed as shown in Fig.3-33.

The element isolation in array configuration is defined as the insertion loss between an

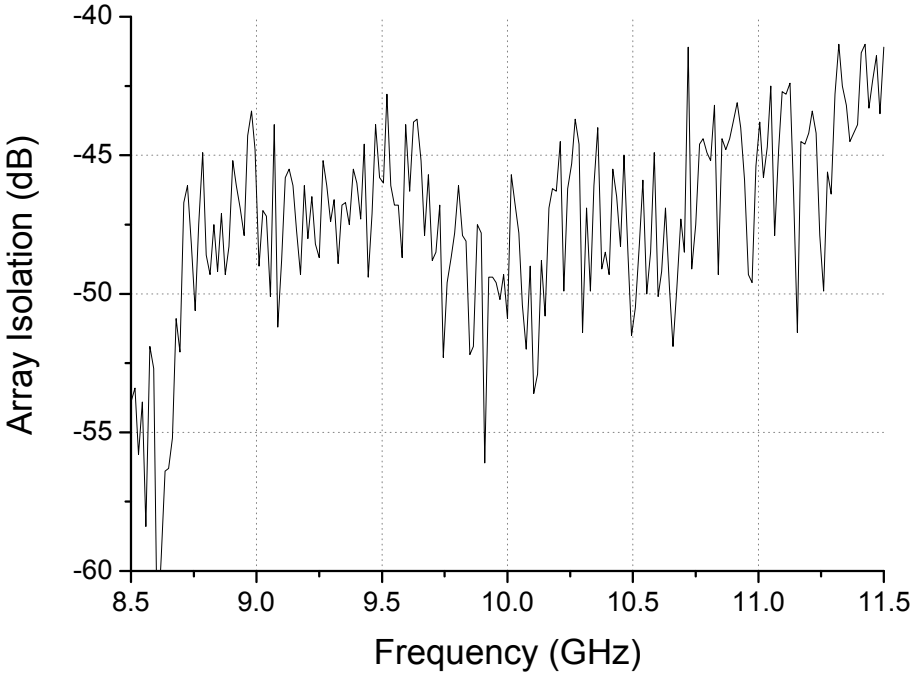

Fig.3 - 33 Array isolation

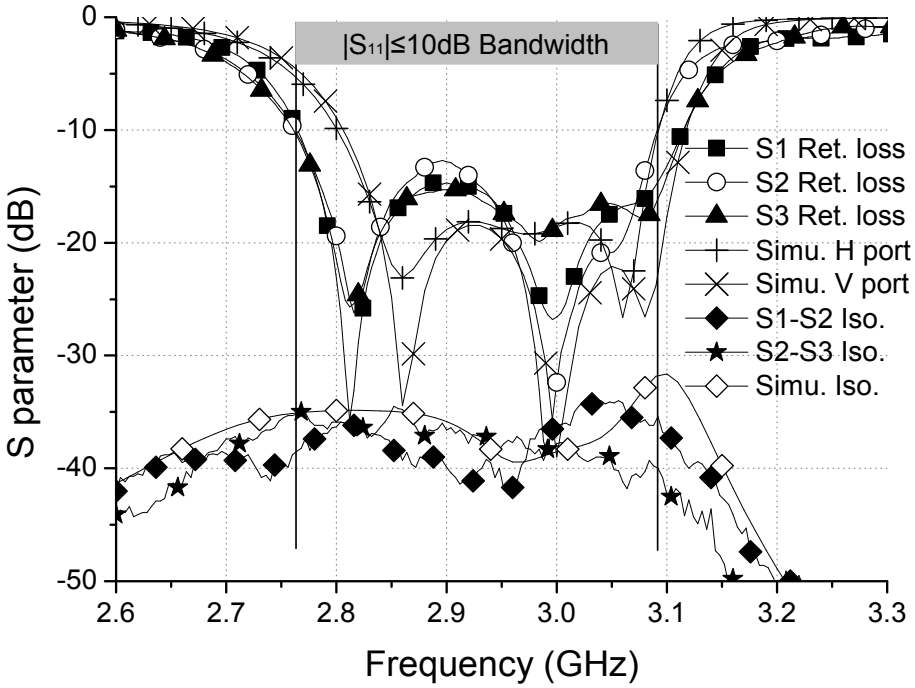

Fig.3 - 34 Measured and predicted S parameters of S-band elements

element's H- and V-polarized ports assuming all other elements are match-terminated. The element isolation will be discussed in Section 3.7.

3.6.2 S-Band Port Parameters

Fig.3-34 shows the measured S parameters of S-band microstrip dipoles. Only data for S1 ~ S3 are presented due to the symmetric structure.

The S3 element, which is located at the center of aperture, has complete symmetric X-band elements surrounding it. It is less affected by the inter-element coupling, and thus, clearly shows the 'tri-resonance' pattern. On the contrary, the S1 element, which stands at the edge of array, is severely affected by the asymmetric boundary condition (BC). Its tri-resonance pattern is not as obvious as that of the S3 element.

From Fig.3-34, the measured $|S_{11}| \leq$ -10 dB bandwidth is 11% (324 MHz, 2.766 GHz ~ 3.09 GHz), and the $|S_{11}| \leq$ -15 dB bandwidth is 10% (300 MHz, 2.78 GHz ~ 3.08 GHz). The higher limits of measured bandwidth agree well with the predicted limits for both polarization ports, while the lower limits are less than theoretical predictions. This is probably due to the tolerance in foam heights, which may raise the in-band ripple factor and correspondingly extend the bandwidth to lower frequencies. The measured polarization isolation between neighboring elements is better than 32dB. This validates good isolation performances of the T-shaped configuration.

3.6.3 Radiation Patterns

The measured X-band radiation patterns agree well with the results derived from array theory, as shown in Fig.3-35. The cross-polarization level is 30 dB lower than the mainlobe in

the main beam area. Limited by the coaxial line quantity (some coaxial lines are damaged during the test), only 8 × 3 elements were excited to calibrate the antenna gain. By comparing with a standard gain horn (SGH), antenna gains of 20.9 dB and 20.6 dB was achieved for ver-

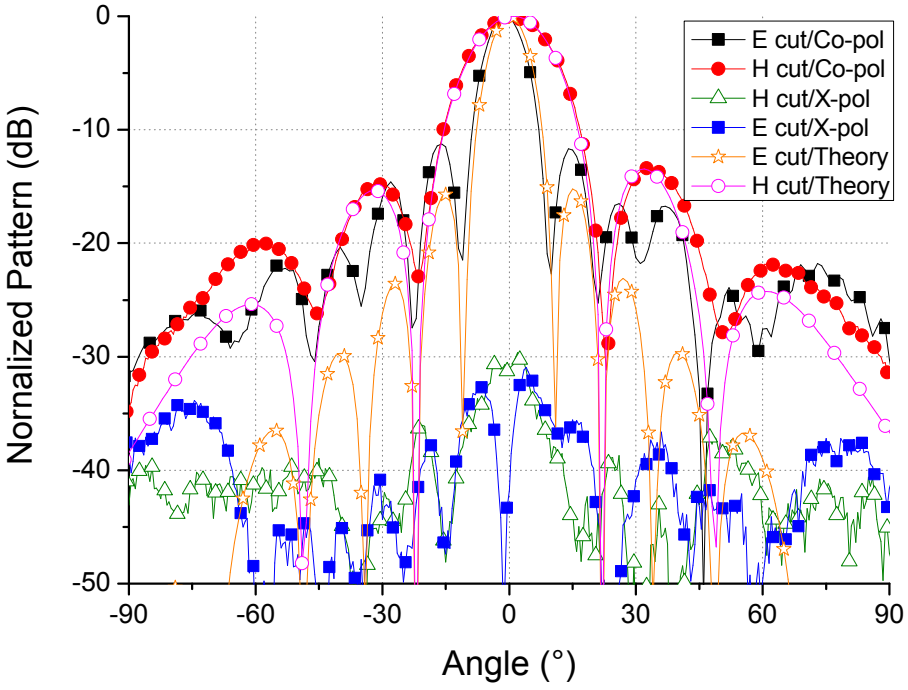

(a) Aperture-coupled port

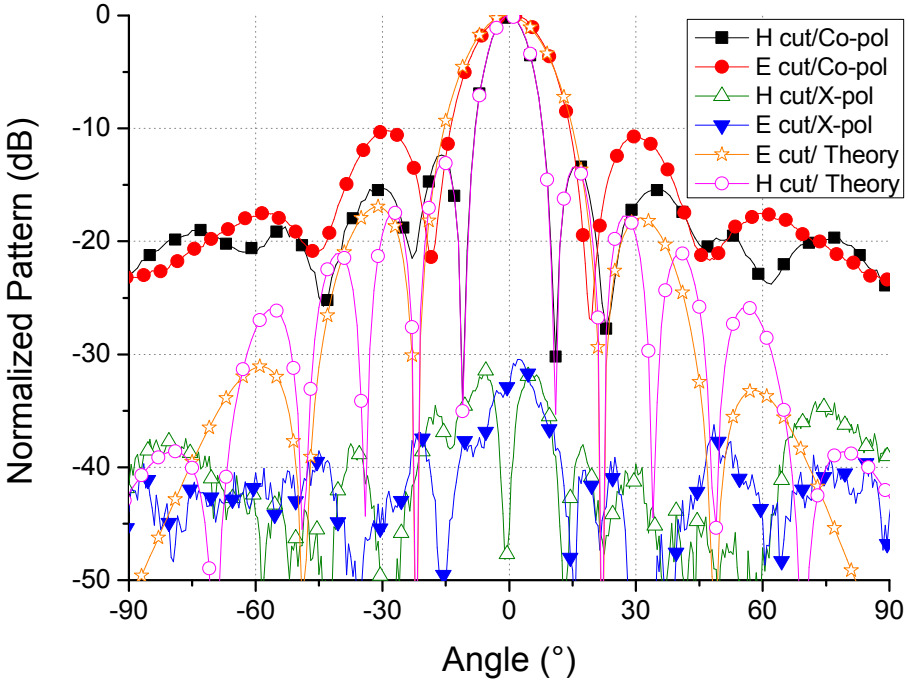

(b) Probe-fed port

Fig.3 - 35 Measured and calculated X-band element radiation pattern

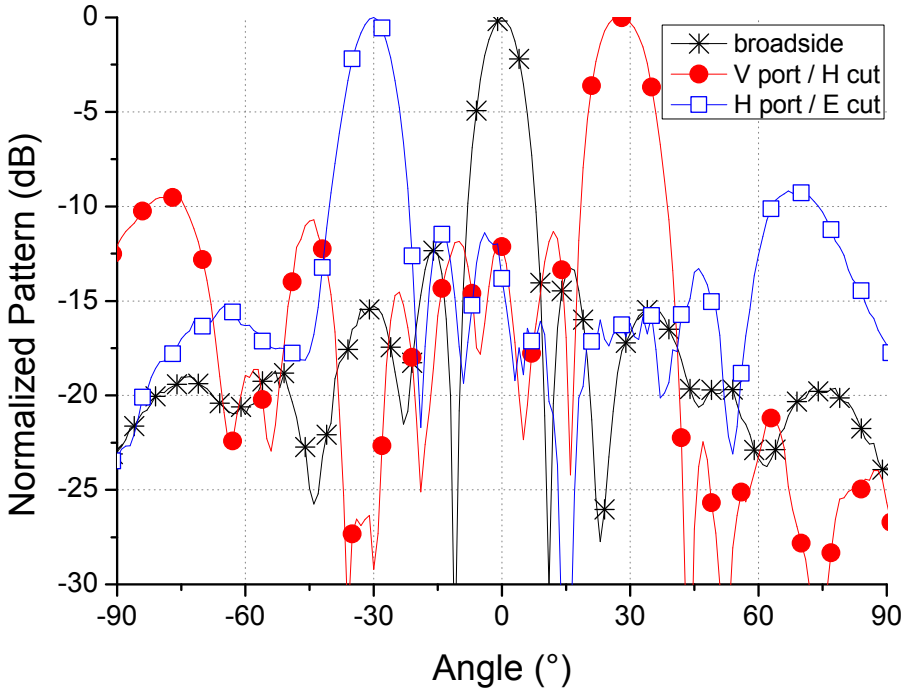

Fig.3 - 36 Measured S-band scan patterns

tical and horizontal polarized ports, which correspond to efficiencies of 91.9% and 85.2%, respectively.

Custom-made coaxial lines were employed to measure scan patterns instead of phase shifters and beam control boards to reduce the cost of the experiment. Scan capability of 28° and 30° was achieved for vertical and horizontal polarizations, as shown in Fig.3-36. Only scan patterns in the E-plane for horizontal polarization and H-plane for vertical polarization were measured, due to the limited element numbers in short aperture directions. For the same reason, the S-band radiation patterns and scan patterns were not measured.

3.7 Element Isolation

In DBDP-SA arrays, achieving good inter-band isolation is not difficult, as the radiators operate in different frequency bands. For challenging applications, a filter can be employed to further improve the inter-band isolation level.

On the contrary, the inter-polarization isolation of elements is more likely to deteriorate in DBDP-SA arrays due to the coupling from the other band. For example, the X-band element standalone has good inter-polarization isolation, however its H-polarized radiation might couple to the S-band elements, which in turn can couple to the X-band V-polarized ports, thereby resulting in poor inter-polarization isolation of the X-band element.

It is interesting to note that the S-band inter-polarization isolation is hardly affected in the DBDP-SA array. Since the X-band patches' dimensions are much smaller than S-band half-wavelength, they can hardly be excited in S-band frequency range. In other words, the coupling from S-band to X-band is very small, as the X-band elements do not bridge the S-band radiation energy from one polarization to the other. In conclusion, inter-polarization isolation of the S-band element is less likely to be influenced in DBDP-SA array configuration.

Therefore, the following sections present only the X-band inter-polarization isolation performance in the S/X DBDP-SA array.

3.7.1 Inter-Band Coupling

For single-band arrays, the relationship between inter-element coupling and element performance is already well studied [158]. In this section, the effects of the lower-band element on the higher-band patches are briefly discussed.

Fig.3-37 shows the configurations of a stand-alone X-band array and S/X DBDP-SA array after interleaving the S band elements into the aperture. Based on the multi-port network theory, an S matrix for the 32 ports of the X band single-band array, shown in Fig. 3-37(a),

can be written as eq.3-2:

$$\begin{bmatrix} V_1^- \\ V_2^- \\ \cdots \\ V_{32}^- \end{bmatrix} = \begin{bmatrix} S_{1,1} & S_{1,2} & \cdots & S_{1,32} \\ S_{2,1} & S_{2,2} & \cdots & S_{2,32} \\ \cdots & \cdots & \cdots & \cdots \\ S_{32,1} & S_{32,2} & \cdots & S_{32,32} \end{bmatrix} \bullet \begin{bmatrix} V_1^+ \\ V_2^+ \\ \cdots \\ V_{32}^+ \end{bmatrix} \tag{3-2}$$

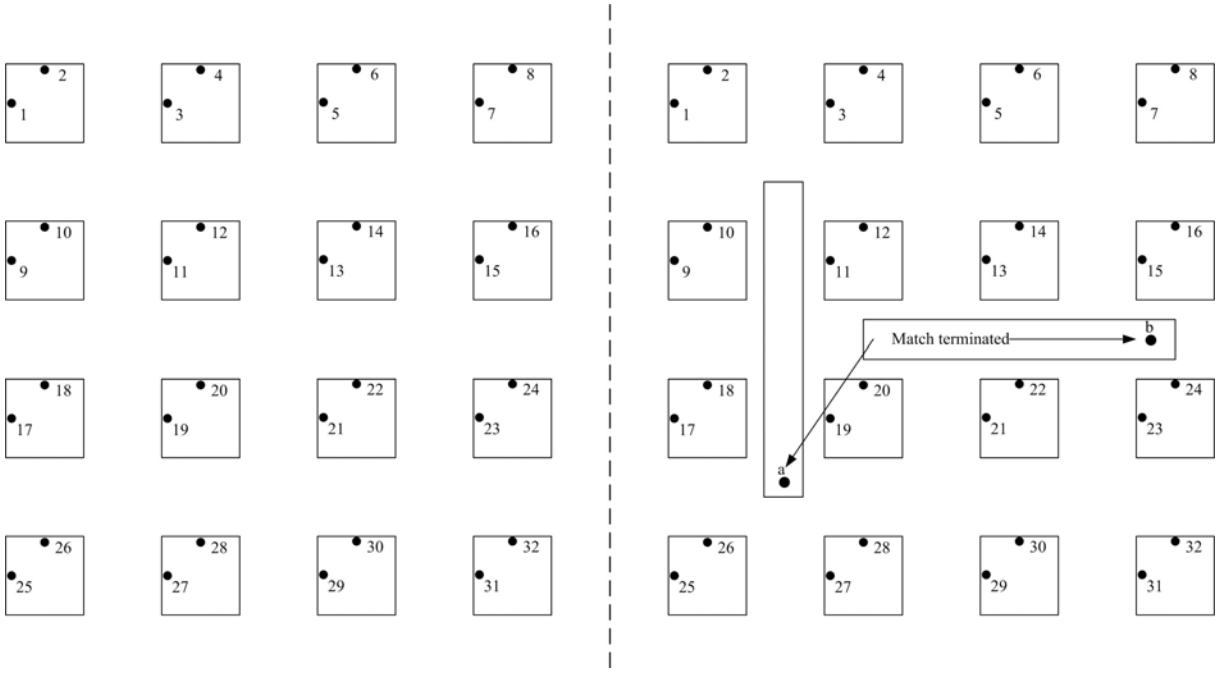

(a) X-band single-band array (b) S/X-band interleaved array

Fig.3 - 37 Inter-polarization isolation and inter-band isolation

where V^- and V^+ are the output and input voltages of corresponding ports, and $S_{m,n}$ are S parameter between m^{th} and n^{th} ports.

When the X-band elements are excited, some near-field energy will be coupled to the S-band element, and some of them will form field distribution in S-band element cavity (higher-order modes for S element), even through S-band elements are matched terminated. Hence, the S-band element can be considered as the parasitic patch working in a higher-order mode, while the X-band element is the driven patch with the fundamental operating mode. This phenomenon is similar to the co-planar proximity-coupled excitation.

Hence, assuming the S-band elements excitations as V_a^+ and V_b^+, eq.3-2 can be written as below:

$$\begin{bmatrix} V_1^- \\ V_2^- \\ \cdots \\ V_{32}^- \end{bmatrix} = \begin{bmatrix} S_{1,1} & S_{1,2} & \cdots & S_{1,32} & S_{1,a} & S_{1,b} \\ S_{2,1} & S_{2,2} & \cdots & S_{2,32} & S_{2,a} & S_{2,b} \\ \cdots & \cdots & \cdots & \cdots & \cdots & \cdots \\ S_{32,1} & S_{32,2} & \cdots & S_{32,32} & S_{32,a} & S_{32,b} \end{bmatrix} \bullet \begin{bmatrix} V_1^+ \\ V_2^+ \\ \cdots \\ V_{32}^+ \\ V_a^+ \\ V_b^+ \end{bmatrix} \tag{3-3}$$

where V_a^+ and V_b^+ are the coupled excitations from the X-band elements. The EM energy captured by the S-band elements can be expressed as:

$$\begin{bmatrix} V_a \\ V_b \end{bmatrix} = \begin{bmatrix} S_{a,1} & S_{a,2} & \cdots & S_{a,32} \\ S_{b,1} & S_{b,2} & \cdots & S_{b,32} \end{bmatrix} \bullet \begin{bmatrix} V_1^+ \\ V_2^+ \\ \cdots \\ V_{32}^+ \end{bmatrix} \tag{3-4}$$

Where V_a and V_b are the coupled EM energy from X-band elements.

Since the S-band elements are match-terminated, some energy received from the X-band elements will be absorbed, and the rest will be re-radiated, and forms coupled excitation for S-band element, as shown in eq.3-3. Factor ω_a and ω_b is used to express the re-radiated scale

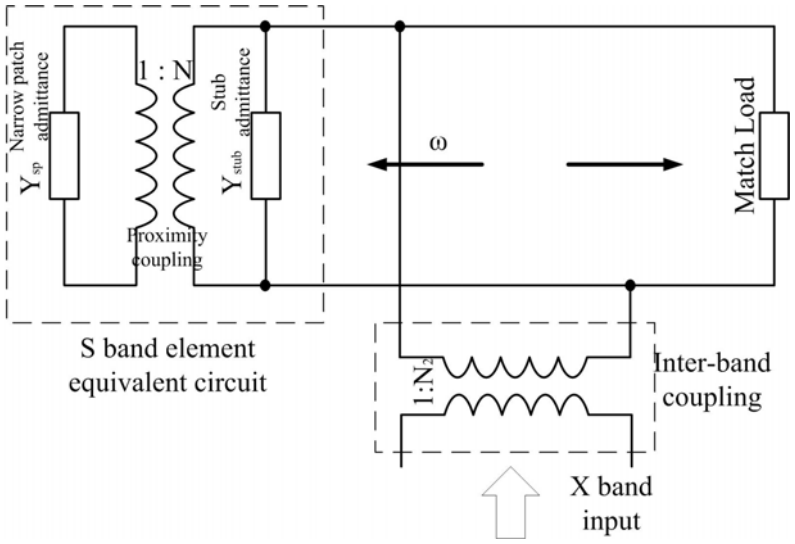

Fig.3 - 38 S-band elements capture X-band radiated energy and form secondary radiation

of the captured energy, as shown in Fig.3-34. By multiplying eq.3-4 with the re-radiation factors and substituting it into eq.3-3, and using the reciprocity ($S_{mn} = S_{nm}$), eq.3-3 can be written as:

$$\begin{bmatrix} V_1^- \\ V_2^- \\ \dots \\ V_{32}^- \end{bmatrix} = \begin{bmatrix} S_{1,1}+\Delta_{1,1} & S_{1,2}+\Delta_{1,2} & \dots & S_{1,32}+\Delta_{1,32} \\ S_{2,1}+\Delta_{2,1} & S_{2,2}+\Delta_{2,2} & \dots & S_{2,32}+\Delta_{2,32} \\ \dots & \dots & \dots & \dots \dots \dots \\ S_{32,1}+\Delta_{2,1} & S_{32,2}+\Delta_{32,2} & \dots & S_{32,32}+\Delta_{32,32} \end{bmatrix} \bullet \begin{bmatrix} V_1^+ \\ V_2^+ \\ \dots \\ V_{32}^+ \end{bmatrix} \quad (3\text{-}5)$$

where Δmn = ωa Sam • San + ωb Sbm • Sbn. The eq.3-5 implies that the overall S-matrix of S/X DBDP-SA array can be expressed as the sum of the S-matrix of X-band single band array and an additional item (Δm,n) which is decided by two factors: 1) the coupling between X and S-band element and 2) the re-radiation factors.

For example, in S/X DBDP-SA array, the isolation between port #11 and #12 can be written as $S_{11,12}' = S_{11,12} + \omega_a S_{a,11} \bullet S_{a,12} + \omega_b S_{b,11} \bullet S_{b,12}$. Therefore, the improvement in isolation can be considered in two aspects: 1) improvement in the element inter-polarization isolation itself; 2) suppression of the coupling between port #11/#12 and the S-band microstrip dipole *a/b*.

3.7.2 Inter-Polarization Isolation

Due to the use of hybrid feeding technique, the element's inter-polarization isolation itself is quite good. Therefore, the element isolation in array configuration depends mainly on the additional item (Δm,n). Referring to the aperture configuration shown in Fig.3-37, the X-band elements adjacent to the S-band elements will have higher mutual coupling, which will ultimately deteriorate the element inter-polarization isolation.

To investigate relationship between inter-polarization isolation and inter-band coupling,

the #3 prototype array is tested and the inter-polarization isolations of A2 ~ A4 and B2 ~ B4 elements are shown in Fig.3-39. Due to the symmetry, the remaining elements are not plotted for clarity. As can be seen, B2 and B4 elements have the worst element inter-polarization isolation due to their close proximity to the S-band elements (see element position definitions in Fig.3-31). The other X-band elements, which are located far from the S-band elements, have good element isolation performances of better than 30dB. These results also support the additional item in eq.3-5: 1) B2 and B4 elements are more easily coupled from the S-band element, because they are close to both the vertical and horizontal S-band elements. $\Delta m,n$ item thus becomes large, which degrades the inter-polarization isolation of B2 and B4 elements; 2) Although B3 element has stronger coupling with the S-band horizontal dipole, it is weakly coupled to the S-band vertical dipole. The $\Delta m,n$ factor is small as it is the product of the coupling levels obtained from both S-band elements. Hence, the inter-polarization isolation of B3 element is better than that of B2 and B4 elements.

Besides improving the (stand-alone) element inter-polarization isolation itself, one can also improve array element inter-polarization isolation by suppressing the inter-band cross talk between S and X-band elements.

For a fixed element spacing, the ‘isolation wall’ [159] and the ‘isolation slot’ [150] have been commonly used for element decoupling. However, these methods are not suitable to implement in the DBDP-SA array due to the presence of congested aperture. In such cases, it is best to suppress S-band element’s higher-order mode, so that it will not be excited in X-band frequencies.

Similar interleaved stacked patch and microstrip dipole structures have been used in

preliminary studies [83, 84], where frequency ratio is 3:1 rather than 3.5:1 in this chapter. Hence, their performances are compared next. Their measured element inter-polarization isolations are shown in Fig.3-40:

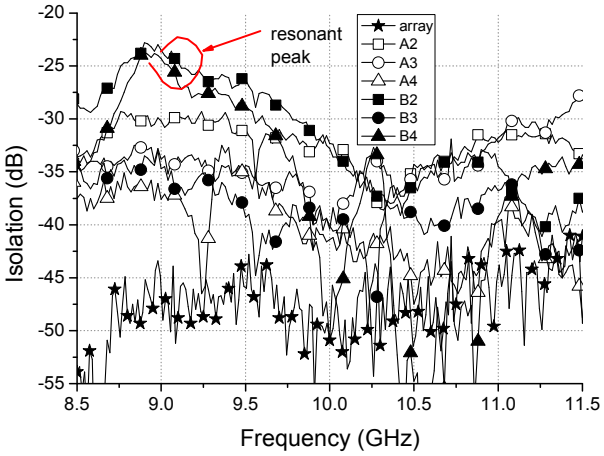

Fig.3 - 39 Element isolation in this chapter

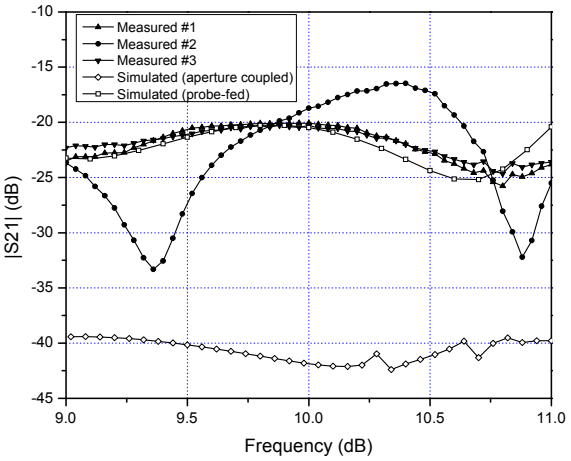

Fig.3 - 40 Element isolation in [83, 84]

1) Both arrays exhibit similar trends in terms of X-band inter-polarization isolation. Most of the elements have well decoupled ports, while few elements have poor inter-polarization isolation level.

2) For this example, most elements' inter-polarization isolations are better than 30dB, which is about 10dB better than that of [83, 84]. It can be attributed to the advantages of using hybrid feed.

3) Both the preliminary study [83, 84] and the design presented in this chapter have coupling peak in the isolation response of several elements. The only difference in this design is that the resonant peak of B2 and B4 elements are outside the operating bandwidth (9.52 GHz - 10.83 GHz), and therefore do not affect the inter-polarization isolation (28 dB). On the other hand, the resonant peak in Fig.3-40 is within the bandwidth, which results in extremely poor isolation level of 16 dB. This variation in resonant peak position may be a result of choosing different frequency ratio.

Furthermore, since [83, 84] presents isolation levels of only three arbitrary elements (without giving the #2 element position), it is hard to claim that the poor isolation level is attributed only to the inter-band coupling.

To further investigate the relationship between the high-order-mode of the S-band element and X-band inter-polarization isolation, another S/X shared-aperture array was designed and fabricated. It also has a similar S-band tri-resonance and the X-band hybrid feed design, but the frequency ratio is 1:3. The S- and X-bands are designed at 3.2 GHz and 10 GHz, respect-

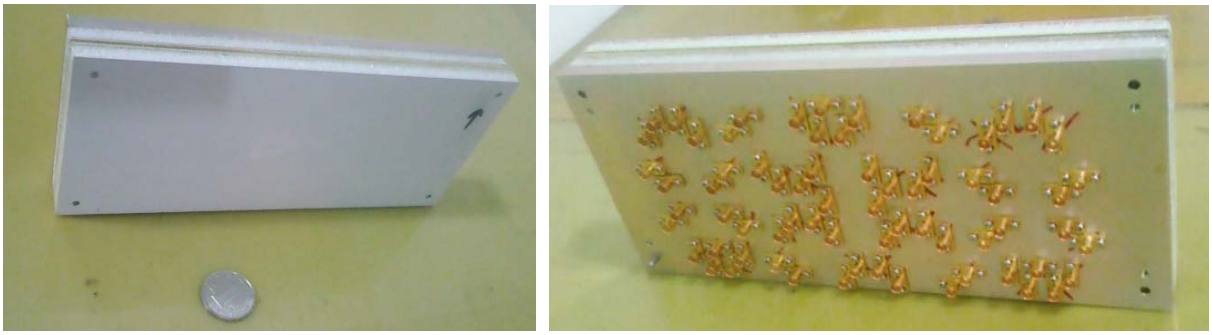

(a) Front view (b) Rear view

Fig.3 - 41 Photo of the reference array

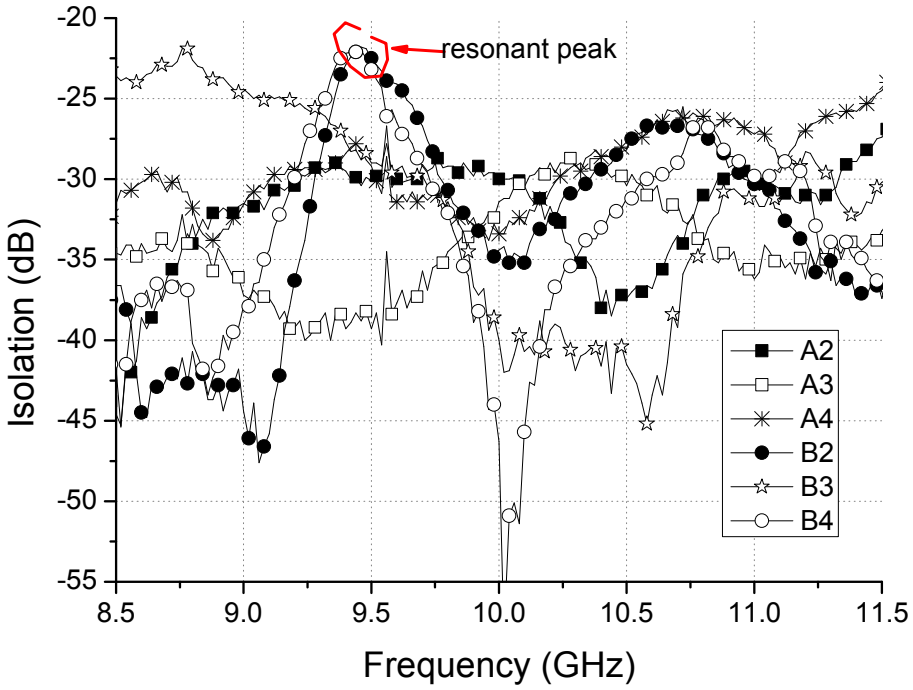

Fig.3 - 42 Measured isolation of the reference array

ively. To avoid confusion, this array is called the reference array and is shown in Fig.3-41.

The measured X-band inter-polarization isolations of the reference array are shown in Fig.3-42. When compared with Fig.3-39, similar trends can be found, including: 1) B2 and B4 elements have the worst inter-polarization isolation; 2) The resonant peaks are located at 8.9 GHz and 9.5 GHz, respectively, which is about three times higher than the S-band center frequency (2.9 GHz and 3.2 GHz). Clearly, these resonant peaks are generated by the coupling of X-band base mode and S-band TM_{03} mode, which significantly increases the $\Delta m,n$ value. The selection of fractional frequency ratio (1:3.5) shifts the resonant peak out of the band by actually moving S-band TM_{03} mode frequency.

For the DBDP-SA array with 1:3 frequency ratio, the inter-band coupling is hard to deal with. Employing filters will only shield the out-of-band-signal coming from the port, but has little effect on re-radiation (excited by inter-band coupling). Besides, the filter will also suffers from the 3rd order mode. The possible solutions are: 1) Etch a slot on S-band elements to suppress TM_{03} mode (decoupling) and 2) separately tune B2 and B4 elements (stand-alone) inter-polarization isolation to cancel the $\Delta m,n$ item (coupling). However, these methods will be computationally-intensive and time consuming. Moreover, due to the narrow structure of the S-band microstrip dipole, slot etching may not be possible.

3.8 Summary

This chapter presents an improved design of S/X DBDP-SA array antenna. The main objective was to investigate techniques to improve array inter-band isolation and element inter-polarization isolation by understanding the relationship between them. To improve

element isolation, a hybrid feed and T-shape configuration are employed in the X- and S-band, respectively. The prototype array was fabricated and tested to validate the feasibility of the design. It is found that the inter-band coupling will also degrade the element inter-polarization isolation.

The prototype array operates at 2.85 GHz / 10 GHz band, with a fractional frequency ratio of 1:3.5. This design verifies that interleaved structure can work at any frequency ratio for DBDP-SA array. Tri-resonance is introduced for the lower-band element to exploit its bandwidth with the given antenna thickness. Overall, the prototype array validates the feasibility of the design. The key measured parameters are concluded in Table 3-4.

Table 3 - 4 Summary of the improved S/X DBDP-SA array specifications

Specification	S-band	X-band
SWR≤1.5 bandwidth (MHz)	300	≈ 1000
SWR≤1.5 bandwidth (%)	10	10
Scan range	Not tested	±30 degree
Element isolation (dB)	≥32	≥28dB
Array isolation	Not tested	≥40dB

Acknowledgement

This work is sponsored by the 863 project of Chinese government under grant number 2007AA12Z125.

Mr C. Gao, Mr W. Wang and Mr W.Y. Wu are highly appreciated for their suggestions and help in the design, fabrication and measurement of array antennas.

Chapter 4
L/S/X Tri-Band Dual-Polarized Microstrip Array

To the best of the author's knowledge, multi-band dual-polarized shared-aperture (MBDP-SA) techniques available in the open literature only focus on the DBDP-SA arrays [83-126], while a few tri-band designs are investigated [99]. This chapter presents a novel multi-band aperture-sharing method for space-borne SAR applications. A tri-band dual-polarized shared-aperture (TBDP-SA) microstrip array is designed and fabricated to validate the feasibility of proposed design technique. The main contents are listed below:

1) For SAR applications, a multi-band shared-aperture array can be decomposed into several dual-band shared-aperture arrays. The L/S/X TBDP-SA array is taken as an example for illustration and its detailed design method is presented.
2) The decomposed DBDP-SA sub-array design method is presented with its partition method. The element designs in DBDP-SA sub-array are also discussed.
3) The measured results of an L/S/X TBDP-SA prototype array are presented. They verify the feasibility of the proposed MBDP-SA array decomposition method.

The requirements of the prototype TBDP-SA array are listed in Table 4-1.

Table 4 - 1 Requirements of L/S/X TBDP-SA array

	L band	S band	X band
Center frequency (GHz)	1.25	2.85	10
Bandwidth (MHz)	80	200	600
Polarization	H polarization	V polarization	Dual linear
Cross-polarization (dB)	-20	-20	-20
Array isolation (dB)	25	25	25
Scan range	±25°@azimuth ±25°@elevation	±25°@azimuth ±25°@elevation	±25°@azimuth ±25°@elevation

4.1 Array Configuration

The design of DBDP-SA array presented in Chapter 3 can be extended to TBDP-SA array by interleaving an extra band into its configuration, and it is called 'add method' below. This method leads to the following design complexity:

1) The final aperture that hosts the elements of the three bands will become congested, thus increasing the inter-band coupling;
2) The antenna structure will become quite complex because more layers are needed to fit the elements and their feed networks in each band. The vertical feeding structure required for such multi-layer configuration will inevitably increase the cost and fabrication complexity.

From the SAR system point of view, a similar beamwidth is desired in the elevation direction for each of the three bands [110] to cover similar swath. This means that the transverse dimension of the aperture in each band should be proportional to its wavelength. As a sample, the transverse aperture dimension of the L-, C- and X-bands in the SIR-C/X-SAR array are 2.95m, 0.75m and 0.4m, respectively, which correspond to a ratio of 7.375 : 1.875 : 1 [07, 08, 12], roughly equal to its wavelength ratio of 8 : 2 : 1.

Even through the 'add method' can be applied in MBDP-SA sub-array design, an aperture with dense element configuration will be formed in the full L/S/X TBDP-SA array, as shown in Fig.4-1(a). The L/S DBDP-SA sub-array must be placed adjacent to the L/S/X TBDP sub-array to avoid the grating lobes in S-band. As a result, most of the elements and their feed networks are congested in the middle of the array, which will surely deteriorate the port

isolation and increase inter-band coupling.

To reduce design complexity and the element congestion, an alternative solution is

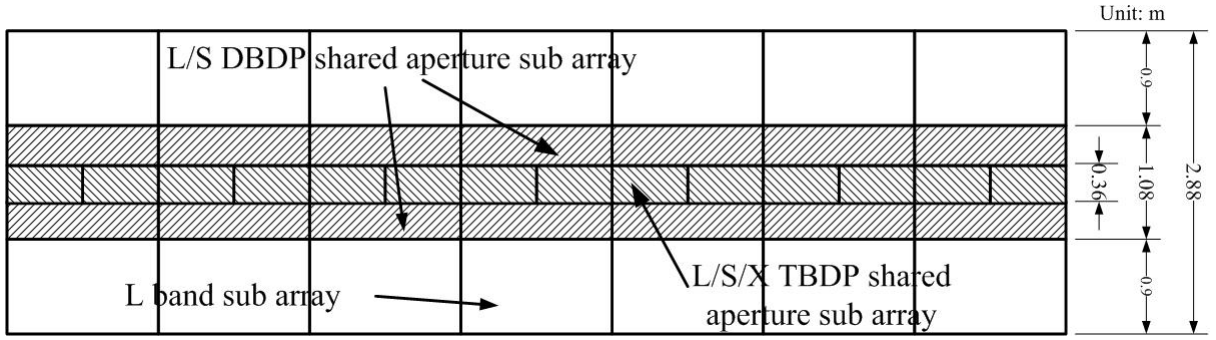

(a) 'Add method'

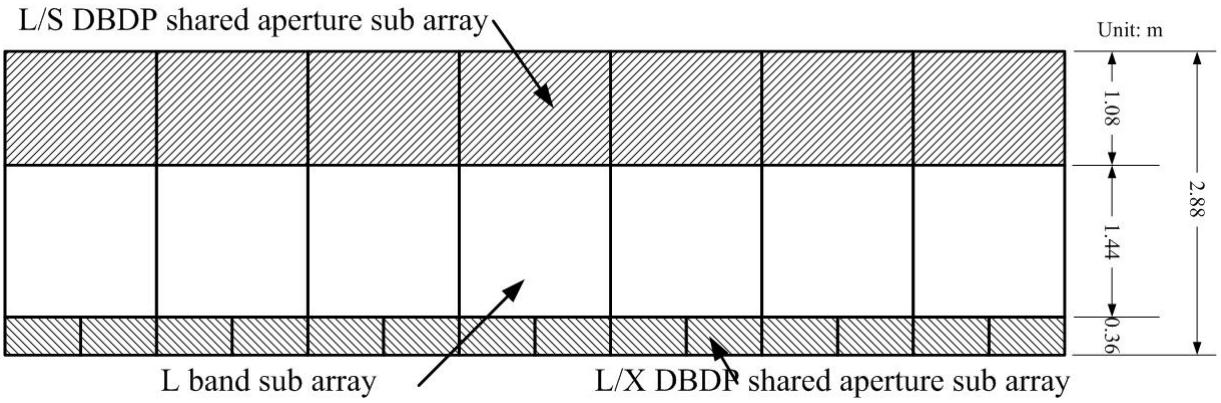

(b) Proposed DBDP-SA sub array combination method

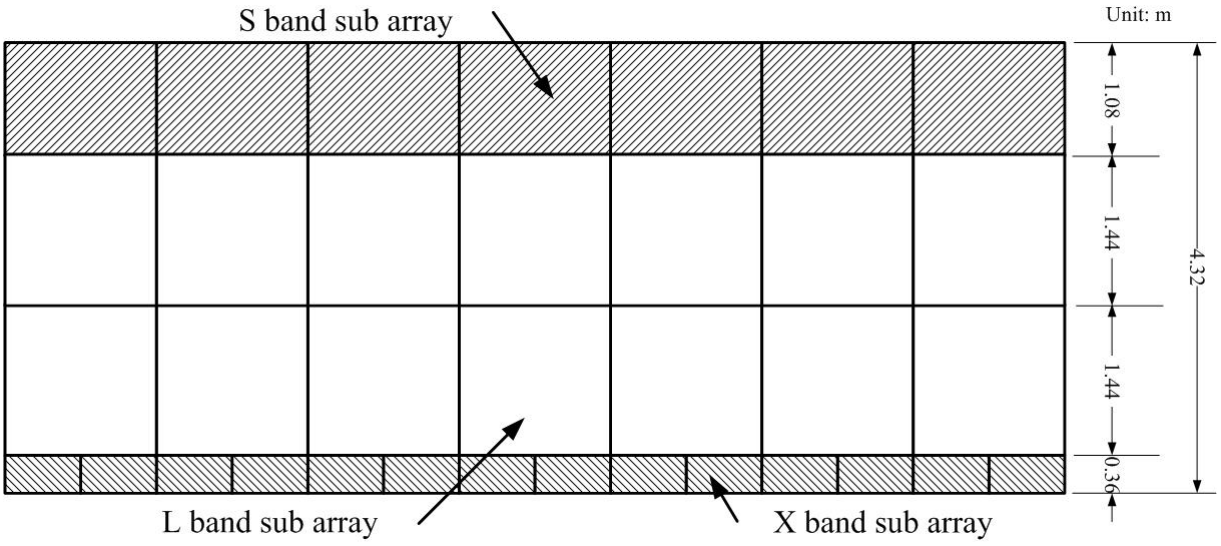

(c) Independent aperture solution

Fig.4 - 1 Different solutions for tri-band antenna array

proposed as shown in Fig.4-1(b). The L/S and L/X DBDP-SA sub-arrays are placed on the two sides of the full array, with an L single band sub-array located in the middle of the full array. The L-band elements in all three sub-arrays make up the L band full aperture area. The transverse dimension of the aperture is $0.72 \times 2 + 1.08 + 0.36 = 2.88$m for L-band, 1.08m for S-band and 0.36m for X-band with the aperture ratio of 8:3:1, which is close to the centre wavelength ratio of each L-, S- and X-bands. The advantages and disadvantages of this design are discussed below:

1) The S- and X-band elements are physically isolated by an L single band large sub-array, and hence the coupling between S- and X-band is minimized.
2) The element density in full array has better distribution when compared with the configuration of Fig.4-1(a) within the same aperture size.
3) Compared with the independent aperture TBDP array in Fig.4-1(c) (same design as that of SIR-C/X-SAR antenna solution [07, 08, 12]), the proposed aperture size is smaller for the same beamwidth. The overall aperture length of independent L/S/X TBDP array in Fig.4-1(c) is $1.08 + 2.88 + 0.36 = 4.32$m, roughly 33% longer than the proposed method.
4) Since the proposed TBDP-SA array consists of two DBDP-SA sub-arrays and one single band dual-polarized (DP) sub-array, the previous design of DBDP-SA arrays can be used as reference.
5) The proposed method can be further extended to achieve quad-band shared-aperture array if we substitute the L single band sub-array with other DBDP-SA sub-array, like L/C DBDP-SA array.

4.2 L, L/S and L/X Sub Array Design

4.2.1 Design Considerations

The designs of L/S, L/X DBDP-SA sub-array and L-band DP sub-array are a crucial step in the overall design of L/S/X TBDP-SA full array. Here we highlight some important issues that need to be considered: 1) the DBDP-SA sub-array design should be self-extendable, *i.e.*, both the lower- and the higher-band elements need to maintain a particular spacing when the DBDP-SA sub-arrays are joined together to ensure the predesigned scan capacity in each

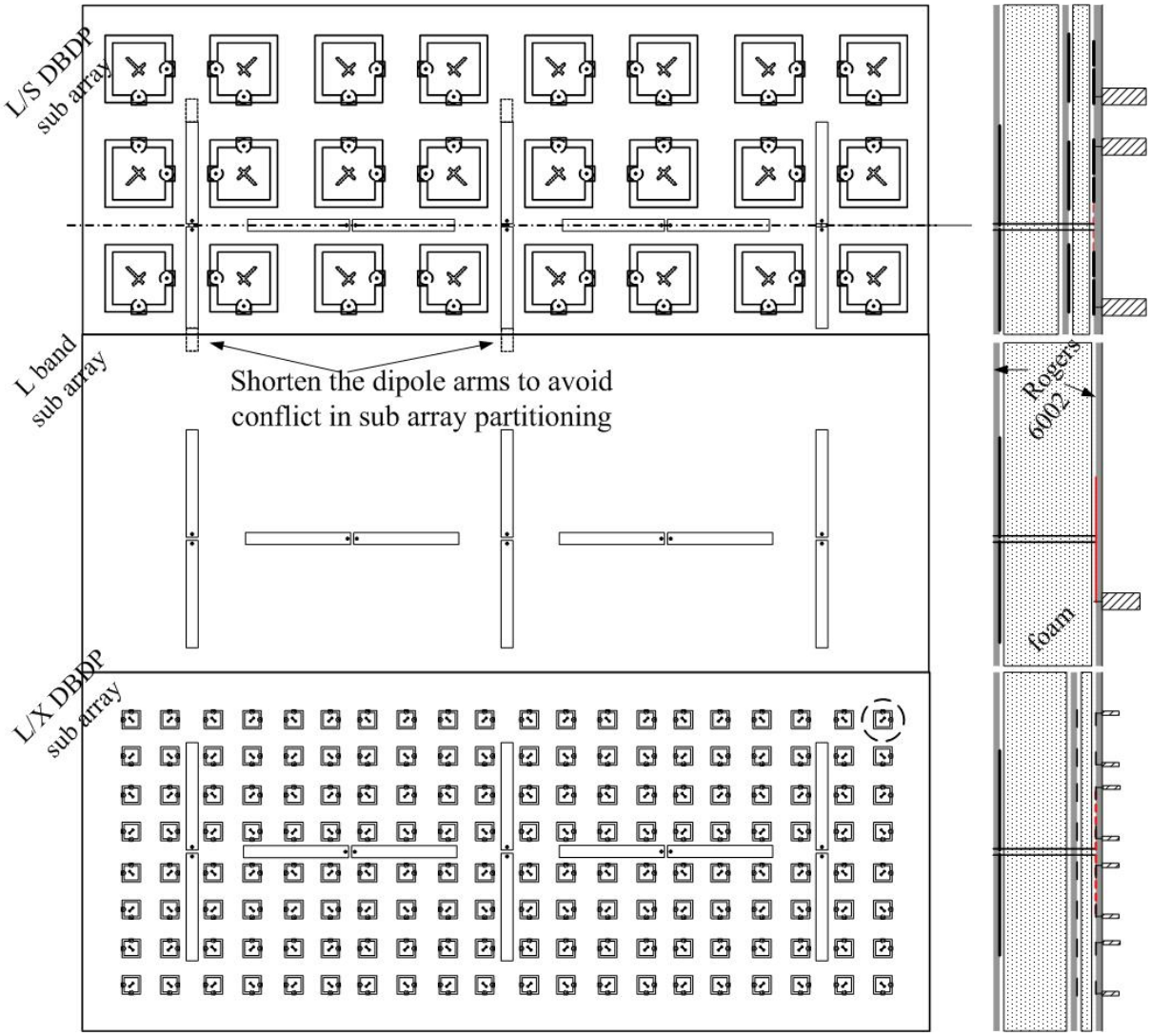

Fig.4 - 2 Proposed TBDP-SA array configuration

frequency band; 2) The different sub-arrays should have the provision to accommodate each other, *e.g.*, the L-band elements should be uniformly distributed when the L-band aperture is combined with the L/S, L/X DBDP-SA array and L-band DP sub-array; 3) Each sub-array should have a modular design so that it can be replaced like a plug and play module. For example, if we replace the L single band DP sub-array in Fig.4-1(b) by L/C DBDP-SA sub-arrays, a quad-band L/S/C/X dual-polarized shared-aperture array can be constructed.

Considering that the frequency ratios of the L/S and L/X DBDP-SA sub-array are 1:3 and 1:8, respectively, the interleaved structure is applied in both sub-arrays. Because the interleaved structure can fit both even and odd frequency ratios in DBDP-SA array [83, 84], and its flexibility is helpful for the sub-array partitioning to meet the aforementioned requirements. The proposed L/S/X TBDP-SA prototype array configuration is shown in Fig.4-2.

4.2.2 Sub-Array Design

The S- and X-band elements in L/S and L/X DBDP sub-arrays are distributed in square lattices to facilitate interleaving of the L-band elements. The ‘pair-wise anti-phase feed’ method [134-136] is employed in both the S- and X-band arrays for cross-polarization suppression and array isolation enhancement.

The same L-band element type is employed in each of the L, L/S and L/X sub-arrays to achieve uniform radiation patterns and port response. Microstrip dipole is employed as the L-band element because it is slim and can be easily interleaved in the dual band array configuration. The microstrip dipoles are T-shape orthogonally configured to achieve dual

band operation and good isolation, as explained in Chapter 3. Similarly, the T-shape configuration will result in non-overlapped phase centers of H- and V-polarizations [110]. One additional vertical microstrip dipole is required in the prototype array so that the phase centers for both polarizations are identically overlapped with the geometric center of the array.

Because the L band aperture is made from L/S, L/X DBDP-SA sub-arrays and L single band DP array, a uniform L-band element spacing is required in these three sub-arrays to ensure that L-band elements of combined full array are properly configured. Thus, the L-band element spacing is taken as the reference value for the three band elements, and is calculated as:

$$d_L = \frac{\lambda}{1+|\sin(\theta)|} = 160mm \tag{4-1}$$

where λ is the wavelength of L band higher frequency (1.3 GHz), and θ is the maximum scan angle (25°).

Because L, S and X bands have the same scan requirements, the elements spacing (d_L, d_S, d_X) should be proportional to their wavelength ratio in order to achieve both the scan capacity and ease dual-band interleaving. Therefore, $d_s = 1/3\ d_L = 53.3mm$, and $d_x = 1/8\ d_L = 20mm$ is applied, which correspond to $0.62\lambda_s$ and $0.67\lambda_x$, respectively for S- and X-band. Note that the choice of S- and X-band element spacing also meets the requirement of eq.4-1.

The scan capacity in each band is further investigated by projecting the scan range into Sinc space [133], as shown in Fig.4-3. The array scan capacity (blue curves) does not intersect with the grating lobe range (red curves) in all three bands, showing the non-grating lobe scan performance for the chosen element spacings. These element spacings are verified by array

theory using a Matlab program. Without the loss of generality, an aperture of 8-by-8 elements

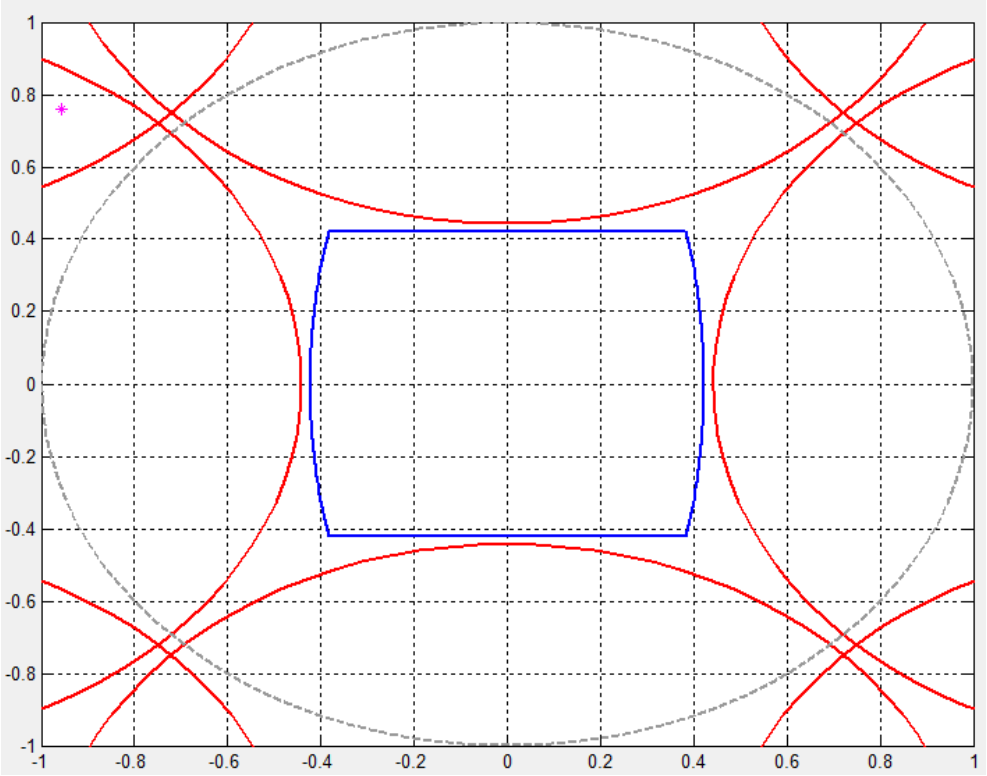

(a) L-band (1.3 GHz)

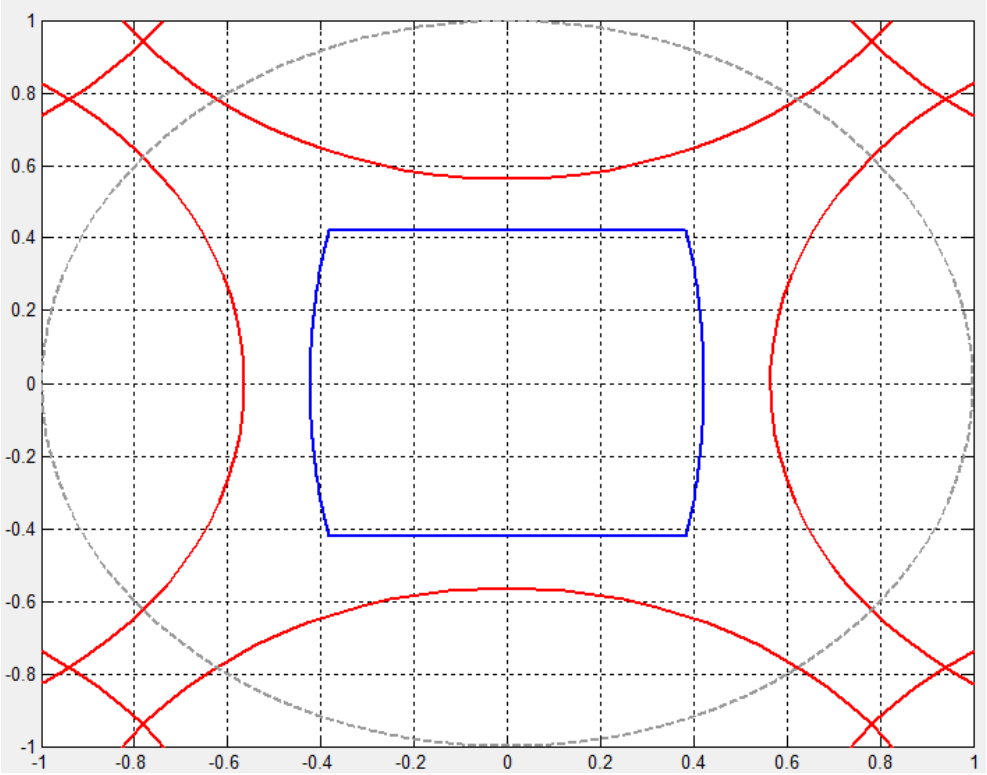

(b) S-band (3.6 GHz)

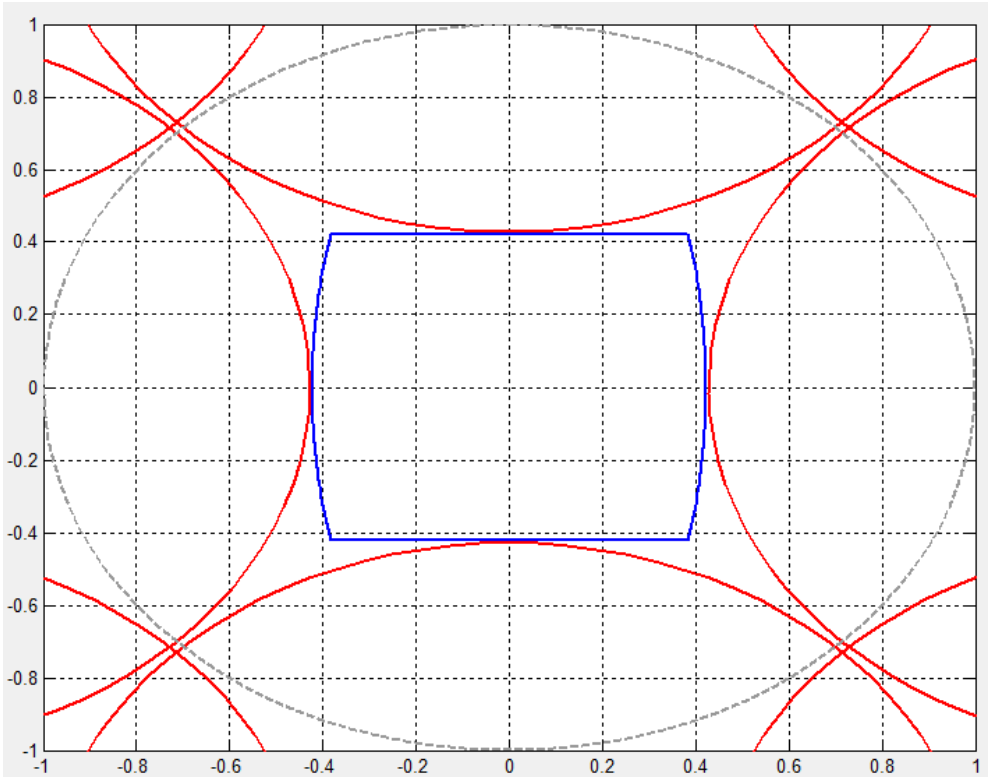

(c) X-band (10.5 GHz)

Fig.4 - 3 Scan range and grating lobes in Sinc space

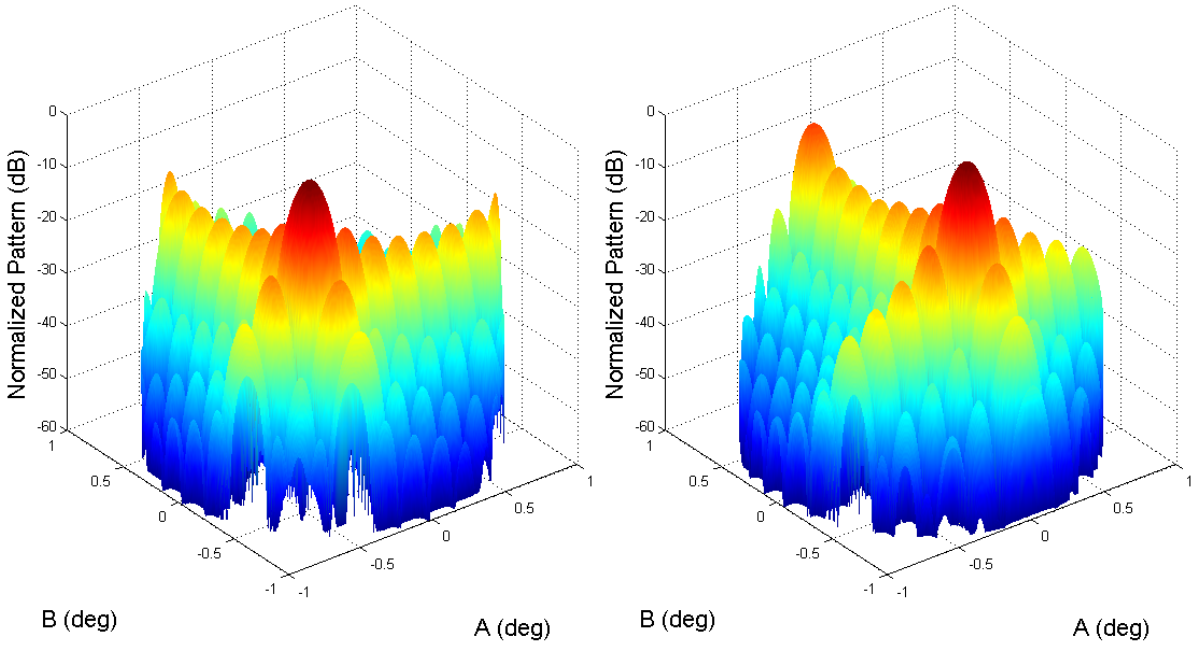

A = 25° / B = 25° A = 0° / B = 25°

(a) L-band at 1.3 GHz

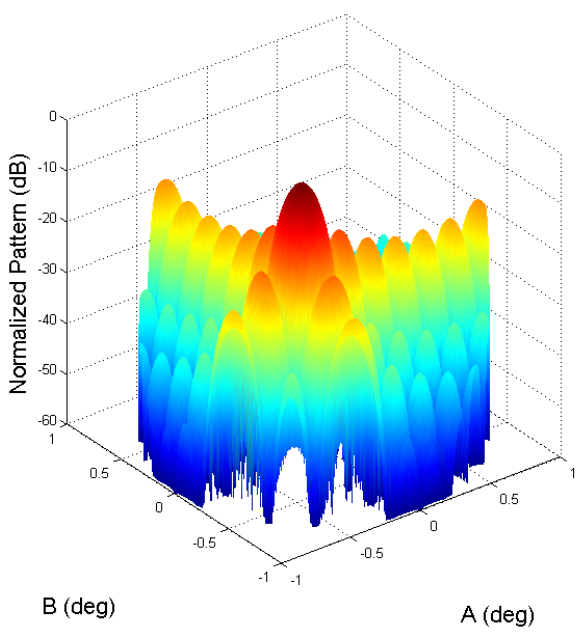

A = 25° / B = 25°

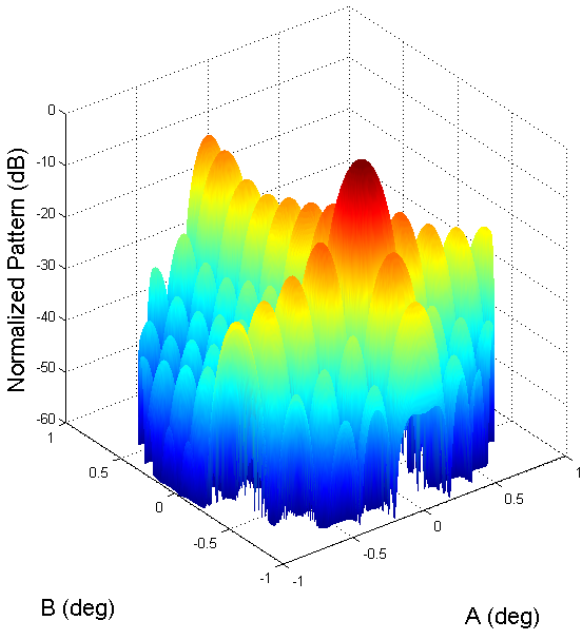

A = 0° / B = 25°

(b) S-band at 3.6 GHz

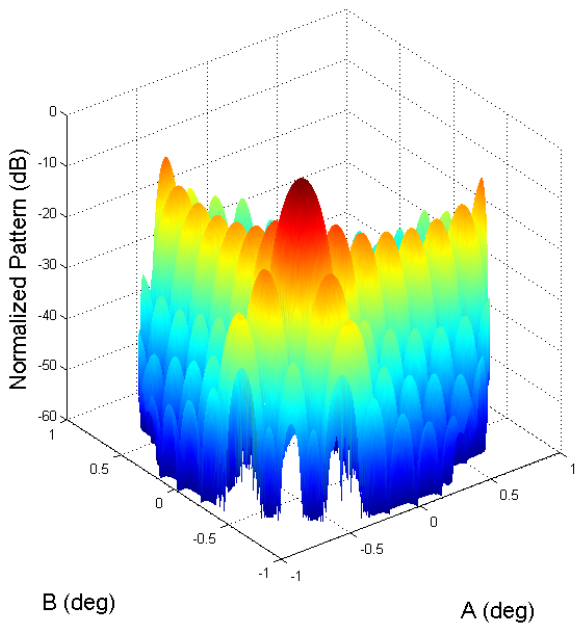

A = 25° / B = 25°

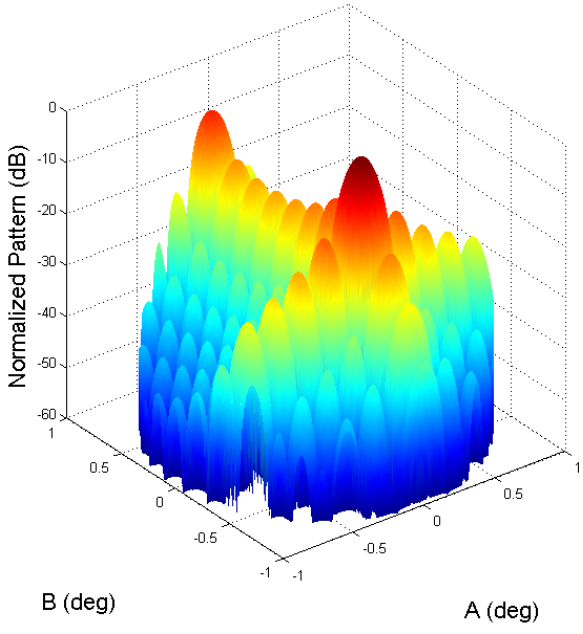

A = 0° / B = 25°

(c) X-band at 10.5 GHz

Fig.4 - 4 Calculated 3D radiation patterns in Sinc space

is employed to calculate the radiation patterns. The radiation patterns for two maximum scan angles (A = 25° / B = 25° and A = 0° / B = 25°) are calculated and shown in Fig.4-4. To make

precise calculations, the element radiation patterns from HFSS prediction have been taken into account in array factor. No grating lobe is found for the chosen element distances.

4.3 Element Design

4.3.1 S and X Band

Stacked patches are employed in both S (in L/S sub array) and X-band (in L/X sub array) to adhere to the bandwidth and cross-polarization level requirements. Their configurations are shown in Fig.4-5. As illustrated in Chapter 3, the square patch shape is chosen due to its better cross-polarization level, good isolation performance and better fabrication tolerance.

Although some feeding methods such as aperture coupling, hybrid feed or balanced feed can provide better isolation level [143-153], based on our previous experience, they result in complex structure and less fabrication reliability. For the case of TBDP-SA array which consists of several different DBDP sub-arrays, its performance is more likely to suffer from the complexity in the feeding structures. Hence, to ensure overall performance in TBDP-SA full-array, simple yet reliable dual probe feed method is employed.

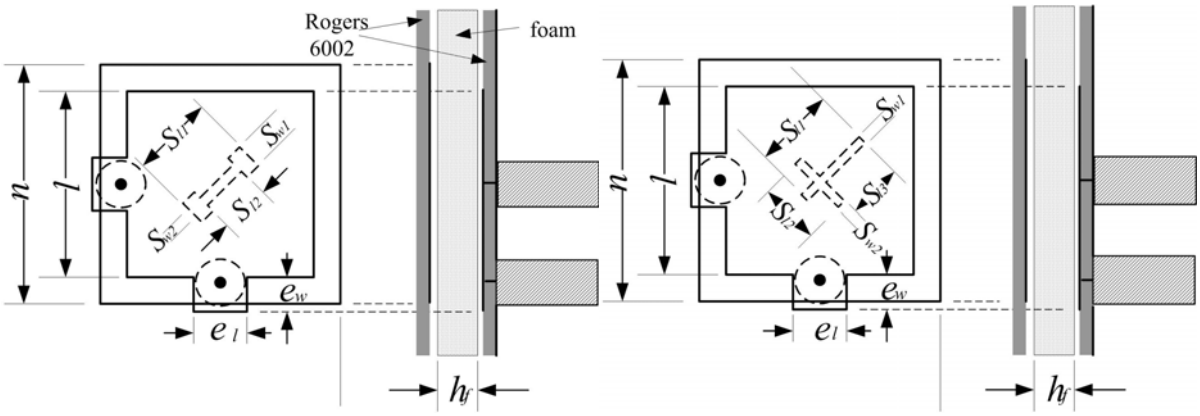

(a) X-band element (b) S-band element

Fig.4 - 5 S and X band element configurations

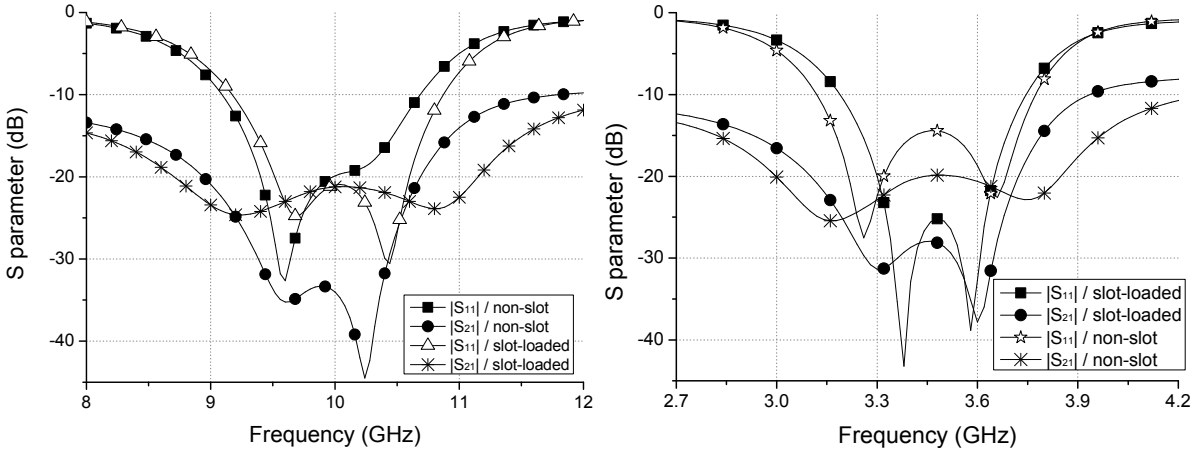

(a) X-band (b) S-band

Fig.4 - 6 Effect of slot loading on S parameters

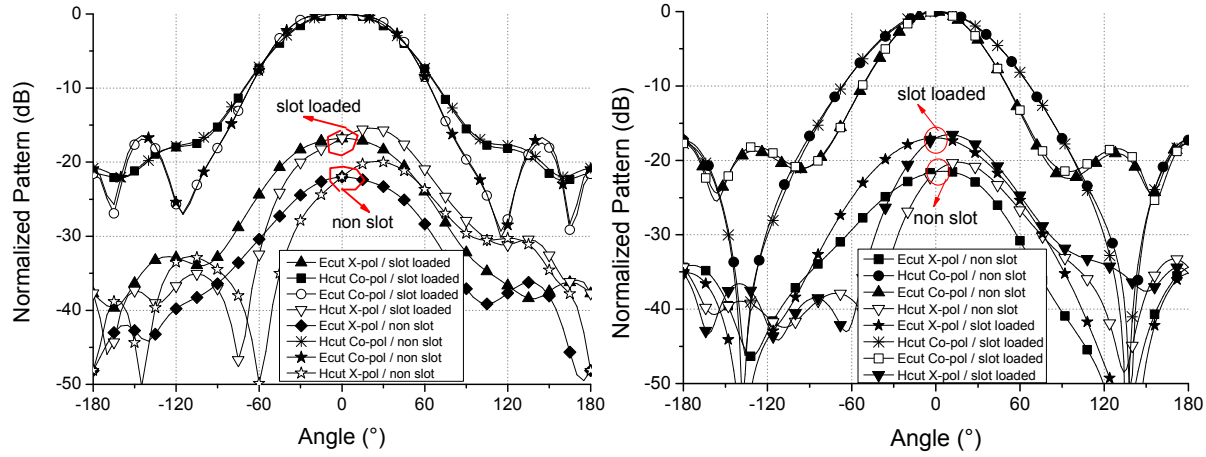

(a) X-band (b) S-band

Fig.4 - 7 Effect of slot loading on the cross-polarization levels

Since a dual probe feed has lower inter-polarization isolation, isolation slots are made on the driven patches [160, 161] to improve it, as shown in Fig.4-5. The inter-polarization isolation of slot loaded element is predicted by Ansoft HFSS 10.0, as shown in Fig.4-6 and Fig.4-7. The plots of element without slot loading are also shown for comparison. As can be seen, better port isolation is achieved, however the element cross-polarization becomes poor due to the interference of the slot. This would not be a problem for the full array, as the array cross-polarization can be improved by using the 'pair-wise anti-phase feeding' technique

[134-136].

The effect of isolation slot on the element performance can be understood in two ways: 1) from the current distribution point of view, the slot on the driven patch can 'cut off' some current components which may affect the $|S_{21}|$ level [160-161]. Hence, the polarization ports are decoupled; 2) from the viewpoint of field modes, the cross-talk mainly comes from the higher-order mode component. In fact, the asymmetrically configured slot serves as a perturbation, and since it is electrically small, it has very little effect on the base mode. However, its asymmetric boundary condition on the driven patch will excite the orthogonal mode, which after careful tuning will cancel out the cross-talk energy from the higher-order mode. On the other hand, the orthogonal mode excited by the slot will contribute to cross-polarized radiation, which is a main cause of poor element cross-polarization performance.

In comparison, polarization isolation improvement method presented in Chapter 3 pursues a symmetric structure, while the isolation slot loading method in this chapter utilizes a new asymmetry in the structure to reduce the cross-talk. However, it is found that the improved isolation bandwidth of the isolation-slot is narrower than that of the symmetric structure designed in Chapter 3.

Table 4 - 2 Parameters of slot-loaded patch

X band (Unit: mm)					
l	8.2	u	8.8	e_l	2.7
S_{l1}	2	S_{l2}	1.4	e_w	1.2
S_{w1}	1	S_{w2}	0.4	h_f	2.5
S band (Unit: mm)					
l	23	u	28.1	e_l	5.5
S_{w1}	0.6	S_{w2}	0.5	e_w	3
S_{l1}	9.5	S_{l2}	9	S_{l3}	7
h_f	6.5				

Isolation slots with different shapes are also tested with S- and X-band elements to find the best geometry. The parameters of the slot-loaded patches are optimized by Ansoft HFSS 10.0, and are listed in Table 4-2.

The simulation results indicate that both shapes of isolation-slot can provide sufficient isolation improvement to the dual probe feed patch. In particular, the bone-shaped slot on the X band driven patch has smaller dimensions than the cross-shaped slot on the S band element due to the capacitive loading on the slot end. The ratio of maximum slot dimension to driven patch edge for bone-shaped slot is 0.24, while it is 0.41 for the cross-shaped slot at S band. Hence, the bone-shaped slot will have less impact to the elements' $|S_{11}|$ curve, while the cross-shaped slot will increase the in-band ripple, and requires slight tuning later on to improve matching.

4.3.2 L Band

As mentioned in Section 4.2.2, L single band, L/S and L/X DBDP-SA sub-arrays employ the same L band microstrip dipole. The only difference is the dipole arm length in L/S sub-array, which is 20% shorter than that of the dipole in L/X and L-band sub-array. The reduced dipole length is necessary to facilitate sub-array partitioning when this dipole is used in odd frequency ratio (S : L = 1 : 3), as shown in Fig.4-2. To reduce the dipole arm length, capacitive loading is employed in the feed network.

As observed in Chapter 3, the lower-band element should be as compact as possible. For example, the radiator of narrow edge patch in Chapter 3 is quite compact, however, its orthogonal tuning stubs on feed line are not. It must stay right in the gaps of the higher band

elements. Hence, two elements with different stub positions are designed for H- and V-polarized lower band elements in Chapter 3. If the same method is used to design TBDP-SA array, the resulting array will become quite complex. Since four different elements will be needed for dual-polarized L band element in L/S and L/X sub-array to fit within the gaps of S- and X-band elements, significant level of optimization will be required in this design stage.

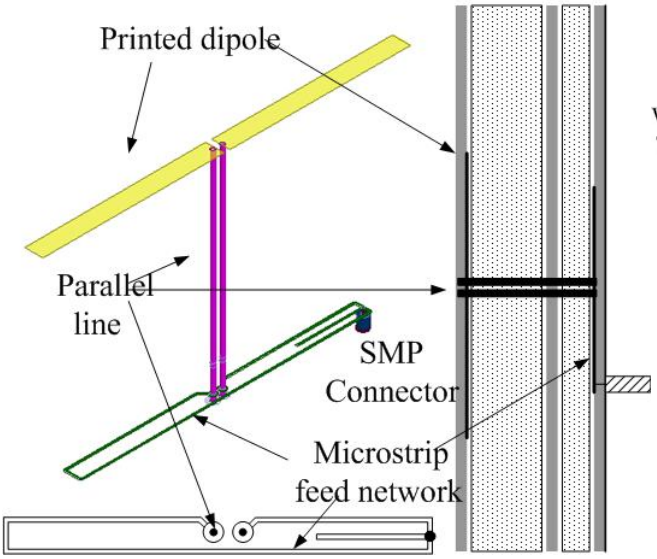

Fig.4 - 8 L band microstrip dipole configuration

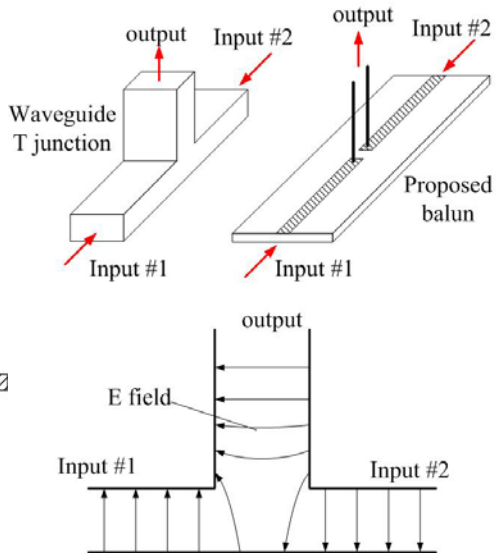

Fig.4 - 9 Microstrip-parallel line balun

The proposed configuration of the L band microstrip dipole is shown in the Fig.4-8. The printed dipole is etched on the bottom of the top layer, which is $\lambda_L/4$ distance above the ground. The ground, in this case, also serves as the reflector. The microstrip feed network of L band microstrip dipole are configured in the gap of the higher-band driven patches, and uses delay lines to generate 180 degree phase shift and a vertical parallel twin-line to feed the microstrip dipole. The microstrip to parallel line transition forms a T junction, similar to the waveguide T junction shown in Fig.4-9. This forms a three-port-network, which can not be reciprocal, loss-free and has all ports matched simultaneously according to [161]. Because a reciprocal network with minimum insertion loss should be ensured, the T junction is

mismatched at its two input ports. An open-ended stub is employed at the SMP feeding point for impedance matching.

The microstrip dipole has a compact structure because the orthogonal tuning stub is avoided. The complete structure including radiator and the feed network can be placed into a narrow space (from up view). This gives great convenience in the design because the microstrip dipole can be used in lower-band element in both L/S and L/X sub-array for both polarizations without considering the stub position. Furthermore, the use of the same L-band element design for three sub-arrays will ensure consistent element radiation patterns, which is helpful in combining the L band apertures.

4.4 Measurements

A prototype L/S/X TBDP-SA array is fabricated and tested to validate the design. The prototype array, shown in Fig.4-10, consists of L/X DBDP-SA sub-array, L single band sub-array and L/S DBDP-SA sub-array. Rogers RO 6002 and Rohacell 51HF foam are used as the substrates and filling material, respectively. The S-parameters of the prototype array is measured using the Agilent N5230A vector network analyzer, while the radiation patterns are obtained in the anechoic chamber at China Electronics Technology Corporation (CETC), 38th research institute. The insertion loss in the coaxial lines, connectors and power dividers are measured and then compensated in the post-processing stage.

Next, we present the measured results for each of the L-, S- and X-band. Similar to that in Chapter 3, the elements of L/S/X TBDP-SA array are marked as shown in Fig.4-11 to avoid confusion in introduction. The S- and X-band elements, from top to bottom, are identified by

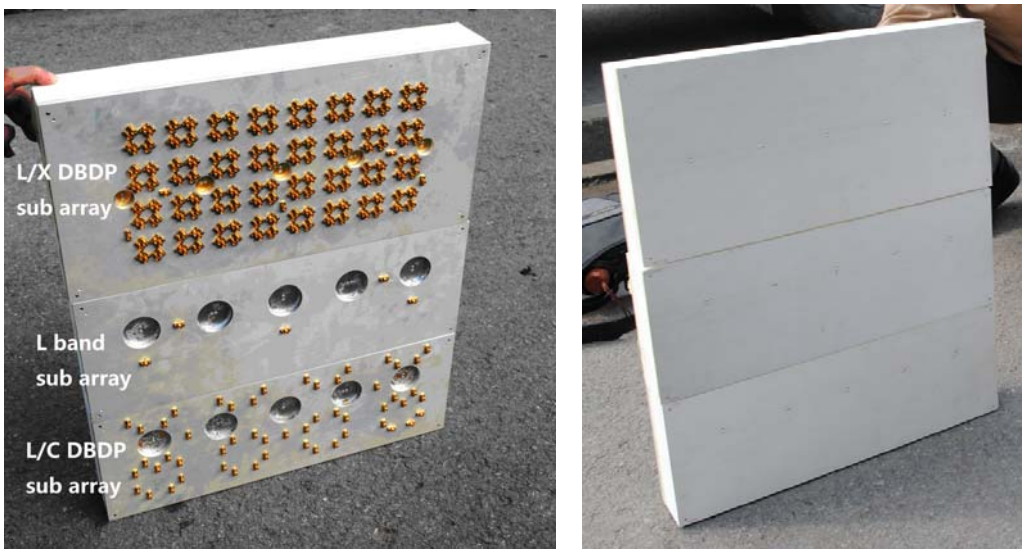

(a) Rear (b) Front

Fig.4 - 10 Photos of the TBDP shared aperture prototype array

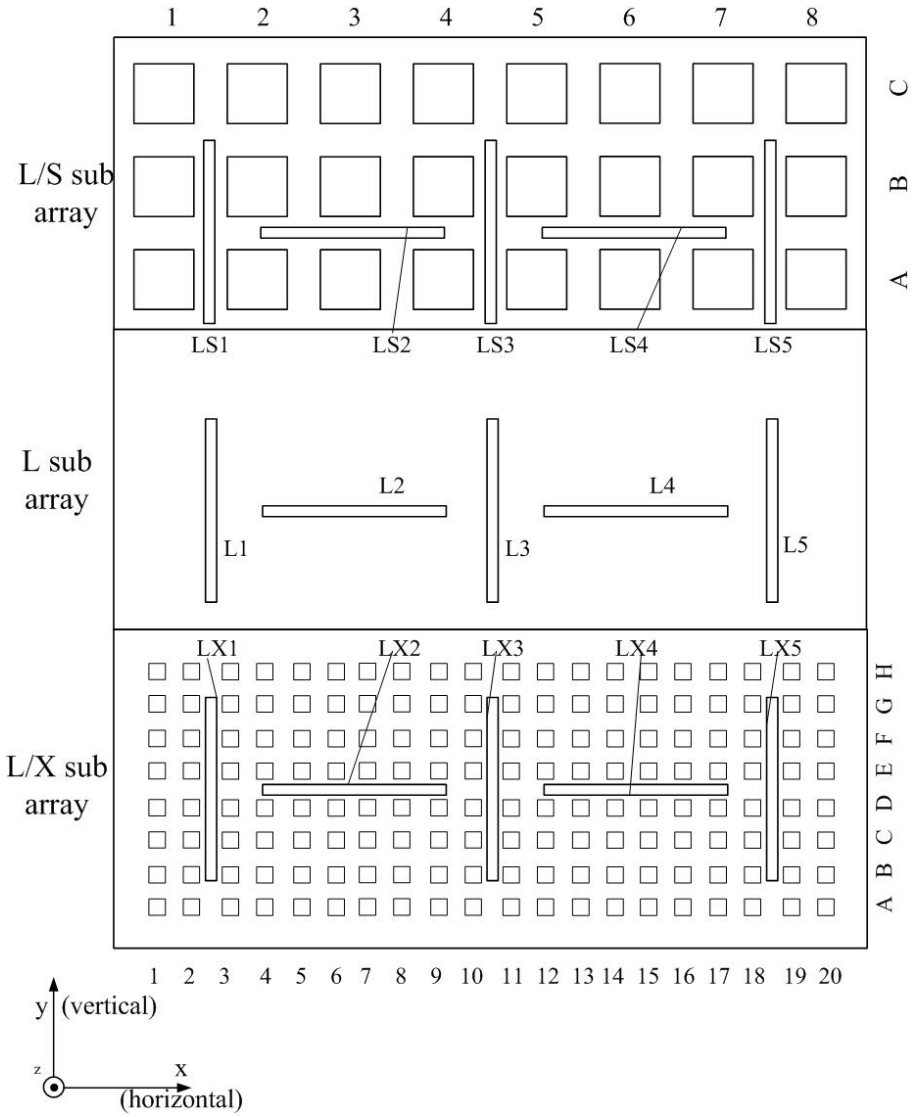

Fig.4 - 11 Element mark definition

alphabets in row from A to C (S-band) or A to H (X-band), and marked by number in column from left to right (1~8 in S-band and 1~16 in X-band). The L band elements are configured in three sub-apertures. They are called LS1 ~ LS5, L1 ~ L5 and LX1 ~ LX 5 from left to right in L/S, L and L/X sub-arrays, respectively. The horizontal and vertical planes are also defined.

4.4.1 L Band

The measured VSWR in the L-band is shown in Fig.4-12. Although the L band elements in each of the L, L/S and L/X sub-arrays have different higher band patches around them, almost similar port responses are achieved. Except for the element LS4, which has an imperfect solder connection, all other results agree well with the predicted results. The minimum VSWR ≤ 2 bandwidth is from 1.163 GHz ~ 1.330 GHz, *i.e.*, 167 MHz or 13.4%. The in-band array isolation is better than 37dB, as shown in Fig.4-13.

The measured L-band radiation patterns of the aperture made up of L, L/S and L/X sub-

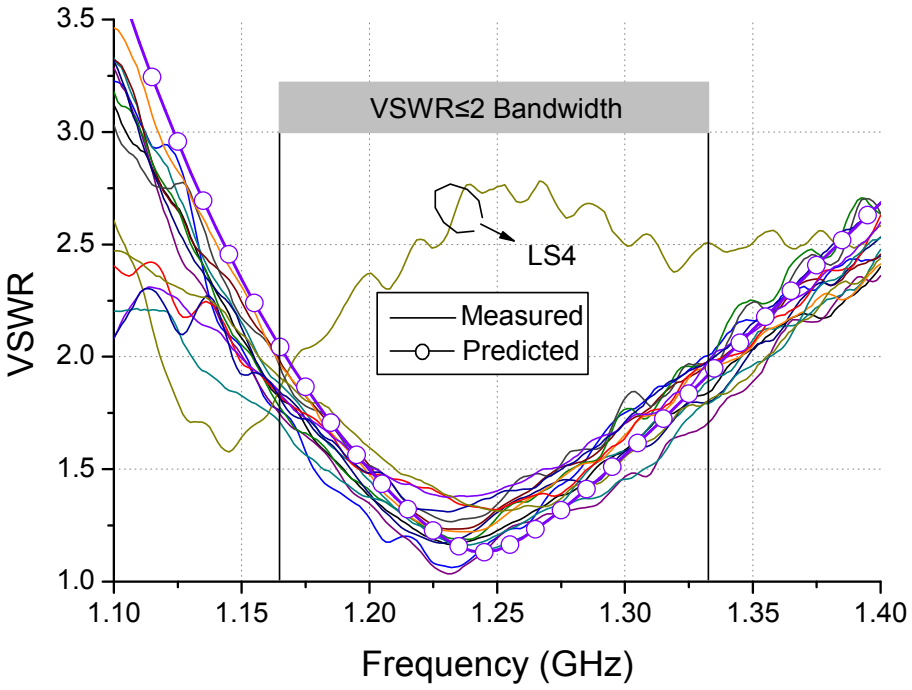

Fig.4 - 12 Measured VSWR of L band elements

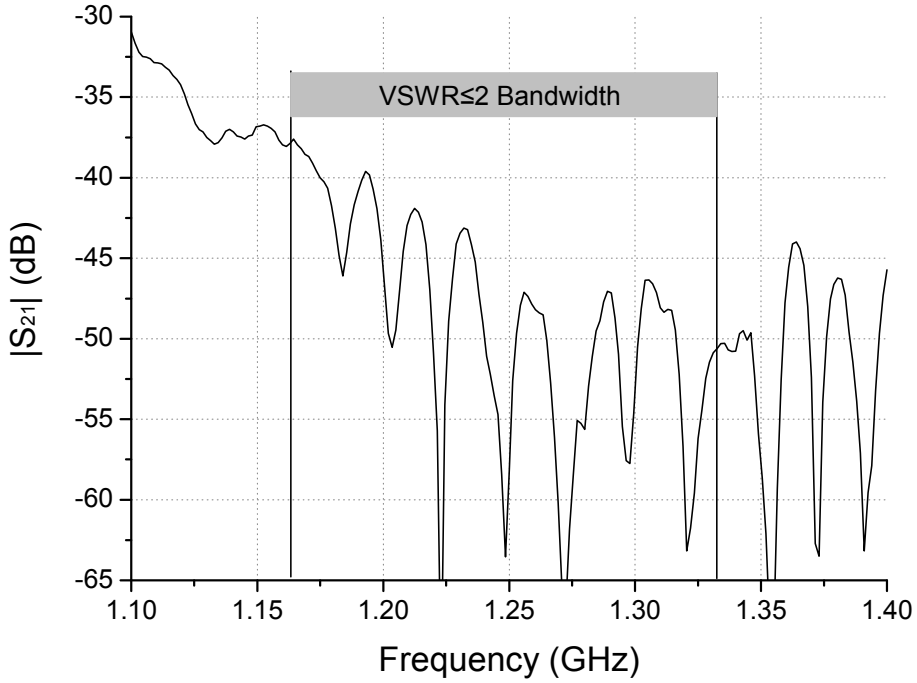

Fig.4 - 13 Measured L band array isolation

array are shown in Fig.4-14. They agree well with the theoretical radiation patterns which are computed as the product of array factor and standalone element radiation pattern obtained from Ansoft HFSS 10.0. The comparison between measured and theoretical radiation patterns confirm that the combined L-band aperture of three sub-arrays (L/S, L and L/X sub-array) brings negligible effects on the L band radiation patterns, even though the L elements in L/S sub-array are shorter than that in other sub arrays. This is due to the fact that S- and X-band patches surrounding the L band elements weakly couple to L band elements. In other words, the existence of S- and X-band patches has negligible effects on the L-band elements' radiation patterns uniformity in each sub-array.

Due to the 'pair-wise anti-feed' technique, the measured cross-polarization levels in the two main planes remain 30dB below the co-polarization levels within the main lobe. By comparing with the standard gain horn, the calibrated gain at 1.25 GHz is 13.2 dB and 14.6 dB for horizontal and vertical polarized ports, respectively while the radiation efficiencies of

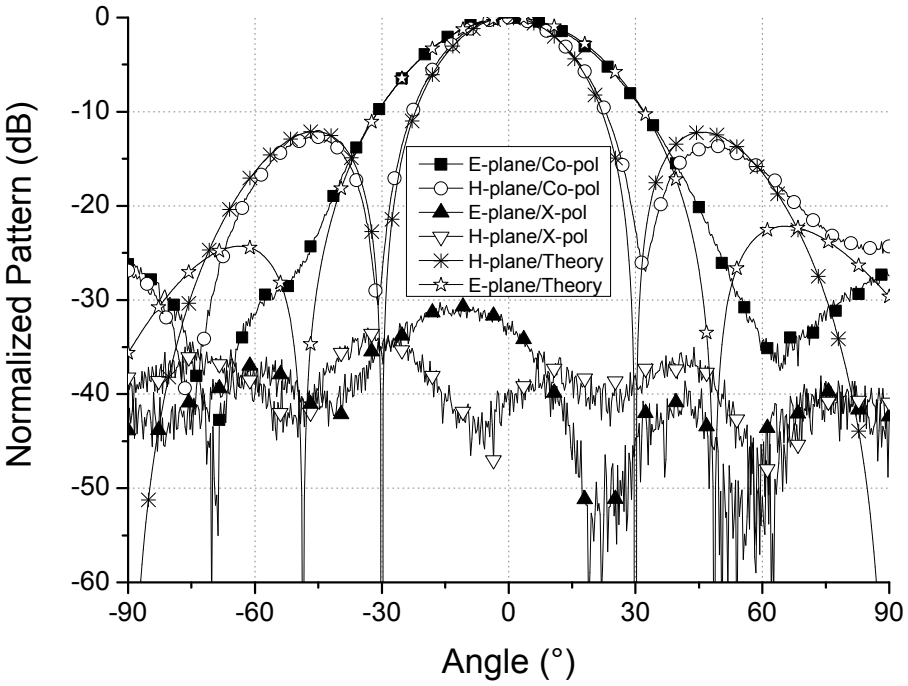

(a) Horizontal polarized port excitation

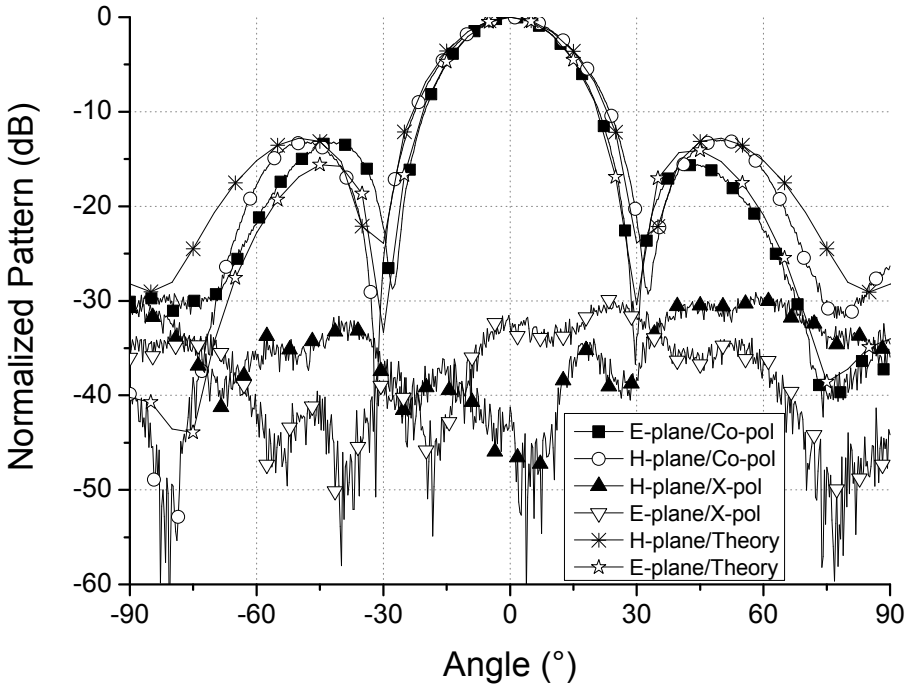

(b) Vertical polarized port excitation

Fig.4 - 14 Measured L band radiation patterns

62% and 61.2%, respectively. The lower efficiency is probably due to the insertion loss from the vertical parallel line and the anti-phase feed network. It can be increased in two ways:

1) By applying silver coating on both the microstrip lines and the parallel line to reduce the

conductive loss. Since in L/X sub-array, the feed network shares the substrate with the X band driven patches, a thinner substrate is used which supports surface waves and the corresponding losses. This can be rectified by using a thicker substrate for the feed network.

2) Similar to the design in Chapter 3, proximity coupling or aperture coupling can be used for L-band element feeding, to completely avoid the insertion loss on the vertical transition and thus simplify the structure.

The L-band scan patterns are not measured because of the few elements in this prototype array. Instead, a predicted scan radiation pattern for the 8-element full array, which consists two L/S, two L/X DBDP-SA sub-arrays and four L single band sub arrays, is shown in Fig.4-15. As can be seen, a scan range of 25° is obtained with no grating lobes.

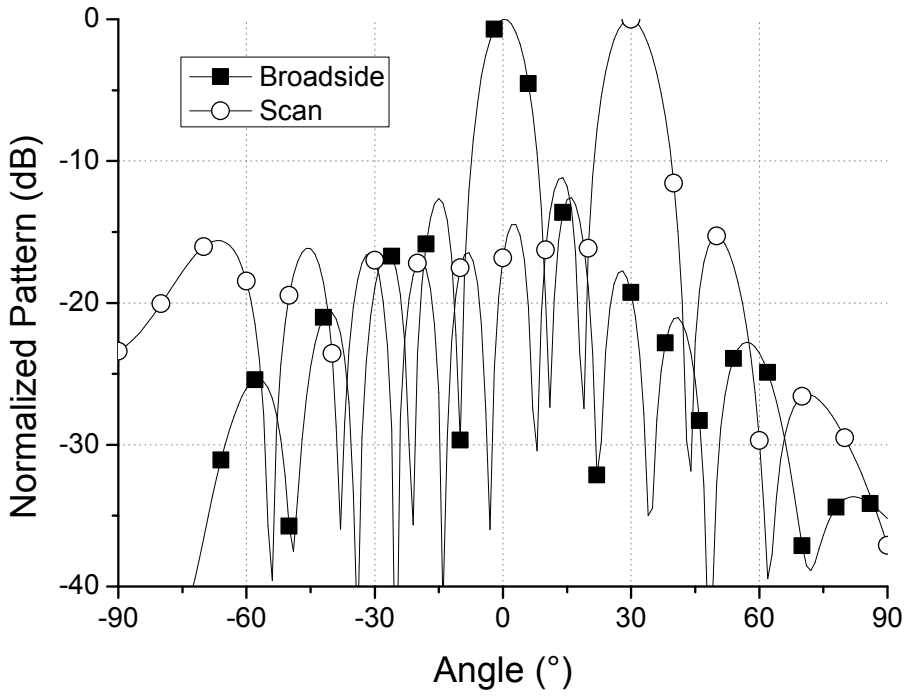

Fig.4 - 15 Predicted 8-element scan pattern for L-band array

4.4.2 S Band

The measured VSWR for S-band elements for both horizontal and vertical ports are shown in Fig.4-16. Here again, the overlapping part of all VSWR ≤ 2 element bandwidths are

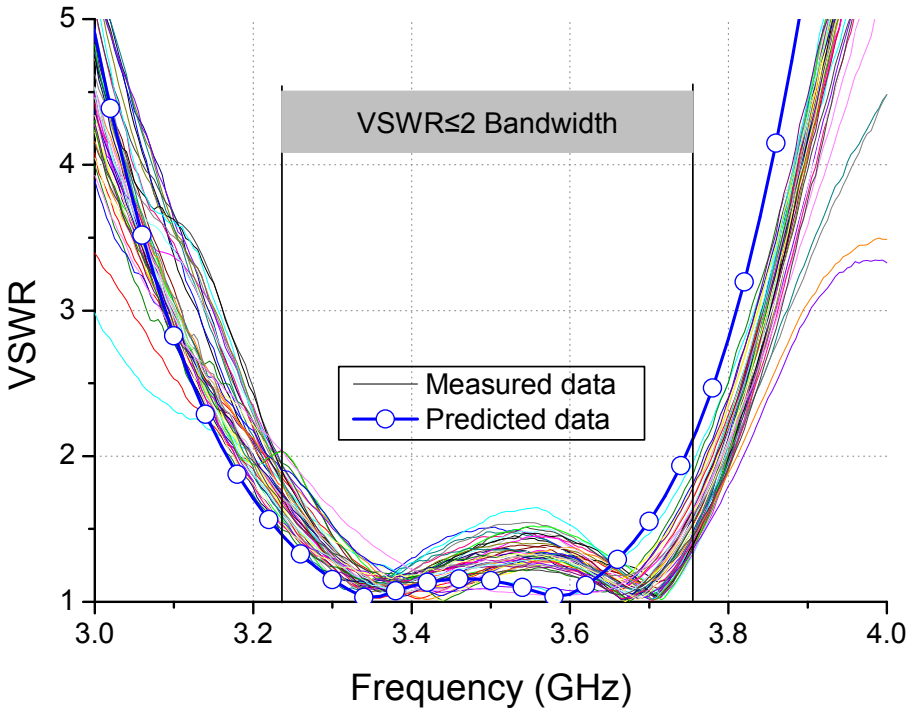

Fig.4 - 16 Measured VSWR of the S-band elements

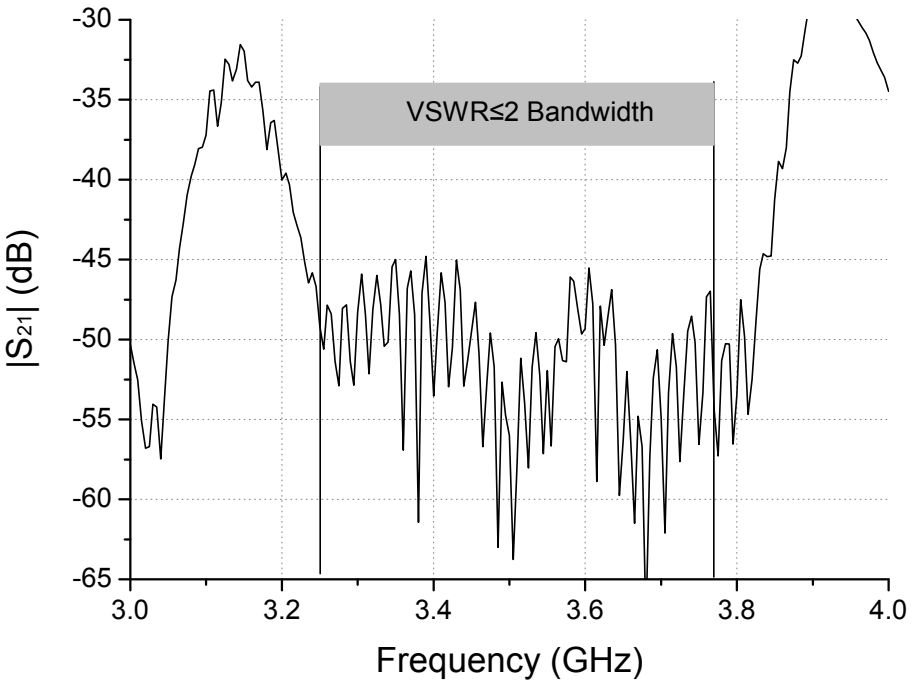

Fig.4 - 17 Measured array isolation in S-band

defined as the array bandwidth. The measured bandwidth is 14.8%, *i.e.*, from 3.25 GHz to 3.768 GHz. Compared with the predicted curve, the S-band measured bandwidth shifts

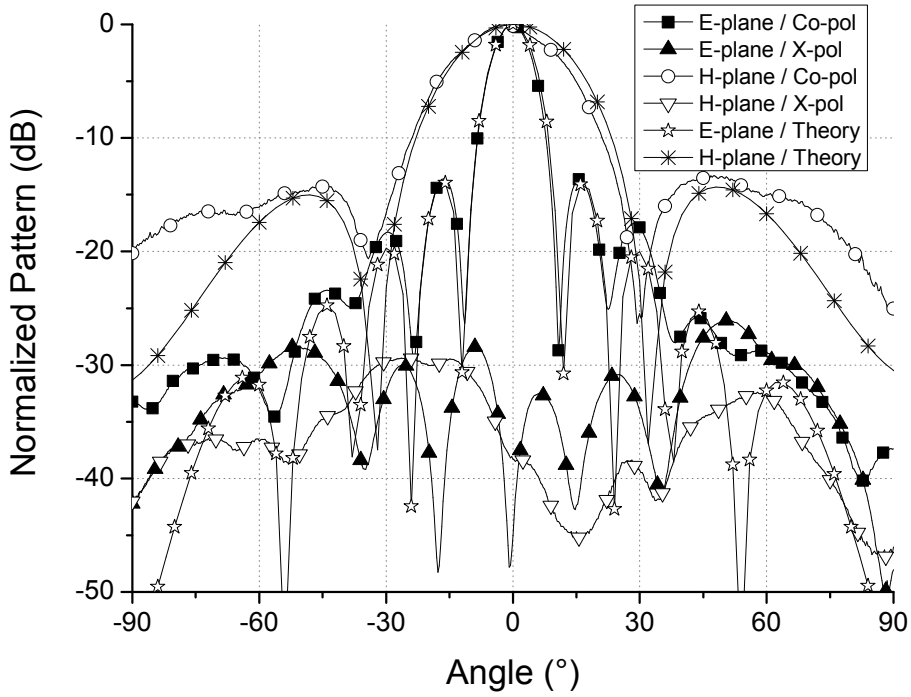

(a) Horizontal port excitation

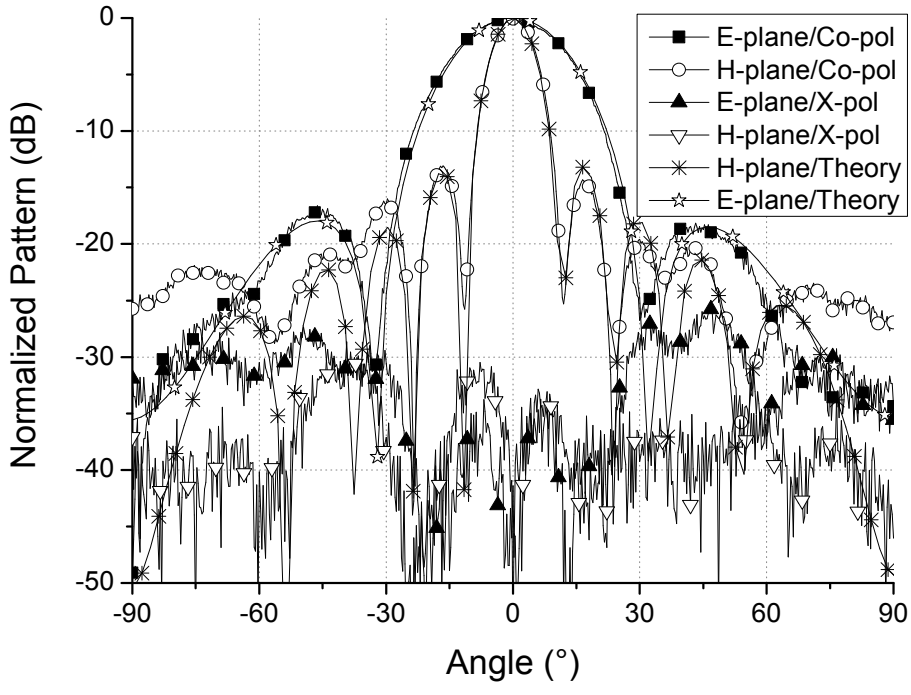

(b) Vertical port excitation

Fig.4 - 18 Measured radiation patterns in S band

slightly towards the higher frequency, and higher in-band ripples are noted. The in-band array isolation level is better than 45dB, as shown in Fig.4-17.

The measured S band radiation patterns agree well with the theoretical prediction, as shown in Fig.4-18. The cross-polarization levels are 30 dB lower than the co-polarization and the front-to-back ratio is better than 37.8 dB. Due to limited availability of the coaxial lines, only 8 × 2 elements are measured for gain calibration. The peak array gain of 18.6 dB is achieved and the radiation efficiency is 92.4%. The scan pattern is only measured along the eight-element direction. To reduce cost, custom made co-axial lines with different lengths are employed instead of the phase shifters and beam control boards. The measured scan capability is ±27°, as shown in Fig.4-19.

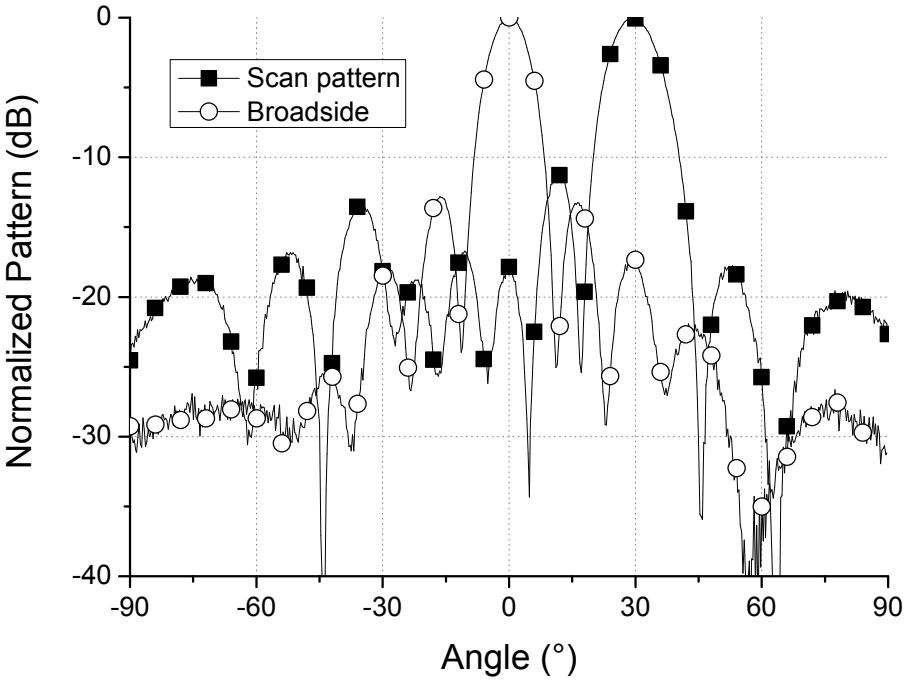

Fig.4 - 19 Measured scan pattern in S band

4.4.3 X Band

Fig.4-20 shows the measured X band element bandwidth. The VSWR ≤ 2 bandwidth of

16.8%, *i.e.*, from 9.098 GHz to 10.781 GHz, is achieved. Due to the 'pair-wise anti-phase feed' technique and large scale array, the cross-talk from the orthogonal polarized port is neutralized in the feed network, giving an array isolation level of better than 43 dB, as shown in Fig.4-21.

The measured X band radiation patterns, shown in Fig.4-22, agree well with the theoretical predictions. Specifically, this agreement is extremely good within ±30° but small difference is noted outside from 30° to 70°. Measured side lobe levels are obviously higher than the theoretical value outside 70° because the radiation pattern level is quite low, making it sensitive to the phase error and spurious radiation from L band element interleaved in the aperture.

The cross-polarization levels within main lobe remain below -35 dB in the two principal planes. Due to the electrically large ground, front-to-back ratio of 42.3 dB is obtained.

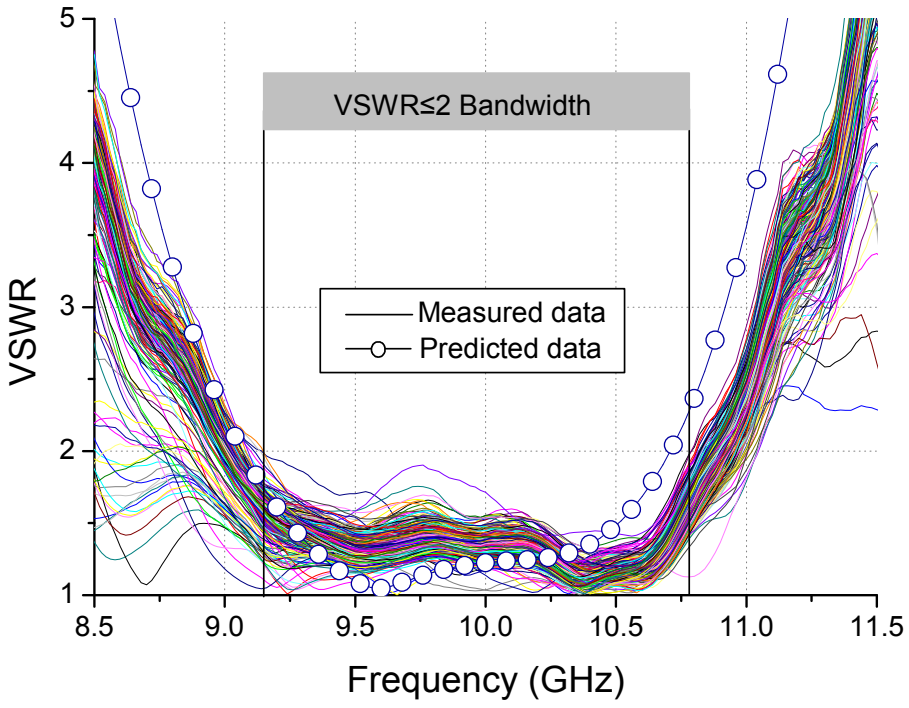

Fig.4 - 20 Measured VSWR of X-band elements

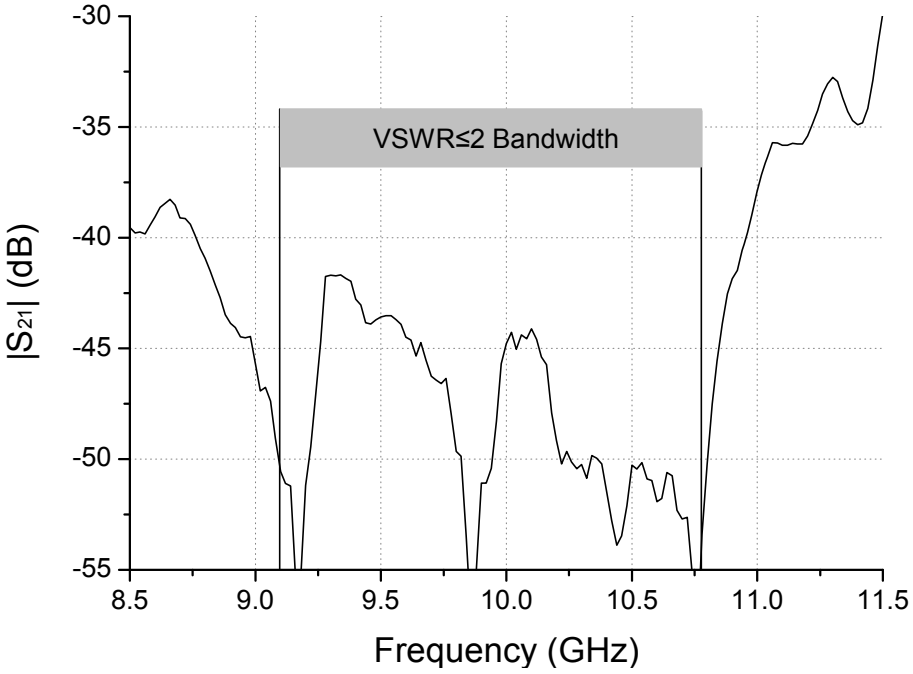

Fig.4 - 21 Measured array isolation in X-band

Calibrated gains are 22.19 dB and 21.79 dB for vertical and horizontal polarized port, respectively, using 16 × 2 elements, which translate into an efficiency of 92.7% and 84.5%, respectively.

The measured scan capability reaches ±30° for both horizontal and vertical polarization, as shown in Fig.4-23. It should be mentioned that all four scan patterns have a small grating lobe at about 75°. This is simply because the array element spacing is designed for ±25° scan but we tested using ±30° steering phase excitation, *i.e.*, the scan test exceed the designed scan capability. This is due to the fact that 30° scan requires six types of custom-made coaxial line lengths, including 0° /60° /120° /180° /240° /300°. But for 25° scan, 32 types of coaxial lines with different lengths should be made. Obviously, the latter choice makes more difficulties in the measurement.

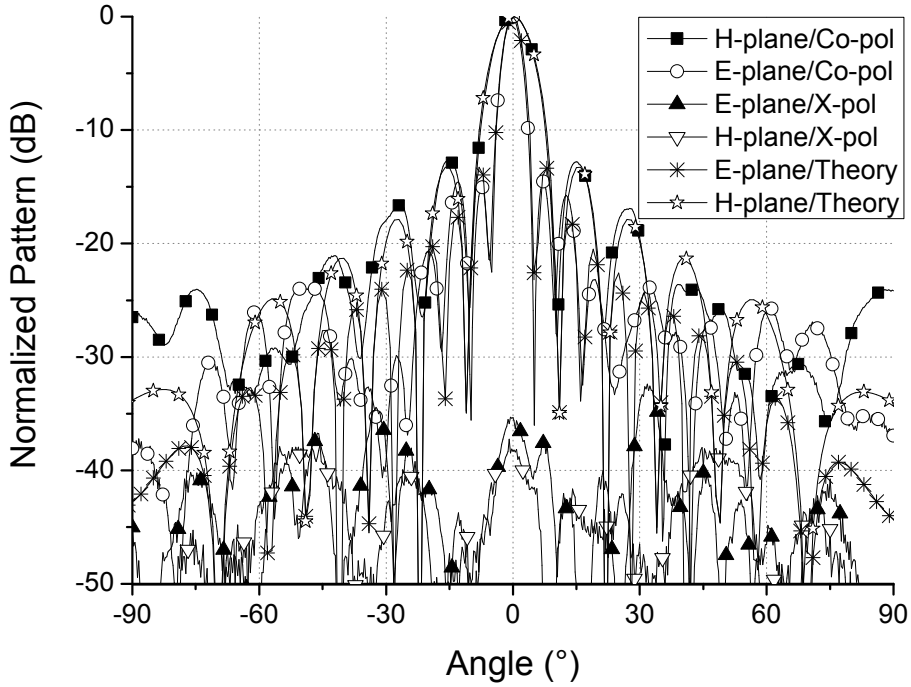

(a) Horizontal port excitation

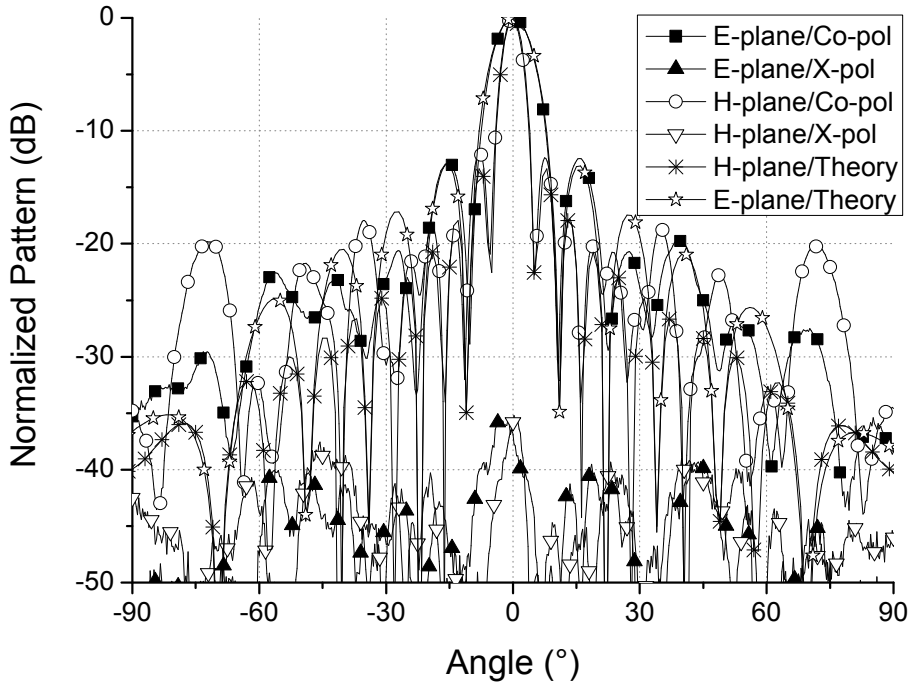

(b) Vertical port excitation

Fig.4 - 22 Measured radiation patterns in X band

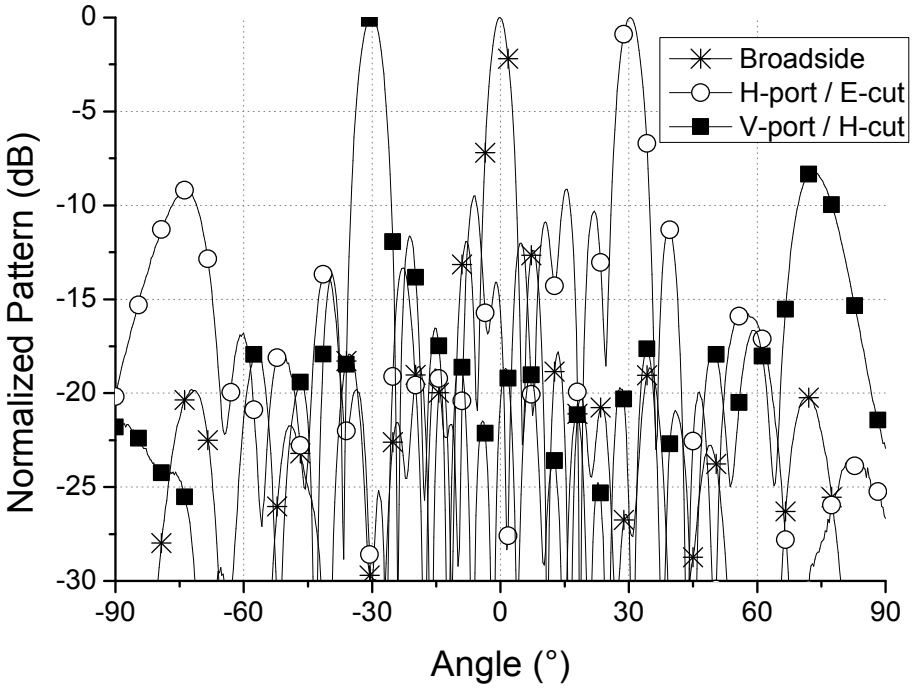

(a) Scan patterns in ZOX plane

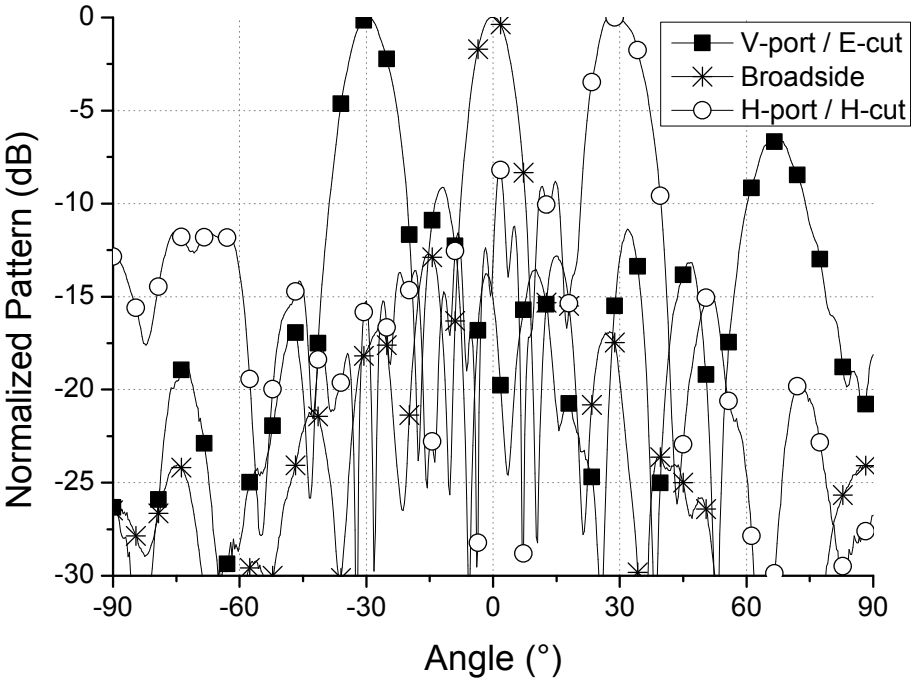

(b) Scan patterns in YOZ plane

Fig.4 - 23 Measured X band scan patterns

To further illustrate the scan capability, the measured scan patterns are compared with the predicted patterns, as shown in Fig.4-24. Take vertical polarization in H plane scan as an example. When the beam steers to 30°, a large grating lobe appears in array factor at 90°.

Although theoretically this grating lobe will be suppressed by the element pattern (achieved by the Ansoft HFSS 10.0 using ideal standalone element) shown by the blue curve in Fig.4-24, the element pattern level at 75° is less likely to be so ideal due to the inter-element and inter-band coupling. Thus, a small grating lobe appears.

Because the measured scan patterns agree well with the predicted curve (theoretical array factor) in Fig.4-24 in terms of the peaks and null positions, side lobe levels, scan direction, *etc*, the array factor method is considered to be accurate to predict the correct scan patterns within designed scan range. The calculated 25° scan pattern is shown in Fig.4-25, where the grating lobe is eliminated in the array factor, which validates the non-grating lobe pattern performances within the designed scan range.

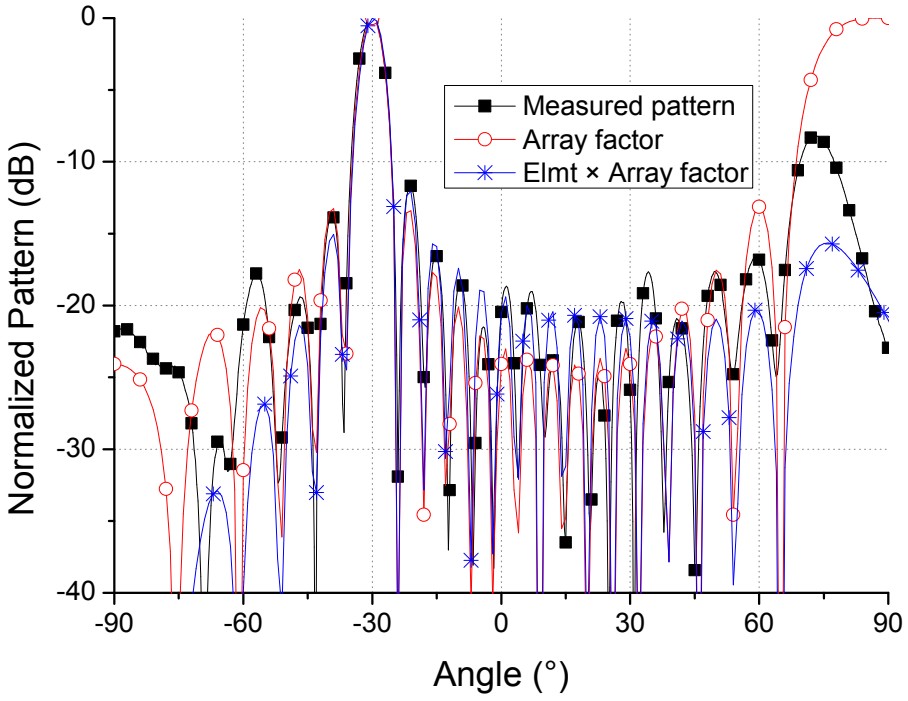

Fig.4 - 24 Measured and theoretical 30° scan pattern

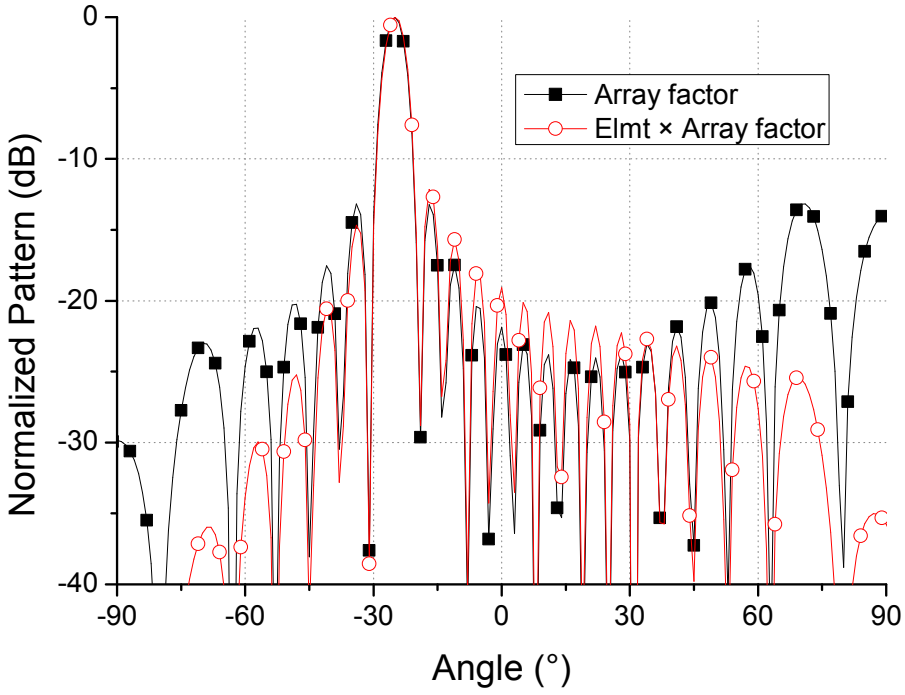

Fig.4 - 25 Predicted 25° scan pattern

Moreover, because the measured X-band pattern agrees very well to the theoretical array factor for both the broadside and the scan direction, it suggests that the X-band radiation patterns are not affected by the L-band elements located above.

4.5 Conclusion

A TBDP-SA array is designed by combining several DBDP-SA sub-arrays. To validate the design methodology, two DBDP-SA sub-arrays (L/S and L/X) and an L-band dual-polarized sub-array are designed and combined to form an L/S/X TBDP-SA array. The measured results confirm that the proposed L/S/X TBDP-SA array can simultaneously operate in three pre-determined frequency bands with good performances including: 1) similar percentage bandwidth for three bands from 13.7% to 16.7%; 2) the in-band array polarization isolation better than 37dB; 3) good measured radiation patterns and in-band cross-polarization level below -30dB and 4) the measured scan range of ±25° for S- and X-

band. The key performances achieved are compared to the required specifications and are listed in Table 4-3.

Table 4 - 3 Measured specifications and design targets of L/S/X TBDP shared aperture array

Specification	L band (1.25 GHz)		S band (2.85 GHz)		X band (10 GHz)	
	Target	Measured	Target	Measured	Target	Measured
BW(MHz)	80	167	180	518	450	1683
BW(%)	6.4	13.4	6.4	14.8	4.5	16.7
Polarization	H-polar	Dual-linear	V-polar	Dual-linear	Dual-linear	Dual-linear
Array Iso.	25dB	37dB	25dB	45dB	25dB	43dB
Scan Range	±25°	untested	±25°	±25°	±25°	±25°
X-polarization	-20dB	-30dB	-20dB	-30dB	-20dB	-35dB

From these measured results, the proposed combination method does not affect the radiation patterns and impedance matching significantly. The TBDP-SA array has a 33% less aperture when compared to the tri-band independent-aperture array. Moreover, by replacing the L-band sub-array with other DBDP-SA sub-arrays such as L/C DBDP-SA sub-array, the current design can be easily extended to the quad-band shared-aperture antenna arrays.

Acknowledgement

The work on L/S/X TBDP-SA array for SAR applications in this chapter is sponsored by the 863 project of Chinese government under grant number 2007AA12Z125.

Mr C. Gao, Mr W. Wang and Mr W.Y. Wu are highly appreciated for their suggestions and help in design, fabrication and measurement of array antennas.

Chapter 5
L/C DBDP-SA Sandwiched Stacked-Patch Array

5.1 Introduction

The perforated patch [109-124] and the interleaved structure [83-108] are the two most widely used DBDP-SA array configurations. Their designs, which have undergone two decades of developments and improvements, are quite mature now. For both configurations, the higher-band elements of DBDP-SA array can typically achieve a large bandwidth of over 20%, while the bandwidth in lower band remains limited to about 12% [104, 105, 118, 120]. Because large bandwidth is generally required in a SAR system for better resolution, lower-band bandwidth improvement is highly desirable in DBDP-SA SAR arrays.

Another possible, but less commonly used, aperture sharing method for DBDP-SA antenna is the overlapped DBDP structure [125-131]. Its higher- and lower-band elements are designed separately and are located at different heights, so that elements in both bands have independent cavities. Hence, the lower band of overlapped DBDP structure has inherently large bandwidth, because its lower-band element's cavity does not need perforations like that of a perforated patch nor it is limited by slim structure like that of interleaved structure configurations. However, the requirement of complex vertical feeding structure prevents its wide application in DBDP-SA arrays, particularly for large scale arrays. Thus, the design of vertical feeding structure is the key parameter in the design of overlapped DBDP-SA antennas.

This chapter presents the design of a novel sandwiched stacked-patch structure for DBDP-SA arrays. Unlike the multi-band shared aperture arrays presented in Chapter 3 and Chapter 4, which were designed for given specifications, this chapter investigates techniques to increase the lower-band bandwidth in DBDP-SA array without focusing too much on practical design considerations. First, the relationship between bandwidth and perforation numbers is studied for the microstrip patch, and then, a novel sandwiched stacked-patch structure is proposed. To further confirm the feasibility of the proposed structure, two unit cells (the proposed sandwiched-stacked patch and an overlapped structure) are designed, fabricated and tested. A large scale L/C DBDP-SA sandwiched stacked-patch array is designed and fabricated based on the experience of unit cell fabrication. The main contributeions of this chapter are:

1) Design and testing of an L/C DBDP unit cell overlapped structure to verify the relation between bandwidth and perforation number.
2) A novel sandwiched stacked-patch for DBDP-SA array with enhanced lower-band bandwidth. A unit cell is designed and fabricated to validate the structure.
3) Design and testing of an improved L/C sandwiched stacked-patch DBDP-SA full array to verify its feasibility in array configuration.

The measured results are compared with published results for classical DBDP-SA arrays to highlight the advantages of the proposed structure.

5.2 Bandwidth and Perforation

The space-borne SAR antenna is an important potential application for DBDP-SA array because of its low weight and compact structure requirement. Furthermore, both large band-

width and low antenna profile is required for better range resolution and ease of stowing. However, large bandwidth requires a low Q factor, which is generally realized by employing thicker resonant cavity in array element design. This is quite challenging for lower band elements in a DBDP array, because the DBDP array's profile is primarily decided by the lower band element thickness; therefore, it makes sense to study how to exploit the antenna bandwidth for the specified thickness.

In perforated patch DBDP-SA array [109-124], lower-band microstrip (stacked) patch is

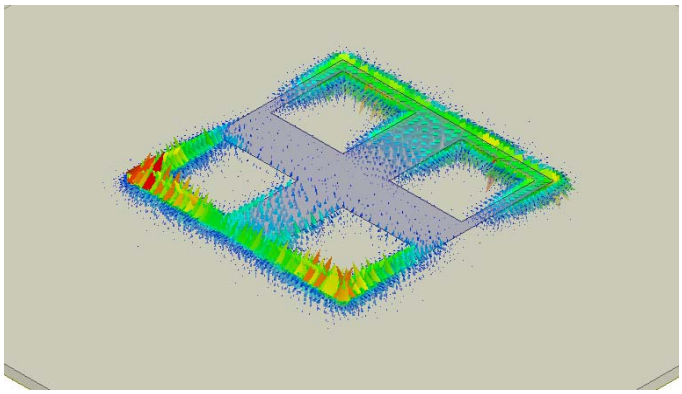

(a) Simulated E-field distribution of the perforated patch

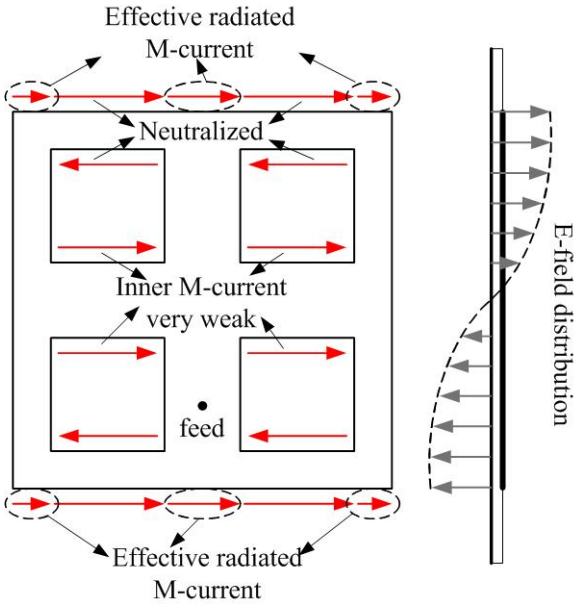

(b) Equivalent magnetic currents

Fig.5 - 1 Field distribution and equivalent M-currents in the perforated patch

commonly perforated to accommodate higher-band elements, hence, the bandwidth performance is first discussed.

The authors of [109, 110] point out that bandwidth of perforated patch is inversely proportional to the perforation size. It can be explained with the help of Fig.5-1. The E-field distribution on a single layer perforated patch is first predicted by Ansoft HFSS 13.0, as shown in Fig.5-1(a). From the field distribution, perforations on the patch can be treated as perturbations, whereas the fields in the non-perforated parts still remains cosine distributed. The equivalent magnetic currents (M-currents) can be plotted as shown in Fig.5-1(b), where two points can be concluded: 1) the magnetic currents at the patch edges, which are considered as the main radiation source from the cavity mode theory [163], are neutralized with those present at the outside edge of perforations. The effective radiation edge is then shortened; 2) M-currents at the inner side of perforations are very weak due to cosine field distribution and thus, contribute little to the radiation. Overall, the perforations on the patch reduce the effective radiation area, leading to a high Q factor and narrow bandwidth.

The explanation above is given for a single-layer perforated patch. For the commonly adopted stacked patches, a comparison is made among three possible structures numerically to get an intuition on bandwidth and perforations. The three structures include: 1) non-perforated stacked patch, 2) partial-perforated stacked patch, and 3) fully-perforated stacked patch, as shown in Fig.5-2.

In this numerical investigation, parameters which may affect the bandwidth are fixed to exclude the disturbance of other factors, including: 1) substrate material (Rogers 4003C); 2) feeding method (co-planar feed); 3) element thickness ($0.074\lambda_0$) and 4) perforation shape

(square shape). The in-band ripple factors are also tuned to the same level (-15dB). All the parameters of the three structures (defined in Fig.5-2) are optimized using commercially available Ansoft HFSS 13.0 software, and they are listed in Table 5-1 for reference.

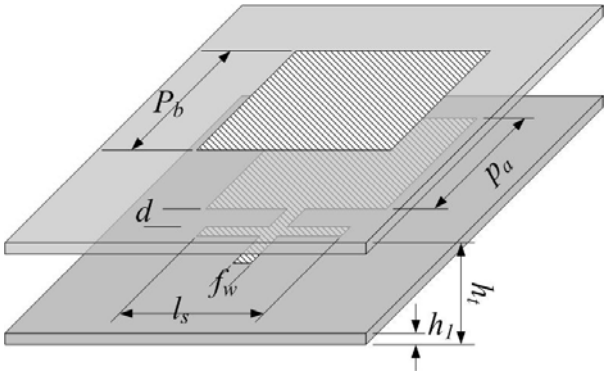

(a) Stacked patch

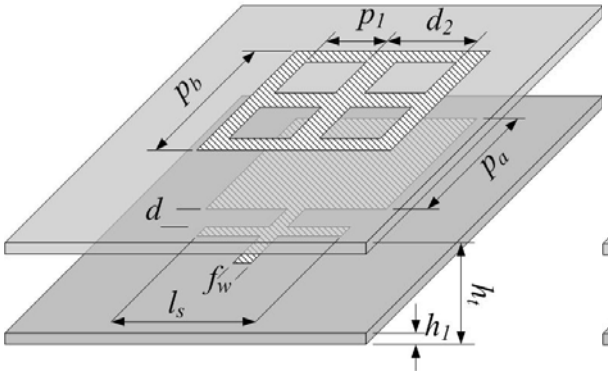

(b) Partial perforated patch

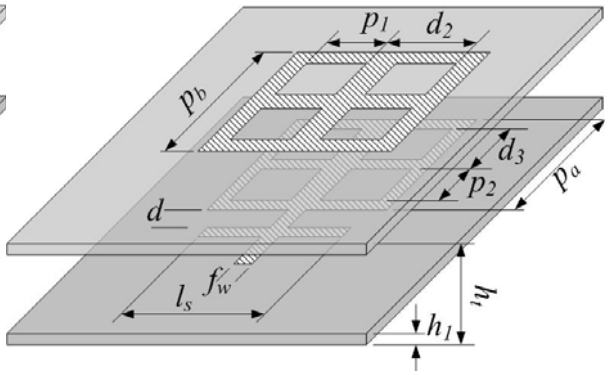

(c) Fully perforated patch

Fig.5 - 2 Configurations of stacked patch with different perforation

Table 5 - 1 Parameters of three types of stacked patch

Non-Perforated Stacked Patch					
P_a	74	P_b	90	h_1	3.048
d	5	f_w	6	h_t	17.861
l_s	49				
Partial Perforated Stacked Patch					
P_a	74	P_b	81	h_1	3.048
d	5	f_w	6	h_t	17.861
l_s	51	P_1	26	d_2	36
Fully Perforated Stacked Patch					
P_a	68	P_b	79	h_1	4.572
d	10	f_w	9	h_t	17.861
l_s	50	P_1	26	d_2	36
P_2	26	d_3	36		

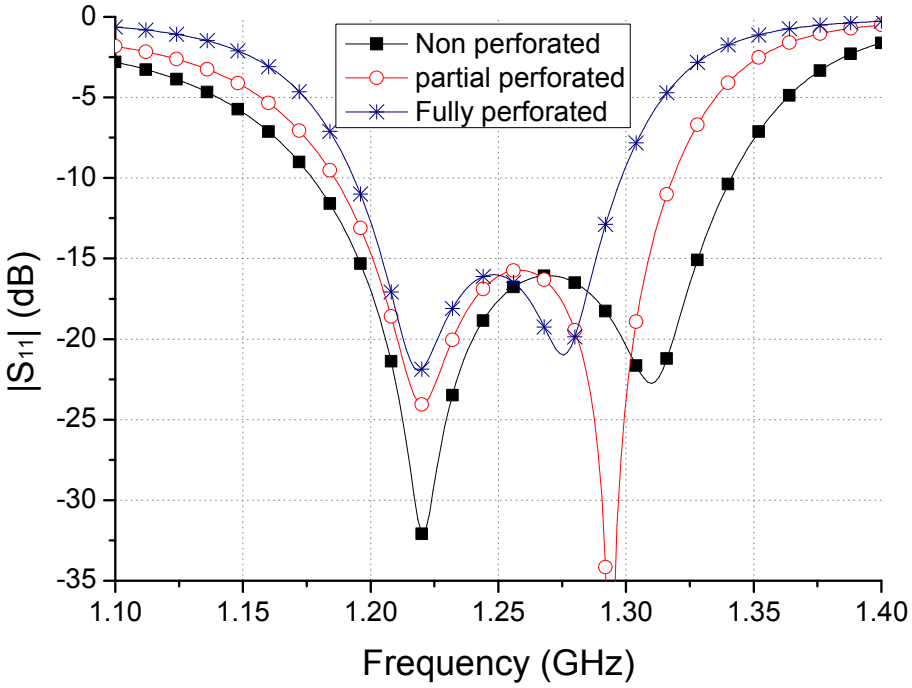

Fig.5 - 3 Computed stacked patch bandwidth for different perforation numbers

Fig.5-3 shows the predicted $|S_{11}|$ as obtained from HFSS 13.0. The stacked patch bandwidth decreases with the increase in perforation number, by a factor of approximately 2.4%, as shown in Table 5-2. Certainly, by adopting a different laminate and overall patch profile, different bandwidth and decreasing factor can be obtained, however, a similar trend is believed to be achieved.

All three stacked patches with different perforations shown in Fig.5-2 can be employed as the lower-band element in DBDP-SA array, leading to three different unit cell DBDP structures, as shown in Fig.5-4.

Table 5 - 2 Bandwidth comparison among the three structures

Structures	Operating band (MHz)	Bandwidth (MHz)	Bandwidth (%)
Fully perforated patch	1194 ~ 1298	104	8.3
Partial-perforated patch	1185 ~ 1318	133	10.6
Non-perforated patch	1177 ~ 1341	164	13.0

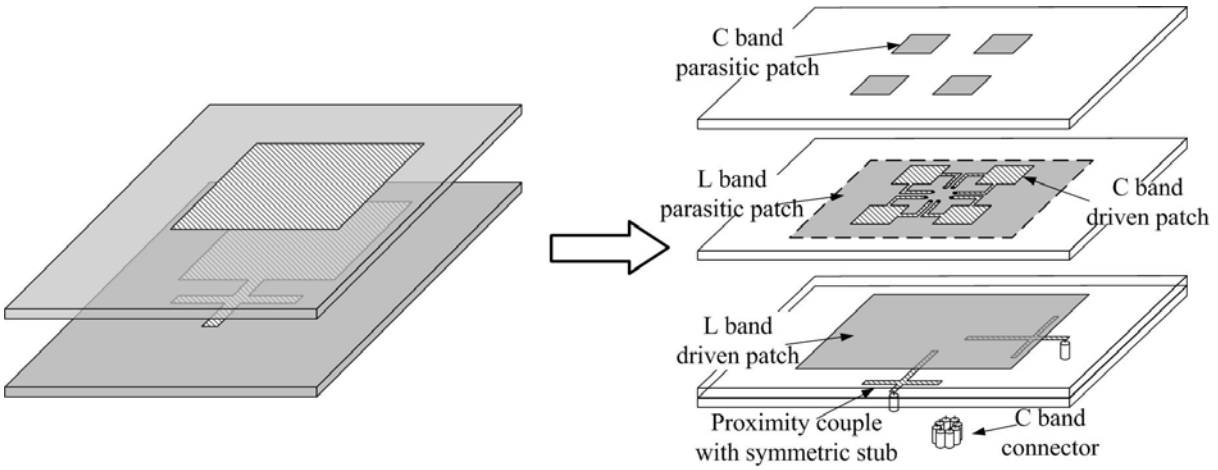

(a) Overlapped DBDP unit cell

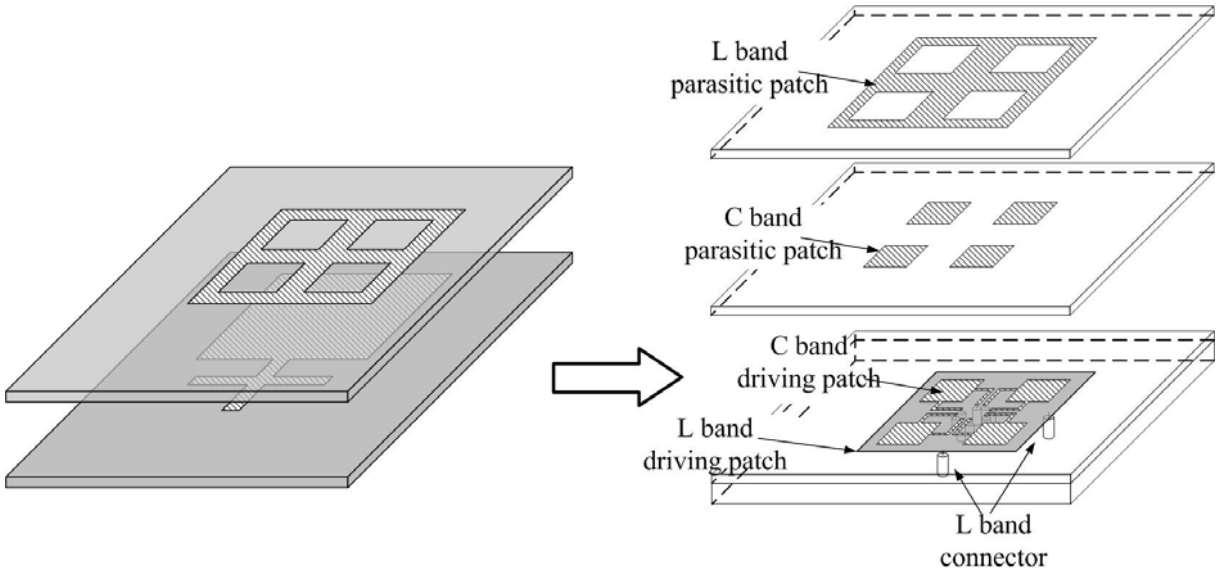

(b) Sandwiched DBDP unit cell

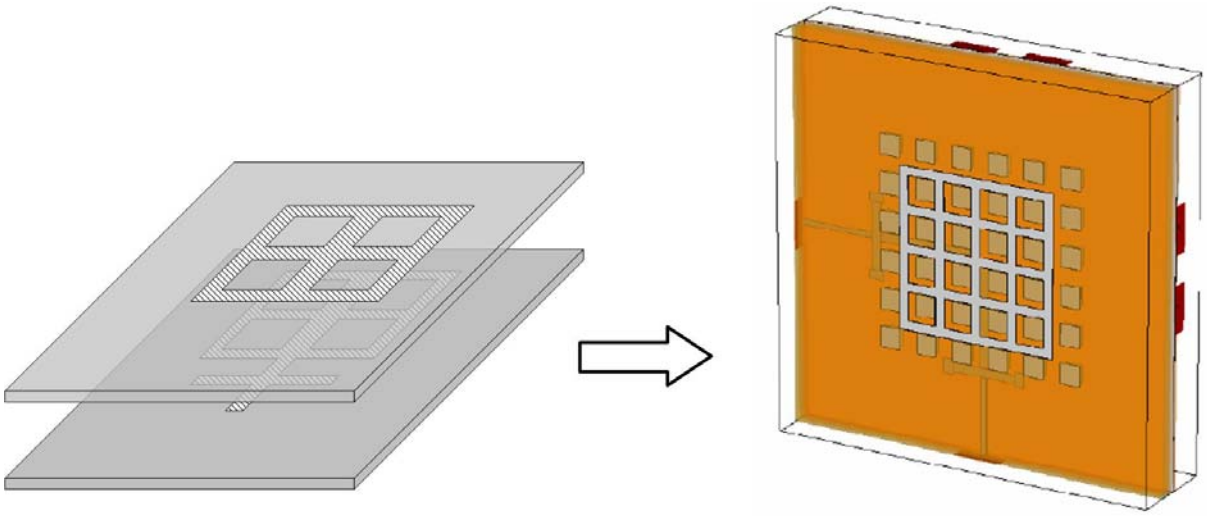

(c) Perforated patch DBDP unit cell [104]

Fig.5 - 4 Different perforated stacked patch and corresponding DBDP structures

The perforated-patch DBDP unit cell in Fig.5-4(c) is the most widely used classical dual-band aperture sharing technique. It is not discussed in this thesis. The overlapped DBDP structure (Fig.5-3(a)) and the proposed sandwiched DBDP structure (Fig.5-3(b)) are studied in the rest of this chapter. These structures are analyzed and compared in terms of the lower-band bandwidth, antenna profile and design complexity for DBDP-SA array applications. The unit cells of both the structures are designed, fabricated and measured. Based on the results, a large scale L/C sandwiched structure DBDP-SA array is proposed.

5.3 Overlapped DBDP Structure

The overlapped DBDP structure has the best lower-band bandwidth performance among the three structures mentioned earlier. However, it is rarely employed in DBDP-SA array configuration probably due to its complicated feed structure. To understand the advantages and disadvantages of using this configuration, an L/C DBDP unit-cell overlapped structure is designed and fabricated.

5.3.1 Design Specifications

In the design, two main aspects are considered: 1) lower-band element bandwidth; and 2) to verify the array flexibility of overlapped DBDP structure. The design specifications are listed in the Table 5-3.

Table 5 - 3 Specifications for L/C DBDP unit cell overlapped structure

	L-band	C-band
Center frequency (GHz)	1.25	5.3
Bandwidth(MHz)	200	600
Polarization	dual-linear	dual-linear
Excitation	Independent	Independent
Scan range	±25° in two dimensions	±25° in two dimensions

5.3.2 Array Design

A. Design Considerations

To achieve the requirements given in Table 5-3, the following design considerations must be made:

1) Elements in each band should have independent feed structure, in order to control the elements in each band separately.
2) The element number and spacing of two bands should scale to the frequency ratio and wavelength ratio in the unit cell design, as shown in Fig.5-5. This is necessary to avoid the (higher-band) grating lobe, as well as to keep the elements in each band regularly distributed in full array configuration.
3) Low Q factor elements, such as stacked-patch and thicker-patch, should be used in the lower band to maximize the bandwidth enhancement in the overlapped structure.

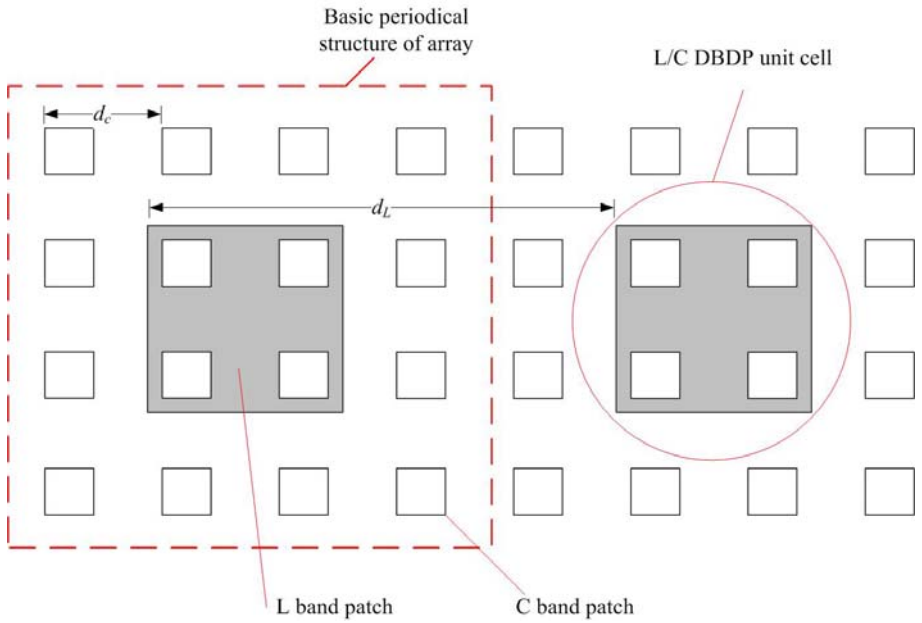

Fig.5 - 5 Schematic diagram of overlapped structure L/C DBDP array

B. Element Spacing

The side-by-side tightly configured lower-band patches presented in [125, 126] will

deteriorate inter-element isolation, impedance matching and radiation patterns in broadband array. Hence, this configuration is not adopted.

To give an intuitive view of the relationship between inter-element isolation and the element spacing, $|S_{11}|$ and $|S_{21}|$ levels between two L band stacked patches are computed for different values of '*d*' (defined in Fig.5-5), as shown in Fig.5-6. The impedance bandwidth ($|S_{11}| \leq$ -10 dB) is extremely small when the lower-band patches are very close to each other while $|S_{21}|$ is also the worst (only 5 dB). Isolation and impedance matching improves when the two patches are placed farther apart. $|S_{11}|$ changes slightly when the lower-patch spacing is increased beyond 130 mm (*i.e.*, roughly $0.5\ \lambda_0$). Hence, the lower-band elements in overlapped array are not recommended to be tightly configured.

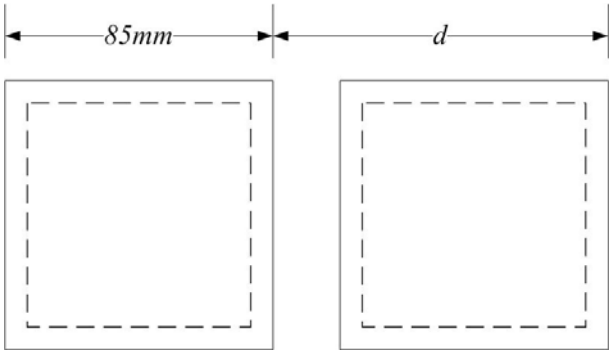

(a) Parameter definition

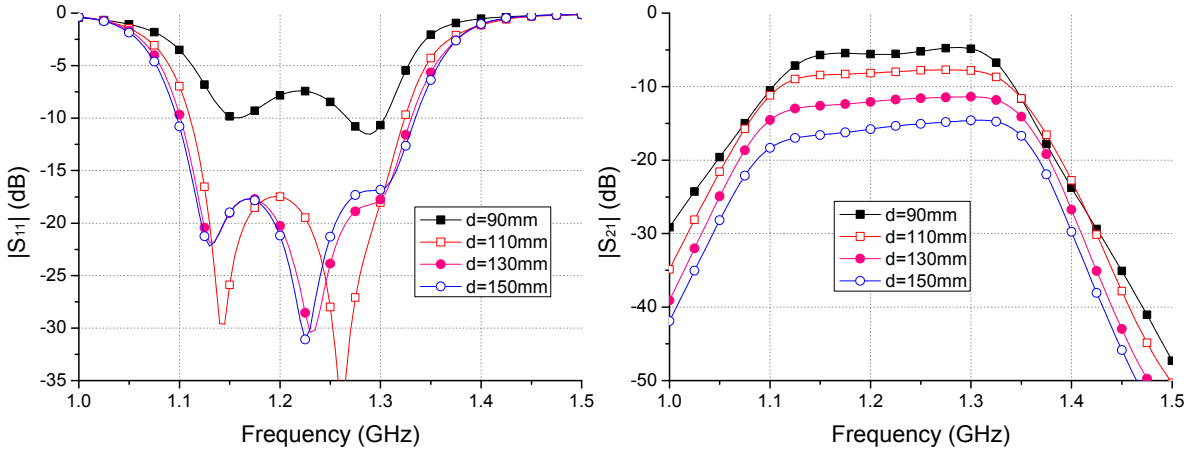

(b) $|S_{11}|$ (c) $|S_{21}|$

Fig.5 - 6 Computed inter-element coupling and |S11| for different element spacing

In this design, both L- and C-band arrays require a scan range of ±25°. The corresponding element spacing can be estimated using eq.5-1

$$d = \lambda_0 / (1 + \sin\theta) \tag{5-1}$$

where θ is the maximum scan range. The calculated C and L band elements spacing are 37.5 mm and 150 mm, respectively, *i.e.* 0.65 λ_0 for each band (λ_0 is the wavelength corresponding to the center frequency).

C. C-Band Array Configuration

Because L- and C-band elements have the same element spacing in terms of wavelength (0.65 λ_0), according to the wavelength ratio every 4-by-4 C band elements and 1-by-1 L band element form a basic periodical structure of the whole array, shown in Fig.5-5. Considering the L-band patch size, the L/C DBDP overlapped unit cell composes 2-by-2 C-band elements and 1-by-1 L-band element, as shown in Fig.5-7(a).

The element spacing (0.65 λ_0) chosen for L band creates wide gaps among the L band elements, see Fig.5-5. C-band elements on L-band patch or in L-band gaps will be distributed

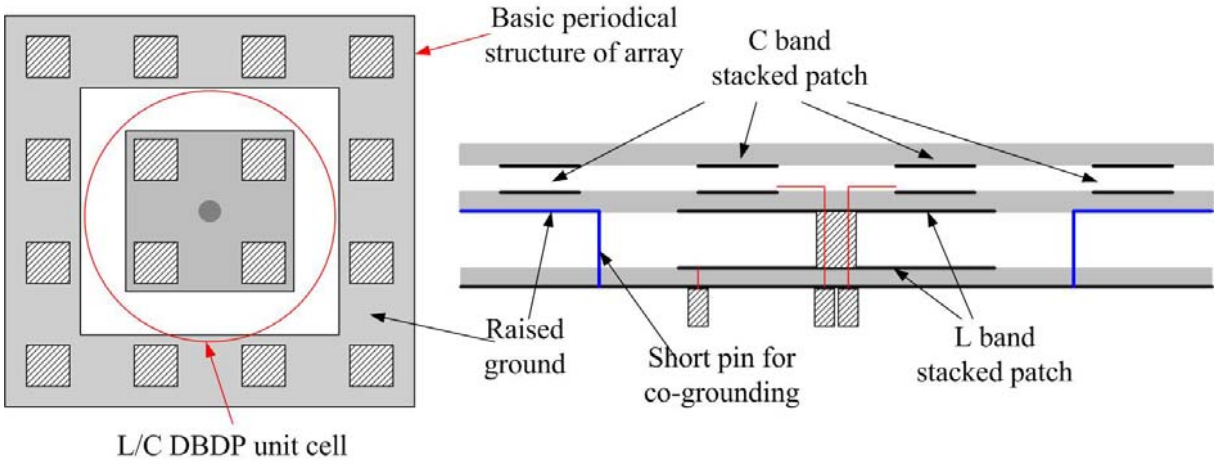

(a) Top view (b) Cross section

Fig.5 - 7 Illustration of the raised ground in L/C overlapped DBDP unit cell

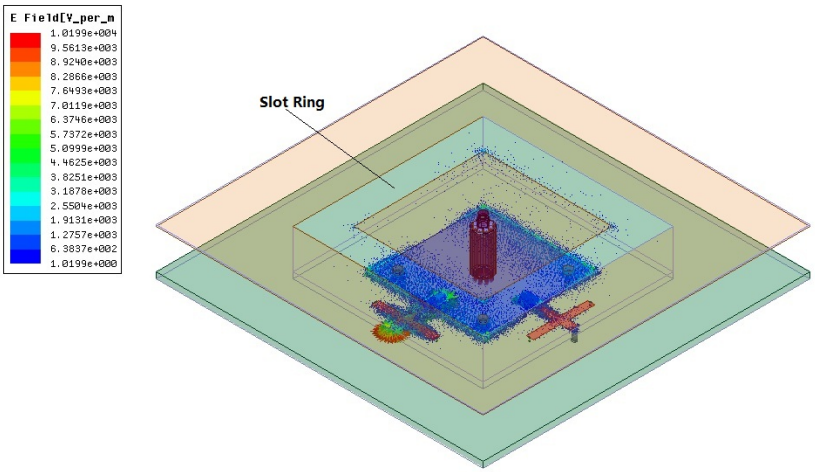

Fig.5 - 8 Simulated field distribution for the lower-band stacked patch

on different height, which requires extra phase distribution to compensate for the space delay of travelling wave at radiation angle. Even by doing so, side lobe levels will inevitably be raised. As a solution, the ground in L-band patches gap is raised to the same level as that of the L-band upper patch (See Fig.5-7(b)) to form a planar array for C band. The excitation for C-band elements is thus facilitated.

D. L/C Band Element Embedding

The raised ground and the L-band upper patch also forms a slot ring, as shown in Fig.5-8. Because the square slot ring is electrically large in L band, it may be excited, which means that: 1) the structure will actually become patch / ring-slot interleaved structure if the slot ring contributes with dominant radiation, rather than the overlapped-stacked patch; 2) the impedance matching and the radiation patterns will also be affected if the slot resonates.

The E-field distribution of the structure, predicted by Ansoft HFSS and shown in Fig.5-8, indicates that most of the energy is distributed in the stacked patch cavity. It implies that the stacked-patch contributes to most of the L-band radiation, while the slot ring just serves as a leakage window.

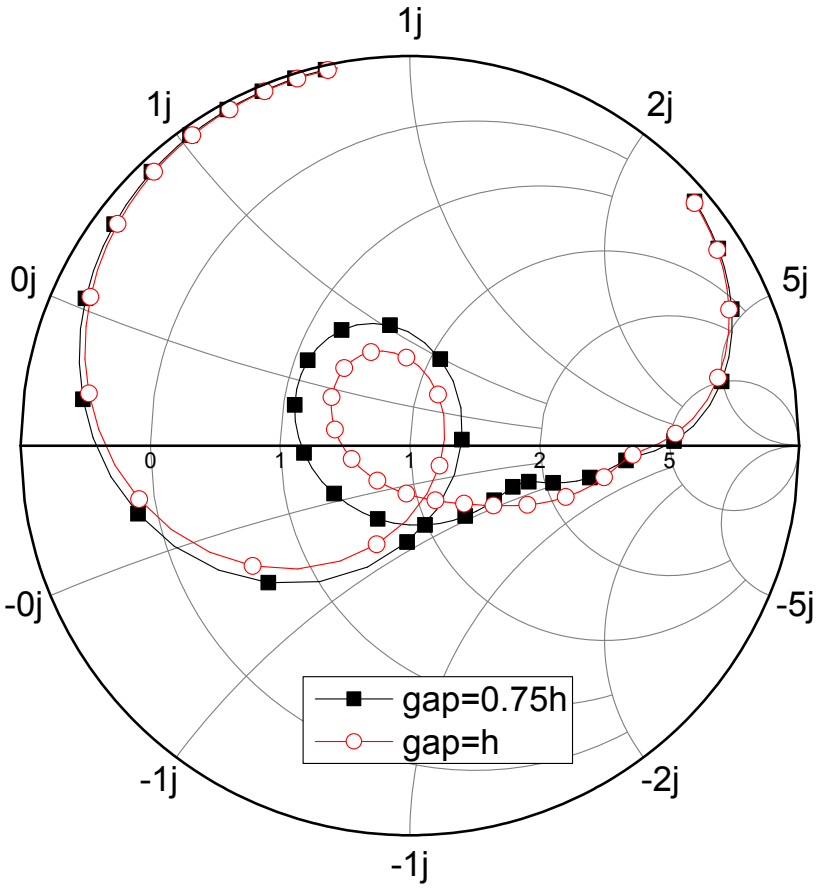

(a) Smith chart

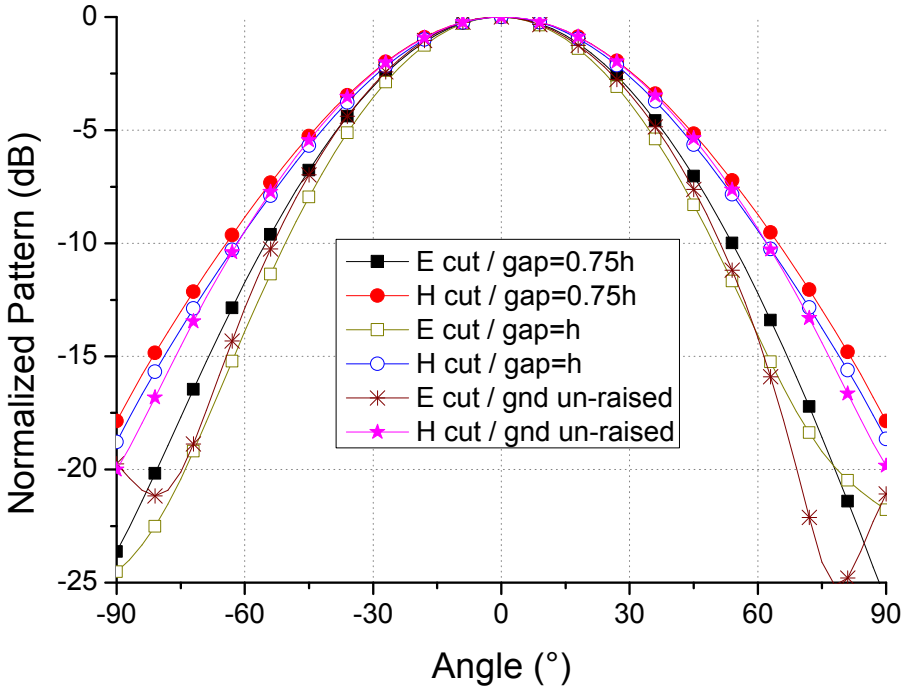

(b) Radiation patterns

Fig.5 - 9 Effect of gap width on the lower band patch's performance

Note: *h* refers to the L band element profile

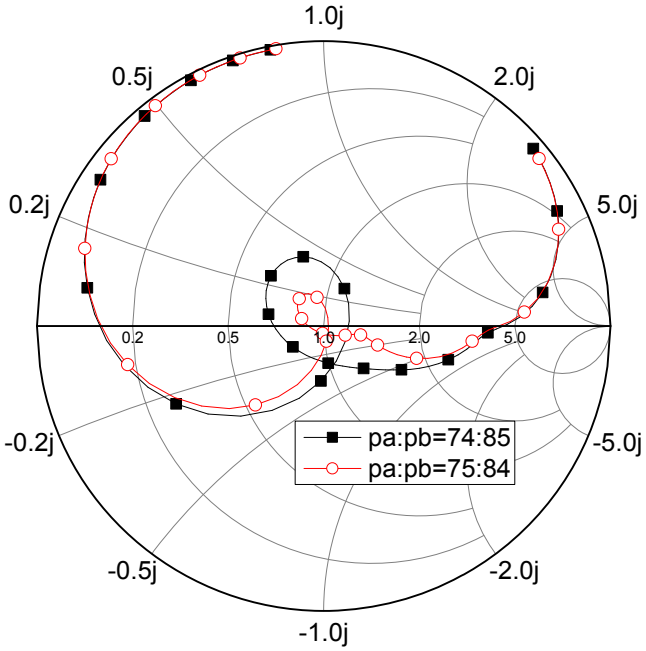

Fig.5 - 10 Impedance matching and the upper-to-lower patch edge ratio of stacked-patch

Note: *pa* and *pb* refer to the driven and the parasitic patch edge length.

A parametric study is carried out to investigate the effect of gap (ring width) on patch performance, and the results are shown in Fig.5-9. Decreasing the gap width will increases the resonant loop circumference, which means that the patch impedance changes rapidly with frequency, and it will also raise the in-band ripple factor. The radiation patterns are insensitive to gap width, and remain stable when the gap is wider than the lower-band element thickness. This result can be explained as radiation leakage: the radiation energy is less likely to leak out from the enclosed stacked-patch cavity with the decreasing gap width, leading to a higher Q factor. A wider gap will surely reduce the disturbance caused by the raised ground. However, the maximum gap width is also limited by the placement of C-band elements. Hence, as a trade off, the lower-band element thickness *h* is finally used as the gap width.

The upper-to-lower patch edge ratio and element height of lower-band stacked-patch can also be used for impedance matching, as shown in Fig.5-10.

5.3.3 Unit-Cell Design

The L/C overlapped unit cell shown in Fig.5-4(a) is a crucial part of the full array design. The unit cell consists of four substrates and two air layers, which are marked as layer #1 to #6 from bottom to top, as shown in Fig.5-11. The L-band driven patch and the parasitic patch are located at the top side of #2 substrate and the bottom side of #4 substrate, respectively. The L-band driven patch is excited by two proximity-coupled feeds, where the microstrip feed lines are located at the top surface of #1 substrate. To reduce spurious radiation [108], balanced open-ended stubs are used on the microstrip feed lines which also provide impedance matching. The feed structures are placed orthogonally to realize dual-linear polarization in L band.

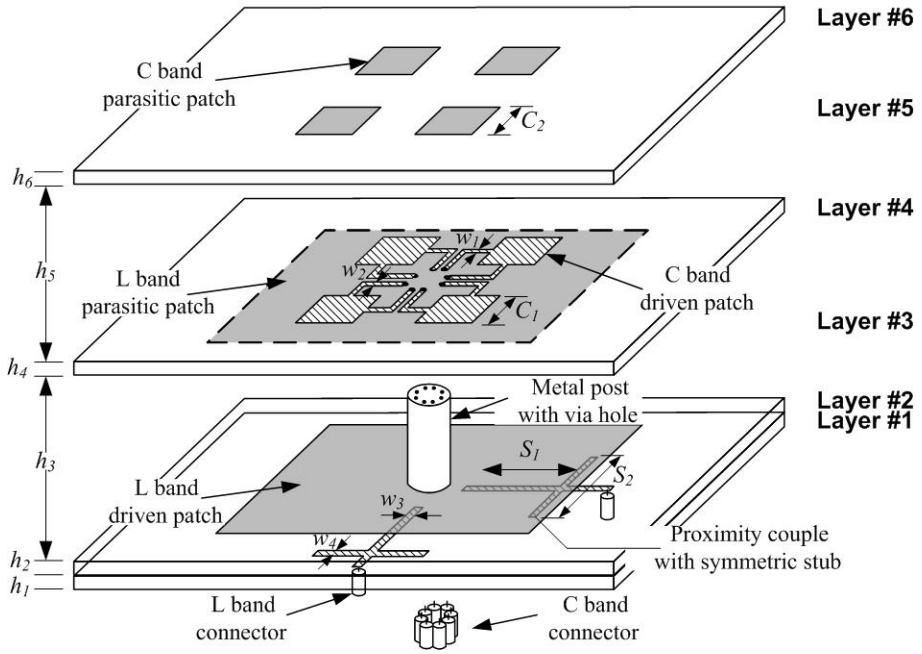

Fig.5 - 11 Exploded view of L/C overlapped stacked-patch unit cell

The C-band driven and parasitic patches are located on the topside of #4 substrate and bottom side of #6 substrates, respectively, where the L band upper patch serves as the ground for C-band driven patch. The 2 × 2 configured C-band elements are designed with an element

spacing of 37.5mm. They use orthogonally coplanar feed at the adjacent edges to achieve dual linear polarization, as shown in Fig.5-11. Each element has independent feeding to realize two-dimensional scanning capability.

In the unit cell, C-band patch feeding passes vertically through the L band cavity, where the vertical transition structures act as shorting pin. Because the L band stacked patch works in dominant TM_{01} mode, the patch center has the E-field null for both H and V polarization; so this point is not sensitive to the shorting pin. Hence, the C-band coplanar feed lines are bent inward towards the L-band patch center, and fed by coaxial lines through the L-band cavity.

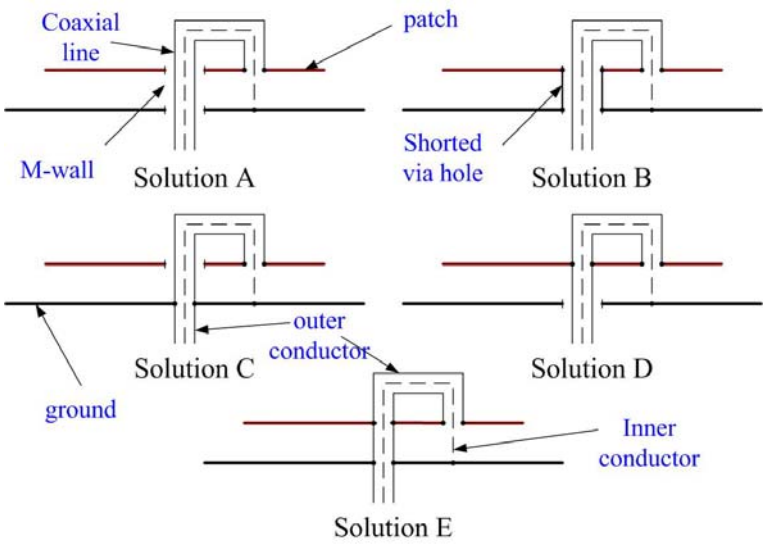

Fig.5 - 12 Existing solutions for vertical coaxial line feeding through the patch cavity [164]

A detailed study on how to get the coaxial lines through the lower-band patch cavity is given in [164], which presents five possible solutions as shown in Fig.5-12. Because microstrip is employed for C-band patch feeding, solutions A to C are excluded, because the opened slot ring on the upper patch will cut off the ground of microstrip feed line.

The solution D and E are implemented in the design and similar port performances are

obtained from the computed results shown in Fig.5-13. The solution E is finally chosen for reliability consideration. A metal post with eight via holes is employed to allow the coaxial feed lines to pass through (see Fig.5-11). The metal post also provides mechanical strength to the overall unit cell structure.

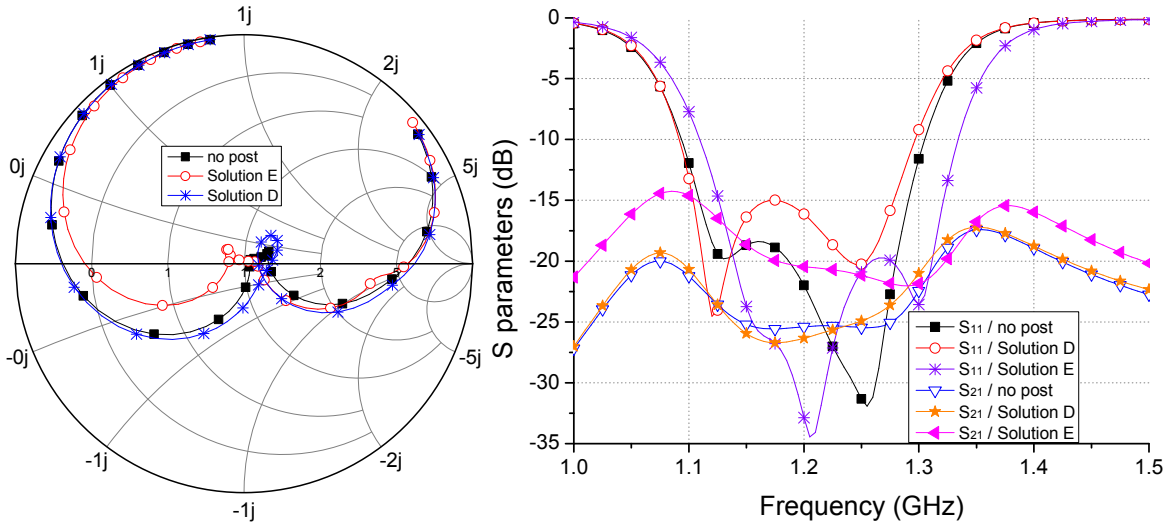

(a) Smith chart (b) S parameters

Fig.5 - 13 Solution comparison (no metal post, solution D & E)

The selection of in-stock laminates for each layer is made as described below:

1) #1 and #2 layers creates L-band driven patch cavity. Because lower frequency is less sensitive to the substrate dielectric constant, a 2mm thick low cost microwave substrate is employed. Its permittivity is 2.55 and loss tangent is 0.0015.

2) #4 layer is for the C-band driven patch cavity and feed line. 0.762mm thick Rogers RO 5880 is used due to its reliability.

3) #6 layer contains C-band parasitic patches. This layer is very thin and isolated from C-band driven patch by a thick air layer, the structure is not sensitive to the superstrate dielectric constant. A low-cost laminate with a thickness of 0.8mm is used. Its dielectric constant and loss tangent are 2.6 and 0.002, respectively.

4) The remaining two layers #3 and #5 are air-filled, where nylon posts are used to keep the desired spacing.

The designs of stacked patches in L- and C-band are similar to the designs presented in Chapter 3 and Chapter 4, and thus are not discussed here. The parameters for L/C overlapped unit cell are optimized by Ansoft HFSS 13.0, and are listed in Table 5-4. For parameter definition, see Fig.5-11.

Table 5 - 4 Parameters of L/C overlapped unit cell (Unit: mm)

Parameters	Value	Parameters	Value	Parameters	Value
L_1	74	L_2	85	C_1	19
C_2	19.8	d	12	W_1	2.5
W_2	2	W_3	5	W_4	5
S_1	23	S_2	40	h_1	2
h_2	2	h_3	26	h_4	0.762
h_5	4	h_6	0.8		

5.3.4 Measurements and Results

A unit cell antenna is fabricated to verify the L/C dual-band overlapped stacked patch design, and shown in Fig.5-14. To expedite the design process, all the fabrication was done using hand-held cutting tools. The port parameters are measured using an Agilent 8720D vector network analyzer, while the radiation patterns are obtained in AusAMF indoor near-field anechoic chamber.

A. L-Band:

Fig.5-15 presents the measured and simulated L-band port responses. Due to the structural symmetry, only the results of one port are shown for clarity. The measured center frequency for L-band element is 1.245 GHz, with the $|S_{11}| \leq$ -10 dB impedance bandwidth of

(a) Top view (b) Bottom view

(c) Side view

Fig.5 - 14 Fabricated L/C band overlapped stacked patch unit cell

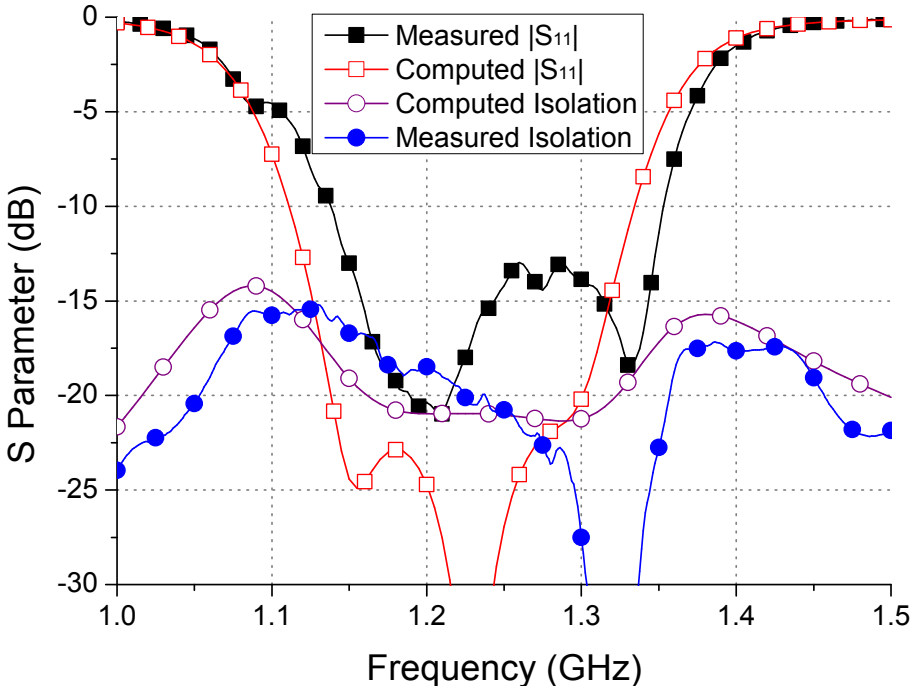

Fig.5 - 15 Measured scattering parameters of one port in L band

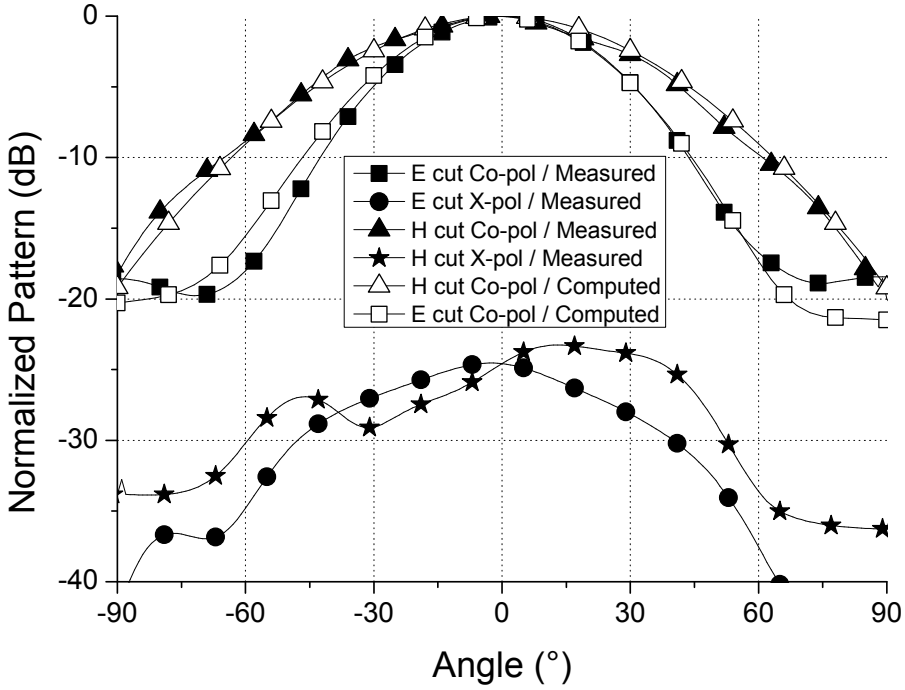

Fig.5 - 16 Measured radiation patterns for L-band element

219 MHz, namely 17.6 %, with measured in-band port isolation level of better than 15 dB.

It is noted that the measured values shift slightly to the higher frequency (approximately 20MHz), which is 1.6% deviation from the center frequency. Nevertheless, the measured return losses agree well with the simulated curves. The in-band ripples are also a bit higher. These inaccuracies are attributed to the fabrication tolerance and the laminates' parameters.

The measured radiation patterns are shown in Fig.5-16. Only the patterns for vertical polarized port excitation are given due to the symmetry. The measured patterns agree very well with the computed results. The calibrated gain at the center frequency is 9.9 dB. The cross-polarization level in the boresight direction is better than -23 dB, which can be further improved by 'pair-wise anti-feed' technique in array configuration [134-136].

B. C-Band:

Fig.5-17 presents the measured and simulated port responses for one C-band element.

The measured results also agree quite well with the HFSS prediction, suggesting that the vertical transition solution is successfully implemented. The measured center frequency of C-band element is 5.275 GHz, with |S11| ≤ -10 dB impedance bandwidth of 790 MHz, or 15 %. The in-band port isolation level is better than 17 dB.

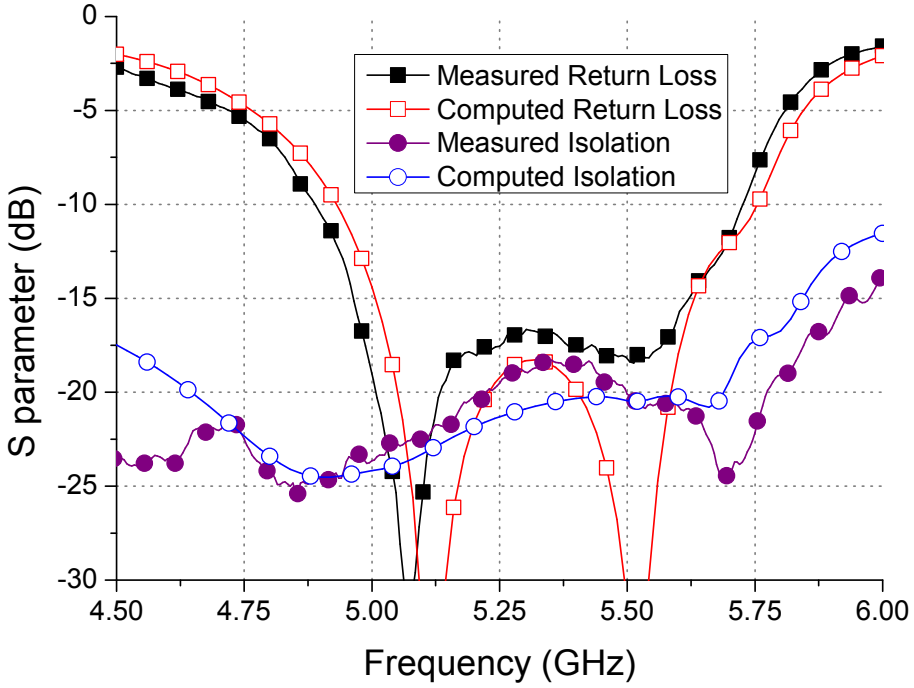

Fig.5 - 17 Measured ports responses of one element in C-band

Measured radiation patterns of C-band 2 × 2 elements for vertical polarization port are shown in Fig.5-18. The measured results show good agreement with the computed results. The calibrated gain for 2 × 2 array at 5.275 GHz is 13.4 dB. The cross-polarization levels for E- and H-cuts are better than -30 dB and -25 dB, respectively in the boresignt direction. It should be noted that H-cut cross-polarization level is a bit worse, which may be caused by the asymmetry introduced during the fabrication by hand. The cross-polarization level is expected to improve by enlarging the aperture size.

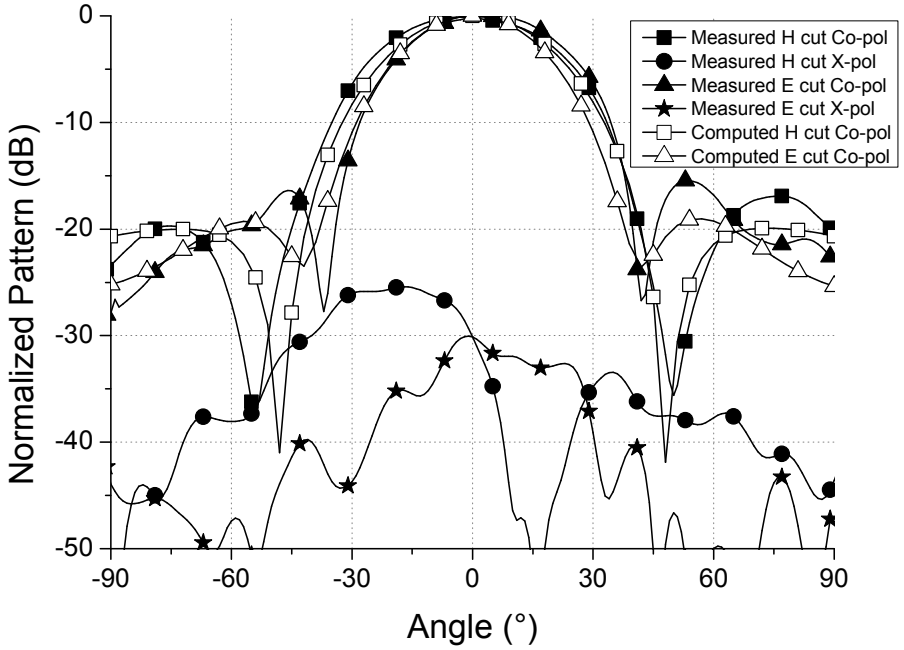

Fig.5 - 18 Measured radiation patterns for C-band array element

5.3.5 Summary

An L/C band overlapped unit cell is designed, fabricated and tested. This preliminary study verifies the design methodology, fabrication technique and the bandwidth performance in the lower-band of overlapped structure DBDP-SA array. The measured results are summarized in Table 5-5.

Table 5 - 5 Measured results for the overlapped L/C band unit cell

Specifications	L band (1.25GHz)		C band (5.3GHz)	
	Target	Measured	Target	Measured
BW (MHz)	200	219	600	790
BW (%)	16	17.6	11.3	15
Polarization	Dual linear	Dual linear	Dual linear	Dual linear
Isolation (dB)	15	15	15	17
X-polar (dB)	-20	-23	-20	-25

5.4 Sandwiched Unit-Cell

A novel sandwiched stacked-patch DBDP structure is proposed based on the partial-

perforated stacked patch shown in Fig.5-4(b). The higher-band stacked patches are sandwiched between the lower-band driven patch and parasitic patches, so that only the parasitic patch should be perforated to avoid shielding of the radiation of higher-band elements. The bandwidth in the lower-band is thus improved when compared with the classical fully perforated stacked patch, as explained in Section 5.2. Moreover, the overall array profile is just equal to the lower-band element thickness, as the higher band is contained within the lower-band element.

Before designing the full scale array, an L/C sandwiched stacked patch DBDP unit cell is fabricated to verify bandwidth improvement for the lower-band element and the feasibility of this structure.

5.4.1 Design Specifications

As a preliminary study on the proposed novel sandwiched stacked patch structure, the unit cell focus mainly on the bandwidth improvement in the lower band. The requirements of the unit cell are listed in Table 5-6.

Table 5 - 6 Requirements of L/C DBDP sandwiched stacked patch array

Specifications	L-band	C-band
Center frequency (GHz)	1.25	5.5
Bandwidth (MHz)	150	600
Polarization	Dual-linear	Dual-linear
Cross-polarization (dB)	-25	-25
Polarization isolation (dB)	25	25
Scan range	±25° in two dimensions	±25° in two dimensions

5.4.2 Unit-Cell Design

This section presents the analysis of a sandwiched DBDP unit cell, while the array

configuration of sandwiched DBDP structure will be introduced Section 5.5.

The unit cell configuration of L/C sandwiched DBDP array is the same as that of the overlapped structure shown in Fig.5-5 and Fig.5-7. The L/C sandwiched DBDP unit cell consists of 1 × 1 L-band element and 2 × 2 C-band elements, as shown in Fig.5-19.

A. L-band:

The partial-perforated stacked patch is employed as L-band element, as shown in Fig. 5-27. The L band driven and parasitic patches are located on the top of #1 substrate and bottom of #6 superstrate, respectively. The L-band parasitic patch, which is placed at a distance *h5* on top of the C-band elements, is perforated to avoid C-band radiation blockage.

A dual probe feed is adopted to excite the L-band element due to its simplicity and reliability. The main aim here is to verify bandwidth enhancement and fabrication technique for the design of sandwiched unit cell.

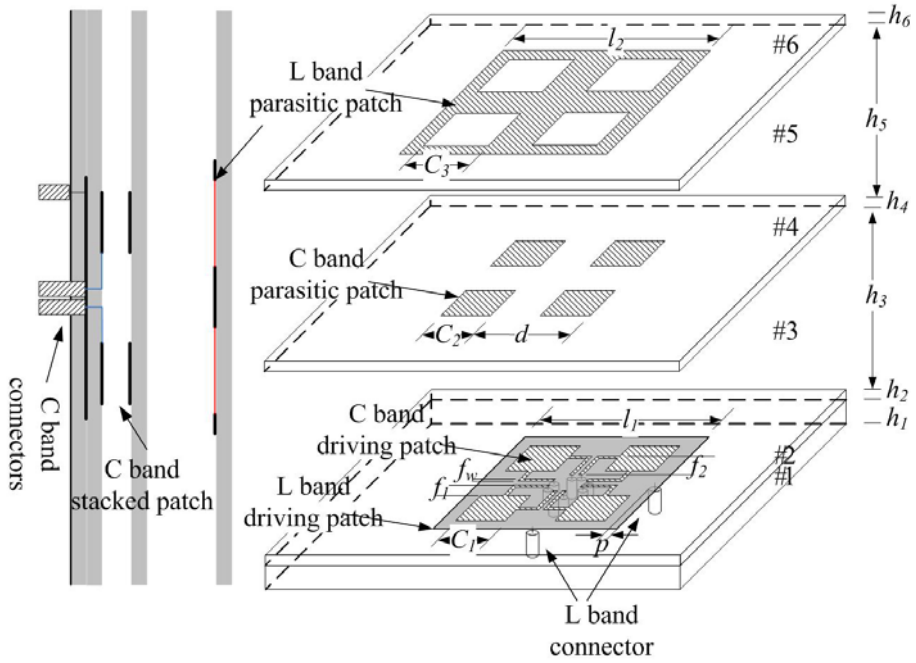

Fig.5 - 19 L/C band single layer perforated stacked-patch unit cell

B. C-band:

The C band elements in sandwiched DBDP unit cell employs the same design as the C-band elements in overlapped DBDP unit cell. A coplanar feed is employed in which the feed lines are bent inwards towards the center of the L-band patch. The C-band driven patches and coplanar feed lines are etched on the top surface of #2 substrate using copper, and the parasitic patches are located at the bottom side of #4 superstrate, as shown in Fig.5-19. The C-band stacked patches are thus sandwiched inside the L-band cavity.

Because the C-band driven patches are situated on top of L-band driven patch, via holes are used to allow feeding through L-band driven patch cavity. Hence, the vertical feeding is much simpler than that of overlapped stacked patch, because the metal post is not needed.

C. Dual-Band Embedding:

In the overlapped DBDP structure, the fields in the higher- and lower-band are completely isolated by the lower-band parasitic patch, *i.e.*, elements in overlapped DBDP structure will not suffer from the inter-band coupling. On the other hand, in L/C sandwiched stacked-patch DBDP embedding structure, the L and C inter-band isolation performance should be analyzed, because L and C cavities are not physically separated like that of overlapped DBDP structure.

A numerical study is carried out to investigate the effect of dual-band embedding on port parameters using HFSS 13.0 and the results are shown in Fig.5-20. Several points can be concluded:

1) The embedding of C band elements into the L-band cavity has almost no effect on the L band port response over the L band frequency range. This is probably because the C band element has much smaller dimension than the half wavelength of L band, making them

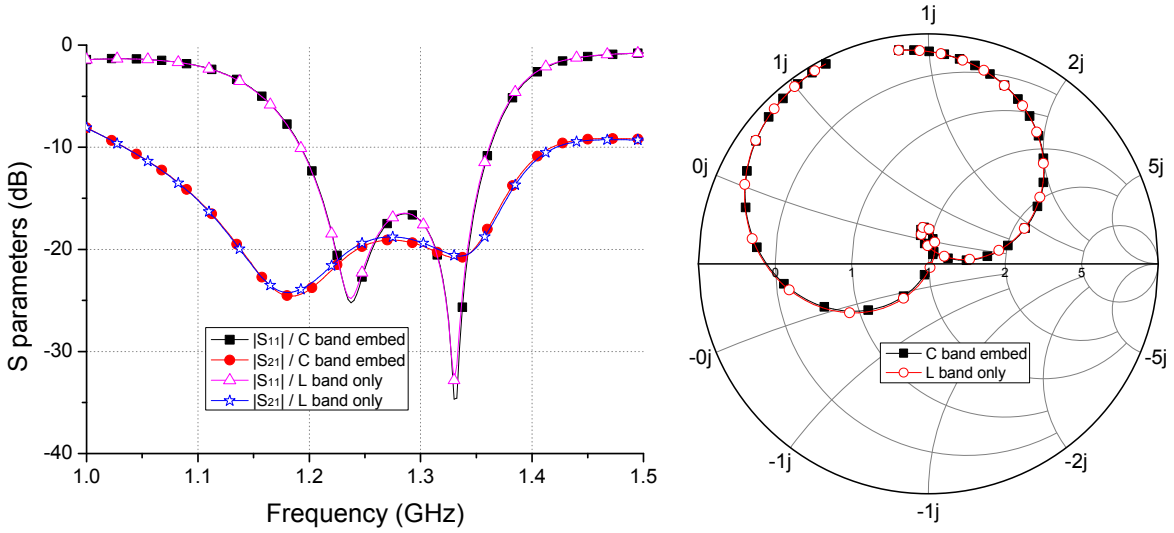

(a) Port response (b) Smith chart

Fig.5 - 20 Effects on L band element port responses of L/C-band elements embedding

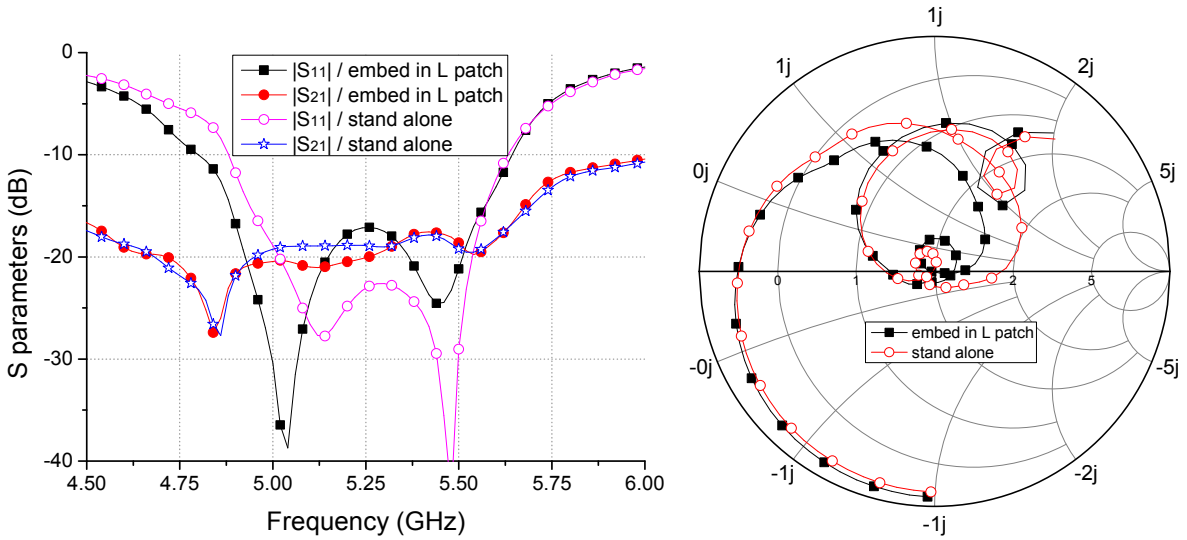

(a) Port response (b) Smith chart

Fig.5 - 21 Effects on C band element port responses of L/C-band elements embedding

difficult to be excited (coupled) in L band frequency;

2) The $|S_{21}|$ of the L-band partial-perforated stacked patch is slightly affected due to the introduction of C-band elements, as shown in Fig.5-21. However, slightly higher in-band ripples are noted, *i.e.*, from -22 dB to -16 dB.

Overall, the L- and C-band elements are sufficiently decoupled which gives great flexibility in the design, because the elements can be designed independently and packaged

together to form a unit cell without seriously degrading the performance of the dual band element. This greatly simplifies the design complexity and reduces the computational load.

Material Parameters:

In stock materials are used for fabrication, as listed below:

1) Due to lower operation frequency, layer #1 and #2 use a low-cost laminate with a permittivity of 2.55, loss tangent of 0.0015 and thickness of 2 mm.
2) Layer #4 (C-band substrate) uses 0.762 mm thick Rogers RO 5880 board with permittivity of 2.2 and loss tangent of 0.0009.
3) Layer #6 is a superstrate of the unit cell, which has a small effect on the unit cell's port response. A low-cost laminate with permittivity of 2.6, loss tangent of 0.002 and thickness of 0.8 mm is used.
4) The remaining layers are filled with the air, and supported by nylon spacers.

All the parameters of unit cell are optimized using Ansoft HFSS 13.0, and listed in Table 5-7. For parameter definitions, see Fig.5-19.

Table 5 - 7 Optimized parameters of L/C sandwiched DBDP unit cell (Unit: mm)

Parameters	Values	Parameters	Values	Parameters	Values
l_1	74	l_2	76	d	37.5
C_1	19	C_2	20	C_3	28
f_1	8.35	f_2	14.5	f_w	2
h_1	4	h_2	0.762	h_3	4
h_4	0.8	h_5	14	h_6	0.8
p	0				

5.4.3 Measurements and Results

A unit cell antenna is fabricated to verify the L/C dual-band sandwiched stacked patch

DBDP design, and its photos are shown in Fig.5-22. To expedite the design process, all the fabrication was done using hand-held cutting tools. The port parameters are measured using an Agilent 8720D vector network analyzer, while the radiation patterns are obtained in AusAMF indoor near-field anechoic chamber.

A. L-band:

The L-band measured port responses are shown in Fig.5-23. Because of the symmetric structure, only port responses of one element are presented. From the measured results, VSWR ≤ 2 bandwidth extends from 1191 MHz to 1357 MHz, *i.e.* 166 MHz or 13.0 %, with in-band isolation level of better than -19 dB. Overall, the measured VSWR and isolation level agree well with the simulation, except for the slightly higher in-band ripples, which may be attributed to the fabrication tolerance.

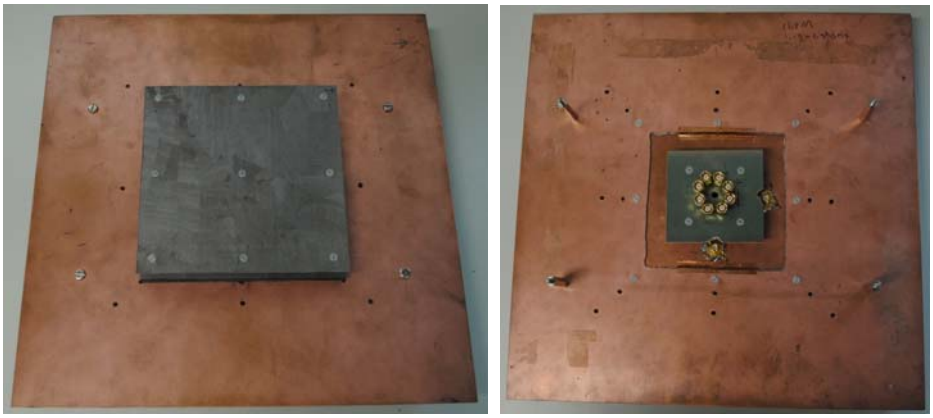

(a) Top view (b) Bottom view

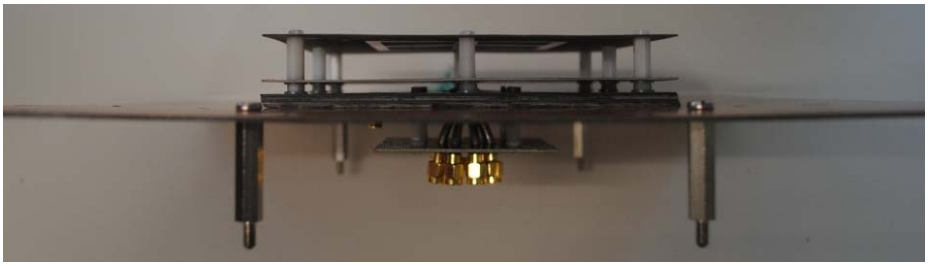

(c) Side view

Fig.5 - 22 Photos of the L/C band sandwiched stacked patch DBDP unit cell

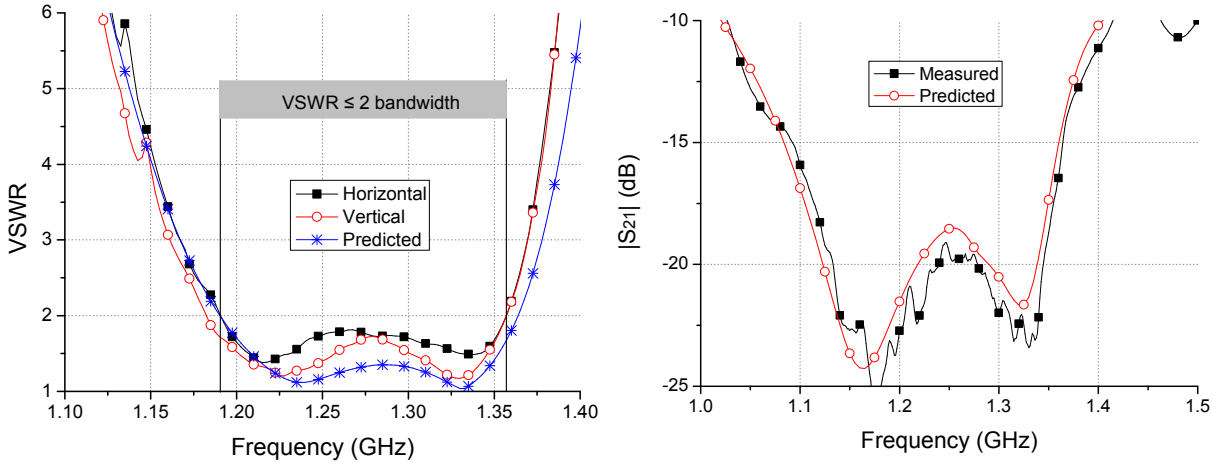

(a) VSWR (b) Isolation

Fig.5 - 23 Measured L-band port responses

Fig.5-24 shows the measured radiation patterns of the L-band element. The measured radiation patterns agree well with the predicted curves. The calibrated gain at the center frequency (1.25GHz) is 9.7dBi, with cross-polarization level of better than -23dB in boresight direction.

B. C-band:

The measured C band port responses are shown in Fig.5-25. The measured VSWR ≤ 2

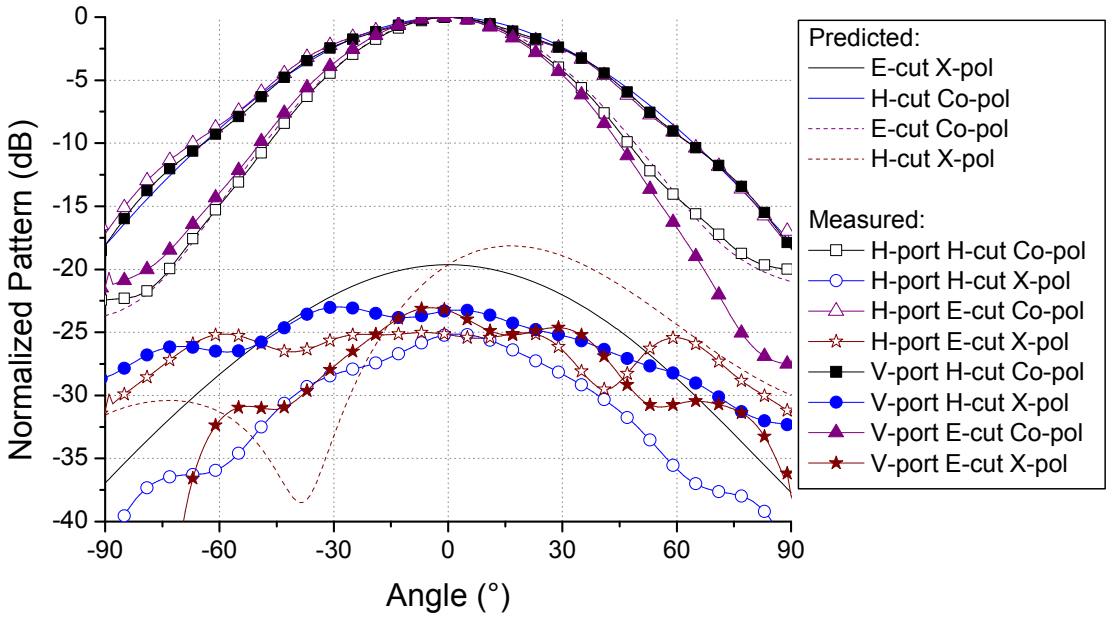

Fig.5 - 24 Measured L-band radiation patterns

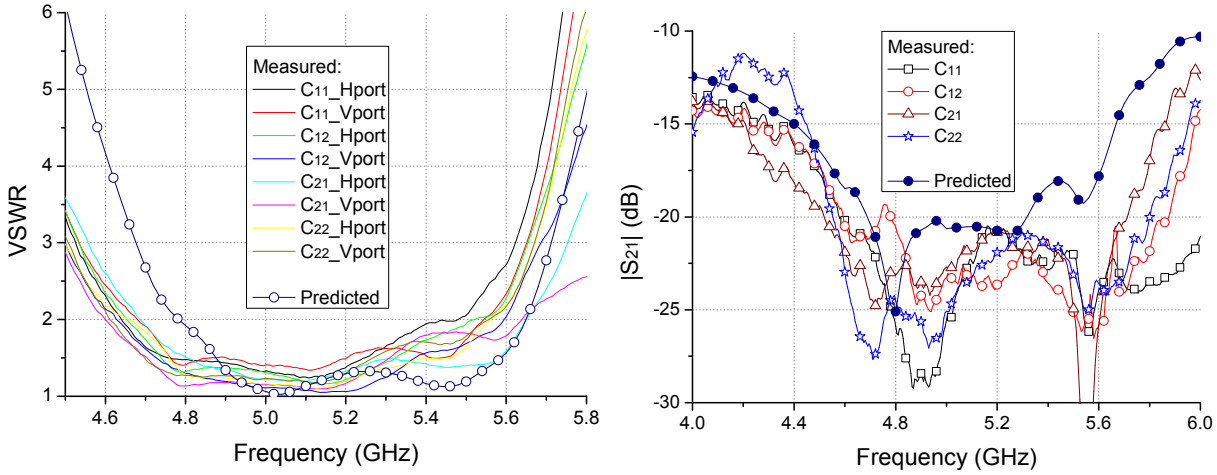

(a) VSWR (b) Isolation

Fig.5 - 25 Measured C-band port responses

bandwidth, refers to the intersection of all curves, is 802 MHz, from 4683 MHz to 5485 MHz, or 15.8 %. The measured in-band isolation level is better than 21 dB.

The measured VSWR curves are shifted slightly towards the lower-frequency, and in-band ripples are noted to be a bit higher than the predicted ones, which can be attributed to the fabrication tolerance.

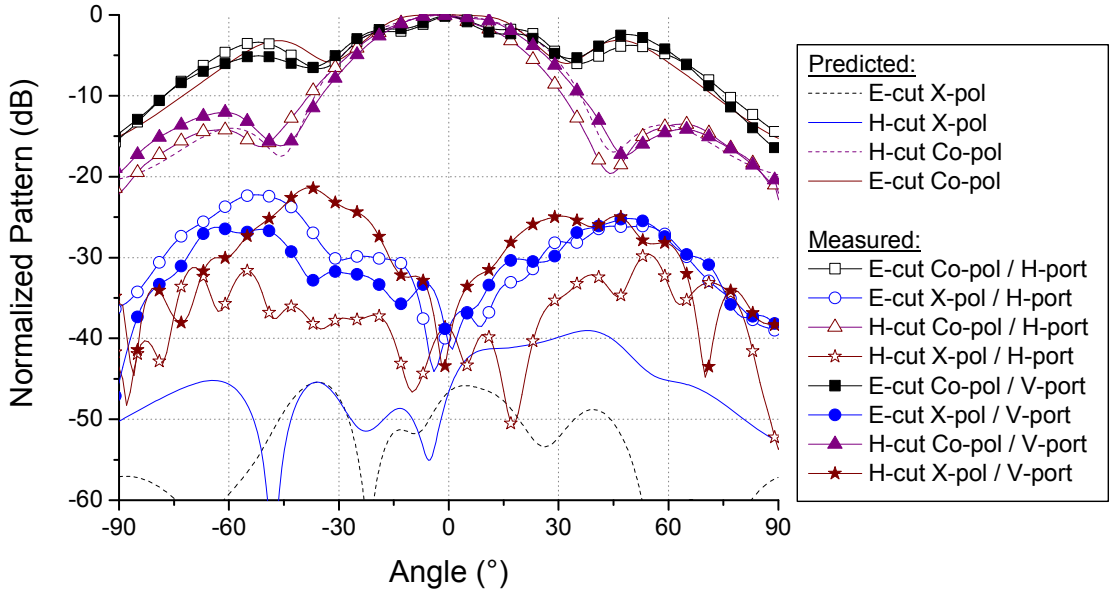

Fig.5 - 26 Measured C-band radiation patterns

The measured radiation patterns of C-band 2 × 2 elements are shown in Fig.5-26. The measured patterns agree well with the predicted results, with cross-polarization level of better than -30dB in boresight direction. The calibrated gain at 5.3 GHz is 10.3 dBi.

It should be noted that the E-plane radiation patterns have a higher first side lobe level of about -5 dB, which reduces the gain by about 3 dB when compared to the 13.4 dB gain of a similar 2 × 2 C-band elements in the overlapped DBDP unit cell.

The ground discontinuity of C-band elements is the main reason for higher side lobe levels: C-band elements situate on the L-band driven patch and the latter one also serves as the ground of C band patch. Limited by the L-band patch size, the C-band elements locate

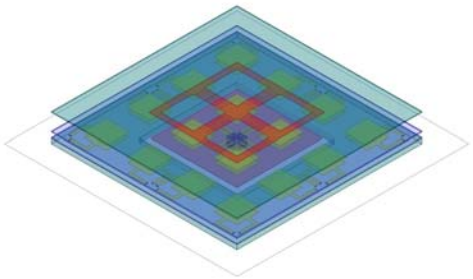

(a) Perspective view

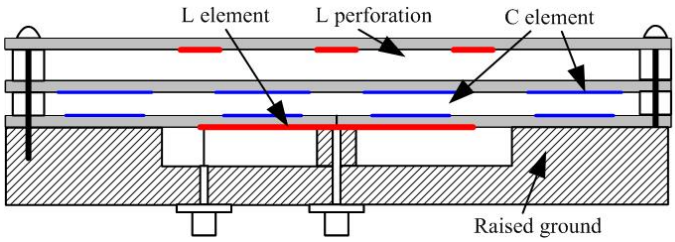

(b) Side view

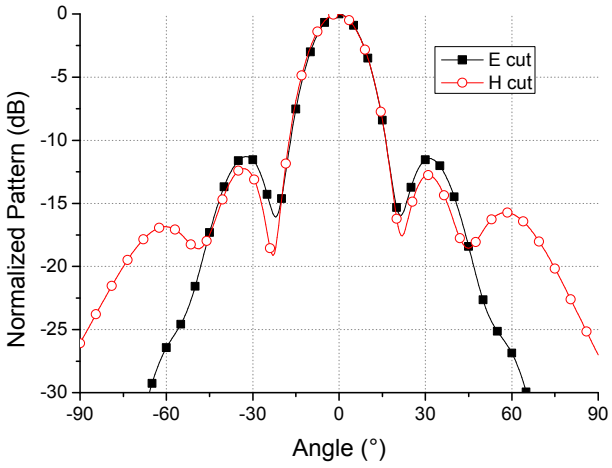

(c) Computed result

Fig.5 - 27 Raised ground and the improved radiation patterns

very closely to the edge of L driven patch, and the asymmetric ground degrades the side lobe performances.

This problem can be solved in sandwiched DBDP full-array by raising the ground surrounding the unit cell at the same level with the L-band driven patch, as shown in Fig.5-27 (b). By doing so, a large quasi-symmetric ground (except for small gaps) is formed for C-band elements in unit cell. The predicted results from HFSS 13.0 shown in Fig.5-27(c), indicate very good quality radiation patterns with much lower side lobe levels, i.e. ≈ -12 dB.

5.4.4 Summary

A preliminary study is carried out on the sandwiched stacked patch DBDP array. With the objective of increasing the lower-band element bandwidth, a small L/C sandwiched DBDP unit cell is designed, fabricated and measured. The measured specifications are summarized in Table 5-8.

Table 5 - 8 Measured specifications of L/Cdual band sandwiched stacked-patch unit cell

Specifications	L band (1.25GHz)		C band (5.3GHz)	
	Target	Measured	Target	Measured
BW (MHz)	125	166	600	802
BW (%)	10	13	11.3	15.8
Polarization	Dual linear	Dual linear	Dual linear	Dual linear
Isolation (dB)	15	19	15	21
X-pol (dB)	-20	-23	-20	-30

Overall, the fabricated sandwiched DBDP unit cell has successfully achieved the desired dual-band performance specifications. A large bandwidth is also obtained in both bands. The measured results agree well with the predicted curves, and consistent C-band elements port responses are observed, thus validating the feasibility of the proposed structure.

5.5 Sandwiched DBDP Full-Array

5.5.1 Performance Specifications

The sandwiched unit-cell structure presented in the previous section verifies the feasibility of the proposed structure. An L/C sandwiched sub-array is then designed subsequently. The sub-array has a large scale, and more complete specifications, as listed in Table 5-9 below.

Table 5 - 9 Requirements of the L/C DBDP sandwiched stacked-patch array

Specifications	L-band	C-band
Center frequency (GHz)	1.25	5.5
Bandwidth (MHz)	150	600
Polarization	Dual-linear	Dual-linear
Cross-polarization (dB)	-25	-25
Polarization isolation (dB)	25	25
Scan range	±25° in two dimensions	±25° in two dimensions

Based on the experience of the previous unit-cell design, the sandwiched and the overlapped DBDP structures are compared as follow:

1) The overlapped and the sandwiched DBDP structure can support dual-band array operation with a frequency ratio of less than 4:1. In DBDP array with large frequency ratio, the lower-band patch should support a large number of higher-band elements, which adds design complexity in the vertical feeding structure.
2) The increased lower-band bandwidth of the overlapped DBDP structure, as presented in Chapter 2, was achieved by reserving additional height for higher-band elements, resulting in a thicker overall antenna thickness.
3) The sandwiched stacked-patch DBDP structure is a trade-off solution between the overlapped structure and the perforated stacked patch. Its lower-band bandwidth is slightly

narrower than the overlapped stacked-patch but wider than the perforated structure, its profile is the same as that of the perforated patch but is thinner than the overlapped structure and it has a moderate structural complexity as compared to the perforated patch and the overlapped structure.

5.5.2 Full-Array Consideration

The sandwiched stacked patch is employed to design L/C DBDP-SA full array. In the sandwiched DBDP full array design, the following aspects are considered:

1) Verification of the radiation pattern performance in full array. Since higher 1st side lobes are observed in the unit cell, raising the ground in L-band element gaps to suppress the side lobes needs validation.
2) Assessing the feasibility of the sandwiched stacked-patch structure in full array configuration.
3) Verifying the scan capability of the sandwiched DBDP full-array structure, which was not tested in the unit cell due to the limited element numbers.
4) Isolation improvement in the lower-band.

5.5.3 Array Design

A. Array Configuration:

The designed sandwiched L/C DBDP-SA sub-array consists of 4 × 1 L-band elements and 16 × 6 C-band elements, as shown in Fig.5-28. Due to the L-band element positioning, the proposed sub-array is not symmetric. The reasons are:

1) In the sub-array design, every 2 × 2 C-band elements (in/out the unit cell) forms the basic periodical structure to keep the C-band element uniformly distributed, it cannot be further

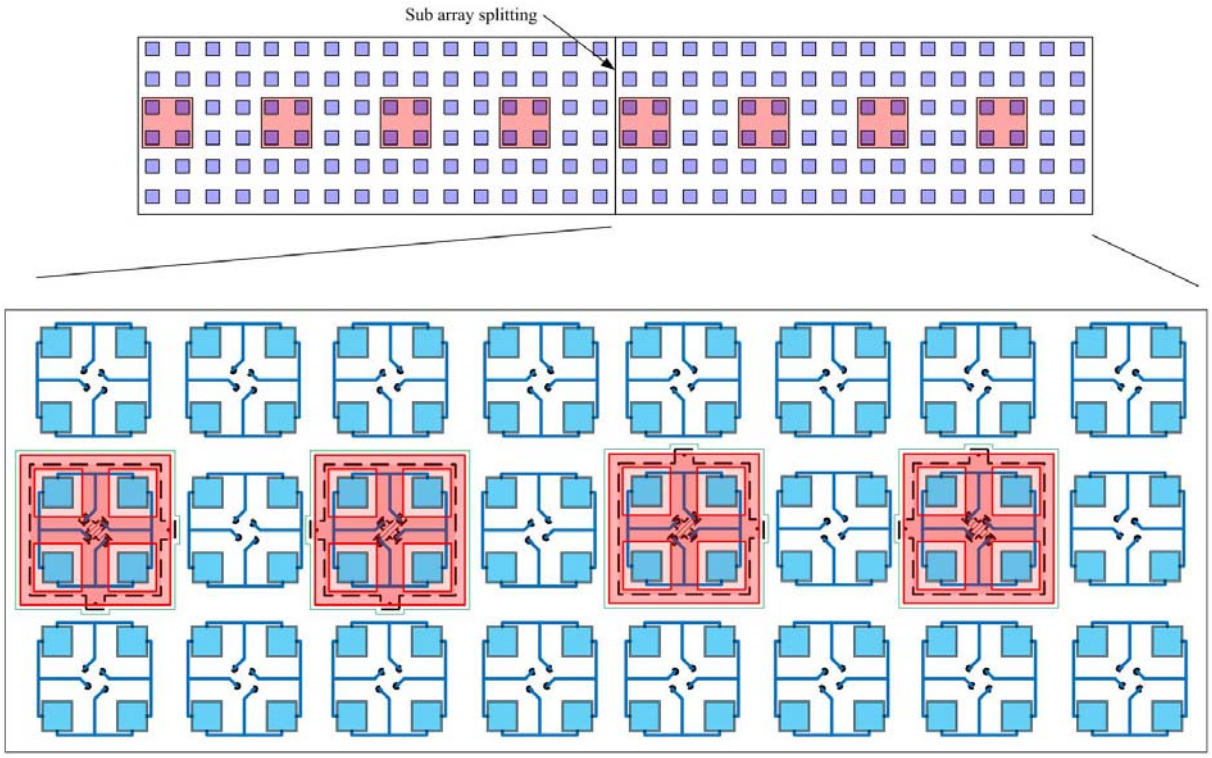

Fig.5 - 28 Schematic layout of the sandwiched stacked-patch full array

divided in the sub-array design, as will be discussed later on.

2) Because L- and C-band elements have the same scan requirement and element spacing (in wavelength), the L- and C-band element numbers should scale to correspond to the frequency ratio.

Hence, to extend the sub-array design, it is splitted as shown in Fig.5-28, forming an asymmetric structure. The asymmetric aperture has minor effect on the C-band radiation patterns because of electrically large scale aperture but noticeable effects on the L-band radiation patterns of the sub-array due to the limited element numbers. However, these effects will be eliminated by increasing aperture size, which is the common case of a SAR antenna [7-10, 32-43].

The L/C sandwiched DBDP sub-array is constructed using 1) an aluminum back plate

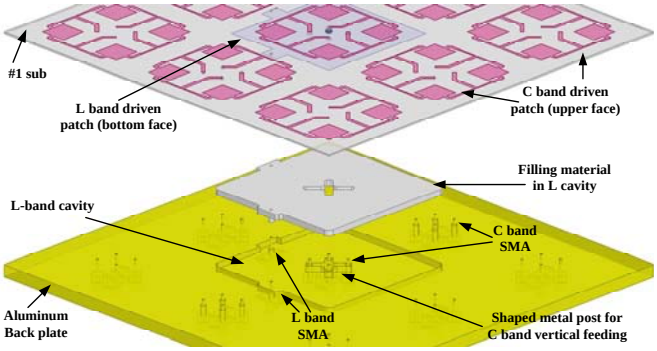

(a) Exploded view of L-band driven patch (local)

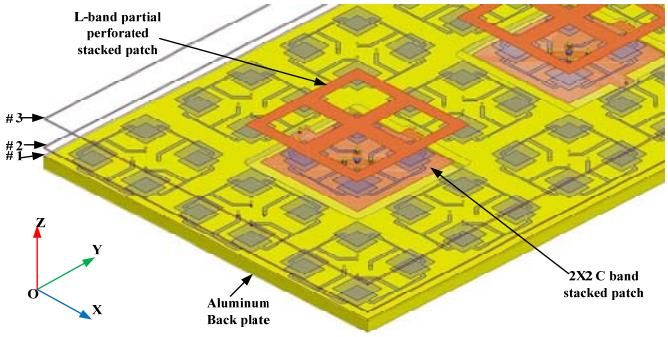

(b) Perspective view (local)

Fig.5 - 29 Configuration of L/C single layer perforated stacked patch full array

(with cut-in L-band cavity) 2) L-band lower cavity filling materials 3) three substrates, and 4) two air filled layers, as shown in Fig.5-29.

B. L-band:

Similar to the sandwiched unit cell design, a partial perforated stacked-patch is employed for L-band element. L-band driven patches are etched on the bottom side of layer #1 using copper, while the parasitic patches are located at the bottom side of layer #3, as shown in Fig.5-29. The driven patch is not located on the filling material in the design because it also serves as the C-band elements' ground, and C-band element is more sensitive to the fabrication tolerances than L band.

The L-band elements are equally spaced with a distance that is decided by two conditions:

1) grating lobe limitation, as can be estimated using eq.5-2:

$$d \le \lambda_{\mathrm{H}}/(1+\sin\theta) \le 156\mathrm{mm} \tag{5-2}$$

where λ_H is the free space wavelength at 1.35GHz, and θ is the scan range (25°);

2) To ease the L- and C-band element embedding, the L/C band element distance ratio is set to an integer number. In this design, $d_L / d_C = 4$ is employed, which corresponds to 144mm for L band element distance (d_C = 36mm, will be introduced).

Hence, d = 144mm is finally adopted as L-band element spacing, as this value satisfies both the conditions.

Similar to the unit cell design, a dual probe-feed is employed for L-band element due to its simplicity and reliability. Although the dual-probe fed patch suffers from poor polarization isolation, it can be improved by adopting perturbation, such as etching an isolation slot on the driven patch [160, 161]. Similar to the magnetic wall isolation slot used in Section 4.3, a cross-shape metal post is employed here as an electric wall perturbation in the L-band cavity, as shown in Fig.5-29(a). By carefully tuning the length of the two arms (l_1 and l_2), the cross talk between orthogonal polarized ports will be eliminated, and hence isolation level can be improved. The results of parametric study to investigate the effects of l_1 and l_2 on isolation are shown in Fig.5-30.

The shaped metal post perturbation will also increase the element cross polarization level. The ‘pair-wise anti-phase’ feeding method [134-136] is thus employed in L band to ensure good array cross-polarization performance, as shown in Fig.5-28.

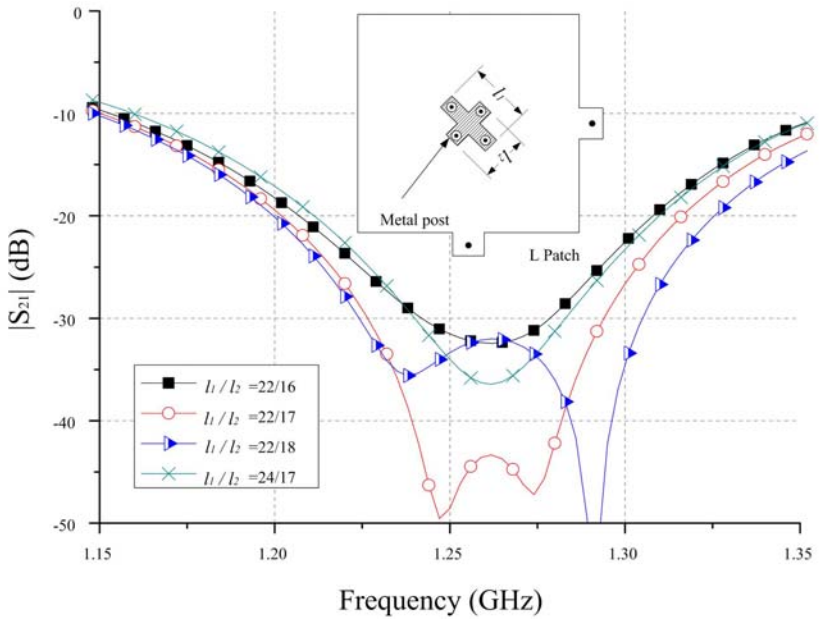

Fig.5 - 30 The effects of metal post shape on isolation (l_1 and l_2 are in mm)

C. C-band:

The square stacked patch with coplanar fed structure is employed for C-band elements. A close-up view of Fig.5-28 is provided in Fig.5-31. The C-band driven patch and the microstrip feed lines are placed on the top side of layer #1, while the parasitic patches are etched on the bottom side of layer #2. The C-band stacked patch is designed according to the method introduced in [137], and the parameters are optimized by Ansoft HFSS 13.0. Square distribution is employed for C band to overlap with the L-band square driven patch. The element distance is designed for 25° scan requirement using eq.5-3:

$$d_c=\lambda_H/(1+\sin\theta)=36\text{mm} \tag{5-3}$$

where λ_H is the free space wavelength at 5.8 GHz.

The feed method for C-band elements, in general, is the same as that of the unit cell feed design in the previous section. Due to the large scale of C-band elements (16 × 6), the independent feeding of each C-band element will require a large number of connectors, coaxial lines and power dividers. To simplify the measurement setup as well as to reduce cost,

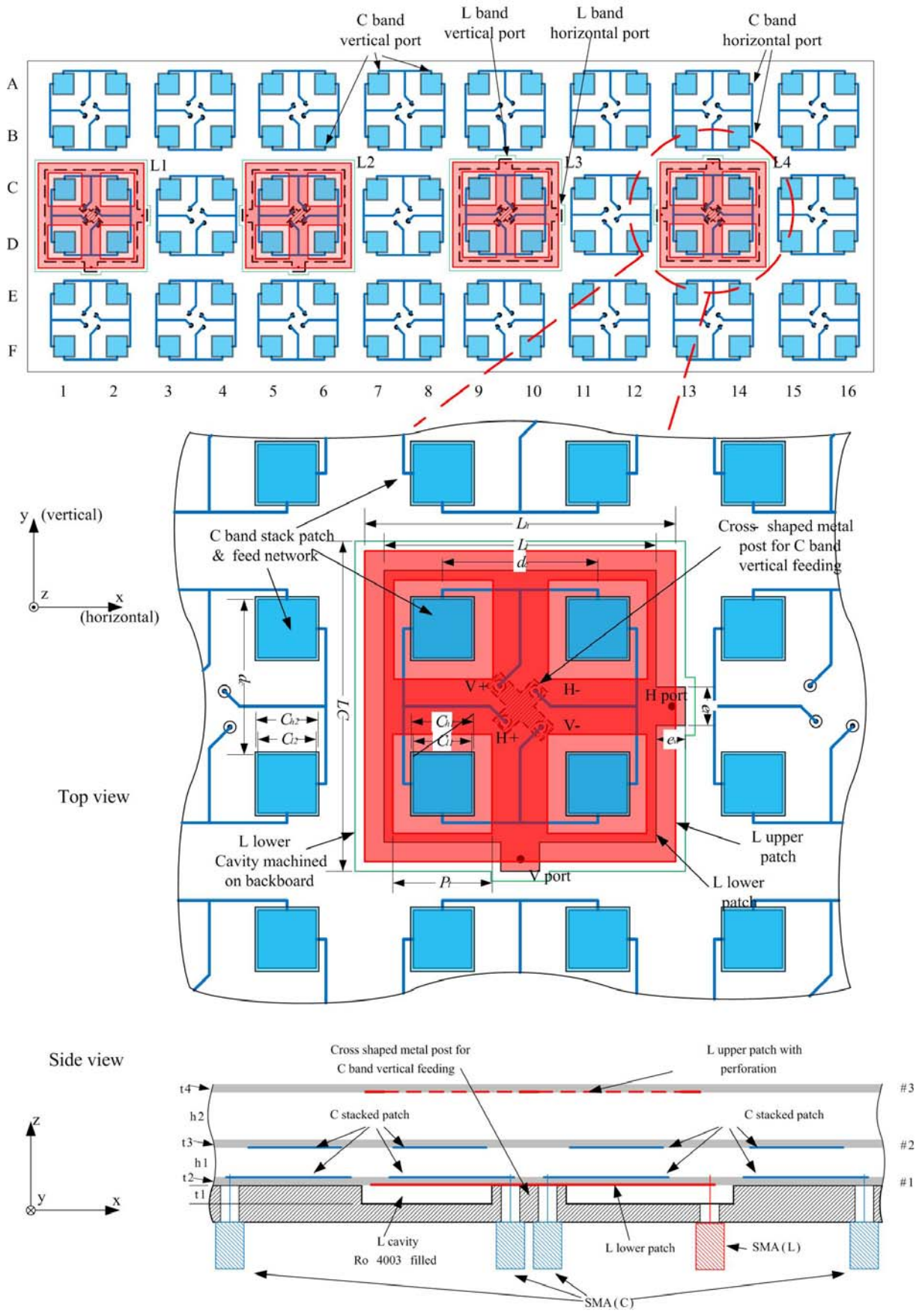

Fig.5 - 31 Local view of array configuration

the adjacent co-polarized C-band element ports are combined before connecting to SMA connectors, as shown in Fig.5-31. The 2 × 1 arraying will definitely limit the antenna's scan capability in two-element direction; however, the scan range in one-element direction is not impacted, which is still enough to validate the scan ability of C band in the sandwiched structure. For example, when H-port is excited, the patterns will support the designed scan range in XOZ plane (the coordinate system is defined in Fig.5-31).

Similarly, the combined C-band microstrip feed lines are located at the L-band patch center, and pass through the L-band cavity for vertical feeding. To fully utilize the structure, C-band microstrip lines pass through the L-band cavity via the cross shaped metal post perturbation. Every 2 × 2 C-band dual-polarized elements form a symmetric unit cell, which has four feed points in their vertical feeding. Each feed point employs one arm of cross perturbation for one polarization, as shown in Fig.5-31. The 2 × 2 C-band unit cells are naturally ‘pair-wise anti-phase’ fed [134-136], so that cross-polarization can be suppressed in the sub-array.

For consistency, C-band elements outside the sandwiched DBDP unit cell employ the same design and feed method. Furthermore, to avoid unexpected increase in side lobe levels, C-band elements outside the sandwiched unit cell are elevated to same level of L-band driven patch, as shown in Fig.5-31 and Fig.5-29(b). In other words, the L-band lower cavities are dug into the back plate, as shown in Fig.5-29(a). Because of the feed structure, the 2 × 2 C-band unit cell is treated as the basic periodical structure in the sub-array design.

D. Optimized Parameters

In the sub-array design, Rogers 4003C laminates are employed for both superstrate and

the L band filling material. Two 1.524 mm thick laminates are stacked to form a 3.048 mm thick dielectric block for L-band cavity, while all the superstrate use 0.813 mm laminates. Although using an air-filled cavity in L-band lower patch can simplify the fabrication, the dielectric filling can reduce the overall antenna thickness and L-band driven patch size (facilitate C-band embedding).

As mentioned earlier, the independently designed L- and C-band elements can perform equally well when they are packaged together due to the good inter-band isolation. They are tuned and optimized separately using Ansoft HFSS 13.0 using the method as described in Chapter 3 and Chapter 4, and hence not repeated here. The optimized parameters of L/C sandwiched stacked patch sub-array are listed in Table 5-10 for reference. For parameter definitions, see Fig.5-29 ~ Fig.5-31.

Table 5 - 10 Parameters of the fabricated sandwiched stacked patch DBDP-SA array

L_h	76	L_l	66	L_C	78.5
P_l	26	C_{h1}	16.7	C_{l1}	14
C_{h2}	17.2	C_{l2}	14	d_c	36
d_L	144	e_l	10	e_w	7.5
l_1	22	l_2	18	p_w	4
h_1	4	h_2	15	t_1	3.048
t_2	0.813	t_3	0.813	t_4	0.813

***** Unit: mm

5.5.4 Measurements and Results

The L/C sandwiched stacked-patch DBDP sub-array, which consists of 4 × 1 L-band elements and 16 × 6 C-band elements, is fabricated and tested to validate the design. Its photographs are shown in Fig.5-32.

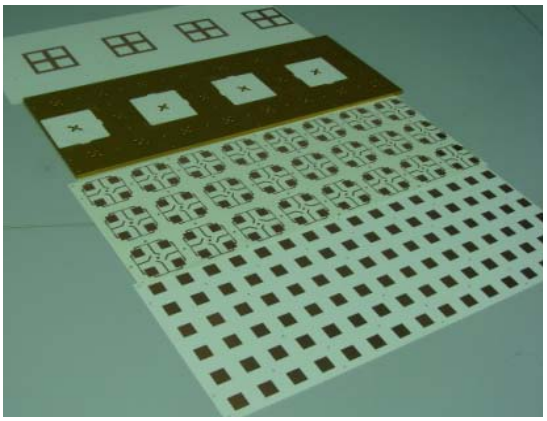

(a) Etched laminate and the back plate

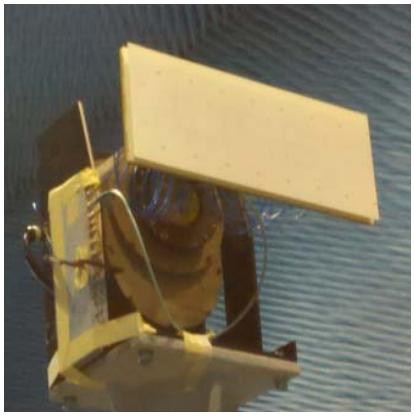

(b) Front view

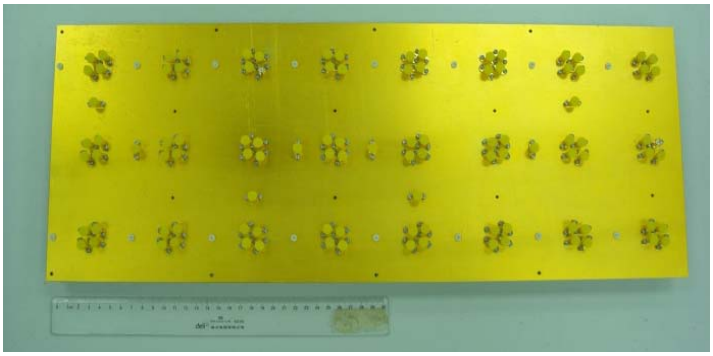

(c) Rear view

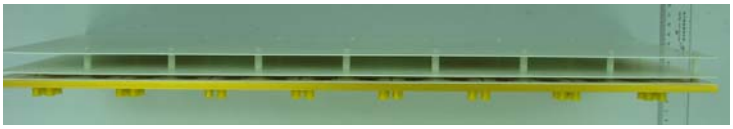

(d) Side view

Fig.5 - 32 Photos of the L/C sandwiched stacked patch DBDP-SA sub-array

The antenna return loss is measured using Agilent 8722ES vector network analyzer, while the radiation patterns are obtained in an indoor far-field anechoic chamber.

A. L-band:

The measured $|S_{11}|$ in L-band are shown in Fig.5-33. For clarity, the results of only few typical ports are plotted. The L-band measured $|S_{11}| \leq$ -10 dB bandwidth extends from 1.186 GHz to 1.347 GHz, which is 161 MHz, or 12.7 %. The measured bandwidth covers a wider frequency span than the computed bandwidth but at the expense of higher in-band ripple factor. The fabrication tolerance might have caused this deviation. Considering that the

overall profile of antenna is only 21 mm (0.09 λ_0), the bandwidth-to-profile ratio is satisfactory.

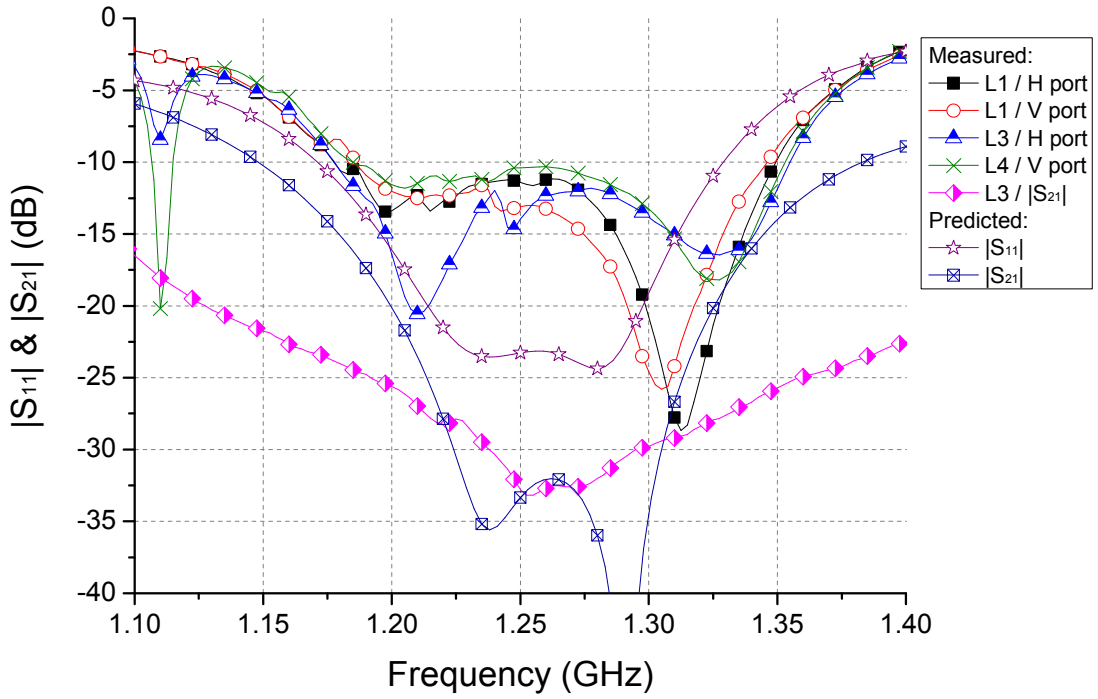

Fig.5 - 33 Measured and computed elements' port responses in L band

The measured polarization isolation level is not as good as the predicted level. Because the isolation is quite sensitive to the perturbation structure, tolerance in both the cavity fabrication and dielectric fitting might have deteriorated the isolation level. The measured isolation level is better than 25 dB over the L-band bandwidth.

Fig.5-34 presents the uniformly excited radiation patterns in L band. In general, the measured patterns agree well with the array factor theory. The higher first side lobe level observed in the left side radiation patterns can be attributed to the limited array scale and asymmetric boundary condition for L-band aperture, as shown in Fig.5-28 and Fig.5-31. One L-band patch is located very close to the array edge. By increasing the array size, the boundary condition for L-band array will become more symmetric and hence more symmetric

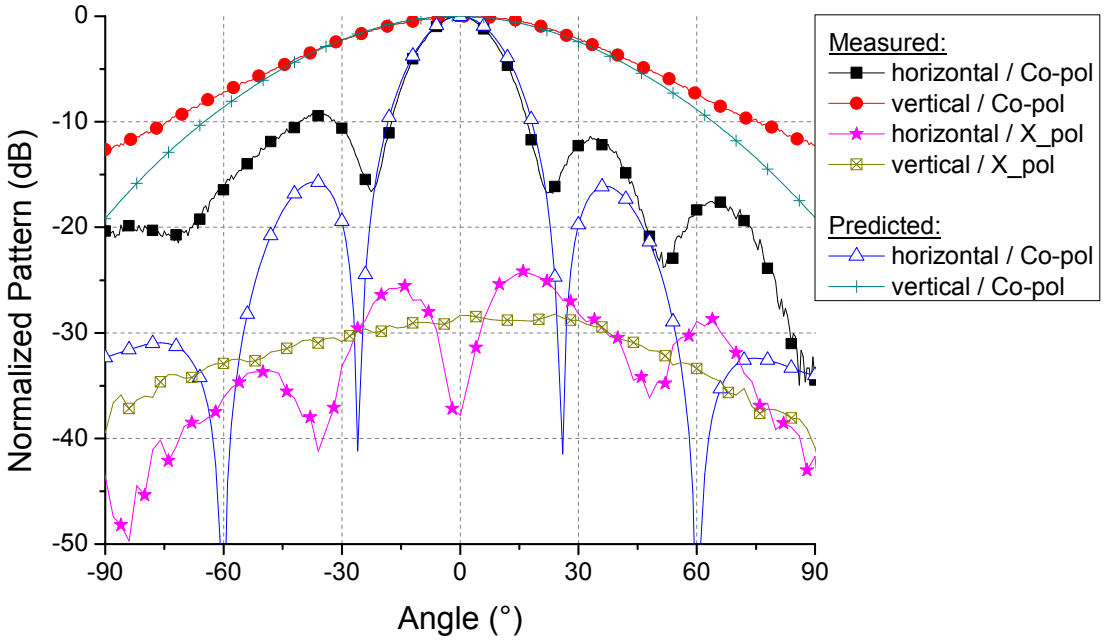

(a) Horizontal port excited

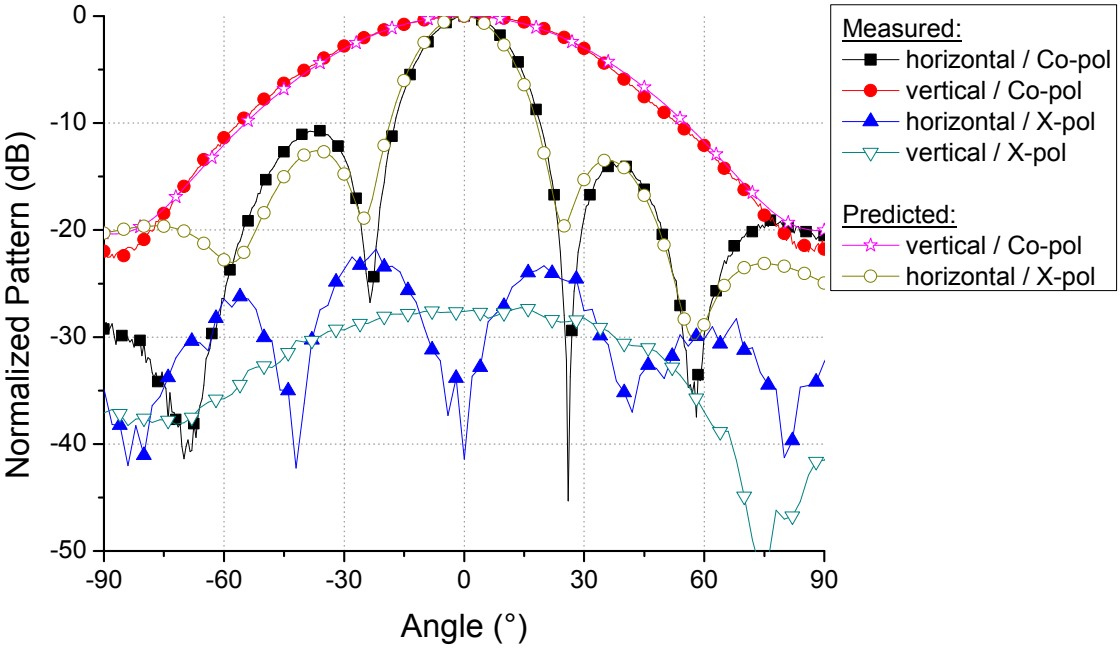

(b) Vertical port excited

Fig.5 - 34 Measured L-band radiation pattern at 1.25GHz

radiation patterns. A good cross-polarization level of better than 28 dB is obtained within mainlobe area, as shown in Fig.5-34.

The calibrated L-band gain is 12.9 dB, which correspond to an efficiency of 86.7 %. Due to the limited number of elements, the scan radiation patterns are not measured.

B. C-band:

The measured and computed S parameters of the C-band elements are plotted in Fig.5-35. The results of only few typical elements are presented for clarity. Although the C-band elements, located inside and outside the sandwiched unit cells, have different boundary condi-

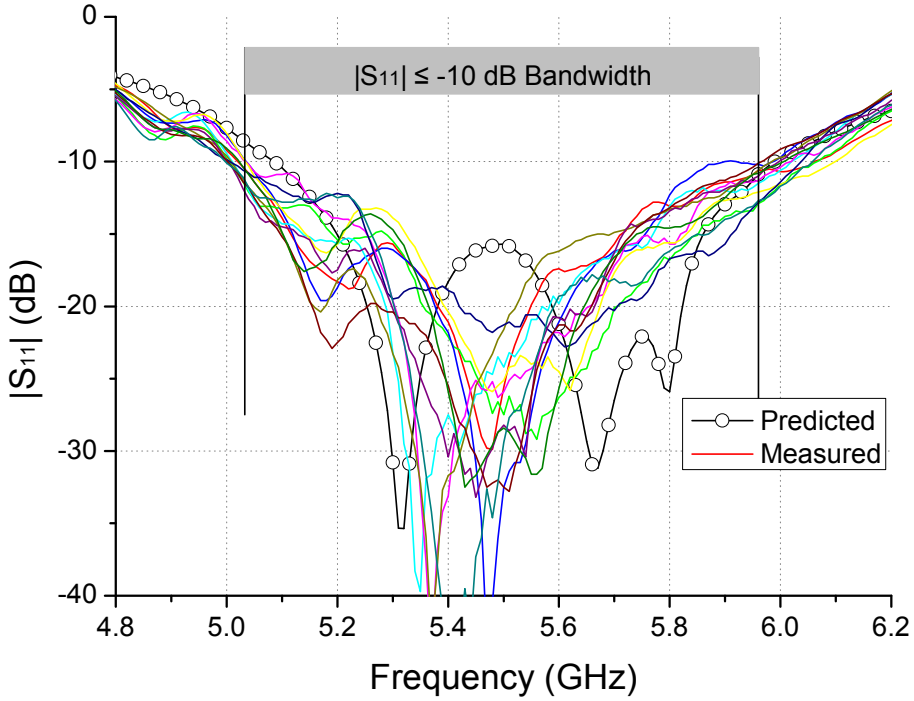

(a) Input reflection coefficient

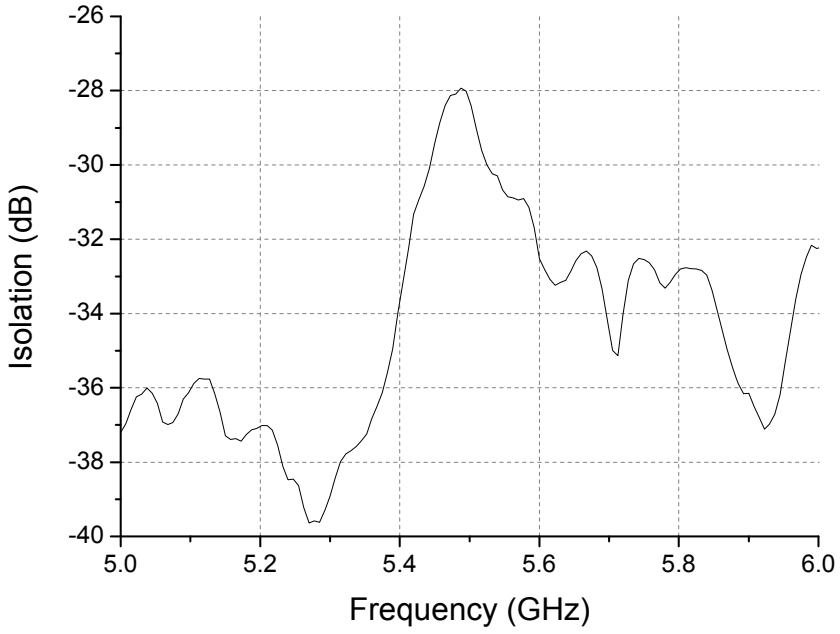

(b) Array polarization isolation

Fig.5 - 35 Measured element port responses in C band

tions, good consistency is observed in C-band measurement. The $|S_{11}| \leq -10$ dB element bandwidth of 16.8 % (5.033 ~ 5.959 GHz) is obtained, with the in-band array polarization isolation ($|S_{21}|$ between overall H- and V-port) level of better than 28 dB, as shown in Fig.5-35(b). The insertion losses from coaxial line and power dividers are measured and compensated in the post processing stage.

The custom-made co-axial lines are employed instead of the commercial phase shifter and beam control boards for radiation pattern measurement to reduce overall cost. Fig.5-36 presents the measured patterns of uniformly excited C-band array. In general, the measured results agree well with the theoretical array factor, with the only exception of the radiation pattern in the smaller aperture dimension (H-cut for H-port and E-cut for V- port), whose near side lobes are slightly higher than ideal array factor, resulting in a slightly narrower beam-width. This is probably due to the limited aperture length and the shielding effect from L band. The side lobe level is expected to become equal to SLL of the ideal array factor by increasing the aperture length, as evident from the larger aperture radiation patterns of Fig.5-36 (E-cut for H-port and H-cut for V-port). The measured cross-polarization level remains better than 28 dB in the main lobe area for both port excitations.

The calibrated gains of C-band array are 26.8 dB and 26.6 dB for H- and V-port, respectively, corresponding to the efficiencies of 81.8 % and 78.1 %, respectively. The lower efficiency values are probably due to the feed line insertion losses.

Although 2 × 1 array elements are employed in C band, the scan capability in E-plane of H-port excited patterns is not affected, see Fig.5-28 and Fig.5-31. The scan patterns at 5.8 GHz are thus measured, as shown in Fig.5-37. The antenna gain-dropping rate agrees well

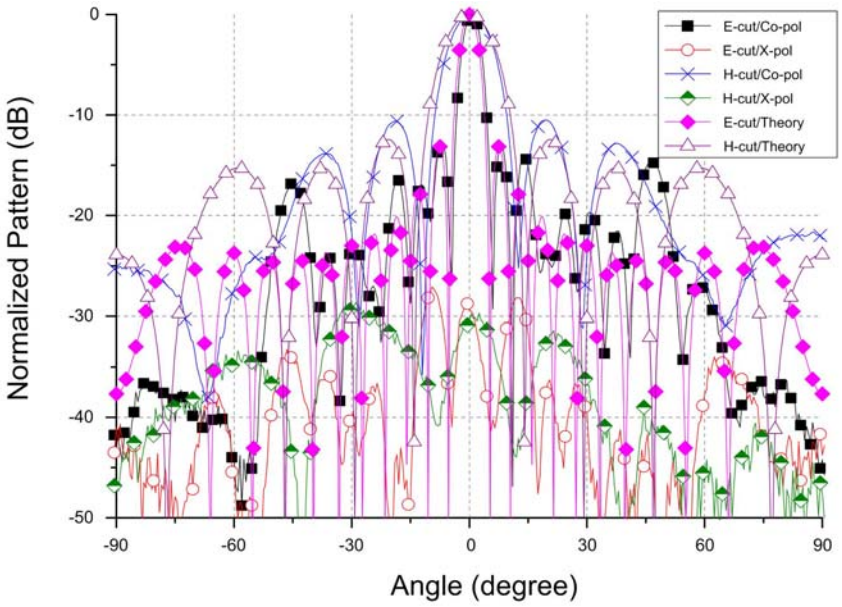

(a) Horizontal port excited

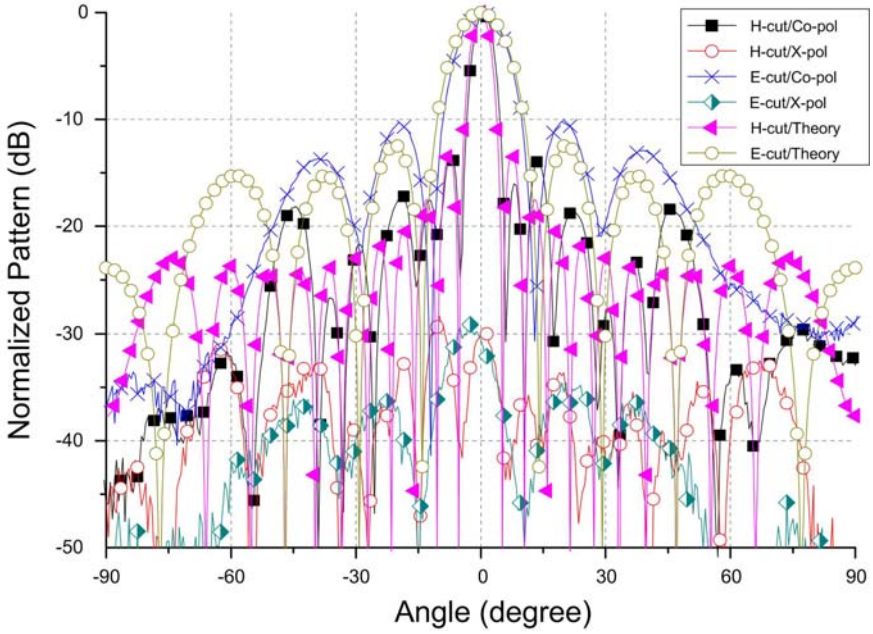

(b) Vertical port excited

Fig.5 - 36 Measured C-band radiation patterns at 5.8 GHz

with the experimental equation: $G=cos^{1.5}\theta$, where θ is the scan angle. The SLL remain below -10 dB within the scan range, and the grating lobes are not observed. A scan capability of 25° is thus achieved.

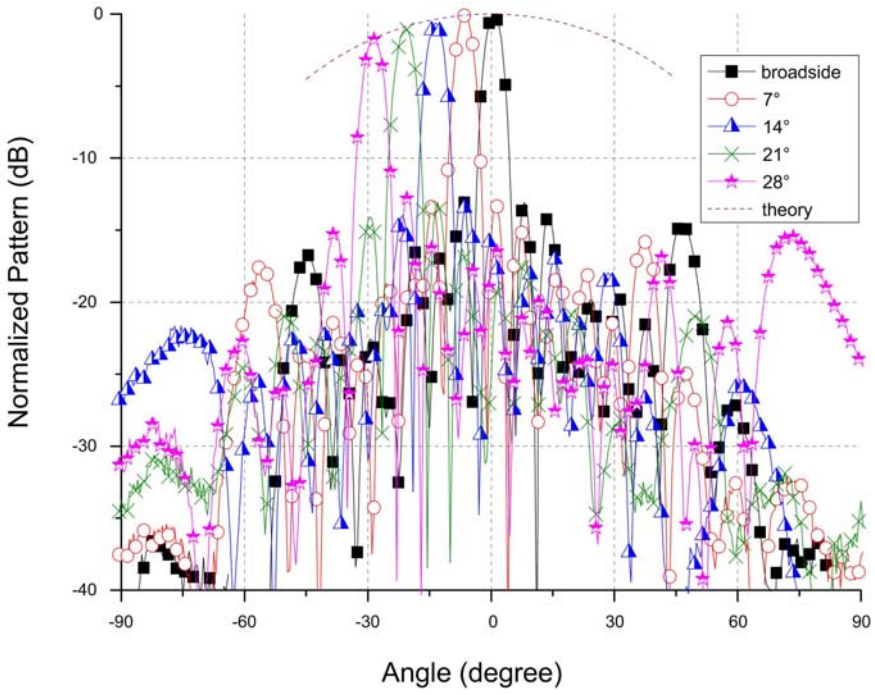

Fig.5 - 37 Measured C-band scan radiation patterns at 5.8 GHz

5.6 Summary

A novel L/C sandwiched stacked patch DBDP-SA sub-array is proposed in this chapter. The partial-perforated stacked-patch structure is employed for the lower-band element to improve the lower-band bandwidth for the given antenna profile. A prototype antenna sub-array, including 4 × 1 L-band elements and 16 × 6 C-band elements is designed, fabricated and measured. The measured port responses and radiation patterns validate the feasibility of the proposed structure. The measured lower-band element bandwidth and antenna profile specifications are the main achievements. They are listed in Table 5-11 and compared with other classical DBDP-SA arrays, including perforated stack patch and interleaved structure available in the literature. The lower-band bandwidth-to-profile (BW/h) ratio is also calculated for DBDP antenna to highlight the achievable bandwidth per thickness.

From Table 5-11, a trend can be observed that the BW/h ratio dropping with the

increasing of antenna thickness from a value of 218 at $0.035\lambda_0$ to 125 at $0.1\lambda_0$. This means more thickness cost will be paid if we want to achieve larger bandwidth. For example, the [109] and [118, 120] (Line #1 and Line #3) present same type DBDP-SA arrays for the same L/C bands. The L-band bandwidth in [118, 120] has increased for about 75%, while the overall thickness is tripled.

As compared to the designs of [114, 118, 120], the proposed sandwich structure has similar lower-band element bandwidth but have lower profile, *i.e.*, the sandwiched structure has a better 'bandwidth-to-profile' ratio.

Table 5 - 11 Performance comparison of the DBDP arrays published in the literature

Paper	Band/Type	BW (%)	Profile	BW/h (%/λ)	X-pol./Iso(dB)
[109]	L/C perforated patch	L:7.56 C:6.5	8.3mm (0.0346λ)	218.5	-30/--
[110]	L/X perforated patch	L:6 C:5.2	7.5mm (0.0313λ)	191.7	-22/19
[118,120]	L/C perforated patch	L:13.2 C:16.3	24.5mm (0.102λ)	129.4	L:--/30 C:--/40
[104]	L/Ku Perforated patch	L:10.6 Ku:10.6	9.1mm (0.0485λ)	218.5	--/--
[165]	L/X perforated patch	L: 6.4 C:8.8	13mm (0.0542λ)	118.2	L:-30/-- X:-50/-- *
[166]	S/X perforated patch	S:19.8 X:25.7	--	--	S:-17/15 X:-17/15
[115]	L/X perforated patch	L:13 X:15.7	27mm (0.104λ)	125	L:-20/25 X:-25/32
Proposed array	L/C Sandwich patch	L:12.7 C:	21mm (0.0886λ)	143.3	L: -28/25 C:-28/28

Note: * means measured results are not available

It should be noted that the proposed sandwiched stacked patch DBDP structure has some design limitations in its current form:

1) It can hardly be used when frequency ratio is larger than 4:1. Since a large number of

higher-band elements will be overlapped on to the lower-band driven patch, it adds complexity in the design of vertical feed for higher-band elements;

2) The choice of feed mechanism, such as aperture coupling, has its own drawback. Because the lower-band driven patch also serves as the ground of higher-band patches, more layers should be used for higher-band aperture-coupled feed network to avoid using an etching slot on the lower-band driven patch, like in [129]. It will make the structure quite complex.

Acknowledgement

This work is supported by the Macquarie University iMQRES scholarship scheme and the Australian Research Council.

Special thanks are given to C.X. Meng, who has undertaken part of the numerical simulations of L/C band sandwiched unit cell, and to Dr. Yong Cai, for his many constructive suggestions to improve the designs.

Chapter 6
Conclusion and Future Research

6.1 Conclusion

The thesis presented design methods for several multi-band dual-polarized shared-aperture (MBDP-SA) phased array antennas primarily (but not restricted) for space-/ air-borne SAR applications. Different aspects of performance improvement in MBDP-SA arrays are addressed and the designs are verified by three sample MBDP-SA arrays, as described below:

1) An S/X dual-band dual-polarized shared-aperture (DBDP-SA) array with improved isolation is designed for the fractional frequency ratio of 3.5:1. New techniques have been investigated to improve array isolation, the lower-band bandwidth and element polarization isolation. Prototype sub-arrays are designed, fabricated and tested to validate the electric performances of the proposed DBDP-SA array. Furthermore, the reliability and feasibility of newly proposed hybrid feed (aperture coupling and probe feed) connectors vertical mounting is also verified.
2) A MBDP-SA array design method, which constructs a MBDP-SA array by combining several DBDP-SA sub-arrays operating in different bands, is proposed. A key issue of the proposed method is to obtain good performance in the lowest band, because its aperture is made up of several different DBDP-SA sub-arrays' lower-band elements. To verify the design, a L/S/X tri-band dual-polarized shared-aperture (TBDP-SA) array is designed and fabricated by combining two DBDP-SA sub-arrays (L/S and L/X one each) and a L

single-band dual-polarized (SBDP) sub-array. Good radiation patterns and port responses are confirmed at L band, as well as that of the higher bands, showing the feasibility of the proposed method. This work makes efforts on how to extend DBDP-SA array to the MBDP-SA array in SAR applications.

3) A sandwiched perforated DBDP-SA structure is proposed. This structure is a trade off between the overlapped DBDP structure and the perforated patch DBDP structure in terms of bandwidth, antenna profile and structure complexity. An L/C band sandwiched perforated DBDP-SA prototype array is fabricated to verify the feasibility of the structure. Good port responses, radiation patterns and scan capability are confirmed in each frequency band. An L/C overlapped DBDP unit cell is also designed and fabricated as a reference. The measured results validate the theoretical analysis, where as under the same conditions (laminate, profile, etc), the proposed sandwiched stacked patch DBDP array has moderate bandwidth but lower overall antenna profile. This work makes efforts on the bandwidth improvement for the lower-band elements in DBDP-SA array with the given overall antenna profile.

As a conclusion, the measured results of three MBDP-SA sample arrays are listed in Table 6-1, together with some other classical DBDP-SA arrays (that are reported in the open literature) for comparison.

Table 6 - 1 The results of different DBDP-SA arrays

Year	Ref.	Bands	Structure	BW(%)	Isolation(dB)
Reported DBDP-SA Arrays					
1995	[102]	S：2.85G X：8.6G	Cross Patch Patch	- -	- -
1995	[129]	P band S band	Single Layer Patch Single Layer Patch	1 2	- -

1998	[94]	C：5.3G X：9.6G	Patch Slot	4-5* 2-3*	- -
1998	[93]	L：1.25G C：5.3G	Slot Patch	>5 >5	>23 >24
2000	[109]	L：1.275G C：5.3G	Perforated Stacked Patch Stacked Patch	7* 5.7*	- -
2001	[110]	L：1.25G X：9.6G	Perforated Stacked Patch Single Layer Patch	6.8 3.1	21 21
2005	[121]	L：1.25G C：5.3G	Perforated Single Patch Single Layer Patch	2 3	42 21
2006	[107]	900MHz 1800MHz	Stacked Patch Stacked Patch	8.86* 10.5*	30 30
2006	[98]	900MHz 1800MHz	Ring Patch Printed Dipole	17.4 23.7	30 28
2006	[83, 84]	S:3.2G X:9.6G	Stacked Printed Dipole Stacked Patch	8.9 17	30 40
2008	[101]	865MHz 1730MHz	Cross Patch Stacked Patch	5.5 25.3	- -
2009	[96]	S：3G X：10G	Patch Slot	1 1.5	25 33
2009	[118,120]	L:1.25G C：5.45G	Perforated Stacked Patch Stacked Patch	8* 7.4*	30 40
2009	[104]	L：1.55G Ku：12G	Cross Slot Stacked Patch	6.5 8	- -
2010	[103]	Ku：13.6G Ka：35.5G	Cross Slot Single Layer Patch	5.8 3.1	- -
2011	[82]	X:9.6G Ka:34G	Stacked Patch** Single Thick Layer Patch**	18 9.5	- -
2012	[166]	S:3.2G X:10G	Perforated Stacked Patch Stacked Patch	19.8 25.7	- -
2013	[86]	900MHz 1800MHz	Printed dipole Printed dipole	22 68	- -
DBDP-SA Arrays in the Thesis					
2010	Chapter 3	S: 2.85GHz X: 10GHz	Stacked Printed Dipole Stacked Patch	10* 10*	28 32
2010	Chapter 4	L: 1.25GHz S: 3.2GHz X: 10GHz	Printed Dipole Stacked Patch Stacked Patch	13.4 14.8 16.7	37 45 43
2011	Chapter 5	L: 1.25GHz C: 5.3GHz	Stacked Patch Stacked Patch	17.6 15	15 17
2011	Chapter 5	L: 1.25GHz C: 5.3GHz	Partial Perforated Stack Patch Stacked Patch	13 15.8	19 21

* VSWR≤1.5

** Single Polarization

6.2 Future Research

The MBDP-SA array designs presented in this thesis has several interesting issues yet to be investigated, as well as some potential application. Hence, the future research effort can be made on:

1) Shared Cavity Array: As analyzed in Chapter 5, the present dual-band array aperture-sharing is achieved by either interleaving two independent cavities in the same aperture or overlapping them at different heights. As large element bandwidth comes from the sufficient cavity volume in the resonant antenna, it can be hardly realized by interleaved structure but can be realized using overlapped structure with extra height profile. A compromise has to be made between the lower-band bandwidth and low overall profile performance. This situation, either narrower bandwidth or extra overall profile, can be attributed to the employing of independent cavity in both bands. Theoretically, sharing cavity in both bands can better use the space, while achieving lower antenna profile and maximum lower-band bandwidth. This concept is similar to the Current Sheet Array in [28], and frequency selective surface (FSS) is perhaps a promising method to realize the cavity shared array, as an sample in [167];
2) Overlapped DBDP-SA full array: As analyzed in Chapter 5, the overlapped structure gives advantages in terms of its broadband performance in lower band, especially for larger frequency ratio, like $f_L : f_C = 1 : 4$. To the best of the authors' knowledge, no large scale overlapped DBDP-SA full array with large lower-band bandwidth is reported. This is perhaps due to the complexity of the overlapped structure. However, it worth studying.

3) The improvement in sandwiched stacked patch: The method proposed in the thesis has some limitations. For example, the complexity of the structure in higher band prevents the implementation of more advanced feeding techniques (such as aperture coupling) which is believed to improve the cross-polarization level and isolation performance.
4) Novel radiators: Other novel radiators can provide great convenience in DBDP-SA array, such as the dielectric resonant antenna (DRA) element [168], which achieves a much smaller element dimension due to the use of extremely higher permittivity material. Perforation and overlapping will then not be required, as the higher-band element gaps will be wide enough for such DRA lower-band elements.

Appendix A
Abbreviations

AusAMF	Australian Antenna Measurement Facility
BW	Bandwidth
BW/h	Bandwidth to Profile Ratio
Co-pol.	Co-Polarization
dB	Decibels
dBi	Decibels Isotropic
DBDP	Dual-Band Dual-Polarized
DBDP-SA	Dual-Band Dual-Polarized Shared-Aperture
DP	Dual-Polarized
EMC	Electro-Magnetic Compatibility
IFF	Identify Friend and Foe
MBDP	Multi-Band Dual-Polarized
MBDP-SA	Multi-Band Dual-Polarized Shared-Aperture
SAR	Synthetic Aperture Radar
SAM	Surface-to-Air Missile
SBDP	Single-Band Dual-Polarized
SIR	Signal to Interference Ratio
SLL	Side Lobe Level
SNR	Signal to Noise Ratio
TBDP	Tri-Band Dual-Polarized

TBDP-SA	Tri-Band Dual-Polarized Shared-Aperture
TLM	Transmission Line Model
VNA	Vector Network Analyzer
VSWR	Voltage Standing-wave Ratio
X-pol.	Cross-Polarization

Bibliography

[1] X.-W. Ruan, *et al*, Performance Experiment of Classification Using Chinese Airborne Multi-Band and Multi-Polar SAR Data, *International Symposium on Image and Data Fusion (ISIDF) 2011*, Tengchong, Yunnan, PRC, pp. 1-4, Aug. 2011.

[2] W.-G. Chang, *et al*, Airborne Multi-frequency-Band SAR system and its information processing, *International Conference on Information and Automation 2008, ICIA 2008*, Changsha, PRC, pp. 1807-1811, Jun. 2008.

[3] E.-C. Zaugg, M.-C. Edwards and A. Margulis, Theoretical and practical design considerations for a small, multi-band SAR: The SlimSAR, *IEEE International Geoscience and Remote Sensing Symposium (IGARSS) 2010*, Honolulu, HI, pp. 126-129, Jul. 2010.

[4] F. Rostan and W. Wiesbeck, Aperture-coupled microstrip patch phased arrays in C- and X-band: a contribution to future multi-polarization multi-frequency SAR systems, *IEEE International Symposium on Phased Array Systems and Technology 1996*, Boston, MA, pp. 141-146, Oct 1996.

[5] F. Bin, J.-S. Yang and W.-G. Huang, Application of multi-band and full-polarization SAR in shallow sea bottom topography measurement, *IEEE International Geoscience and Remote Sensing Symposium 2004, IGARSS '04. Proceedings*, Anchorage, AK, Vol. 7, pp. 4711-4714, Sept. 2004.

[6] P.-L. Frison, *et al*, Analysis of L- and C-Band SAR Image Time Series Over a Sahelian Area, *IEEE Geoscience and Remote Sensing Letters*, Vol. 10, No. 5, pp. 1016-1020, Sept. 2013.

[7] R.-L. Jordan, B.-L. Huneycutt and M. Werner, The SIR-C/X-SAR Synthetic Aperture Radar System, *IEEE Transactions on Geoscience and Remote Sensing*, Vol. 33, No. 4, pp. 829-839,

1995.

[8] F. Stuhr, R.-L. Jordan and M. Werner, SIR-C/X-SAR: An Advanced Radar, *IEEE Aerospace Applications Conference*, Snowmass at Aspen, Colorado, Vol. 2, pp. 5-16, Feb. 1996.

[9] F. Stuhr, R. Jordan, and M. Werner, SIR-C/X-SAR: a multifaceted radar, *Record of the IEEE International Radar Conference 1995*, Alexandria, VA, pp. 53-61, May 1995.

[10] R.-L. Jordan, B.-L. Huneycutt and M. Werner, The SIR-C/X-SAR Synthetic Aperture Radar system, *IEEE Transactions on Geoscience and Remote Sensing*, Vol. 33, No. 4, pp. 829-839, Jul. 1995.

[11] A. Freeman, *et al*, The “Myth” of the minimum SAR antenna area constraint, *IEEE International Geoscience and Remote Sensing Symposium 1999, IGARSS '99 Proceedings*, Hamburg, Germany, Vol. 3, pp. 1770-1772, 1999.

[12] D.-B. Smith, *et al*, SIR-C/X-SAR Free Flyer Engineering Concept, Jet Propulsion Laboratory, Pasadena, CA, pp. 1-13.

[13] Q. Luo, W.-X. Zhou and L. Ma, World Ground Based Radar Handbook (in Chinese), *National Defense Industry Press*, 2005.

[14] R. Waterhouse, Printed Antennas for Wireless Communications, *John Wiley & Sons, Ltd*, 2007.

[15] Mimo and Smart Antennas for 3G and 4G Wireless Systems – Practical Aspects and Deployment Consideration, May 2010.

[16] L. Hung, J.-P. Weem and Z. Popovic, A dual-band dual-polarized nested Vivaldi slot array with multilevel ground plane, *IEEE Transactions on Antennas and Propagation*, Vol. 51, No. 9, pp. 2168-2175, Sept. 2003.

[17] J. So, J. Kim and C. Cheon, Modelling and design of a finite dual-polarised notch phased-array antenna, *IEE Proceedings of Microwaves, Antennas and Propagation*, Vol. 153, No. 1, pp. 43-48, Feb. 2006.

[18] H. Holter, Dual-Polarized Broadband Array Antenna with BOR-Elements, Mechanical Design

and Measurements, *IEEE Transactions on Antennas and Propagation*, Vol. 55, No. 2, pp. 305-312, Feb. 2007.

[19] J.-J. Lee, S. Livingston and R. Koenig, A low-profile wide-band (5:1) dual-pol array, *IEEE Antennas and Wireless Propagation Letters*, Vol. 2, No. 1, pp. 46-49, 2003.

[20] S. Livingston and J.-J. Lee, A Wide Band Low Profile Dual-pol "Thumbtack" Array, *IEEE International Symposium on Phased Array Systems and Technology (ARRAY) 2010*, Waltham, MA, pp. 477-483, Oct. 2010.

[21] H. Holter, C. Tan-Huat and D.-H. Schaubert, Experimental results of 144-element dual-polarized endfire tapered-slot phased arrays, *IEEE Transactions on Antennas and Propagation*, Vol. 48, No. 11, pp. 1707-1718, Nov. 2000.

[22] C.-T. Rodenbeck and S.-G. Kim, Ultra-wideband low-cost phased-array radars, *IEEE Transactions on Microwave Theory and Techniques*, Vol. 53, No. 12, pp. 3697-3703, Dec. 2005.

[23] I. Tzanidis, K. Sertel and J.-L. Volakis, An interweaved spiral array (ISPA) providing a 10:1 bandwidth over a ground plane, *IEEE Antennas and Propagation Society International Symposium (APSURSI) 2010*, Toronto, ON, pp. 1-4, Jul. 2010.

[24] E.-O. Farhat, *et al*, Ultra-wideband tightly coupled fractal octagonal phased array antenna, *International Conference on Electromagnetics in Advanced Applications (ICEAA) 2013*, Torino, pp. 140-144, Sept. 2013.

[25] K. Kalbasi, R. Plumb and R. Pope, An analysis and design tool for a broadband dual feed circles array antenna, *Antennas and Propagation Society International Symposium 1992, AP-S. 1992 Digest*, Held in Conjuction with: *IEEE URSI Radio Science Meeting and Nuclear EMP Meeting*, Chicago, IL, USA, Vol. 4, pp. 2085-2088, Jul. 1992.

[26] J.-J. Rawnick, *et al*, Enhanced Bandwidth Dual Layer Current Sheet Antenna, United States Patents, No. US 6771221 B2, Aug. 2004.

[27] S.-S. Holland, Vouvakis and N. Marinos, A 7-21GHz Planar Ultrawideband Modular Array, *IEEE Antennas and Propagation Society International Symposium (APSURSI) 2010*, Toronto,

ON, pp. 1-4, Jul. 2010.

[28] M. Jones and J. Rawnick, A New Approach to Broadband Array Design using Tightly Coupled Elements, *IEEE Military Communications Conference 2007, MILCOM 2007*, Orlando, FL, USA, pp. 1-7, Oct. 2007.

[29] T.-F. Xia, S.-W. Yang and Z.-P. Nie, Design of a Tapered Balun for Broadband Arrays With Closely Spaced Elements, *IEEE Antennas and Wireless Propagation Letters*, Vol. 8, pp. 1291-1294, 2009.

[30] D.-M. Le Vine, M. Haken and C.-T. Swift, Development of the synthetic aperture radiometer ESTAR and the next generation, *IEEE International Geoscience and Remote Sensing Symposium 2004 Proceedings, IGARSS '04*, Anchorage, AK, pp. 1260-1263, Sept. 2004.

[31] W.-D. Armin and F.-M. Dickey, Synthetic Aperture Radar, *Optics and Photonics News*, pp. 28-33, Nov. 2004.

[32] C. Ozdemir, *et al*, ASAR-antenna synthetic aperture radar imaging, *IEEE Transactions on Antennas and Propagation*, Vol. 46, No. 12, pp. 1845-1852, Dec. 1998.

[33] R.-L. Jordan, The Seasat-A synthetic aperture radar system, *IEEE Journal of Oceanic Engineering*, Vol. 5, No. 2, pp. 154-164, Apr. 1980.

[34] J. Cimino, C. Elachi and M. Settle, SIR-B - The Second Shuttle Imaging Radar Experiment, *IEEE Transactions on Geoscience and Remote Sensing*, Vol. GE-24, No. 4, pp. 445-452, Jul. 1986.

[35] R.-K. Raney, *et al*, Radarsat, Proceedings of the IEEE, Vol. 79, No. 6, pp. 839-849, Jun. 1991.

[36] S. Riendeau and C. Grenier, RADARSAT-2 Antenna, *IEEE Aerospace Conference 2007*, Big Sky, MT, pp. 1-9, Mar. 2007.

[37] R. Petersson, E. Kallas, and K. van't Klooster, Radiation performance of the ERS-1 SAR EM antenna, *Antennas and Propagation Society International Symposium 1988*, AP-S Digest, Syracuse, NY, USA, Vol. 1, pp. 212-215, Jun. 1988.

[38] M. Hutchinson, M.-D. Gibbons, ENVISAT ASAR - Design & Performance with a View to the Future, *Symposium on Space-Based Observation Technology*, Island of Samos, Greece, pp. 34-1 – 34-8.

[39] B. Grafmuller, A. Herschlein and C. Fischer, The TerraSAR-X Antenna System, *IEEE International Radar Conference 2005*, pp. 222-225, May 2005.

[40] A. Torre and P. Capece, COSMO-SkyMed: the advanced SAR instrument, *5th International Conference on Recent Advances in Space Technologies (RAST) 2011*, Istanbul, pp. 865-868, Jun. 2011.

[41] K. Yukihiro, The Overview of the L-band SAR Onboard ALOS-2, *Progress In Electromagnetics Research Symposium Proceedings*, Moscow, Russia, pp. 735-738, Aug. 2009.

[42] Y.-L. Desnos, *et al*, The ENVISAT advanced synthetic aperture radar system, *IEEE International Geoscience and Remote Sensing Symposium 2000 – Proceedings, IGARSS 2000*, Honolulu, HI, Vol. 3, pp. 1171-1173, Jul. 2000.

[43] A. Moreira, *et al*, TanDEM-X: a TerraSAR-X add-on satellite for single-pass SAR interferometry, *IEEE International Geoscience and Remote Sensing Symposium 2004 - Proceedings, IGARSS '04*, Vol. 2, pp. 1000-1003, Sept. 2004.

[44] M. Stangl, *et al*, TerraSAR-X technologies and first results, *IEE Proceedings of Radar, Sonar and Navigation*, Vol. 153, No. 2, pp. 86-95, Apr. 2006.

[45] Electronic Warfare & Radar Systems Engineering Handbook, *Naval Air Warfare Center Weapons Division*, 1997.

[46] IEEE standard, 521-2002 - IEEE Standard Letter Designations for Radar-Frequency Bands, 2002.

[47] C.-C. Schmullius and D.-L. Evans, Tabular summary of SIR-C/X-SAR results: synthetic aperture radar frequency and polarization requirements for applications in ecology and hydrology, *Geoscience and Remote Sensing 1997, IGARSS '97, IEEE International Remote Sensing - A Scientific Vision for Sustainable Development*, Vol. 4, pp. 1734-1736, Aug. 1997.

[48] Z.-Z. Zhang, Introduction of Air-Borne and Space-Borne SAR (in Chinese), *Publish House of Electronics Industry*, Beijing, 2004.

[49] D.-M. Pozar, S.-D. Targonski, A Shared-Aperture Dual-Band Dual-Polarized Microstrip Array, *IEEE Transactions on Antennas and Propagation*, Vol. 49, No. 2, pp. 150-157, 2001.

[50] J. Granholm and K. Woelders, Dual Polarization Stacked Microstrip Patch Antenna Array with Very Low Cross-Polarization, *IEEE Transactions on Antennas and Propagation*, Vol. 49, No. 10, pp. 1393-1402, 2001.

[51] A.-C. Ludwig, The Definition of Cross Polarization, *IEEE Transactions on Antennas and Propagation*, Vol. 21, No. 1, pp. 116-119, 1973.

[52] D.-M. Pozar, *et al*, A Dual-Band Dual-Polarized Array for Spaceborne SAR, *IEEE Antennas and Propagation Society (APS) International Symposium*, Atlanta, Georgia, Vol.4, pp. 2112-2115, Jun. 1998.

[53] D.-R. Jahagirdar, Novel X+Ku dual band monopulse array antenna, *IEEE Antennas and Propagation Society International Symposium (APSURSI) 2012*, Chicago, IL, pp. 1-2, Jul. 2012.

[54] J. Holtzman, A dual band array, *IEEE Transactions on Antennas and Propagation*, Vol. 16, No. 5, pp. 603-604, Sept. 1969.

[55] Y.-Y. Liu, F.-W. Yao and Y.-B. Shang, Co-aperture dual-band waveguide monopulse antenna, *Proceedings of the International Symposium on Antennas & Propagation (ISAP) 2013*, Nanjing, China, Vol. 2, pp. 685-687, Oct. 2013.

[56] M.-N.-M. Kehn and P.-S. Kildal, Miniaturized Rectangular Hard Waveguides for Use in Multi-frequency Phased Arrays, *IEEE Transactions on Antennas and Propagation*, Vol. 53, No. 1, pp. 100-109, Jan. 2005.

[57] G. Colangelo and R. Vitiello, Shared Aperture Dual Band Printed Antenna, *International Conference on Electromagnetics in Advanced Applications (ICEAA 2011) 2011*, Torino, Italy, pp. 1092-1095, Sept. 2011.

[58] K. Lee, *et al*, A dual band phased array using interleaved waveguides and dipoles printed on

high dielectric substrate, *Antennas and Propagation Society International Symposium 1984*, pp. 886-889, Jun. 1984.

[59] T. Clark and E. Jaska, Million Element ISIS Array, *IEEE International Symposium on Phased Array Systems and Technology*, Waltham-Boston, Massachusetts, pp. 29-36, Oct. 2010.

[60] E. Arnieri, L. Boccia and G. Amendola, A Ka-Band Dual-Frequency Radiator for Array Applications, *Antennas Wireless Propagation Letters*, Vol. 8, pp. 894-897, 2009.

[61] E. Arnieri, *et al*, A Dual-Band Dual-Polarized Ka Printed Array, *IEEE Antennas Propagation Society (APS) International Symposium 2006*, Albuquerque, New Mexico, pp. 3617-3620, Jul. 2006.

[62] W.-M. Dorsey and A.-I. Zaghloul, Dual-Polarized Dual-Band Antenna Element for ISM Bands, *IEEE Antennas Propagation Society (APS-URSI) International Symposium 2009*, Charleston, South Carolina, pp. 1-4, Jun. 2009.

[63] W.-M. Dorsey and A.-I. Zaghloul, Evolutionary Development of a Dual-Band Dual-Polarization Low-Profile Printed Circuit Antenna, *International Conference on Electromagnetics in Advanced Applications (ICEAA) 2009*, Torino, Italy, pp. 994-997, Sept. 2009.

[64] W.-S. Gregorwich, A multipolarization dual-band array, *Antennas and Propagation Society International Symposium*, Vol. 13, pp. 189-192, Jun. 1975.

[65] L. Duchesne, *et al*, Dual polarised dual frequency axial array with iso flux pattern for low orbit space applications, *IEEE International Symposium on Antennas and Propagation (APSURSI) 2011*, Spokane, WA, pp. 153-155, Jul.2011.

[66] Y.-B. Jung and S.-Y. Eom, Dual-Band Horn Array Design Using a Helical Exciter for Mobile Satellite Communication Terminals, *IEEE Transactions on Antennas and Propagation*, Vol. 60, No. 3, pp. 1336-1342, Mar. 2012.

[67] C.-A. Chen and T.-K. Tung, A Dual-Frequency Antenna with Dichroic Reflector and Microstrip Array Sharing a Common Aperture, *IEEE Antennas Propagation Society (APS) International Symposium 1982*, Albuquerque, New Mexico, Vol. 20, pp. 296-299, May 1982.

[68] A.-I. Zaghloul, V. Blacksburg and B.-A. Pontano, Hybrid Reflector-Array Antenna Concept, *IEEE Antennas and Propagation Society International Symposium 2006*, Albuquerque, NM, pp. 4311-4314, Jul. 2006.

[69] A. Yu, *et al*, Experimental Demonstration of a Single Layer Tri-band Circularly Polarized Reflectarray, *Antennas and Propagation Society (APS-URSI) International Symposium 2010*, Toronto, Ontario, Canada, pp. 1-4, Jul. 2010.

[70] C. Guclu, J. Perruisseau-Carrier and O.-A. Civi, Dual frequency reflectarray cell using split-ring elements with RF MEMS switches, *IEEE Antennas and Propagation Society International Symposium (APSURSI) 2010*, Toronto, ON, pp. 1-4, Jul. 2010.

[71] M.-R. Chaharmir, J. Shaker and H. Legay, Dual-band Ka/X reflectarray with broadband loop elements, *IET Microwaves, Antennas & Propagation*, Vol. 4, No. 2, pp. 225-231, Feb. 2010.

[72] T. Smith, An FSS-Backed 20/30 GHz Circularly Polarized Reflectarray for a Shared Aperture L- and Ka-Band Satellite Communication Antenna, *IEEE Transactions on Antennas and Propagation*, Vol. 62, No. 2, pp. 661-668, Feb, 2014.

[73] S.-H. Hsu, *et al*, An Offset Linear-Array-Fed Ku/Ka Dual-Band Reflectarray for Planet Cloud / Precipitation Radar, *IEEE Transactions on Antennas and Propagation*, Vol. 55, No. 11, pp. 3114 -3122, Nov. 2007.

[74] Y. Rahmat-Samii, A novel lightweight dual-frequency dual-polarized sixteen-element stacked patch microstrip array antenna for soil-moisture and sea-surface-salinity missions, *IEEE Antennas and Propagation Magazine*, Vol. 48, No. 6, pp. 33-46, Dec. 2006.

[75] P. Valle, *et al*, Efficient Dual-Band Planar Array Suitable to Galileo, *First European Conference on Antennas and Propagation 2006, EuCAP 2006*, Nice, pp. 1-7, Nov. 2006.

[76] S. Soodmand, A Novel Circular Shaped Dual-Band Dual-Polarized Patch Antenna and Introducing a New Approach for Designing Combined Feed Network, *Loughborough Antennas and Propagation Conference (LAPC) 2009*, Loughborough University, UK, pp. 401-404, Nov. 2009.

[77] A. Sondas, M.-H.-B. Ucar and Y.-E. Erdemli, Loop-loaded printed dipole array design for a

dual-band radar application, *Antennas and Propagation Conference 2009, LAPC 2009,* Loughborough, pp. 529-532, Nov. 2009.

[78] S.-E.-V. Amaldoss, M. Simeoni and A. Yarovoy, Comparative analysis of dual-band array radiator interactions in rectangular and triangular grids, *6th European Conference on Antennas and Propagation (EUCAP) 2012*, Prague, pp. 607-610, Mar. 2012.

[79] A. Sondas, M.-H.-B. Ucar and Y.-E. Erdemli, Dual-band loop-loaded printed dipole array with a corporate balun/feed structure, *IET Microwaves, Antennas & Propagation*, Vol. 6, No. 10, pp. 1109-1116, Jul. 2012.

[80] A.-S.-E. Valavan, M. Simeoni and A.-G. Yarovoy, Impact of truncation on finite-sized dual-band linear phased arrays, *9th European Radar Conference (EuRAD) 2012*, Amsterdam, pp. 622-625, Oct. 2012.

[81] S.-E. Valavan, *et al*, Dual-Band Wide-Angle Scanning Planar Phased Array in X/Ku-Bands, *IEEE Transactions on Antennas and Propagation*, Vol. 62, No. 5, pp. 2514-2521, May 2014.

[82] M. Wei, *et al*, Design of an X/Ka Dual-Band Co-Aperture Broadband Microstrip Antenna Array, *IEEE Microwave Technology and Computational Electromagnetics (ICMTCE)*, Beijing, China, pp. 217-220, May 2011.

[83] X. Qu, *et al*, Design of an S/X Dual-Band Dual-Polarised Microstrip Antenna Array for SAR Applications, *IET Microwaves, Antennas & Propagation*, Vol. 1, No. 2, pp. 513-517, 2007.

[84] X. Qu, S.-S. Zhong and Y.-M. Zhang, Dual-Band Dual-Polarised Microstrip Antenna Array for SAR Applications, *Electronic Letters*, Vol. 42, No. 24, pp. 1376-1377, 2006.

[85] K.-M. Lee, A.-T.-S. Wang and R.-S. Chu, Dual-Band Dual-Polarization Interleaved Cross-Dipole and Cavity-Backed Disc Elements Phased Array Antenna, *IEEE Antennas Propagation Society (APS) International Symposium*, Montreal, Quebec, Canada, Vol. 2, pp. 694-697, Jul. 1997.

[86] Y.-H. Cui, R.-L. Li and P. Wang, Novel Dual-Broadband Planar Antenna and Its Array for 2G/3G/LTE Base Stations, *IEEE Transactions on Antennas and Propagation*, Vol. 61, No. 3, pp.

1132-1139, Mar. 2013.

[87] K. Naishadham, *et al*, A Shared-Aperture Dual-Band Planar Array With Self-Similar Printed Folded Dipoles, *IEEE Transactions on Antennas and Propagation*, Vol. 61, No. 2, pp. 606-613, Feb. 2013.

[88] C. Li and X. Lu, A L/X Dual-Frequency Co-Aperture Microstrip Array Design, *IEEE Antennas Propagation Society (APS) International Symposium 2005*, Washington DC, Vol. 1B, pp. 795-798, Jul. 2005.

[89] Nishizawa, *et al*, Multi-Frequency Array Antenna, *United State Patent*, No. US 6426730 B1, Jul. 2002.

[90] S. He and J. Xie, Analysis and Design of a Novel Dual-Band Array Antenna With a Low Profile for 2400/5800-MHz WLAN Systems, *IEEE Transactions on Antennas and Propagation*, Vol. 58, No. 2, pp. 391-396, 2010.

[91] J.-C. Eade and J. Whitehurst, Dual Band Phased Array Antenna Design for Radar Applications, *11th International Conference on Antennas and Propagation (ICAP) 2001*, Manchester, UK, Vol. 1, pp. 77-81, Apr. 2001.

[92] Wong, *et al*, Multi-Frequency Band Phased-Array Antenna Using Multiple Layered Dipole Arrays, *United States Patent*, No. 5485167, Jan. 1996.

[93] D.-M. Pozar, *et al*, A dual-band dual-polarized array for spaceborne SAR, IEEE Antennas and Propagation Society International Symposium 1998, Atlanta, GA, USA , Vol. 4, pp. 2112-2115, Jun. 1998.

[94] R. Pokuls, J. Uher and D.-M. Pozar, Dual-Frequency and Dual-Polarization Microstrip Antennas for SAR Applications, *IEEE Transactions on Antennas and Propagation*, Vol. 46, No. 9, pp. 1289-1296, 1998.

[95] Y.-J. Ren, *et al*, A dual-frequency dual-polarized planar airborne array antenna, *IEEE Antennas and Propagation Society International Symposium 2008, AP-S 2008*, San Diego, CA, pp. 1-4, Jul. 2008.

[96] S.-H. Hsu, Y.-J. Ren and K. Chang, A Dual-Polarized Planar-Array Antenna for S-Band and X-Band Airborne Applications, *IEEE Transactions on Antennas and Propagation*, Vol. 51, No. 4, pp. 70-78, 2009.

[97] L. Shafai and W. Chamma, Bandwidth and Polarization Characteristics of Perforated Patch Antennas, *10th International Conference on Antennas and Propagation (ICAP)*, Edinburgh, UK, Vol. 1, pp. 43-46, Apr. 1997.

[98] X. Liu, *et al*, A Novel Low-Profile Dual-Band Dual-Polarization Broadband Array Antenna for 2G/3G BaseStation, *IET International Conference on Wireless, Mobile Multimedia Networks (ICWMMN) 2006*, Hangzhou, China, pp. 1-4, Nov. 2006.

[99] W. Hunsicker, K. Naishadham and R. Hasse, Integration of an X-Band Microstrip Patch Array and Beamformer for a Multifunction Antenna Array, *IEEE International Symposium on Phased Array Systems and Technology*, Waltham-Boston, Massachusetts, pp. 898-905, Oct. 2010.

[100] C. Mangenot and J. Lorenzo, Dual band dual polarized radiating subarray for synthetic aperture radar, *IEEE Antennas and Propagation Society International Symposium 1999*, Orlando, FL, USA, Vol. 3, pp. 1640-1643, Jul. 1999.

[101] K. Wincza, S. Gruszczynski and J. Borgosz, Integrated Dual-Band Antenna Array for Application in Nonlinear Junction Detection Device, *38th European Microwave Conference (EuMC)*, Amsterdam, Netherlands, pp. 1078-1081, Oct. 2008.

[102] C. Salvador, *et al*, Dual Frequency Planar Antenna at S and X bands, *Electronics Letters*, Vol. 31, No. 20, pp. 1706-1707, 1995.

[103] G. Gao, *et al*, Shared-Aperture Ku/Ka Bands Microstrip Array Feeds for Parabolic Cylindrical Reflector, *International Conference on Microwave and Millimeter Wave Technology (ICMMT) 2010*, Chengdu, China, pp. 1028-1030, May 2010.

[104] H. Schippers, *et al*, Development of Dual-Frequency Airborne Satcom Antenna with Optical Beamforming, *IEEE Aerospace Conference 2009*, Big Sky, Montana, pp.1-16, Mar. 2009.

[105] A. Thain, *et al*, A dual-band low profile phased array antenna for civil aviation applications, *3rd*

European Conference on Antennas and Propagation 2009, EuCAP 2009, Berlin, pp. 1337-1341, Mar. 2009.

[106] J. Granholm, Dual-Frequency and Dual-Polarization Antennas - An Investigation of Their Suitability for High-Resolution Airborne SAR, *The Technical University of Denmark Ph.D. Dissertation*, 2000.

[107] N. Amiri and K. Forooraghi, Dual-Band and Dual-Polarized Microstrip Array Antenna for GSM900/DCS1800 MHz Base Stations, *IEEE Antennas and Propagation Society (APS) International Symposium 2006*, Albuquerque, New Mexico, pp. 4439-4442, Jul. 2006.

[108] C. McCarrick, Dual-Frequency Antenna Aids WLAN Applications, *Microwave and RF*, pp. 174-178, 1993.

[109] L.-L. Shafa, *et al*, Dual-Band Dual-Polarized Perforated Microstrip Antennas for SAR Applications, *IEEE Transactions on Antennas and Propagation*, Vol. 48, No. 1, pp. 58-66, 2000.

[110] D.-M. Pozar and S.-D. Targonski, A Shared-Aperture Dual-Band Dual-Polarized Microstrip Array, *IEEE Transactions on Antennas and Propagation*, Vol. 49, No. 2, pp. 150-157, 2001.

[111] S.-D. Targonski and D.M. Pozar, An L/X dual-band dual-polarized shared-aperture array for spaceborne SAR, *IEEE Antennas and Propagation Society International Symposium 1999*, Orlando, FL, USA, Vol. 4, pp. 2306-2309, Jul. 1999.

[112] D. Isleifson and L. Shafai, A study on the design of dual-band perforated microstrip antennas for SAR applications, *15th International Symposium on Antenna Technology and Applied Electromagnetics (ANTEM)*, Toulouse, pp. 1-3, Jun. 2012.

[113] Y. Lee, *et al*, A dual band and dual polarization array antenna for AMRFC application, *IEEE Antennas and Propagation Society International Symposium (APSURSI) 2012*, Chicago, IL, pp. 1-2, Jul. 2012.

[114] S.-G. Zhuo and T.-H. Chio, Dual-wideband and dual-polarized shared aperture antenna, *International Symposium on Antennas and Propagation (ISAP) 2012*, Nagoya, pp. 798-801, Oct. 2012.

[115] S.-G. Zhou and T.-H. Chio, Dual-wideband, dual-polarized shared aperture antenna with high isolation and low cross-polarization, *10th International Symposium on Antennas, Propagation and EM Theory (ISAPE) 2012*, Xian, pp. 30-33, Oct. 2012.

[116] S.-D. Targonski and D.M. Pozar, Dual-band dual polarised printed antenna element, *Electronics Letters*, Vol. 34, No. 23, pp. 2193-2194, Nov. 1998.

[117] J. Granholm and N. Skou, Dual-frequency, dual-polarization microstrip antenna development for high-resolution, airborne SAR, *Asia-Pacific Microwave Conference 2000*, Sydney, NSW, pp. 12-20, 2000.

[118] G. Jaworski, *et al*, Dual Frequency & Dual-Linear Polarization Integrated Antenna Array for Application in Synthetic Aperture Radar, *European Microwave Conference (EuMC) 2010*, Paris, France, pp. 523-526, Sept. 2010.

[119] G. Jaworski, K. Wincza and S. Gruszczyski, Dual-Polarized Stacked C-band Antenna Element with Novel Hairpin-Type Contactless Stripline to Stripline Transition in Multilayer Integrated Structure for SAR Applications, *Loughborough Antennas and Propagation Conference (LAPC) 2009*, Loughborough University, UK, pp. 337-340, Nov. 2009.

[120] K. Wincza, S. Gruszczynski, and J. Grzegorz, Integrated Dual-Band Dual-Polarized Antenna Element for SAR Applications, *IEEE Wireless Microwave Technology Conference (WAMICON '09) 2009*, Clearwater, Florida, pp. 1-4, Apr. 2009.

[121] G. Vetharatnam, C.-B. Kuan and C.-H. Teik, Combined Feed Network for a Shared-Aperture Dual-Band Dual-Polarized Array, *IEEE Antennas Wireless Propagation Letters*, Vol. 4, pp. 297-299, 2005.

[122] A. Margomenos, Dual-Band Antenna Array and RF Front-End for mm-Wave Imager and Radar, *United States Patent*, No. US 8022861 B2, Sept. 2011.

[123] A. Vallecchi, G.-B. Gentili and M. Calamia, Dual-Band Dual Polarization Microstrip Antenna, *IEEE Antennas and Propagation Society (APS) International Symposium*, Columbus, Ohio, Vol. 4, pp. 134-137, Jun. 2003.

[124] A.-A. Abdelaziz, A. Henderson and J.-R. James, Dual Band Planar Antenna with Interference Suppression, *IEE Colloquium on Multi-Band Antennas*, London, UK, pp.1-5, Oct. 1992.

[125] M. Moghaddam, et al, Dual Polarized UHF/VHF Honeycomb Stacked-Patch Feed Array for a Large-Aperture Space-borne Radar Antenna, *IEEE Aerospace Conference*, Big Sky, Montana, pp. 1-10, Mar. 2007.

[126] K.-S. Kona, M. Manteghi and Y.-R. Samii, A Novel Dual-Frequency Dual-Polarized Stacked Patch Microstrip Array Feed for Remote Sensing Reflector Antennas, *Microwave and Optical Technology Letters*, Vol. 48, No. 7, pp. 1250-1258, 2006.

[127] J. Anguera, *et al*, Broadband Triple-Frequency Microstrip Patch Radiator Combining a Dual-Band Modified Sierpinski Fractal and a Monoband Antenna, *IEEE Transactions on Antennas and Propagation*, Vol. 54, No. 11, pp. 3367-3373, 2006.

[128] K.-L. Lau and K.-M. Luk, A Wide-Band Circularly Polarized L-Probe Coupled Patch Antenna for Dual-Band Operation, *IEEE Transactions on Antennas and Propagation*, Vol. 53, No. 8, pp. 2636-2644, 2005.

[129] T. Chan and Y. Hwang, A Dual-Band Microstrip Array Antenna, *IEEE Antennas and Propagation Society (APS) International Symposium 1995*, Newport Beach, California, Vol. 4, pp. 2132 -2135, Jun. 1995.

[130] B. Lindmark, A Dual Polarized Dual Band Microstrip Antenna for Wireless Communications, *IEEE Aerospace Conference*, Snowmass at Aspen, Colorado, Vol. 3, pp. 333-338, Mar. 1998.

[131] P. Li, K.-M. Luk and K.-L. Lau, A Dual-Feed Dual-Band L-Probe Patch Antenna, *IEEE Transactions on Antennas and Propagation*, Vol. 53, No. 7, pp. 2321-2323, 2005.

[132] S.-G. Zhou, P.-K. Tan and T.-H. Chio, Wideband, low profile P- and Ku band shared aperture antenna with high isolation and low cross-polarisation, *IET Microwaves, Antennas and Propagation*, Vol. 7, No. 4, pp. 223-229, Mar. 2013.

[133] L. Corey, A graphical technique for determining optimal array antenna geometry, *IEEE Transactions on Antennas and Propagation*, Vol. 33, No. 7, pp. 719-726, Jul. 1985.

[134] K. Woelders and J. Granholm, Cross-Polarization and Sidelobe Suppression in Dual Linear Polarization Antenna Arrays, *IEEE Transactions on Antennas and Propagation*, Vol. 45, No. 12, pp. 1727-1740, 1997.

[135] J. Granholm and K. Woelders, Dual Polarization Stacked Microstrip Patch Antenna Array with Very Low Cross-Polarization, *IEEE Transactions on Antennas and Propagation*, Vol. 49, No. 10, pp. 1393-1402, 2001.

[136] X.-L. Liang, S.-S. Zhong and W. Wang, Cross-Polarization Suppression of Dual-Polarization Linear Microstrip Antenna Arrays, *Microwave and Optical Technology Letters*, Vol. 42, No. 6, pp. 448-451, 2004.

[137] R.-B. Waterhouse, Design of Probe-Fed Stacked Patches, *IEEE Transactions on Antennas and Propagation*, Vol. 47, No. 12, pp. 1780-1784, 1999.

[138] M. Edimo, *et al*, Simple Circuit Model for Coax-Fed Stacked Rectangular Microstrip Patch Antenna, *IEE Proceedings - Microwave, Antennas and Propagation*, Vol. 145, No. 3, pp. 268-272, 1998.

[139] F. Croq and D.-M. Pozar, Millimeter-Wave Design of Wide-Band Aperture-Coupled Stacked Microstrip Antennas, *IEEE Transactions on Antennas and Propagation*, Vol. 39, No. 12, pp. 1770-1776, 1991.

[140] S.-D. Targonski, R.-B. Waterhouse and D.-M. Pozar, Design of Wide-Band Aperture-Stacked Patch Microstrip Antennas, *IEEE Transactions on Antennas and Propagation*, Vol. 46, No. 9, pp. 1245-1251, 1998.

[141] M. Himdi, J.-P. Daniel and C. Terret, Transmission Line Analysis of Aperture-Coupled Microstrip Antenna, *Electronics Letters*, Vol. 25, No. 18, pp. 1229-1230, 1989.

[142] J. Huang, Microstrip antenna developments at JPL, *IEEE Antennas and Propagation Magazine*, Vol. 33, No. 3, pp.33-41, Jun. 1991.

[143] Z. Sun, S.-S. Zhong and X.-R. Tang, C-Band Dual-Polarized Stacked Patch Antenna with Low Cross-Polarization and High Isolation, *European Conference on Antennas and Propagation*

(EuCAP), Berlin, Germany, pp. 2994-2997, Mar. 2009.

[144] S.-C. Gao, *et al*, Dual-Polarized Slot-Coupled Planar Antenna with Wide Bandwidth, *IEEE Transactions on Antennas and Propagation*, Vol. 51, No. 3, pp. 441-448, 2003.

[145] S.-K. Padhi, *et al*, A Dual Polarized Aperture Coupled Circular Patch Antenna Using a C-Shaped Coupling Slot, *IEEE Transactions on Antennas and Propagation*, Vol. 51, No. 12, pp. 3295-3298, 2003.

[146] G.-S. Parker, *et al*, Dual Polarised Microstrip Ring Antenna with Good Isolation, *Electronics Letters*, Vol. 34, No. 11, pp. 1043-1044, 1998.

[147] J. Lu, *et al*, A High-Isolation Dual-polarization Microstrip Patch Antenna with Quasi-Cross-Shaped Coupling Slot, *IEEE Transactions on Antennas and Propagation*, Vol. 59, No. 7, pp. 2713-2717, 2011.

[148] M. Yamazaki, E.-T. Rahardjo and M. Haneishi, Construction of a Slot-Coupled Planar Antenna for Dual Polarisation, *Electronics Letters*, Vol. 30, No. 22, pp. 1814-1815, 1994.

[149] M. Kaboli, S.-A. Mirtaheri and M.-S. Abrishamian, High-Isolation X-Polar Antenna, *IEEE Antennas Wireless Propagation Letters*, Vol. 9, pp. 401-404, 2010.

[150] H. Wong, K.-L. Lau and K.-M. Luk, Design of Dual-Polarized L-Probe Patch Antenna Arrays with High Isolation, *IEEE Transactions on Antennas and Propagation*, Vol. 52, No. 1, pp. 45-52, 2004.

[151] K.-L. Wong, H.-C. Tung and T.-W. Chiou, Broadband Dual-Polarized Aperture-Coupled Patch Antennas with Modified H-Shaped Coupling Slots, *IEEE Transactions on Antennas and Propagation*, Vol. 50, No. 2, pp. 188-191, 2002.

[152] Y.-X. Guo, K.-M. Luk and K.-F. Lee, Broadband Dual Polarization Patch Element for Cellular-Phone Base Stations, *IEEE Transactions on Antennas and Propagation*, Vol. 50, No. 2, pp. 251-253, 2002.

[153] T.-W. Chiou and K.-L. Wong, Broad-Band Dual-Polarized Single Microstrip Patch Antenna With High Isolation and Low Cross Polarization, *IEEE Transactions on Antennas Propagation*,

Vol. 50, No. 3, pp. 399-401, 2002.

[154] W. Wang, S.-S. Zhong and X.-L. Liang, A Dual-Polarized Stacked Microstrip Antenna Subarray for X-Band SAR Application, *IEEE Antennas and Propagation Society International Symposium 2004*, Monterey, California, Vol. 2, pp. 1603-1606, Jun. 2004.

[155] D.-M. Pozar and S.-D. Targonski, Improved coupling for aperture coupled microstrip antennas, *Electronics Letters*, Vol. 27, No. 13, pp. 1129-1131, Jun. 1991.

[156] V. Rathi, G. Kumar and K.-P. Ray, Improved coupling for aperture coupled microstrip antennas, *IEEE Transactions on Antennas and Propagation*, Vol. 44, No. 8, pp. 1196-1198, Aug. 1996.

[157] H.-F. Pues and A.-R.-V.-D. Capelle, An Impedance-Matching Technique for Increasing the Bandwidth of Microstrip Antennas, *IEEE Transactions on Antennas and Propagation*, Vol. 37, No. 11, pp. 1345-1354, 1989.

[158] T.-P. Wong, K.-M. Luk and D.-Y. Lin, Isolation enhancement of dual polarized L-probe coupled patch antenna arrays, *IEEE Antennas and Propagation Society International Symposium 2004*, Vol. 4, pp. 4364-4367, Jun. 2004.

[159] R. Li, *et al*, Radiation-Pattern Improvement of Patch Antennas on a Large-Size Substrate Using a Compact Soft Surface Structure and its Realization on LTCC Multilayer Technology, *IEEE Transactions on Antennas and Propagation*, Vol. 53, No. 1, pp. 200-208, 2005.

[160] A.-U. Zaman, L. Manholm and A. Derneryd, Dual Polarised Microstrip Patch Antenna with High Port Isolation, *Electronics Letters*, Vol. 43, No. 10, pp. 551-552, 2007.

[161] L.-B. Kong, S.-S. Zhong, Z. Sun, Broadband Microstrip Element Design of a DBDP Shared-Aperture SAR Array, *Microwave and Optical Technology Letters*, Vol. 54, No. 1, pp. 133-136, Jan. 2012.

[162] D.-M. Pozar, Microwave Engineering, *Wiley*, 2004.

[163] C.-A. Balanis, Antenna Theory: Analysis and Design, 3rd Edition, *Wiley-Interscience*, Apr. 2005.

[164] K.-S. Kona and Y.-R. Samii, Novel Probe-Feeding Architectures for Stacked Microstrip Patch Antennas, *Microwave and Optical Technology Letters*, Vol. 38, No. 6, pp. 467-475, 2003.

[165] D. Isleifson and L. Shafai, A study on the design of dual-band perforated microstrip antennas for SAR applications, *15th International Symposium on Antenna Technology and Applied Electromagnetics (ANTEM) 2012*, Toulouse, pp. 1-3, Jun. 2012.

[166] Y. Lee, *et al*, Design of a Bandwidth Enhanced Dual-Band Dual Polarized Array Antenna, *Proceedings of ISAP 2012*, Nagoya, Japan, pp. 1281-1284, 2012.

[167] B. Li and Z.X. Shen, Dual-band frequency selective structure with large frequency band ratio, *IEEE MTT-S International Microwave Workshop Series on RF and Wireless Technologies for Biomedical and Healthcare Applications (IMWS-BIO) 2013*, Singapore, pp. 1-3, Dec. 2013.

[168] L.-N. Zhang, S.-S. Zhong and X.-L. Liang, Dual-band Dual-polarized Hybrid Antenna Array, *2010 PIERS Proceedings*, Xi'an, China, pp. 294-298, Mar. 2010.